

Design and optimisation of a heliostat field and a sodium receiver for next-generation CSP plants



Australian
National
University

A thesis submitted for the degree of
Doctor of Philosophy of
The Australian National University
by

Shuang Wang

Supervisory Panel

Assoc. Prof. Joe Coventry

Primary Supervisor and Chair

Assoc. Prof. John Pye

Associate Supervisor

Dr. Charles-Alexis Asselineau

Associate Supervisor

November 2022

© Copyright by Shuang Wang 2022
All Rights Reserved

Except where otherwise indicated, this thesis is my own original work.

Shuang Wang
3 November 2022

This thesis is dedicated to my wife Junjie Hu, who has supported me through everything.

Acknowledgments

First and foremost, I would like to express my sincere thanks to my primary supervisor, Assoc. Prof. Joe Coventry. I learnt from him how to do scientific research, how to make research schedule, how to write academic publications, and how to live a life out of research. I would like to thank my associate supervisors, Assoc. Prof. John Pye and Dr. Charles-Alexis Asselineau. John is always patient and generous in sharing his knowledge and experience. Charlie is a professional guider, and also a friend and a brother for me. I furthermore gratefully acknowledge Prof. Wojciech Lipinski. I always learn from his enthusiasm, dedication and meticulousness towards research.

Special thanks are expressed to Dr. Ye Wang, who contributed to the optical and system-level modelling work in this thesis, to Dr. Charles-Alexis Asselineau, who established the receiver heat balance model, to Mr. William Logie, who generated the allowable maximum flux tables, and to Mr. Armando Fontalvo and Mr. Salvatore Guccione, who established the original system-level model. Thanks all!

I would like to thank all colleagues from the Solar Thermal Group. It has been a pleasure working alongside the whole team and observing the progress of the group. It is hard to say goodbye to any members in the group. I would like to express my thanks to the ASTRI Gen3L team. We have jumped over a big research gap with everyone's dedication to the project. Nice work!

This research was performed as part of the Australian Solar Thermal Research Institute (ASTRI), a project supported by the Australian Government, through the Australian Renewable Energy Agency (ARENA). The funding support is gratefully acknowledged.

The computationally heavy simulations were mostly performed through the 'xa1' project on Gadi, the supercomputer of the Australian National Computational Infrastructure (NCI). The support is gratefully acknowledged.

Last but not least, I would like to extend my gratitude to my parents, Junhong Wang and Chunfang Wang, and my wife, Junjie Hu.

Abstract

The heliostat field and receiver subsystems are crucial in a concentrated solar power (CSP) plant, where solar irradiance is converted into thermal power. It is essential to optimise the subsystems at the design stage to maximise the energy yield and to minimise the cost. This thesis presents different modelling methodologies and case studies for the optimal design of the heliostat field and tubular receiver subsystems for next-generation CSP plants.

Firstly, heliostat aiming strategy affects the thermo-mechanical performance of the receiver and is a key factor for receiver reliability and interactions between the field and receiver. For the external cylindrical receiver, the modified deviation-based aiming (MDBA) method is proposed as a fast and accurate heliostat aiming strategy based on ray-tracing. The new aiming model enables efficient use of ray-tracing together with receiver thermal and mechanical models to closely match the flux distribution to local values of allowable flux on the receiver. The MDBA method maximises the thermal output while respecting thermal stress limits on the receiver, and is then coupled to a new co-optimisation technique to design the heliostat field and receiver together.

In the co-optimisation method, instantaneous optical, thermal and mechanical models are integrated in an annual system-level model to capture the highly transient behaviour of the subsystem, and the design is optimised using a genetic algorithm. Several techniques are implemented to make this complex and computationally expensive problem tractable. The co-optimisation method can be used to maximise the annual solar-to-thermal efficiency or to minimise the levelised cost of energy (LCOE).

It is found that the receiver flow configuration, including the flow path pattern and pipe diameter, affects receiver performance. Hence, the proposed integrated design methodology is used to explore the optimal flow configuration for a receiver with an oversized field at both design-point and annual conditions. The results show that the optimal receiver flow configuration achieves a low fraction of heliostat defocusing with a 20% oversized field, although the benefits on the annual energy yield are weakened by capacity limits of other system components.

Therefore, a system-level optimisation is implemented with relative sizing of the field, receiver, sodium-salt heat exchanger, storage and power block to achieve the lowest LCOE. An iterative surrogate-based optimisation (SBO) technique is proposed to accelerate the optimisation process. The best achieved LCOE is below 60.0 US-D/MWh, within the range targeted by the DoE Gen3 program. A high capacity factor of 83.2% is achieved in the optimal design.

A further topic in this PhD thesis is the option of spillage skirts and secondary reflectors for performance enhancement of a cavity receiver.

List of Publications

Journal articles

1. S. Wang, C.A. Asselineau, W.R. Logie, J. Pye, J. Coventry, MDBA: An accurate and efficient method for aiming heliostats. *Solar Energy*, 2021, 225: 694-707.
2. S. Wang, C.A. Asselineau, Y. Wang, J. Pye, J. Coventry, Performance enhancement of cavity receivers with spillage skirts and secondary reflectors in concentrated solar dish and tower systems. *Solar Energy*, 2020, 208: 708-727.

Conference

1. S. Wang, C.A. Asselineau, J. Pye, J. Coventry, Maximising receiver output with an oversized heliostat field. *SolarPACES2021*, Virtual Conference. 2021. Poster.
2. S. Wang, C.A. Asselineau, J. Pye, J. Coventry, Performance co-optimisation of a heliostat field and a cylindrical receiver. *APSRC2020*, Virtual Conference. 2020. Oral presentation.
3. S. Wang, C.A. Asselineau, J. Pye, J. Coventry, An efficient method for aiming heliostats using ray-tracing. *SolarPACES2020*, Virtual Conference. 2020. Oral presentation.
4. C.A. Asselineau, W.R. Logie, J. Pye, F. Venn, S. Wang, J. Coventry, Design of a heliostat field and liquid sodium cylindrical receiver for the Gen3 Liquids Pathway. *SolarPACES2020*, Virtual Conference. 2020.
5. A. Fontalvo, S. Guccione, Y. Wang, S. Wang, C.A. Asselineau, J. Coventry, J. Pye, System-Level Comparison of Sodium and Salt Systems in Support of the Gen3 Liquids Pathway. *SolarPACES2020*, Virtual Conference. 2020.
6. S. Wang, C.A. Asselineau, J. Pye, J. Coventry, Enhancement of performance of a cavity receiver on a solar tower system by employing spillage skirts and secondary reflectors. *APSRC2019*. Oral presentation.
7. S. Wang, C.A. Asselineau, J. Pye, J. Coventry, Augmenting cavity receiver performance: Spillage skirts and secondary reflectors. *AIP Conference Proceedings*. 2020, 2303(1): 030035. Oral presentation.

Research report

1. C. Turchi, S. Gage, J. Martinek, ..., Wang S, et al. CSP Gen3: Liquid-Phase Pathway to SunShot[R]. National Renewable Energy Lab.(NREL), Golden, CO (United States), 2021.

Contents

Acknowledgments	vii
Abstract	ix
List of Publications	xi
List of Figures	xix
List of Tables	xxvii
Nomenclature	xxix
1 Introduction	1
1.1 Next-generation CSP plants	1
1.1.1 Background for 3rd generation CSP plants	1
1.1.2 Liquid sodium as the heat transfer fluid	2
1.2 Literature review	4
1.2.1 Heliostat field layout	4
1.2.2 Receiver	6
1.2.2.1 External receiver	6
1.2.2.2 Cavity receiver	7
1.2.3 Heliostat aiming strategy	10
1.2.4 Co-optimisation of the heliostat field and the receiver	12
1.2.5 System-level optimisation	12
1.3 Research objectives	13
1.4 Thesis outline	14
2 Modelling methodology	17
2.1 Introduction	17
2.2 Instantaneous modelling methodology	17
2.2.1 Optical modelling	17
2.2.2 Heat transfer modelling	22
2.2.3 Thermomechanical stress limits	25
2.3 Annual modelling technique	26
2.3.1 Annual optical modelling	26
2.3.2 Annual heat transfer modelling	28
2.4 System model and modelling technique	30
2.4.1 Gen3L system	30

2.4.2	System-level model	32
2.4.2.1	SolarTherm model	32
2.4.2.2	Heliostat field defocusing strategies	33
2.5	Conclusion for this chapter	35
3	Performance enhancement of cavity receivers with spillage skirts and secondary reflectors	37
3.1	Introduction	37
3.2	Physical models	38
3.2.1	The cylindrical cavity receiver	38
3.2.2	The spillage skirts	38
3.2.3	The secondary reflectors	39
3.2.4	Combination of spillage skirt and secondary reflectors	42
3.3	Modelling methodology	42
3.3.1	Energy balance	42
3.3.1.1	Optical processes	42
3.3.1.2	Heat transfer processes	42
3.3.1.3	Efficiencies and losses definitions	43
3.3.2	Progressive Monte Carlo Evaluation method	43
3.4	Performance enhancement of cavity receivers in a dish system	45
3.4.1	The SG4 Big Dish	45
3.4.2	Parametric study and optimisation of the cylindrical cavity receiver	45
3.4.3	Optimisation of the cylindrical receiver with spillage skirts	47
3.4.4	Optimisation of a cylindrical receiver with secondary reflectors	49
3.4.5	Optimisation of the cylindrical receiver with both spillage skirts and secondary reflectors	52
3.5	Performance enhancement of a cavity receiver in a tower system	52
3.5.1	The PS10 tower field	53
3.5.2	Analysis and optimisation of the cylindrical cavity receiver for the tower configuration	54
3.5.3	Optimisation for the tower receiver with spillage skirts	55
3.5.4	Optimisation for the tower receiver with secondary reflectors	56
3.5.4.1	Parametric study of the tower receiver with a conical reflector	57
3.5.4.2	Parametric study of the tower receiver with a trumpet reflector	59
3.5.4.3	Parametric study of the tower receiver with a CPC reflector	61
3.5.4.4	Optimisation of the tower receivers with secondary reflectors	62
3.5.4.5	Optimisation of the tower receiver with both a spillage skirt and secondary reflectors	64
3.6	Conclusion for this chapter	65

4	MDBA: an accurate and efficient method for aiming heliostats	67
4.1	Introduction	67
4.2	Models and methodology	68
4.2.1	The reference system	68
4.2.2	Methodology	68
4.2.2.1	Optical model	68
4.2.2.2	Heat transfer model	69
4.2.2.3	Thermo-mechanical stress limits	69
4.3	Aiming strategy reference cases	70
4.3.1	Image Size Priority method	70
4.3.2	Deviation-based aiming strategy	70
4.3.3	Comparison of DBA with ISP	71
4.4	The modified deviation-based aiming (MDBA) method	73
4.4.1	Description of the method	73
4.4.2	Effect of the aiming extent E	75
4.4.3	Effect of the shape exponent S	76
4.4.4	Effect of the asymmetry factor A	76
4.5	MDBA parameter determination methods	80
4.5.1	Optimisation-based MDBA method	80
4.5.1.1	Problem formulation	80
4.5.1.2	Choice of the optimisation method	81
4.5.1.3	Results of the optimisation-based method	81
4.5.1.4	Optimisation-based method with division into sub-problems	83
4.5.2	Sequential determination of MDBA parameters	85
4.5.2.1	Search algorithm	85
4.5.2.2	Fitting algorithm	87
4.5.2.3	Adjustment algorithm	87
4.5.2.4	Results of the sequential method	88
4.5.2.5	Sensitivity analysis of the factor m	89
4.5.3	Feedback-based MDBA method	90
4.5.3.1	Determination of the asymmetry factor A	90
4.5.3.2	Determination of the shape exponent S	92
4.5.3.3	Results of the feedback-based method	94
4.6	Use of the MDBA method in annual simulations	95
4.6.1	Determination of aiming variables with clear-sky irradiance	95
4.6.1.1	Aiming interpolation method	95
4.6.1.2	Validation of the interpolation method	96
4.6.2	Use of the MDBA method in annual simulations with varying DNI	98
4.7	Conclusion for this chapter	98

5	Co-optimisation of the heliostat field and the receiver	101
5.1	Introduction	101
5.2	Models and methodology	102
5.2.1	The reference system	102
5.2.2	Instantaneous energy balance methodology	102
5.3	Annual simulation co-optimisation methodology	102
5.3.1	Generation of the field layout	102
5.3.2	Annual optical performance	104
5.3.3	Trimming of the large heliostat field	105
5.3.4	Determination of the receiver configuration	106
5.3.5	Aiming strategy	108
5.3.6	Annual receiver performance	109
5.3.7	Integration with system-level simulation	109
5.3.8	Techno-economic model	110
5.3.9	Optimisation algorithm	110
5.4	Results and discussion	111
5.4.1	Design parameter space	111
5.4.2	Optimisation for maximum annual solar-to-thermal efficiency using the reference tower height	112
5.4.3	Comparison with optimisation at instantaneous condition	116
5.4.4	Optimisation for maximum annual solar-to-thermal efficiency using a range of tower heights	117
5.4.5	Optimisation for lowest LCOE	119
5.5	Conclusion for this chapter	120
6	Exploration of optimal receiver flow configurations with an oversized heliostat field	123
6.1	Introduction	123
6.2	Physical models	123
6.3	Methodology	124
6.3.1	Generation of an oversized heliostat field	124
6.3.2	Instantaneous and annual simulation methods	124
6.3.3	Improvement of MDBA for defocusing capability	124
6.3.3.1	Definition of heliostat field defocusing	125
6.3.3.2	Instantaneous heliostat field defocusing	125
6.3.3.3	Heliostat field defocusing in annual simulations	126
6.4	Results and Discussion	129
6.4.1	Effect of different flow paths	129
6.4.1.1	Investigation of the injection direction	130
6.4.1.2	Investigation of the pairing option of tube banks	132
6.4.1.3	Investigation of the east-west crossover option	133
6.4.2	Effect of different pipe outer diameters	134
6.4.3	Annual performance with different flow configurations	137
6.4.4	Selection procedure	139

6.4.5	Application on a triple-pass receiver	139
6.5	Conclusion for this chapter	144
7	Surrogate-based optimisation with varying relative sizing of system components	145
7.1	Introduction	145
7.2	Models and methodology	145
7.3	Parametric study on relative sizing of system components	146
7.3.1	Effect of varying the oversizing factor f_{hst}	146
7.3.2	Effect of varying the heat exchanger capacity ratio f_{HX}	147
7.3.3	Effect of varying the storage hours t_{storage}	148
7.3.4	Parametric study varying both the heat exchanger capacity ratio and the storage hours	149
7.4	Optimisation of the system	150
7.4.1	Optimisation problem	150
7.4.2	Choice of the receiver configuration	152
7.4.3	Determination of the heat exchanger capacity ratio and the storage hours	153
7.4.4	The iterative surrogate-based optimisation (SBO) method	153
7.4.5	Results of the optimisation	155
7.5	Conclusion for this chapter	158
8	Conclusions and future work	161
8.1	Summary of the contributions	161
8.1.1	Contribution to the topic of cavity receiver performance enhancement	161
8.1.2	Contribution to the topic of heliostat field aiming strategy	161
8.1.3	Contribution to the optimisation of the design of central receiver systems	162
8.2	Future work	163

List of Figures

1.1	Illustration of four main CSP technologies [1].	1
1.2	View of the Gemasolar Plant [3]	2
1.3	View of the Vast Solar's Jemalong Solar Station.	3
1.4	Illustration of different field layouts [34]	5
1.5	Illustration of a solar external receiver [58]	8
1.6	Illustration of the spillage skirt at ANU SG3 receiver [73]	9
1.7	The incident flux is controlled below the maximum allowable flux by adjusting the aiming strategy for a molten salt receiver [99]. 'F' and 'AFD' represent the incident flux and flux limit.	11
2.1	Illustration of the optical process in a CSP plant [124].	19
2.2	Sankey diagram of the energy flow in the optical process.	19
2.3	Comparison results of SolarPILOT with five ray-tracing tools at different sun positions [104].	21
2.4	Optical simulation of the heliostat field in SOLSTICE.	22
2.5	Illustration of the heat transfer process at the receiver.	23
2.6	Sankey diagram of the energy flow at the receiver.	24
2.7	Flowchart of the receiver thermal model.	25
2.8	AFD dependent on sodium temperature and velocity (as calculated by Will Logie based on the method in Section 2.2.3 [88, 143]). The pipe outer diameter is 60.3 mm and the pipe thickness is 1.2 mm. The tube material is Alloy 740H. The AFD data can then be integrated with the optical and thermal simulation tools in this thesis.	26
2.9	The sun path for the latitude of Alice Springs. The independent points on the sampling grid are marked by dots [146]	27
2.10	Schematic representation of a reference CSP system based on the Gen3 Liquids Pathway plant.	31
2.11	Exemplar illustration of the heat exchanger and storage defocusing strategies. $\dot{Q}_{\text{rec,max}}$ is the maximum receiver output respecting receiver limits.	34
3.1	The cylindrical cavity receiver	38
3.2	The cavity receiver with spillage skirts	39
3.3	The cavity receiver with a conical reflector	40
3.4	The cavity receiver with a trumpet reflector	41
3.5	The cavity receiver with a CPC reflector	41
3.6	Illustration of the energy flow.	44

3.7	Results of the parametric study for the cylindrical cavity receiver	46
3.8	Optimisation results for cylindrical receiver	47
3.9	Temperature and heat flux distributions of the optimised cylindrical receiver, shown as a plane “unwrapped” from the cylindrical shape, where x represents the angular range, and y represents the vertical height.	48
3.10	Optimised structures and receiver efficiencies for receivers with and without spillage skirts (Black dots represent the focal points, and the shadows represent the shapes of the optimised cylindrical receiver). . .	48
3.11	Efficiencies at different skirt angles	49
3.12	Optimised structures and receiver efficiencies for receivers with secondary reflectors.	50
3.13	Receiver efficiencies at different CPC acceptance angles.	51
3.14	Heat flux distribution of the receiver with CPC surface (configuration D8, $\alpha = 0$)	52
3.15	Optimised structures and receiver efficiencies for receivers with skirt and secondary reflectors.	53
3.16	Illustration of the tilt angle	54
3.17	Optimised structures and receiver efficiencies for receivers with and without the skirt.	55
3.18	Flux map of the optimised cavity receiver	56
3.19	Heliostats’ efficiencies for the optimised cavity receiver	56
3.20	Parametric study for receivers with conical reflectors ($R_{\text{cyl}}=5.29$ m, $H_{\text{cyl}}=9.68$ m).	57
3.21	Heliostats’ efficiencies at different reflector lengths and angles. The black line marks the boundary of the acceptance area, which is the intersection of the acceptance cone with the heliostat field plane. . . .	58
3.22	Receiver efficiencies and reflector shapes for the trumpet at different a ($b=2$, $R_{\text{out}}=10$ m).	59
3.23	Receiver efficiencies and reflector shapes for the trumpet at different b ($a=5.39$, $R_{\text{out}}=10$ m).	60
3.24	O’Gallagher’s trumpet, $b=8.4$, $\eta_{\text{rec}}=58.8\%$, $\eta_{\text{interc}}=67.9\%$, $\eta_{\text{trans}}=99.7\%$. .	61
3.25	Receiver efficiencies and reflector shapes for the trumpet at different R_{out} ($a=5.39$, $b=2$).	61
3.26	Receiver efficiencies and reflector geometries for the CPC reflectors at different θ	62
3.27	Heliostats’ efficiencies at different acceptance angles relevant to the optimised receiver. The black line marks the boundary of the acceptance area, which is the intersection of the acceptance cone with the heliostat field plane.	63
3.28	Optimised structures and receiver efficiencies for receivers with secondary reflectors.	64
3.29	Optimised structures and receiver efficiencies for receivers with spillage skirts and reflectors.	65

4.1	Flow path of the sodium receiver. The receiver is composed of 16 tube banks and 8 flow paths. In each flow path, the HTF is introduced into the top of a north-facing bank, and leaves the receiver at the top of a symmetrically positioned south-facing bank. The equatorial line is located at the vertical centre of the receiver.	69
4.2	Results of the heat transfer model for case S1	69
4.3	Illustration of the aiming extent (E) in the original DBA method.	71
4.4	Flux maps of the four reference aiming cases. The cylindrical surface of the receiver is unfolded to show the flux maps. Left to right parts of the map correspond to tube banks 1 to 16.	72
4.5	Curves of net flux and flux limit at different cases. The grey solid line represents the net flux along the flow path. The red solid and dashed lines represent the variations of the flux limit and safe limit, respectively.	74
4.6	Sectoral division of the heliostat field. The colour-bar represents the normalised focal lengths of each heliostat. The field sectors correspond to the tube banks.	74
4.7	Results at different aiming extent E ($S = 1.5$, $A = 0.5$).	76
4.8	Results at different shape exponents S ($E = 0.8$, $A = 0.5$).	77
4.9	Flowchart for the index matrix algorithm. The algorithm determines the order of +1 and -1 in the index matrix with an input of the asymmetry factor.	78
4.10	Results of the index matrix at different asymmetry factors.	78
4.11	Results with different asymmetry factors A ($E = 0.8$, $S = 1.5$). Case CS-A1: $A = 0.3$ for all south-facing tube banks (T1-T4, T13-T16), $A = 0.7$ for all north-facing tube banks (T5-T12). The opposite setting is applied for the second case.	79
4.12	Location of aiming points for case CS-A1. The colour of the dots gives an indication of the heliostat locations with relation to Figure 4.6.	80
4.13	Definition of D_{over} and D_{under}	81
4.14	Net flux and flux limit for all flow paths (Case O1).	82
4.15	Progress of the optimisation in Case O1. The problem converges when the pattern size is contracted to 0.1 of the original size.	83
4.16	Illustration of the optimisation sub-problems in case O2.	84
4.17	Algorithm flowchart of the search algorithm.	86
4.18	Net flux and flux limit for all flow paths after completion of the search algorithm in the sequential method. The crossover only occurs on tube bank 4 and 13.	86
4.19	Algorithm flowchart of the fit algorithm.	87
4.20	Algorithm flowchart of the adjustment algorithm.	88
4.21	Net flux and flux limit for all flow paths after completion of the sequential method (case S1).	89
4.22	Algorithm flowchart of the feedback-based MDBA method.	90

4.23	Linear regression of the net flux and safe limit curves with varying asymmetry factor A . The dash-dot lines are the results of the linear regression. LB_1 and RB_1 indicate the boundary of aiming range. k_1 and k_2 are calculated slopes for the safe limit and net flux curves.	91
4.24	Flowchart to adjust A	92
4.25	Net flux with varying the shape exponent S . LB_1 and RB_1 are the boundary of aiming range. LB_2 and RB_2 are halved based on the distance from the centre to LB_1 and RB_1	93
4.26	Flowchart to adjust the shape exponent S	94
4.27	The flux profile using the new algorithm. $\eta_{int}=96.5\%$, $N_{evals}=8$	94
4.28	Interpolated results for the aiming extent at tube bank 4. Dots at the black grid represent the points used to validate the interpolated results. The blue solid triangle marks the sun position for case D1.	96
4.29	Comparison of the optimised and interpolated results in case D1 ($\delta = 23.0^\circ$, $\omega = 20.0^\circ$, $DNI = 937.9 \text{ W/m}^2$, $\eta_{int} = 97.0\%$). Grey solid line and blue dashed line represent the net flux calculated from optimisation and interpolation, respectively.	97
4.30	Net flux and flux limit for all flow paths ($\delta = 23.0^\circ$, $\omega = 20.0^\circ$, $DNI = 1031.7 \text{ W/m}^2$, $\eta_{int} = 96.4\%$).	99
5.1	Allowable absorbed flux density at different pipe outer diameter (D_o). .	103
5.2	Flowchart of the co-optimisation method. The algorithm returns the annual solar-to-thermal efficiency or the LCOE as the objective function in the genetic algorithm. N_{gen} represents the number of populations.	103
5.3	Verification of the annual optical simulation method. $\Delta Q/Q_{rec,inc,nom}$ is the difference between simulated and interpolated values of the receiver incident power normalised to the nominal incident power (543 MWth). The dots represent sun positions where optical simulations are performed. Receiver thermal simulations are implemented after the optical simulations on the black-dotted sun positions, as introduced in section 5.3.6. The contour lines show the field efficiency and the colour map highlights the difference between the field outputs calculated from the real simulation and the interpolated values. Sunrise and sunset hours are calculated from equations from Duffie et al. [169]. . . .	105
5.4	Flow path configuration of the receiver. For the double pass configuration, flow exiting a first tube bank then crosses the cylinder to enter the tube bank diametrically opposite (noting there is no interconnection between pipes at the centre of the cylinder, despite the arrows in this figure crossing each other at that point). Each flow path is plotted with a unique colour in the double-pass configuration to help the illustration.	107
5.5	Progression of the optimisation. 'Average' and 'Best' means the average and best values of the objective function within each generation. . .	112

5.6	Evolution of the optimised variables. The grey dots represent all values of the corresponding parameters on the generation while the red triangles represent the best values.	113
5.7	Sensitivity of the system efficiencies to relative variation of optimised variables.	114
5.8	The optimal field layout that achieves the highest annual solar-to-thermal efficiency for a 175m tower height.	114
5.9	Net heat flux and outer wall temperature profiles at design point of the optimal receiver that achieves the highest annual solar-to-thermal efficiency for a 175 m tower height.	115
5.10	Flux profiles along the flow-paths. Red solid lines represent the flux limit and dashed lines the safe limit. Grey solid line represents the net flux. The safe limit is defined as 0.9 of the flux limit. The index of the flow path corresponds to the single-pass configuration as shown in Figure 5.4.	115
5.11	The optimal field layout that achieves the highest design-point solar-to-thermal efficiency for a 175 m tower height. The colour-bar represents the instantaneous optical efficiency of each heliostat.	116
5.12	Heliostat field and receiver breakdown of annual energy losses. The definitions of all energy losses can be found in Chapter 2. Q_{defoc} is the total accumulated value of all defocused losses.	118
5.13	Optimised field layout for a tower height of 250 m.	118
5.14	The optimal field layout that achieves the lowest LCOE.	120
5.15	Tornado chart showing sensitivity of LCOE to key components' costs. The optimised LCOE changes with adjusting the cost of each component by +/- 25 %.	120
6.1	Algorithm flowchart for the MDBA method with a defocusing strategy.	126
6.2	Results after the optimisation for the reference case with a 20% oversized field.	127
6.3	The heliostat field after defocusing for the reference case with a 20% oversized field. Defocused heliostats are represented by grey dots. . . .	127
6.4	Illustration of the DNI ratio. Optical simulations at different DNI ratios are represented by different colours illustrated in the legend. Defocused heliostats are represented by grey dots.	128
6.5	Cumulative distribution of the DNI ratio at Daggett, CA.	128
6.6	Comparison of the simulated, 2D and 3D interpolated results.	129
6.7	Flow path patterns with double passes.	130
6.8	Performance comparison with different injection directions.	131
6.9	Temperature profiles for the absorber surface temperature, internal pipe wall temperature and sodium bulk fluid temperature.	132
6.10	Performance in Case 3 at design point, $D_o=60.33$ mm.	133

6.11	Performance comparison with different crossing flow path strategies in the afternoon, $D_o=60.33$ mm. Cases 5 and 6 correspond to patterns 1 and 4, respectively.	135
6.12	Performance comparison with different crossing flow path strategies in the afternoon, $D_o=48.26$ mm. Cases 5 and 6 correspond to patterns 1 and 4, respectively.	136
6.13	Results of the annual simulations. The annual solar-to-thermal efficiency is illustrated at the top of the bar-chart. It is noted that this is a stacked bar chart and only loss mechanisms are highlighted. The receiver output (shown in white) is truncated at the bottom of the figure, but the values are indicated. Units are GWh. N_{pass} is the number of passes, D_o is the pipe outer diameter, and flow path patterns correspond to the patterns in Figure 6.7.	138
6.14	Flowchart of the selection procedure to choose the best receiver flow configuration.	139
6.15	Illustrations of the flow path pattern for the Gen3L receiver.	140
6.16	Different flow path patterns.	141
6.17	Performances of the Gen3L receiver with Pattern 3-4.	142
6.18	Performances of the Gen3L receiver with the original pattern in Figure 6.15(b).	142
6.19	Results of the annual simulation for the Gen3L receiver. Similar to Figure 6.13, this figure is a stacked bar chart and only loss mechanisms are highlighted. The receiver output (shown in white) is truncated at the bottom of the figure, but the values are indicated. Units are GWh. N_{pass} is the number of passes, D_o is the pipe outer diameter, and flow patterns correspond to the patterns in Figure 6.7.	143
7.1	Effect of the oversizing factor on the number of heliostats (N_{hst}), the annual electricity output (Q_{ele}), the annual solar-to-thermal efficiency ($\eta_{a,st}$), the capacity factor (CF), the capital cost (C_{cap}) and the LCOE. . .	147
7.2	Plot of the power over a year. $\dot{Q}_{rec,max}$ is the maximum receiver output respecting receiver limits. $\dot{Q}_{HX,max}$ is the maximum heat exchanger capacity. $\dot{Q}_{PB,in}$ is the power block nominal input.	148
7.3	Defocusing losses at different oversizing factors.	148
7.4	Effect of the heat exchanger capacity ratio. Both the heat exchanger and storage defocusing losses are plotted in (a).	149
7.5	Plot of the power at a selected week in summer. Shaded area is attributed to defocusing losses.	149
7.6	Effect of the storage hours.	150
7.7	Results of the parametric study varying both the heat exchanger and storage capacities.	150
7.8	Results of the optimal heat exchanger and storage capacities at different heliostat field oversizing factors. The LCOE values are indicated with units of USD/MWh.	151

7.9	Algorithm flowchart for the objective function evaluation.	151
7.10	Illustration of the algorithm to select pipe outer diameters. Blue dots are the selected cases, while red dots are discarded.	152
7.11	Illustration of the bi-directional search to find the optimal storage hours at a given heat exchanger capacity ratio.	153
7.12	Flowchart of a surrogate-based optimisation	154
7.13	Illustration of the process in the iterative SBO method. The inner loop in Figure 7.12 is repeated at each iteration with sampling - true simulation - surrogate building - GA optimisation. Blue dashed lines are the original boundaries. The red dots present the optimal solution at the current iteration. The black dashed lines are the parametric space for the current iteration.	155
7.14	Process of the optimisation. Red dots represent the optimal value at each iteration. The number of simulations is 500, 20% of the GA method.	156
7.15	Variation of the objective function. Grey dots represent the sampling results evaluated by the true model. Red triangles and dots represent the optimal point evaluated by the surrogate and true models, respectively.	157
7.16	Energy breakdown of the field and the receiver subsystem.	158
7.17	Annual optical efficiency of heliostats for the optimal design. The optical efficiencies are evaluate using the method presented in Section 5.3.2	158

List of Tables

2.1	Performance of the receivers with and without spillage skirts	30
3.1	Parameters for the cylindrical cavity receivers	39
3.2	Parameters of the dish model	45
3.3	Performance of the receivers with and without spillage skirts	47
3.4	Efficiencies and losses for receivers with reflectors	50
3.5	Efficiencies and losses for receivers with skirt and reflectors	53
3.6	Parameters of the PS10 tower field	54
3.7	Optimisation results for receivers with the spillage skirts	55
3.8	Efficiencies and losses for receivers with reflectors	64
4.1	Parameters for the cylindrical cavity receivers	68
4.2	Parameters for the cylindrical cavity receivers	72
4.3	Effect of the aiming extent on peak flux and intercept efficiency ($S = 1.5$, $A = 0.5$).	75
4.4	Effects of the shape exponent on peak flux and intercept efficiency ($E = 0.8$, $A = 0.5$).	77
4.5	Results of the optimisation-based method (case O1). T1-T16 point to tube banks in Figure 4.6.	82
4.6	Summary of the results for the optimisation-based method. $N_{\text{parameters}}$, $N_{\text{sub-problems}}$ and $N_{\text{evals,sub}}$ represent the number of parameters, number of sub-problems and number of evaluations per sub-problem.	85
4.7	Results of the sequential method (case S1). T1-T16 point to tube banks in Figure 4.6.	88
4.8	Results of the sensitivity study. $\eta_{\text{int,search}}$ is the efficiency after the search algorithm. The tube bank index points to banks with cross-over after the search algorithm. N_{evals} is the number of evaluations.	90
4.9	The look-up table for the aiming extent E at tube bank 4 ($\delta_0 \times \omega_0$, unit: $^\circ$).	96
4.10	Results with varying the DNI ratio in case D1. $\eta_{\text{int,equ}}$ is 97.6% at this time point.	98
5.1	Verification of the annual optical model. The relative deviation is calculated with results from hour-by-hour simulations as reference.	104

5.2	Comparison of system efficiencies between an "Optimised" aiming strategy at three design points and a fixed "Design point" aiming strategy that is optimised only for design point (equinox solar noon). "SS", "WS" and "SS +3h" refer to summer solstice solar noon, winter solstice solar noon and summer solstice solar noon +3 hours, respectively. η_{st} is the solar-to-thermal efficiency.	108
5.3	Correlation coefficients in Eq. 2.15 to 2.18 for the reference case.	109
5.4	Verification of the annual receiver models. The relative deviation is calculated with results from hour-by-hour simulations as reference. . .	109
5.5	Cost function parameters and references.	111
5.6	Parameter space of the optimisation. 'LB' and 'RB' represent the lower and upper boundaries. Notably, the tower height (H_{tower}) is only included as an optimisation parameter in the LCOE-based optimisation.	112
5.7	Comparison of the optimal configurations based on design point and annual performances.	116
5.8	Co-optimisation results for different cases. Cases 1 to 5 represent performance-based optimised cases with fixed, but increasing tower height. Case 6 is an LCOE-based optimised case, where tower height was a parameter in the optimisation.	117
6.1	Performance comparison of different cases of flow path. D_0 is the pipe outer diameter. \dot{Q}_{rec} is the receiver thermal output. Patterns 1 to 4 correspond to different flow path patterns in Figure 6.7. 'SS +3h' points to three hours after Summer Solstice (SS) solar noon. Cases 1 and 2 are compared in Section 6.4.1.1. Case 3 is mentioned in Section 6.4.1.2. Cases 4 to 8 are referenced in Section 6.4.1.3.	131
6.2	Results with variation of pipe outer diameter (D_o).	137
6.3	Results at different pipe diameters for the Gen3L receiver	141
6.4	Results for the Gen3L receiver with Pattern 3-4 and the original pattern	142
7.1	Setup of the optimisation.	151
7.2	Comparison of the reference and optimal designs.	157

Nomenclature

Abbreviations

AFD	Allowable Flux Density
ANN	Artificial Neural Network
ANU	Australian National University
ARENA	Australian Renewable Energy Agency
ASTRI	Australian Solar Thermal Research Institute
CFD	Computational Fluid Dynamics
COBYLA	Constrained Optimisation by Linear Approximation
CPC	Compound Parabolic Collector
CSP	Concentrating Solar Power
DBA	Deviation-Based Aiming
DNI	Direct Normal Irradiation
DOE	Department of Energy
GA	Genetic Algorithms
Gen3	The Third Generation of CSP Technology
HTF	Heat Transfer Fluid
ISP	Image Size Priority
LCOE	Levelised Cost of Energy
LHS	Latin Hypercube Sampling
MCRT	Monte Carlo ray-tracing
MDBA	Modified Deviation-Based Aiming
MIP	Mixed Integer Programming
N-S	Navier-Stokes

NCI	National Computational Infrastructure
OELT	Optical Efficiency Look-up Table
PB	Power Block
PMCE	Progressive Monte Carlo Evaluation
PSA	Plataforma Solar de Almeria
PSO	Particle Swarm Optimisation
PV	Photovoltaic
RELT	Receiver Efficiency Look-up Table
SAM	System Advisor Model
SBO	Surrogate-based optimisation
SG	Solar Generator
SOLSTICE	SOLar Simulation Tool In ConcEntrating optics
STG	Solar Thermal Group
TES	Thermal Energy Storage
TMY	Typical Meteorological Year

Symbols

\dot{Q}	power, MW
\dot{q}	flux, MW/m ²
\bar{T}	average temperature, K
A	area, m ² or asymmetric factor
a	hyperboloid coefficient or scaling exponent
b	hyperboloid coefficient
C	cost, (M)USD or coefficient
CF	capacity factor
CI	confidence interval
D	diameter, m or extent
E	aiming extent

f	focal length, m or factor or percentage, %
H	height, m
h	convective heat transfer coefficient, W/m ² K or enthalpy, J/kg
I	Solar irradiance, W/m ²
L	Initial step length
l	length, m
M	index vector
m	factor determining safe and crossover extents
N	number
Q	energy, kW or MW or GW
R	radius, m
r	discount rate
S	shape exponent
T	temperature, K
t	time, h
V	speed, m/s
v	velocity, m/s
SM	solar multiple

Greek symbols

α	absorptivity
β	cost coefficient, %
Δr	radial spacing
Δ	initial delta
δ	converging threshold or solar declination angle, rad or distance, mm
η	efficiency, %
λ	solar ecliptic angle, rad
ω	solar hour angle, rad

θ angle, °

Subscripts

a, field	annual field
a, hst	annual optical efficiency of a heliostat
a, rec	annual receiver
a, st	annual solar-to-thermal
aa	air attenuation loss
abs	absorbed
aim	aiming point
amb	ambient
block	blocking loss
b	banks
cap	capital
con, aa	after air attenuation
con, abs	absorbed by concentrators
con, ap	incident to concentrators' aperture
con, inc	incident to concentrators
con, ref	reflected from concentrators
contra	contraction
conv, for	forced convective
conv, nat	natural convective
conv	convective
con	from concentrators
cyl	cylindrical receiver
c	conical
defoc, ele	elevation defocusing loss
defoc, HX	heat exchanger defocusing loss

defoc, max	maximum load defocusing loss
defoc, min	minimum load defocusing loss
defoc, storage	storage defocusing loss
defoc, wind	wind defocusing loss
eff	effective
ele	electricity
emi	emissive
estim	estimated
evals	evaluations per sub-problem
evals	evaluations
field	heliostat field
foc, A	area of focused heliostat
fp	flow path
f	focus point
hst, estim	estimated heliostat
hst, large	large heliostat field
hst, max	maximum number of heliostat
hst, tot	total number of heliostat
hst, up	heliostat aiming at upper section
hst	heliostat
HX, max	maximum capacity related to heat exchanger
HX	heat exchanger
inner	inner aperture
interc	secondary interception
int	interception
ite	iteration
lim	limit

loss, th	thermal losses
net, fp	net power per flow path
O&M	operational & maintenance
ope, field	field on operation
opt	optical
outer, spi	spillage over outer aperture
outer	outer aperture for secondary reflector
out	outer aperture
over	crossover extent
o	outer pipe
PB, in	into power block
rec, estim	estimated receiver
rec, fixed	receiver fixed
rec, inc, nom	normalised incident power to receiver
rec, inc	incident to receiver
rec, int	receiver and interception
rec, loss	receiver losses
rec, max, inc	maximum incident to receiver
rec, max	receiver maximum load
rec, ref	receiver reference
rec, size	receiver size-dependent
rec	receiver
ref	reflective
sec, abs	absorbed by secondary reflector
sec, block	blocked by secondary reflector
sec, ref	reflected by secondary reflector
shading	shading loss

spi	spillage loss
st	solar-to-thermal
s	skirt or spacing
th	thickness
tilt	tilt angle
trans	secondary transmission
t	trumpet
under	safe extent
w	wall

Introduction

1.1 Next-generation CSP plants

1.1.1 Background for 3rd generation CSP plants

In concentrated solar power (CSP) plants, mirrors are used to reflect sunlight onto receivers, where the solar energy is collected and converted to thermal energy. The thermal energy can then be used to drive a heat engine and to produce electricity. Unlike solar photovoltaic (PV) technologies, CSP plants have an inherent capacity for thermal energy storage (TES) and thus can continue to produce electricity in the early morning, after shutdown or during cloud disturbances.

The four predominant CSP technologies are linear Fresnel, central receiver (power tower), parabolic dish, and parabolic trough systems, as illustrated in Figure 1.1. These technologies differ in the nature of the mirror design, receiver shape and heat transfer fluid (HTF), and the thermal storage option. Most current CSP plants are based on trough technology, but tower technology is expected to see more widespread commercial deployment.

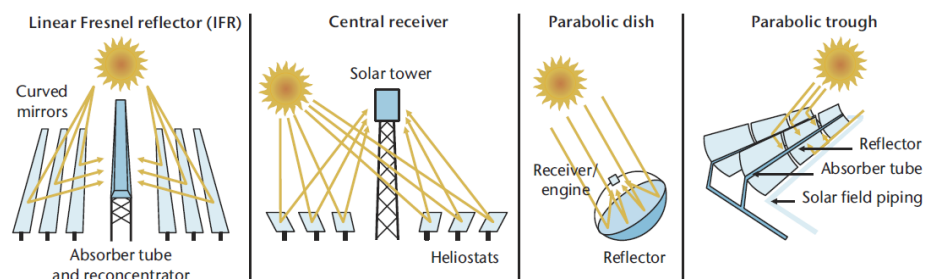


Fig. 1.1: Illustration of four main CSP technologies [1].

Today's commercial power tower technologies trace their lineage to the 10 MWe pilot demonstration of Solar Two in the 1990s [2]. The heliostat field and receiver subsystems are integrated with a two-tank thermal energy storage system, where the HTF (mostly molten salt) is heated to 565°C and transfers thermal energy to steam Rankine power cycles. Famous commercial projects include the 20 MWe Gemasolar plant in Spain [3] (see Figure 1.2), the 110 MWe Crescent Dunes plant in US [4] and

the 50 MWe Delingha plant in China [5]. However, the cost of CSP technologies has not kept pace with the falling cost of PV systems.



(a) Aerial view of the Gemasolar Plant in December 2010.



(b) View of the Gemasolar Plant on July 2011.

Fig. 1.2: View of the Gemasolar Plant [3]

The next-generation CSP plants are based around the concept of a step-change in power cycle efficiency by operation at a higher temperature and operation with a supercritical carbon dioxide ($s\text{CO}_2$) power cycle. The $s\text{CO}_2$ power cycle has been identified as a likely successor to steam Rankine power cycles and can achieve higher thermo-electric conversion efficiency [6, 7]. To achieve the targeted cycle efficiency greater than 50%, the solar energy collected by the receiver and stored in the TES must be delivered to the power turbine at a temperature above 700°C ¹. At the elevated temperature level, molten salt becomes chemically unstable [8], producing oxide ions that are highly corrosive, resulting in significant mass loss [9]. New HTF options are needed to replace molten salt.

The form of the HTF in the receiver can be divided into liquid, solid [10], and gas [11, 12]. Of the three forms, liquid HTF is the most similar option to commercial systems. Conceptually there is no change from the current state-of-the-art power tower design. In designing a next-generation CSP plant, selection of a high-temperature fluid is needed. Also as well as its impact on containment materials, there are other properties that are essential in the selection of a fluid. Martinek et al. [13] analysed the optical, thermal and structural performance of traditional external tubular solar receiver configurations applied with a chloride salt HTF and inlet/outlet temperatures of $500^\circ\text{C}/735^\circ\text{C}$. Another option is to use liquid metals such as liquid sodium. The advantages and recent research using liquid sodium as the HTF in CSP systems will be introduced in the next section.

1.1.2 Liquid sodium as the heat transfer fluid

Liquid sodium has been studied as a possible HTF for central receiver systems. Liquid sodium has versatility across many temperature ranges and is suitable for next-generation systems operating at temperatures above 700°C [14, 15]. The high

¹The $s\text{CO}_2$ power cycles are also being considered at lower temperatures (650°C), where efficiency is not as high, but challenges of high-temperature operation are less severe.

thermal conductivity of liquid sodium allows higher solar fluxes on the receiver and greater receiver efficiency [16]. This is particularly important for high-temperature operation, as thermal losses from the receiver may otherwise negate the performance gains downstream in the power cycle. The first central receiver tests using sodium were conducted in the 1980s at Sandia National Laboratories and Plataforma Solar de Almeria (PSA). The tests at Sandia consisted of a $3\text{ m} \times 1.2\text{ m}$ sodium-cooled receiver panel designed and constructed by Rockwell International. Results showed that the receiver thermal efficiency exceeded 90% with irradiances up to 1.5 MW/m^2 , total power on the receiver of 1.85 MW_t , and sodium inlet/outlet temperatures of $290^\circ\text{C}/590^\circ\text{C}$ [16]. A 1986 fire at PSA marked the end of sodium receiver experiments, and there has been very little development of sodium receivers since. In 2012, Vast Solar commissioned a sodium receiver module known as the Jemalong Solar Station in NSW, Australia. After successful testing of a single module, Vast Solar began construction of a 6 MW_{th} sodium power plant in 2014, consisting of five receiver modules and heliostat fields (see Figure 1.3).

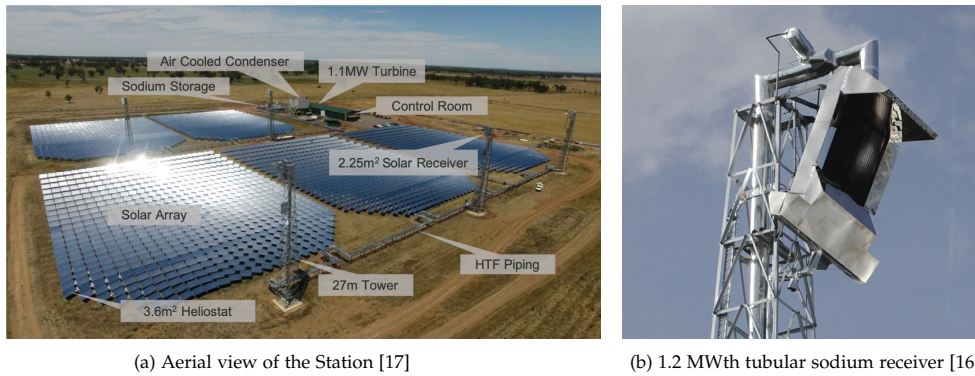


Fig. 1.3: View of the Vast Solar's Jemalong Solar Station.

In parallel with industrial efforts, academic research on liquid sodium receivers gained momentum in recent years. Boerema et al. [14] compared liquid sodium with Hitec (a ternary molten salt) as the HTF in solar thermal central receiver systems and suggested that liquid sodium, with its high heat transfer coefficient and low heat capacity, could potentially be a desirable alternative to molten salts in next-generation CSP plants. Polimeni et al. [18] investigated the performance of a CSP plant integrated with a sCO_2 power cycle using different HTFs in the receiver. The results showed that the system using a sodium receiver could achieve higher solar-to-electric efficiency than the use of KCl-MgCl_2 at 750°C at both designed and annual conditions. Cagnoli et al. [19] established a new system-level model of a billboard-type sodium-cooled receiver using the Computational Fluid Dynamic (CFD) method. CFD was used to evaluate the convective losses needed for system-level modelling, and the system-level model successfully simulated transient operations. In another system-level analysis, a sodium receiver-integrated CSP system was compared with a reference system with a molten salt receiver, two-tank storage, and steam Rankine cycle [20]. The reference and sodium-based systems' plant performances were com-

pared at the same solar multiple and storage capacity. The results showed that a better annual solar-to-electric efficiency of the sodium-based system (19.6%) is achieved compared to the reference system (15.6%). In a techno-economic analysis, Fritsch et al. [21] found that sodium-based concepts result in up to 16% lower electricity generation costs compared to a reference system with molten salt. Conroy et al. produced a series of studies on sodium receivers that included thermal and mechanical analysis [22, 23] along with system-level analysis [24].

Liquid sodium, an appealing HTF option in the design of next-generation CSP plants, is studied as the HTF in the receiver in this thesis. The research focus is on the development of the heliostat field and receiver subsystems, where the subsystems can represent around 50% of the total investment and can generate about 40% of the total losses in the system [25]. New models and modelling methodologies concerning the development of the subsystems need to be established for its design and optimisation. It is highlighted here that the developed methods, while based on a sodium HTF, are applicable to any other type of CSP system.

1.2 Literature review

This section gives an overview of recent progress in the heliostat field layout, receiver design and optimisation, heliostat aiming strategy, co-optimisation of the field and the receiver, and system-level simulation.

1.2.1 Heliostat field layout

In a solar tower system, the heliostat field, with thousands of individual heliostats, is a complex subsystem of major importance. The complexity in optical analysis, design, annual performance, and optimisation of heliostat fields necessitates the development of a variety of design and optimisation methods. A key challenge related to heliostat field design is to position the heliostats in the field such that there is minimum blocking and shading but also sufficient density so that they can deliver the required energy to the receiver. The design methods are divided into two categories: pattern-based and pattern-free approaches [26, 27].

In pattern-based algorithms, several parameters define the positions of the heliostats. The number of parameters is not large, and a classic optimisation (gradient-based and simplex) can yield several parameters that generate the best field. The radial-staggered configuration, originally proposed by Lipps and Vant-Hull [28], is the most popular and commonly-used field layout and has been adopted widely in many heliostat field projects for both polar and surround fields. As shown in Figure 1.4(a), it is characterised by the placement of heliostats along successive rows or circles with the tower axis as the centre, where any heliostat row is rotated half the azimuth distance between adjacent heliostats with respect to the previous or next row, so back-to-back mirrors do not share the same azimuth angle. This pattern can minimise the shadowing and blocking losses. Several codes are based on radial-staggered patterns, such as DELSOL/WinDELSOL [29], MUEN [30] and Campo

[31]. Another promising heliostat field layout is the biomimetic spiral configuration proposed by Noone et al. [32]. The authors claimed that the transition between high and low-density sections of the field is not continuous in the radial-staggered layout and that this impacts the optical efficiency. Thus, a new heuristic is suggested based on the spiral patterns of the phyllotaxis discs. Several authors have already compared the radial-staggered layout against the biomimetic pattern (see Figure 1.4(b)). Zhang et al. [33] found that the spiral layout works better than the radial-staggered for polar fields but that the spiral layout efficiency is lower in surround fields. However, the differences are always less than 1%. Gadalla and Saghafifar [34] showed through a full thermo-economic optimisation that the radial-staggered layout efficiency is marginally higher than that of the biomimetic pattern, i.e., 61.6% vs. 61.5%. In other studies by Les et al. [35] and Leonardi et al. [36], the differences between the optimal optical efficiency (both design point and annual-based) using different layouts are below 1%.

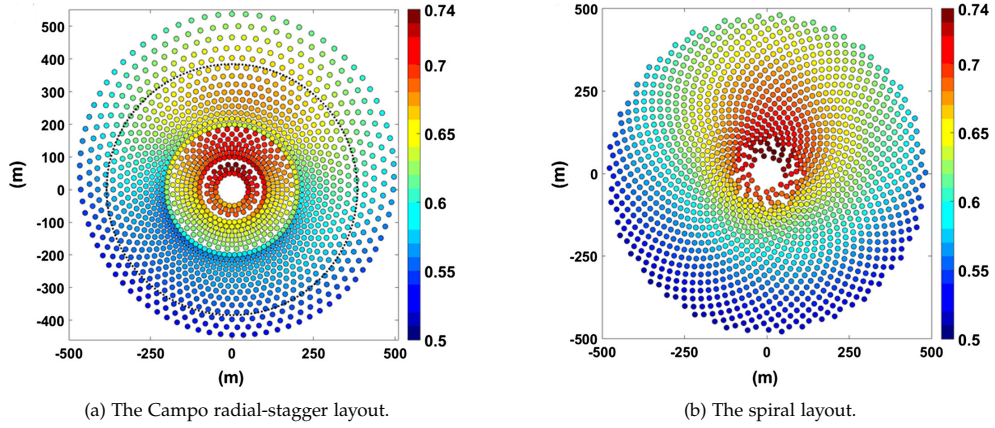


Fig. 1.4: Illustration of different field layouts [34]

For the pattern-free algorithms, the HGM algorithm [27] utilises the yearly normalised energy surface maps to identify the locations in the heliostat field, showing the highest annual optical efficiency for mirror placement. Similarly, the Greedy algorithm was used to position mirrors one by one at the best feasible locations of the field while measuring the effect of the newly added mirror on the existing ones [37]. To compare between pattern-based and pattern-free methods, pattern-based methods simplify the optimisation problem because the positions are defined by only a limited number of parameters. It is also argued that pattern-based approaches are more likely to be implemented in real plants [38, 39].

Non-linear, derivative-free optimisation methods are typically used to generate the optimal field, such as genetic algorithms (GA), particle swarm optimisation (PSO) algorithms or COBYLA [40]. Schmitz et al. [41] studied a north-oriented heliostat field with single-aperture and multiple-aperture designs and applied the GA algorithm to optimise the heliostat field. Besarati et al. [42] proposed the use of GA to tackle the problem of heliostat field optimisation at 50 MWth scale in the Daggett region, California. The maximum yearly insolation-weighted efficiency obtained for

Daggett was 0.683 using 594 heliostats. Corsi et al. [43] developed tools and methodologies to optimise the heliostat field in multi-receiver configurations. The results showed that the optimised heliostat field has an annual DNI-weighted optical efficiency of more than 76%. Piroozmand and Boroushaki [44] used the PSO algorithm to study the multi-tower heliostat field, ensuring the highest possible instantaneous efficiency. However, the results showed that the annual efficiency of the multi-tower field is only slightly higher than two separated single tower fields. A hybrid PSO-GA algorithm was developed by Li et al. [45] to optimise a heliostat field in Lhasa, China.

Given the research progress presented above, exploring the optimal heliostat field layout is a complex, high-dimensional optimisation problem, and it is not determined yet in literature which method is the best. The focus of this thesis is not to find the optimal heliostat field generation method but to study the interaction between heliostat field and receiver designs. Notably, the optimal heliostat field layout changes as the receiver dimensions vary. For example, the interception efficiency is increased with larger receiver dimensions. Hence the field layout can be more widely expanded without increasing spillage, which simultaneously alleviates the shading & blocking losses. The scope of this thesis is to present a method that can consider such inter-dependent relationships between the heliostat field and the receiver and determine optimal trade-offs.

1.2.2 Receiver

The receiver is a crucial component of a concentrated solar power (CSP) plant since it performs the conversion of concentrated sunlight into thermal energy and can significantly impact the total performance of the system. Recent research has sought to develop systems to achieve higher operating temperatures, which lead to a higher power generation efficiency according to Carnot's theorem. Receivers can be either cavity or external receiver designs [46].

1.2.2.1 External receiver

Conventional tubular external receivers consist of an array of thin-walled tubes that are typically arranged to transport the HTF in multiple passes through incident concentrated sunlight (see Figure 1.5). The receiver performance is impacted by factors including receiver dimensions, pipe size, flow path configurations and aiming strategy [23, 47].

Many existing studies use fixed or parametrically determined receiver designs. However, such an approach involves manual adjustments and hinders the potential significantly for integrated optimisation of the entire system, potentially resulting in sub-optimal design overall. As opposed to parametric design, receiver design optimisation remains an active research topic. Different strategies have been proposed to increase the efficiency of external receivers, including geometric optimisation or investigation on different flow path configurations. Smith et al. [48] proposed a method for the optimisation of a tube-type solar receiver panel to achieve minimum

receiver cost. The effects of the pipe diameter and the flow path pattern were investigated by Boerema et al. [49] for a billboard receiver. The results showed that the receiver with a triple-pass flow path pattern has the highest efficiency by reducing both the maximum surface temperatures under standard irradiance and the risk of high temperatures from irradiance changes. The flow pattern of the external receivers was optimised by Rodríguez-Sánchez et al. [50] to enlarge the useful lifetime of the receivers. Different flow pattern options were investigated, including single or multiple flow paths with or without crossovers. Here, 'crossover' points to the pipe routing that requires the flow path to cross from a panel on one side of the cylindrical receiver to a panel on the other side. The selection of the optimal flow path option was based on increasing the receiver availability and the global efficiency of the CSP plant. Augsburg et al. [51] presented an optimisation method for external molten salt receivers to maximise the receiver output with a given heliostat field. A few receiver flow configurations were ranked and selected from a list of hundreds of thousands of possible options. Asselineau et al. [52] and Zou et al. [53] presented geometric optimisation of receivers by varying the geometric parameters to get the highest receiver efficiency. A novel Variable Velocity Receiver was proposed by Rodríguez-Sánchez et al. [54], which consisted of a conventional external receiver equipped with valves that allow the division of each panel of the receiver in two independent panels, increasing the velocity of the heat transfer fluid in specific zones of the receiver. Results showed that the size of the solar field required by this receiver is 12.5% smaller in comparison to a traditional one. A novel fin-like receiver was proposed by Wang et al. [55]. The results showed that a receiver with horizontal fins and a flat bottom has the maximum optical efficiency of 60.3% at equinox noon, which is 0.4% higher than a traditional cylindrical receiver. As mentioned in Schöttl et al. [56], although the transient behaviour of the receiver can be modelled by different integrated optical-thermal models [57], methods permitting fast and accurate annual assessment of the receiver are scarce. Schöttl et al. [56] used an artificial neural network (ANN) together with a detailed receiver thermal model to calculate the annual output of the receiver. In SolarPILOT [40], the receiver losses are calculated from reduced-order correlations related to thermal load and wind speed.

1.2.2.2 Cavity receiver

The cavity type of receivers may be a better option than an external receiver geometry for high-temperature CSP systems because of the reduced thermal losses [46]. Various strategies have been proposed to reduce thermal losses of cavity receivers, including geometry optimisation [56, 59, 60, 61], heat transfer enhancement of the working fluid [14, 62], addition of a glass cover [63, 64, 65], and use of an air curtain [66, 67, 68]. Besides thermal efficiency, optical performance is also important for cavity receivers. The optical losses related to a cavity receiver include spillage and reflective losses, mostly independent of the receiver temperature. A trade-off exists between thermal and optical efficiencies: a smaller aperture size leads to lower thermal losses, but the spillage loss will simultaneously increase, resulting in less en-

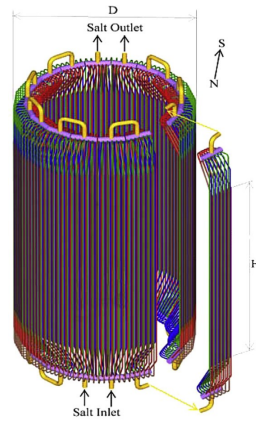


Fig. 1.5: Illustration of a solar external receiver [58]

ergy input into the cavity receiver. The optimal aperture size for isothermal cavities with planar structure has been studied by Steinfeld and Schubnell [69]. The optimal aperture dimensions are a function of the cavity temperature and the focal plane flux distribution. Furthermore, the receiver performance can be enhanced if the spillage loss can be maintained or even reduced while reducing the thermal losses with a smaller aperture.

To achieve this aim, one option is to extend the active receiver absorption area beyond the aperture of the cavity itself, while retaining the high temperature areas inside the cavity. Different terms have been used in literature for the extended absorption area, such as wind skirt, edge section, pre-heater section, frustum, top-hat, pancake, or circum-aperture regions. In this thesis, this extended region is named the spillage skirt because it is a skirt-like absorption region aimed at reducing spillage loss. A solar receiver with a top-hat geometry was proposed by Luzzi et al. [70] for a dish system. The receiver was made of a circumferentially-arranged tube bundle, placed inside an insulated 'top-hat' receiver cavity. A cylindrical cavity receiver with a 'wind skirt' was investigated by Prakash et al. [71], and a correlation to calculate the convective loss at a temperature range between 100°C and 300°C was proposed. In the designs of the Solar Generator 3 (SG3) [72] and SG4 receivers [73, 74] at the Australian National University (ANU), the concepts of the spillage skirt were also used. The SG3 receiver consisted of a pre-heater section and a steam generation section, with water entering the 'frustum' as part of the pre-heat. Figure 1.6 shows an illustration of the SG3 receiver. The receiver efficiency of the SG3 receiver was calculated to be 93.6% with an inlet temperature of 60°C. For the SG4 receiver, the design of the skirt was retained and the cone angle of the 'circum-aperture region' was optimised to minimise spillage loss. Simulation results showed the SG4 receiver can reach an efficiency of 98.7%, and experimental tests showed an average thermal efficiency of $97.1 \pm 2.1\%$ [74]. While spillage skirts are beneficial in these previous studies, as yet they have not been assessed at the higher temperature operation range targeted for next-generation receivers [75].

Apart from extending the aperture absorption area, another option to minimise



Fig. 1.6: Illustration of the spillage skirt at ANU SG3 receiver [73]

spillage of incident radiation is to add non-imaging secondary reflectors. The effectiveness of reflectors in intercepting and retaining radiation is vital to this concept. Conical, trumpet and Compound Parabolic Collector (CPC) reflectors are three of the most common secondary reflectors. Hahm et al. [76] compared the performance of a single cavity receiver with a cavity receiver combined with a fabricated cone reflector. It was shown that with fixed dimensions for the reflector's inlet aperture, a significant fraction of light was rejected if the cavity aperture was too small. On the other hand, thermal losses increased as the cavity aperture size increased, and therefore, an optimal cone geometry was shown to be essential. The trumpet-shaped reflector was first introduced by Winston et al. [77]. It comprises a hyperboloid of revolution with an asymptotic angle that must be at least as large as the rim angle to intercept all the radiation from the primary concentrator. In experimental work on a two-stage trumpet concentrator for point focus dishes by Winston et al. [78], an actively cooled trumpet reflector readily attained the expected optical performance and operated continuously in a high flux environment. A heat transfer model was developed by Suresh et al. [79] to analyse the thermal behaviour of a passively cooled trumpet secondary reflector, and the thermal analysis showed that the reflectors do not require active cooling but dissipate the absorbed heat load through passive surfaces. Bean and Diver [80] performed testing with a silvered trumpet aperture on a CPG-460 faceted dish Stirling system, which gives insights into the practical application of a trumpet receiver. Chang et al. [81] proposed a cavity receiver with a glass window and trumpet reflector, with results showing that the heat loss can be reduced by 56% compared to an initial reference design. The CPC reflector was first proposed by Hinterberg and Winston in the mid-1960s [82] and has gained special attention for solar energy applications since [83]. Madala and Boehm [84] reviewed non-imaging concentrators (including the CPC) for stationary and passive tracking applications and found them most suitable for low to medium concentration ratios. Li et al. [85] designed a CPC concentrator for a high-flux solar simulator to reduce the spillage loss from 79% to 32%. A convection analysis for cavity receivers with these three types of reflectors was conducted by Reddy and Kumar [60]. It was found that the

trumpet reflector showed the best performance in reducing the natural convective loss.

1.2.3 Heliostat aiming strategy

The interaction between the heliostat field and thermal receiver plays a crucial role in the design and operation of the plant [86, 87]. The role of an aiming strategy is to control the radiative flux distribution at the receiver surface to avoid thermally induced damage. For maximum interception, all heliostats should be aimed at the “centre” of the receiver. However, only maximising the captured radiation with central aiming causes highly localised heat loads, which for tubular receivers, leads to the risk of exceeding the stress limits of the receiver materials constrained by the damage mechanisms of creep and fatigue [46, 88]. Therefore, the goal of an aiming strategy is to reduce the flux levels by spreading the incoming concentrated light over the receiver surface while minimising spillage losses and maximising the receiver thermal efficiency [89, 90].

Several heliostat aiming methods have been investigated to reduce the peak flux and flatten the flux profile. For a billboard receiver, a square-gridded aiming model is commonly applied [91, 92], while other gridded aiming models can be applied on cylindrical receivers [90]. Different optimisation methods are used to optimise the aiming model in order to flatten the flux distribution [92, 93, 94, 95]. However, with increasing the number of heliostats, the dimension of the optimisation problem dramatically increases, and the gridded method becomes inefficient. Aiming models based on parameterisation of heliostat target locations were proposed to reduce the number of parameters to determine significantly. A single-parameter strategy was proposed by Vant-Hull [96], in which aiming points were determined by one aiming parameter to control the opening angle of the beam coming from heliostats. A similar idea, the “aiming factor” proposed in Sánchez-González et al. [97, 98] is used to control the beam radius at the receiver surface and further applied in subsequent research [99, 100]. However, as pointed out in Collado and Guallar [89], the one-parameter model could lead to two hot spots (“shoulders”) as the irradiation images come closer to the upper and lower edge of the receiver. A two-parameter aiming model was proposed by Collado and Guallar to avoid these shoulders [89]. Other two-parameter aiming models were also investigated by Flesch et al. [90] and Garcia et al. [101].

Besides reducing peak flux, an aiming strategy typically needs to be designed to operate up to some specific flux limit. Flux limitations arise from factors including the HTF stability limits and thermo-mechanical stress limits in receiver tubes [88]. Flux limitations need to be updated continuously in accordance with the local HTF conditions, and the flux over the whole receiver surface needs to comply with the limits. This imposes more stringent requirements for the aiming strategy, as it needs to update flux limits with changing HTF temperatures. The concept of “Allowable Flux Density” (AFD) was proposed by Vant-Hull [96] following its successful application in the design of the Solar Two molten nitrate salt receiver [48]. In this concept,

the stress and peak salt temperature at the wall were transferred into a flux density limit, a function of salt temperature and velocity. An aiming strategy was developed to comply with the AFD for molten salt central receivers [99]. Figure 1.7 shows the results after adjusting the aiming strategy. The incident flux can be controlled below the maximum allowable flux. The concept of the AFD has also been used by Garcia et al. [101, 102] and Acosta et al. [103] with a two-parameter aiming model, and by Flesch et al. [90] with a gridded aiming model to obtain reliable flux patterns. Conroy et al. [23, 24] used the AFD method to determine receiver geometry and aiming strategy for sodium-cooled billboard receivers. The Image Size Priority (ISP) method has been used to optimise aiming points of heliostats, using fast convolution-based optical simulations to evaluate individual flux maps [40].

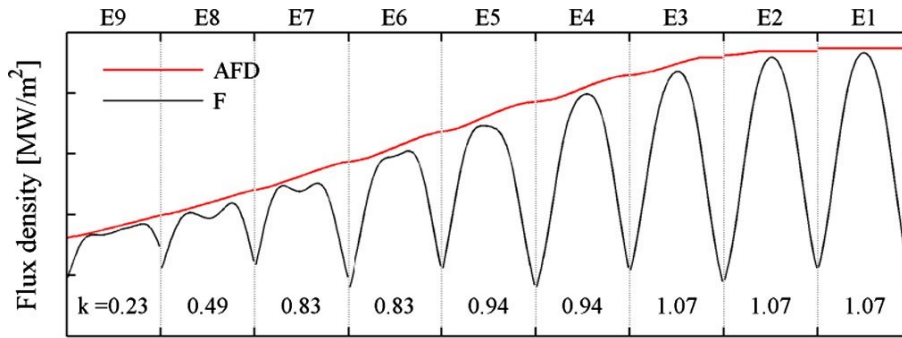


Fig. 1.7: The incident flux is controlled below the maximum allowable flux by adjusting the aiming strategy for a molten salt receiver [99]. 'F' and 'AFD' represent the incident flux and flux limit.

Most of the above studies rely on fast convolution-based optical simulations because flux maps of individual heliostats need to be calculated, or quick responses of the aiming strategy are sought-after. Monte Carlo ray-tracing (MCRT) is a more accurate method to simulate heliostat fields, but it is computationally expensive and determination of the aiming points for every heliostat independently potentially leads to an impractical simulation time. However, ray-tracing is preferred to accurately determine receiver flux distributions because of its high accuracy. In a previous study [104], the analytical model in SolarPILOT [40] was compared with five ray-tracing tools. The results showed that performance calculated from SolarPILOT is typically consistent with ray-tracing codes, with a few exceptions: the analytical convolution method has limitations in precise modelling of non-Gaussian distributions, can lead to inaccurate results at off-design sun positions and cannot capture the multi-reflection process for cavity receivers. The MCRT method has been used previously for heliostat aiming [56, 105, 106, 107, 108]. The goal of most of the studies found in the literature aims to reduce peak flux rather than achieve an accurate match between actual and maximum allowable flux across the whole receiver. This is mainly because of the high computational load brought by MCRT with conventional aiming models. Wang et al. [108] applied a coupled MCRT-thermal-stress model with a multi-point aiming strategy to ensure safe operation of a cylindrical receiver, however, noted that further optimisation of the aiming strategy was required to maximise performance

concurrently.

1.2.4 Co-optimisation of the heliostat field and the receiver

The heliostat field and the receiver are interdependent, and a co-optimisation method is needed to obtain an optimal configuration minimising the Levelised Cost of Energy (LCOE) or maximising the annual energy yield [87, 109]. A GA-based algorithm was proposed by Schmitz et al. [41] to optimise the radial-staggered field layout parameters, the tower height, the receiver dimension and tilt angle. The field was simulated with convolution optics, and the receiver was assumed as an aperture similar to most optics-focused studies. Ramos and Ramos [109] designed the field and receiver by optimising eleven parameters. The performance was simulated using convolution optics for the heliostat field and data fitting to get the receiver efficiency. Carrizosa et al. [26] co-optimised a field and receiver using a pattern-free field layout, but the receiver was again simplified as an aperture. Collado and Guallar [110] proposed a two-stage optimised design method, with the first step optimising the heliostat field to get the maximum annual field output, and the second step optimising the tower height and receiver size from the economic aspect. Convolution optics was used here as well in the optical simulation, and the annual receiver model was simplified, assuming average thermal losses over a year. Li et al. [85] investigated the option of including a compound parabolic concentrator (CPC) at the receiver aperture and carried out performance and economic optimisations at different operating temperature ranges. The optical simulation used MCRT, and the receiver was assumed to be an isothermal aperture operating at a nominal temperature. The System Advisor Model (SAM) [111] and SolarPILOT [40] are two well-known system-level tools for the design of CSP plants and the optimisation of heliostat field layout and receiver geometries and includes the implementation of an aiming that uses convolution optics. However, the receiver model uses a simplified polynomial fit approach, and the aiming strategy cannot be automatically adjusted to comply with operational constraints.

1.2.5 System-level optimisation

Apart from the heliostat field and receiver subsystems, other crucial system components in a CSP plant include the TES subsystem and the power block. The design of the heliostat field and the receiver subsystems needs to be adapted to the overall plant configuration to achieve the best techno-economical performance.

Regarding system-level modelling of CSP systems, SAM has been widely used for the design and optimisation of molten salt systems [112, 113, 114, 115]. However, even though SAM offers some flexibility, it is not feasible to model specific CSP plant characteristics like alternative receiver designs or control strategies. Alternative system-level models have also been proposed to adjust design parameters to optimise LCOE. Martín et al. [116] presented a method for optimisation of year-round operation of a CSP plant in the south of Europe. The system-level optimisation is for-

mulated as a Non-linear Programming problem (NLP) that is solved for the highest annual electricity production defining the main operating variables of the thermal and cooling cycles. Casati et al. [114] developed a novel model based on the SAM reference software. Optimal control problems were formulated and solved, and different operating strategies were compared based on a detailed financial analysis over the project lifetime. Zhu et al. [117] applied a LCOE model to analyse and benchmark the electricity generation costs of different operational CSP plants in China. A simple LCOE model was applied, accounting for lifetime costs, inflation and discount rate. Schinko and Komendantova [118] employed a LCOE model to find that comprehensively de-risking CSP investments leads to a 39% reduction in the mean LCOE for this case based in North Africa, although this reduction is still not sufficient to achieve economic competitiveness with fossil fuels plants. González-Roubaud et al. [119] used a LCOE calculation to assess the economic value of different TES systems in order to compare the cost of electricity among different power generation sources. Ren et al. [120] adopted the net present value and discounted cash flows techniques to develop a mathematical model and calculated LCOE by taking the CSP industry of China as an example. Scott et al. [121] introduced SolarTherm, which is a new open-source system-level simulation tool and compared SolarTherm with SAM for trough and tower systems. The results showed strong agreements between the results of the two tools. De la Calle et al. [20] established a system-level model for a CSP plant with a molten salt receiver, two-tank storage, and a subcritical steam Rankine cycle by using the SolarTherm framework. Differences of $< 1\%$ in annual receiver output and $< 2\%$ in net electrical output were achieved when comparing SolarTherm and SAM simulations.

1.3 Research objectives

Next-generation CSP plants using liquid sodium as the HTF in the receiver are expected to achieve higher system efficiency and lower LCOE than second-generation plants. The heliostat field and receiver subsystems are crucial components of CSP plants. Optimal designs of the field-receiver subsystems can significantly increase the system efficiency and reduce the LCOE. This thesis aims to develop modelling methodologies and apply these newly established methods to determine optimal field and receiver designs for next-generation CSP plants. Firstly, cavity receiver design concepts are studied because of their potential high efficiency, even at high temperatures. It has been identified that the performance of cavity receivers can potentially be enhanced by the addition of a spillage skirt and secondary reflectors. However, the benefit of these features has not been examined systematically. This thesis quantifies and discuss the impact of skirts and reflectors on receiver performance.

A drawback of the cavity receiver is that a single-cavity system cannot be coupled with a surround field because of the limited view angle of the receiver. Although multiple cavities can potentially alleviate this issue [41, 122], one of the appealing

features of the conventional cylindrical external receiver design is that there are no limitations relating to the field of view, and heliostats may completely surround the tower. This has benefits in terms of cost-efficient use of the tower and is an essential factor in large, commercial-scale CSP plants. Therefore, the research focus in this thesis turns to the subsystems with a surround field and an external receiver.

The receiver needs to be protected from damage caused by high solar flux by implementing a suitable heliostat aiming strategy. Concentrated solar radiation on receiver tubes results in thermally induced stresses, and flux limits must be set and adhered to in order to avoid shortening receiver lifetime through creep and fatigue damage. As discussed in the literature review in Section 1.2.3, MCRT simulations are needed to obtain accurate flux maps at the receiver, and new approaches are necessary to reduce the computational requirements in finding optimal aiming parameters. This thesis introduces a new method that allows accurate and efficient aiming of heliostats to closely match flux distributions to local values of allowable flux on the receiver.

In all but one of the co-optimisation studies reviewed in Section 1.2.4, the fast convolution optics approach is used in optical simulations, mainly because it is computationally cheaper than MCRT, especially in annual simulations. For receivers, correlations or simplified analytical models are always used in annual simulations instead of detailed receiver modelling. No prior work can be found that enables aiming strategy optimisation within an annual system design optimisation. Therefore, a novel co-optimisation is presented in this thesis to simultaneously optimise the heliostat field, receiver and aiming strategy based on the annual performance.

In co-optimising the heliostat field and the receiver, it is found that oversizing the heliostat field increases the capacity factor and the annual energy yield of the plant. This is because oversizing has the benefit that consistently high irradiance levels can be maintained even under low DNI conditions, such as in winter or due to haze or light clouds. However, oversizing also means that there is a risk of exceeding safe operational limits. Therefore, an extension of the new aiming strategy is developed in this thesis, whereby the receiver is operated under as high irradiance as possible but does not exceed these safe operational limits.

The electricity generation of a CSP plant is not only affected by the heliostat field and the receiver subsystems but also impacted by the TES capacity and the solar multiple. A system-level optimisation is presented in the last part of the thesis to achieve the best techno-economic performance.

1.4 Thesis outline

The outline of this thesis is as follows:

- Chapter 2 summarises the modelling methodologies used for the design and optimisation of the heliostat field and the receiver subsystems in the following chapters.

- Chapter 3 investigates the usage of spillage skirts and secondary reflectors to enhance the performance of a cavity receiver.
- Chapter 4 turns the focus to an external receiver and introduces a newly-developed aiming strategy that enables efficient use of MCRT to comply with the flux limits.
- Chapter 5 introduces a novel co-optimisation method for designing the heliostat field and the receiver based on the best performance and the lowest LCOE.
- Chapter 6 discusses the best receiver flow configurations to maximise the receiver output with an oversized field.
- Chapter 7 presents the results of a system-level optimisation with varying capacity of critical system components.
- Chapter 8 presents the conclusions of this thesis and introduces suggested future work.

Modelling methodology

2.1 Introduction

The methodologies introduced in this chapter are the basis of the modelling work concerning the heliostat field and the receiver subsystems in this thesis. Considering that there is significant overlap between the modelling methodology used in Chapters 3-7, it is deemed appropriate to introduce common theory in this chapter and more specific modelling techniques for each study within subsequent chapters where appropriate.

The detailed modelling methods for instantaneous performance of the heliostat field and the receiver subsystems are introduced, including methodologies behind modelling optical concentrators, receiver thermal response and receiver mechanical reliability. The instantaneous models are used to simulate the behaviour of subsystems for a given set of environmental and operating conditions. The operational states of a CSP system change significantly across a year due to highly fluctuating ambient conditions. Annual modelling methods for the subsystems are introduced, which allow fast and accurate modelling of the annual performance. The annual modelling methods are then integrated into the system-level modelling tool to calculate the annual yield and the LCOE of the system.

2.2 Instantaneous modelling methodology

2.2.1 Optical modelling

The optical process starts from the sun, where solar irradiance is emitted. The solar irradiance reaching the heliostat field is reflected by heliostat mirrors and then hits the receiver, where it is converted into thermal power.

Solar radiation reaches the surface of the Earth with a specific angular intensity distribution. The angular intensity distribution on the surface of the earth is called “sunshape” in CSP research. Buie et al. [123] give a good overview of the motivations and development of the different sunshape models and measurements. Widely applied sunshape models include Buie sunshape [123], pillbox sunshape and Gaussian sunshape.

An individual heliostat comprises a reflector (one or more mirror facets), a supporting structure including foundations, and an actuation system. Realistic concentrator surfaces deviate from the designed shape as a result of manufacturing flaws and impacts from gravity and wind. Therefore, real-world concentrators' reflective surfaces are not ideal, which restricts the effectiveness of concentrating optics by resulting in off-focus reflections. During the design phase, it is important to understand the impact of sunshape and surface slope errors because they have a direct impact on the reflected solar radiation, spreading the image on the receiver, and hence influencing the design process.

A commercial-scale heliostat field is composed of thousands of individual heliostats. The heliostat field can be categorised into surround and polar fields. Circumferential irradiation of a central receiver is allowed with a surround field, while a polar field results in highly asymmetric irradiation, with heliostats in a polar field arranged on one side of the tower. Polar fields are generally used with a cavity receiver, while surround fields are always used with an external receiver.

Figure 2.1 illustrates the optical process of a heliostat field. Energy losses are presented along the path from the source to the surface of the receiver. Figure 2.2 shows a Sankey diagram of the energy flow corresponding to the illustration. The energy terms are defined as follows:

- GA is the total energy irradiated from the sun that covers all the surface area of the heliostats, which can be calculated by multiplying the DNI, G , with the total heliostat area, A .
- $f_{\text{foc},A}$ is the focusing ratio, defined as the percentage of the solar field that is operational, measured in terms of collectors' aperture area. Sometimes certain heliostats need to be taken off sun to reduce the flux on the receiver and to comply with operational limits. This strategy is called heliostat defocusing strategy. $f_{\text{foc},A}$ is equal to one if no heliostat is defocused.
- \dot{Q}_{shading} is the energy loss caused by the solar irradiation coming from the sun direction but gets shaded.
- \dot{Q}_{cos} is the energy loss due to the angle between the incident solar beam and the surface normal.
- $\dot{Q}_{\text{con,abs}}$ is the energy loss due to absorption by the heliostat surface accounting for the fact that a mirror is not a perfect reflector, which includes the energy loss caused by soiling.
- \dot{Q}_{block} is the energy lost due to blockage of reflected light by other heliostats on its way towards the receiver.
- \dot{Q}_{aa} is the energy loss due to absorption of reflected light in the near-ground region as light travels from the heliostat to the receiver. In dusty regions, this can be quite significant due to absorption or scattering of light by dust particles.

- \dot{Q}_{spi} is the energy loss due to reflected light from the heliostats but missing the receiver.
- $\dot{Q}_{rec,inc}$ is the energy incident on the receiver after considering all the above optical losses related to the heliostat field. The energy balance across the entire heliostat field is expressed as:

$$GA = (1 - f_{foc,A})GA + \dot{Q}_{shading} + \dot{Q}_{cos} + \dot{Q}_{con,abs} + \dot{Q}_{block} + \dot{Q}_{aa} + \dot{Q}_{spi} + \dot{Q}_{rec,inc} \quad (2.1)$$

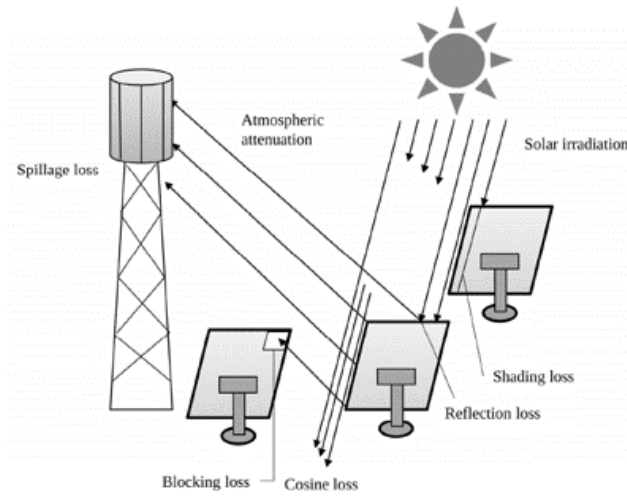


Fig. 2.1: Illustration of the optical process in a CSP plant [124].

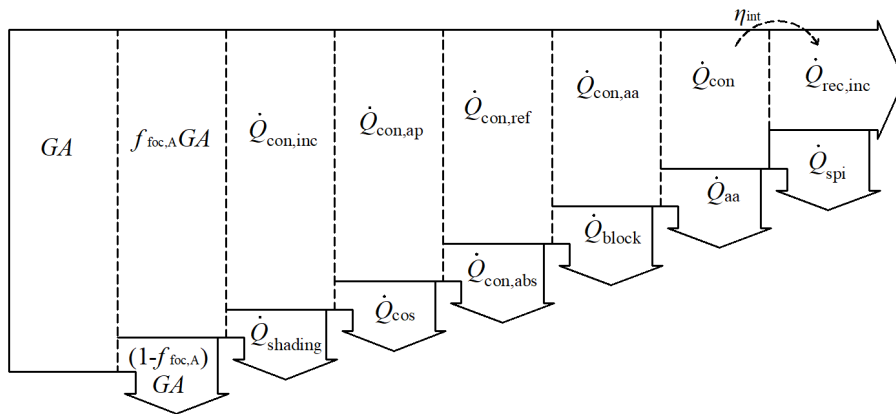


Fig. 2.2: Sankey diagram of the energy flow in the optical process.

The instantaneous optical efficiency of the heliostat field (or instantaneous field efficiency) is the ratio of the incident energy on the receiver to the total energy inci-

dent on the heliostat field:

$$\eta_{\text{field}} = \frac{\dot{Q}_{\text{rec,inc}}}{GA} = f_{\text{foc,A}} \eta_{\text{ope,field}} \quad (2.2)$$

where $\eta_{\text{ope,field}}$ is the instantaneous optical efficiency of the heliostat field in operation:

$$\eta_{\text{ope,field}} = \frac{\dot{Q}_{\text{rec,inc}}}{f_{\text{foc,A}} GA} \quad (2.3)$$

Typically, the instantaneous field efficiency (η_{field}) is equal to the field efficiency in operation ($\eta_{\text{ope,field}}$) when no heliostat is defocused.

The interception efficiency is defined as the amount of energy intercepted by the receiver related to the energy coming from the concentrators (\dot{Q}_{con} , see Figure 2.2) and is expressed as:

$$\eta_{\text{int}} = \frac{\dot{Q}_{\text{rec,inc}}}{\dot{Q}_{\text{con}}} \quad (2.4)$$

Optical models are applied to simulate the above processes and calculate the optical losses. Optical modelling tools are typically divided into convolution and MCRT methods. The convolution-based methods rely on the mathematical superposition of error cones, representing sunshape, concentration and mirror errors, for fast optical modelling. The convolution method is also commonly referred to as the “cone optics” method. Several of the most known convolution models are UNIZAR [125], DELSOL [126], HFLCAL [127] and SolarPILOT [40].

MCRT is a stochastic method suitable for simulating light propagation, approximated as bundles of rays, in a three-dimensional scene. Because of the randomness associated with MCRT, accuracy and resolution level are directly proportional to the number of rays. Commonly used MCRT tools include Tonatiuh [128], Soltrace [129], Tracer [130], SOLSTICE [131] and Heliosim [132].

As a general rule, MCRT is not as fast as convolution models, but the accuracy of convolution methods is lower than MCRT. In a previous study [104], the convolution model in SolarPILOT was compared with five ray-tracing tools. In a verification test, flux distributions from SolarPILOT were compared to Tonatiuh and four other MCRT techniques assuming a pillbox sunshape at both solar noon and morning sun positions. The heliostat field was a PS10-like heliostat field. Figure 2.3 shows the comparison of receiver flux maps. The flux distribution from SolarPILOT showed reasonably significant differences from the other MCRT-based simulation methods. The maximum local flux difference is around 9.3% in the noon case, and around 15.1% in the morning case. The general conclusion from the study of Wang et al. [104] was that performance calculated from SolarPILOT is typically consistent with that calculated using ray-tracing codes, with a few exceptions: the analytical convolution method has limitations in precise modelling of non-Gaussian distributions, can lead to inaccurate results at off-design sun positions and cannot capture the

multi-reflection process for cavity receivers.

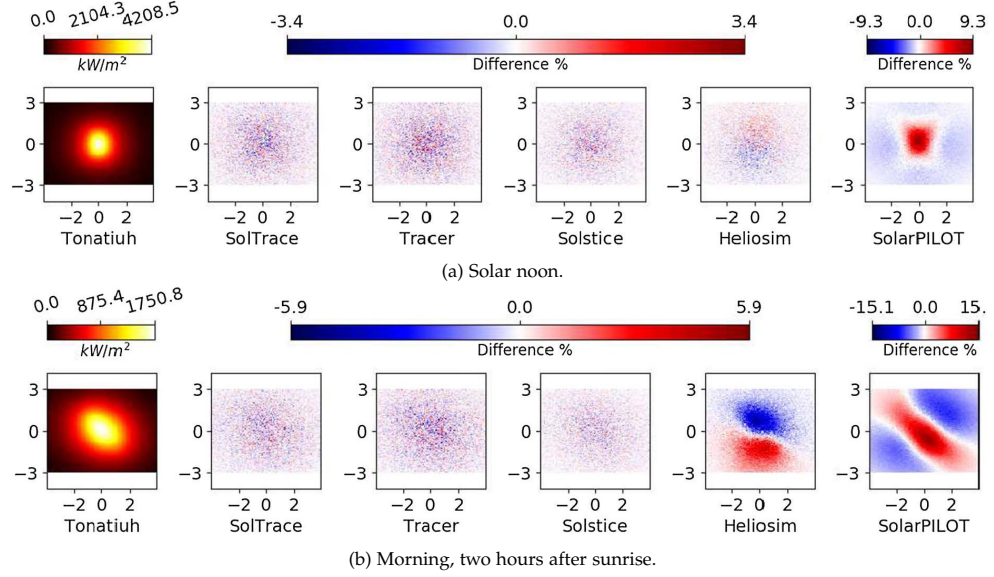


Fig. 2.3: Comparison results of SolarPILOT with five ray-tracing tools at different sun positions [104].

Therefore, the MCRT method is adopted for optical modelling in this thesis due to its high accuracy while simultaneously addressing the challenges associated with the high computational requirements of this method. Among MCRT tools, Tracer and SOLSTICE are currently being developed or extended for heliostat field and receiver simulations by the Solar Thermal Group (STG) at the Australian National University (ANU) and are introduced as follows.

The ray-tracing code ‘Tracer’ is an object-oriented library in Python. Originally created by Yosef Meller at Tel Aviv University (TAU) in Israel¹, Tracer was further developed by the STG at ANU for modelling CSP systems². A tracer simulation is composed of two elements: an assembly object locating and orienting the geometry, and a ray-bundle object describing the position, direction of propagation, the energy carried and any other property borne by a group of rays. The assembly object contains surface objects at the core of the geometrical and optical definition of the geometry. The assembly and ray bundle objects are used as arguments to create an instance of the Tracer engine class that will propagate the rays from the ray-bundle, interrogate the surfaces for any potential intersection, find the intersection for all rays, iterate until the energy in the bundle depletes and store the history of each ray in a ray-tree object that can be interrogated once the simulation is complete. Wang et al. [104] did a preliminary validation of Tracer and found that Tracer agreed well with DELSOL, HELIOS [133], SolTrace and Tonatiuh. Tracer has been used for the design of the ‘SG4’ Big Dish at ANU [74, 134].

SOLSTICE (SOLAR Simulation Tool In ConcEntrating optics) is a free, open-source ray-tracing software jointly developed by PROMES-CNRS and MésO-Star [131]. It is

¹Tracer (Y. Meller): <https://github.com/yosefm/tracer>

²Tracer (ANU): <https://github.com/anustg/Tracer>

a command-line tool with simple input and output file formats that facilitate automated or manual operation. SOLSTICE applies the energy-partitioning method to achieve a faster convergence rate than collision-based algorithms. It is efficient in large field simulations by sampling rays at the first intersection on the primary reflector surface. In addition, it is fully parallelisable on shared-memory architecture, which enables parallel computing. SOLSTICE takes input files for the solar facility, including geometric elements such as stereolithography (STL) geometry files and spectral data (solar radiative intensity, refractive index, extinction coefficient and reflectivity), and computes the flux maps on solar receivers. Results can be visualised using ParaView [135]. SOLSTICE has been benchmarked with other optical tools by Wang et al. [104] and has been experimentally validated by Benjamin et al. [136]. A Python package Solsticepy³ is being developed by ANU STG to script the use of SOLSTICE to model CSP systems, including heliostat field design, aiming strategy, and further integration with system modelling tools. Figure 2.4 shows the simulated optical process of the heliostat field in SOLSTICE. All the optical losses in Equation 2.2.1 can be obtained after post-processing the flux files in SOLSTICE.

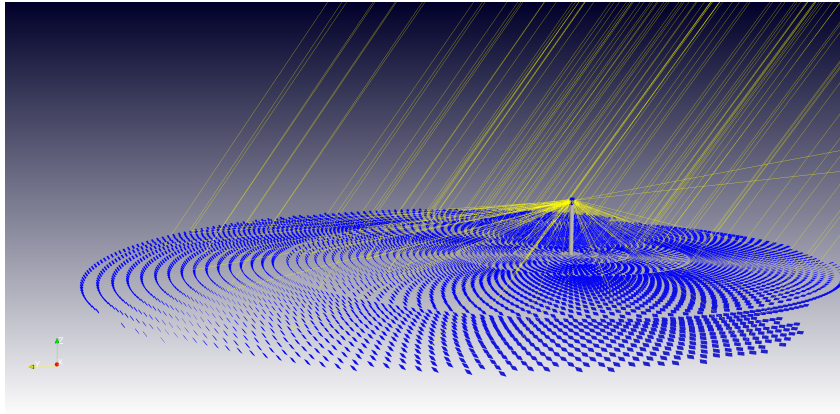


Fig. 2.4: Optical simulation of the heliostat field in SOLSTICE.

2.2.2 Heat transfer modelling

The heat transfer process occurs in the receiver, where solar irradiance is converted into thermal power. The heat transfer process includes thermal radiation, convective heat exchange with the environmental air, conductive heat transfer through the tube walls, and convective heat transfer to the HTF. Figure 2.5 illustrates the heat transfer process of the receiver.

The receiver surfaces are considered opaque, with incident radiation partially absorbed or reflected. The reflected radiation leads to reflective loss. In calculating the absorbed energy, a two-band semigrey approximation is commonly used because of the distinct regions of the spectrum occupied by solar radiation on short wavelengths

³Solsticepy: <https://github.com/anustg/solstice-scripts>.

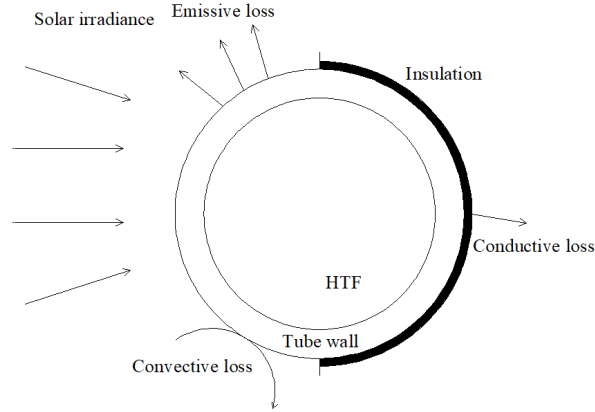


Fig. 2.5: Illustration of the heat transfer process at the receiver.

and thermal emissions on long wavelengths [137]. The receiver surfaces are assumed to be rough and exhibit diffuse reflection behaviour.

Detailed calculation of convective heat transfer needs the solution of the Navier-Stokes (N-S) equations, which is always obtained using CFD software. In some situations with simple receiver geometry, correlations are developed to estimate the convective heat transfer coefficient (h_{conv}) without solving the full N-S equations. For external receivers, the convection with wind influence is geometrically similar to a vertical cylinder in a cross-flow; therefore, respective correlations can be used. The correlation by Siebers and Kraabel [138] is one of those models, in which model correlations for natural and forced convection are presented separately and mixed to obtain a single heat transfer coefficient for the surface:

$$h_{\text{conv}} = (h_{\text{conv,nat}}^{3.2} + h_{\text{conv,for}}^{3.2})^{1/3.2} \quad (2.5)$$

where $h_{\text{conv,nat}}$ and $h_{\text{conv,for}}$ are the natural and forced convective heat transfer coefficients. For cavity receivers, bulk air in the cavity and the surrounding air is calculated with a two-zone model introduced by Clausen [139]: the convective zone in the lower part of the cavity and the stagnant zone in the upper part of the cavity.

The conductive loss of the receiver is generally a small amount for high-temperature receivers compared to the emissive and convective losses and is assumed to be negligible.

The heat conduction from the surface to the inner tube wall can be calculated according to the Fourier law of heat conduction and its integration over a cylindrical shell. The heat is then transported to the HTF by convection. Empirical correlations can be adopted for the calculation of inner wall convection. For instance, one of the first correlations developed for liquid sodium is the Lyon-Martinelli correlation [140]:

$$Nu = 7 + 0.025(Re Pr)^{0.8} \quad (2.6)$$

where Nu is the Nusselt number, Re is the Reynolds number and Pr is the Prandtl number.

The Sankey diagram illustrating the energy balance of the receiver is shown in Figure 2.6. The heat balance is expressed as:

$$\dot{Q}_{\text{net}} = \dot{Q}_{\text{rec,inc}} - \dot{Q}_{\text{emi}} - \dot{Q}_{\text{conv}} - \dot{Q}_{\text{ref}} \quad (2.7)$$

where \dot{Q}_{net} is the net energy absorbed by the HTF, \dot{Q}_{emi} , \dot{Q}_{conv} and \dot{Q}_{ref} are the emissive, convective and reflective losses. Then, the instantaneous receiver efficiency is defined as:

$$\eta_{\text{rec}} = \frac{\dot{Q}_{\text{net}}}{\dot{Q}_{\text{rec,inc}}} \quad (2.8)$$

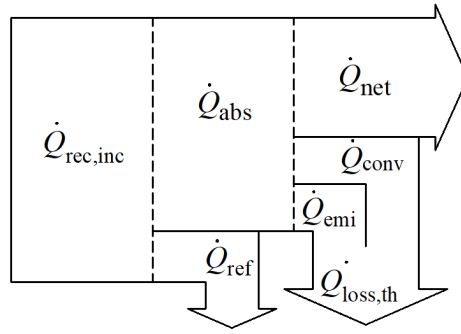


Fig. 2.6: Sankey diagram of the energy flow at the receiver.

The heat transfer process can be solved in detailed CFD simulation, but the computational effort is too high for the receiver optimisation goal. Therefore, semi-empirical models are proposed based on the discretisation of receiver tubes. A semi-empirical model has been compared with CFD simulations by Rodríguez-Sánchez et al. [58], and the results showed that the simplified model can predict the heat fluxes, the salt and the tube wall temperature with a deviation lower than 6% compared to CFD simulations. Other reported semi-empirical models have been proposed by Conroy et al. [22] and Schöttl et al. [141] for receiver design and optimisation. In this thesis, the receiver thermal model developed by Asselineau [142] is adopted to simulate the thermal performance of the receiver.

The model assumes that flux and temperature vary only in the axial direction of each tube bank. Each tube bank is vertically meshed into flat surfaces. The flux and temperature are assumed to be uniform at each mesh element. The flowchart of the receiver model is illustrated in Figure 2.7. Using the incident flux distribution from the optical simulation, an estimate of the net heat flux to the tubes is made to solve the HTF temperatures with a 1D finite difference (FD) method. The HTF temperatures are then used to re-evaluate the net heat flux using the radiosity method, and the net heat flux estimations are adjusted. The above process is repeated until the discrepancy between the assumed net heat fluxes and the calculated fluxes fall below a convergence threshold, at which point the energy balance is assumed to be converged. Then, the mass flow rate, HTF temperature and surface temperature are obtained. After solving the energy balance model, the net flux, surface and HTF

temperatures, thermal losses and the receiver efficiency can be obtained.

More details of the thermal model can be referred to in the work of Asselineau [142], and the code for modelling external cylindrical and billboard receivers can be found in Github⁴.

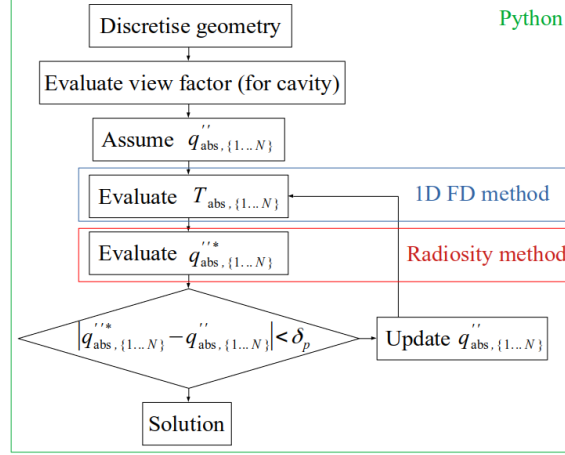


Fig. 2.7: Flowchart of the receiver thermal model.

2.2.3 Thermomechanical stress limits

Thermo-mechanical stresses are caused by temperature and pressure gradients in the receiver tube during operations. The mechanical reliability of solar receivers is investigated considering severe thermal loading conditions that instigate creep-fatigue. In this thesis, the methodology proposed by Logie et al. [88, 143] is applied to calculate the thermomechanical limits. The ASME Boiler & Pressure Vessel Code Section VIII Div. 2 is used to predict maximum allowable flux incident on tubes using linear-elastic analysis. To simplify the incorporation of flux limits derived from structural integrity considerations into coupled optical-thermal models, allowable flux density (AFD) values are calculated for a range of values of HTF fluid temperature and mass flow. Thus, the thermal models did not need to resolve the circumferentially varying temperature profile of the tube, yielding a significant saving in calculation while providing a satisfactory balance of energy arriving at, absorbed and re-emitted by the tube at any given location. Figure 2.8 illustrates the AFD tables as functions of HTF temperature and bulk flow velocity for a given tube geometry with Alloy 740H. The AFD tables are then coupled to this work's optical and thermal simulation tools. After solving the heat transfer model, the obtained net flux and velocity at each mesh element of the receiver are introduced to calculate the flux limit using a 2D linear interpolation. The flux limits can then be compared to the net flux distribution to judge the thermo-mechanical safety of the receiver.

The AFD is expressed in terms of net (absorbed) flux, rather than incident flux, as in some literature [99]. This is because the net flux is directly related to thermal

⁴Open_CSPERB: https://github.com/casselineau/Open_CSPERB.

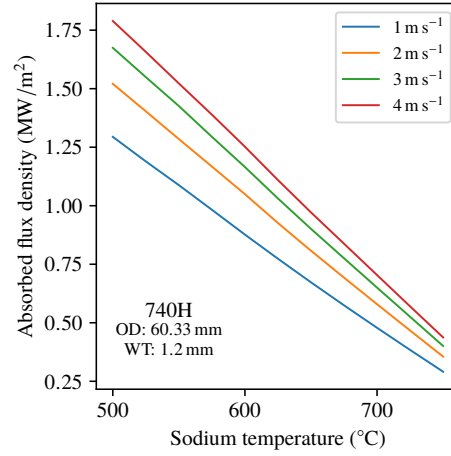


Fig. 2.8: AFD dependent on sodium temperature and velocity (as calculated by Will Logie based on the method in Section 2.2.3 [88, 143]). The pipe outer diameter is 60.3 mm and the pipe thickness is 1.2 mm. The tube material is Alloy 740H. The AFD data can then be integrated with the optical and thermal simulation tools in this thesis.

stresses in tubes, while the incident flux is not directly related because of the thermal losses. The heat transfer model needs to be used each time after ray-tracing to obtain the net flux distribution.

2.3 Annual modelling technique

The solar radiative flux on the receiver is highly transient across the year, mainly because of sun positions and the DNI variations. The variable incident flux into the receiver, together with the change of ambient environmental factors (i.e. ambient temperature, wind speed), brings great fluctuation on receiver performances. A conventional annual modelling technique simulates the system using the instantaneous modelling methods at a short time interval, for instance, every hour. However, with the detailed optical-thermal models discussed above, the conventional method requires a high computational load for annual simulations. Therefore, new modelling techniques are introduced in this section to achieve an accurate and efficient assessment of the heliostat field and receiver efficiencies in annual simulation. It is noted that the annual models are developed for cylindrical external receivers but can be applied to other types of receiver systems in the future.

2.3.1 Annual optical modelling

To overcome the high computational costs for optical annual simulations, the simplest approach is based on a single time point, which can be the solar noon of either equinox or solstice [46]. However, the accuracy of such a method is limited. Better options include choosing one representative day for each month [144] or using

a sun position discretisation method [145]. In this thesis, a sun sampling approach with an interpolation method presented by Grigoriev et al. [146] is applied.

The sun's apparent motion is caused by the orbital and axial rotation of Earth. The corresponding rotation angles can be described in terms of solar angles. In this method, the sun position is described in terms of ecliptic longitude ($\lambda \in (-\pi, \pi]$) and solar hour angle ($\omega \in (-\pi, \pi]$). The domain of sun positions is discretised using a two-dimensional grid of N by M points with equidistant steps. Figure 2.9 shows the discretisation of the sun positions.

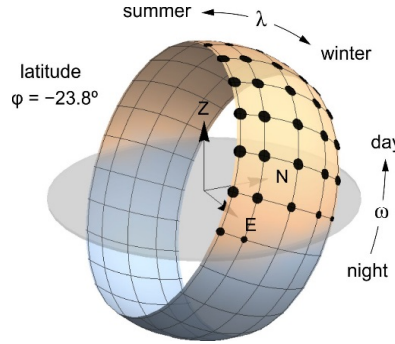


Fig. 2.9: The sun path for the latitude of Alice Springs. The independent points on the sampling grid are marked by dots [146]

After discretisation, MCRT simulations are implemented for the entire heliostat field on sun positions with elevation angles larger than zero to get the instantaneous optical efficiencies. The optical simulations are performed under clear-sky irradiance conditions. The Meinel clear-sky model [147] is applied, which is defined as:

$$I = I_0 \times 0.7^{AM^{0.678}} \quad (2.9)$$

where $I_0 = 1365 \text{ W/m}^2$, $AM = 1/\cos(z)$, z is the zenith angle. Notably, sun positions have spring–autumn symmetry, so only half a year needs to be simulated. The spring–autumn symmetry can be formulated as:

$$f(\lambda, \omega) = f(\pi - \lambda, \omega) \quad (2.10)$$

where $f(\lambda, \omega)$ represents any function on the sun's position and is the instantaneous field efficiency in this thesis. East-west symmetry mostly holds for a radial-staggered field layout, so only half a day needs to be simulated. The east-west symmetry is expressed as:

$$f(\lambda, \omega) = f(\lambda, -\omega) \quad (2.11)$$

The simulated optical results on different sun positions are stored in the form of an optical efficiency look-up table (OELT). After obtaining the OELT, the optical efficiency at any sun position can be interpolated from the OELT. The Akima splines in the CombiTable2D model from the OpenModelica library [148] are applied for the

interpolation.

The annual field efficiency is expressed as:

$$\eta_{a,field} = \frac{\sum_{i=1}^{i=365} \int_{sunrise}^{sunset} GA(t) \eta_{field}(\lambda(t), \omega(t)) dt}{\sum_{i=1}^{i=365} \int_{sunrise}^{sunset} GA(t) dt} \quad (2.12)$$

The validation of the 2D interpolation method with the hour-by-hour simulation will be presented in Chapter 5 with a reference system compatible with the Gen3 Liquid Pathway project.

2.3.2 Annual heat transfer modelling

Solving a semi-empirical receiver energy balance model is normally not as time-consuming as the ray-tracing simulation of a heliostat field. However, hour-by-hour simulation is still too heavy for annual receiver simulations. To accelerate this process, Schöttl et al. [56] used a ANN model to get the receiver output from $\dot{Q}_{rec,inc}$, T_{amb} , the ground-level wind speed V_{wind} and solar angles. In this thesis, acceleration of the receiver annual performance estimation is obtained by using an accurate reduced-order model.

A series of carefully selected time points are used to generate a database of receiver performance information. This database, labelled Receiver Efficiency Look-up Table (RELT), is subsequently used to fit the coefficients in regression models. To generate the trained database, Schöttl et al. [56] selected nine characteristic days for simulation:

- Minimum, maximum and mean daily cumulative DNI
- Minimum, maximum and mean daily average wind speed
- Minimum, maximum and mean daily average ambient temperature

The selected time points represent the variation of the three input parameters: $\dot{Q}_{rec,inc}$, T_{amb} and V_{wind} , however, more than 50 time points are needed on those nine characteristic days, and the computationally expensive ray-tracing simulation needs to be performed at each time point. To further reduce the computational load, in this thesis, selected results from ray-tracing simulations in generating the OELT are reused for receiver simulations, which accounts for the variance of $\dot{Q}_{rec,inc}$. This saves computational time because no further ray-tracing simulation is needed in generating the RELT. To capture the impact of T_{amb} and V_{wind} variations, the maximum and minimum values for these two parameters in the TMY file are found, and the receiver models are run with varying T_{amb} and V_{wind} between their maximum ranges after running ray-tracing simulations on selected sun positions.

The RELT is subsequently used to fit a receiver model in which we focus on receiver energy loss components rather than the integrated receiver output directly, as is typically the case in other works [56, 111].

The reflective loss is obtained using interpolated data of $\dot{Q}_{\text{rec,inc}}(t)$ from the OELT. The reflective loss at time t is calculated as:

$$\dot{Q}_{\text{ref}}(t) = (1 - \alpha_{\text{eff}})\dot{Q}_{\text{rec,inc}}(t) \quad (2.13)$$

where the effective absorptivity is defined based on pipe surface properties and assuming diffuse reflections between neighbouring pipes leading to the following equation:

$$\alpha_{\text{eff}} = \frac{\alpha}{\alpha + A_{\text{aperture}}/A_{\text{wall}}(1 - \alpha)} = \frac{\alpha}{\alpha + \frac{2}{\pi}(1 - \alpha)} \quad (2.14)$$

where A_{aperture} and A_{wall} are the surface areas of the aperture and the adjacent pipe walls. α is the pipe absorptivity.

The convective loss and radiative loss require estimates of the average wall temperature (\bar{T}_w), average convective heat transfer coefficient (\bar{h}_{conv}) and the average of the fourth power wall temperature (\bar{T}_w'). These variables are the ones that are fitted with polynomial functions. \bar{T}_w is interpolated as:

$$\bar{T}_w = C_0 + C_1\dot{Q}_{\text{rec,inc}} + C_2T_{\text{amb}} + C_3V_{\text{wind}} \quad (2.15)$$

The convective heat transfer coefficient is mainly affected by the wind speed. Similar to the polynomial fitting in Scott et al. [149], a four-degree fitting is made to determine the relationship between \bar{h}_{conv} and V_{wind} :

$$\bar{h}_{\text{conv}} = C_4 + C_5V_{\text{wind}} + C_6(V_{\text{wind}})^2 + C_7(V_{\text{wind}})^3 + C_8(V_{\text{wind}})^4 \quad (2.16)$$

Similar to the treatment of \bar{T}_w , \bar{T}_w' can be expressed as:

$$\bar{T}_w' = C_9 + C_{10}\dot{Q}_{\text{rec,inc}} + C_{11}T_{\text{amb}} + C_{12}V_{\text{wind}} \quad (2.17)$$

The 'LinearRegression' model in Python Sklearn is applied to obtain the coefficients in Eq. 2.15 and 2.17. The 'polyfit' model in Python Numpy is used for the polynomial fit in Eq. 2.16. The coefficients C_0 to C_{12} are then used to calculate the receiver losses and get the receiver efficiency via Eq. 2.7 in the annual simulation. The major difference between this method and more conventional integrated output models is that independent losses mechanisms are fitted independently.

For verification, a comparison will also be conducted between the results obtained from the proposed model and a direct regression model following Eq. 2.18.

$$\dot{Q}_{\text{rec}} = C'_0 + C'_1\dot{Q}_{\text{rec,inc}} + C'_2T_{\text{amb}} + C'_3V_{\text{wind}} \quad (2.18)$$

The annual receiver efficiency is expressed as:

$$\eta_{\text{a,rec}} = \frac{\sum_{i=1}^{i=365} \int_{\text{sunrise}}^{\text{sunset}} \dot{Q}_{\text{rec}}(t) dt}{\sum_{i=1}^{i=365} \int_{\text{sunrise}}^{\text{sunset}} GA(t)\eta_{\text{field}}(\lambda(t), \omega(t)) dt} \quad (2.19)$$

The annual solar-to-thermal efficiency represents the efficiency of the field and

receiver subsystem over a year and is defined as:

$$\eta_{a,st} = \frac{\sum_{i=1}^{i=365} \int_{sunrise}^{sunset} Q_{rec,inc}(t) dt}{\sum_{i=1}^{i=365} \int_{sunrise}^{sunset} GA(t) dt} \quad (2.20)$$

The validation of the annual heat transfer model will be validated against the hour-by-hour simulation and the direct regression model as presented later in Chapter 5.

2.4 System model and modelling technique

The annual simulations and economic evaluations are established using a system-level modelling technique, which is implemented in Modelica language through SolarTherm [121]. This system-level approach, incorporating all components of the CSP plant, is used to simulate a Gen3 Liquid Pathway system (Gen3L system). In this section, the Gen3L system is firstly introduced, followed by design point assumptions of the system. The details of the modelling method are then presented using the Gen3L system as reference.

2.4.1 Gen3L system

Figure 2.10 is a schematic representation of the Gen3L system. Apart from the field, tower and receiver, other crucial components of the system include a sodium/salt heat exchanger, thermal energy storage (TES) subsystem and a power block. Table 2.1 lists the assumptions related to key system components. The inlet and output temperatures of the sodium receiver are 520°C and 740°C, respectively. The sodium-to-salt heat exchanger is designed as a shell and tube heat exchanger to maintain a minimum approach temperature difference of 20°C. The TES system is a two-tank thermal energy storage system with chloride salt as the storage medium. The power cycle is modelled assuming a partial-cooling supercritical carbon dioxide (sCO₂) Brayton cycle, with a 51% gross efficiency at the design point.

Table 2.1: Performance of the receivers with and without spillage skirts

Component	Notes	Capacity
Heliostat field	Surround field	$\dot{Q}_{rec,inc}$
Receiver	Cylindrical external receiver	\dot{Q}_{rec}
Heat exchanger	A shell and tube heat exchanger [150]	$\dot{Q}_{HX,max}$
TES	Two tanks with chloride salt [151]	$t_{storage}$
Power block	sCO ₂ Brayton cycle [152]	\dot{W}_{net}

The system components are operated at their design capacity at a particular design point, based here on a date corresponding to the equinox and at a time corresponding to solar noon. The power block is assumed to be working at a fixed net capacity (\dot{W}_{net}), which is 100 MWe. The gross output of the power block is calculated

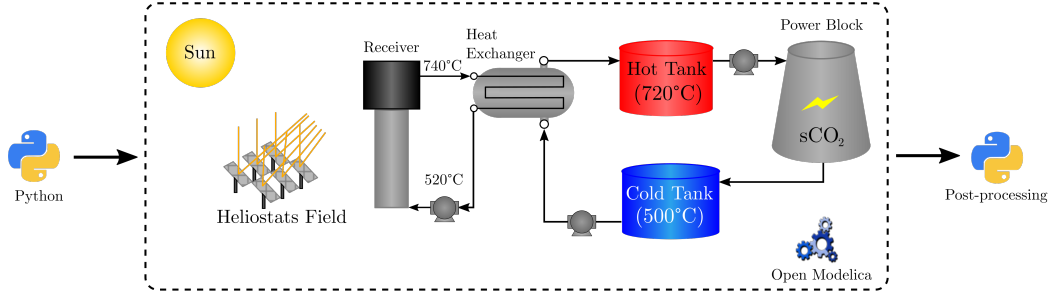


Fig. 2.10: Schematic representation of a reference CSP system based on the Gen3 Liquids Pathway plant.

considering the parasitic electrical loads in the plant:

$$\dot{W}_{\text{gross}} = \dot{W}_{\text{net}} / \eta_{\text{parasitics}} \quad (2.21)$$

where $\eta_{\text{parasitics}}$ is the parasitic efficiency assumed as 0.9. The power block nominal input is then calculated from:

$$\dot{Q}_{\text{PB,in}} = \dot{W}_{\text{gross}} / \eta_{\text{PB}} \quad (2.22)$$

where η_{PB} is the power block efficiency and is assumed to be 51% at design point for the sCO_2 power cycle [152]. The receiver nominal output (\dot{Q}_{rec}) is then calculated from:

$$\dot{Q}_{\text{rec}} = \dot{Q}_{\text{PB,in}} \times SM \quad (2.23)$$

where SM is the solar multiple. The nominal output of the heliostat field is then expressed as:

$$\dot{Q}_{\text{rec,inc}} = \dot{Q}_{\text{rec}} / \eta_{\text{rec}} \times f_{\text{hst}} \quad (2.24)$$

where f_{hst} is defined as the oversizing factor and allows the heliostat field to be oversized related to the design capacity. f_{hst} is equal to one if the heliostat field is not oversized.

It is assumed that the sodium-salt heat exchanger has a finite size and thus can only transfer a certain amount of power from sodium to salt. The heat exchanger maximum capacity is related to the receiver nominal output as:

$$\dot{Q}_{\text{HX,max}} = \dot{Q}_{\text{rec}} \times f_{\text{HX}} \quad (2.25)$$

where f_{HX} is defined as the heat exchanger capacity ratio.

The capacity of the storage subsystem is determined by the storage hours (t_{storage}) as follows:

$$Q_{\text{storage}} = \dot{Q}_{\text{PB,in}} \times t_{\text{storage}} \quad (2.26)$$

t_{storage} represents the time period that the power block can operation under nominal

conditions without thermal input from the receiver.

The capacity of system components is controlled by SM , f_{HX} , $t_{storage}$ and f_{hst} . Those design parameters will be fixed as default values in Chapters 4 to 6 and will be varied in the system-level optimisation in Chapter 7.

2.4.2 System-level model

The system-level model applied in this thesis is adjusted from the model established by Fontalvo et al. [153] and Guccione [150], which is firstly introduced in this section. The major contribution from this thesis, which is the integration of heliostat defocusing strategies with the system-level model, will then be presented. The method to calculate the LCOE is also introduced⁵.

2.4.2.1 SolarTherm model

SolarTherm consists of a library of CSP components and systems and a simulation framework. Firstly, the *DataTable* class within SolarTherm imports the hourly solar resource and meteorological data from a TMY file and interpolates the DNI, ambient temperature, atmospheric pressure, and wind speed throughout the simulation.

To model the sun, SolarTherm uses the class *Sun*, which calculates the value of the solar angles corresponding to the sun position for each time step in the year. The DNI and solar angles data are then transferred to the *HeliostatsField* class for optical simulation.

Next, the model *HeliostatsField* class computes field output ($\dot{Q}_{rec,inc}$) from the product of mirror area (A_{field}), DNI and field efficiency. The optical model within the *HeliostatsField* class interpolates the field efficiency as a function of solar angles from the OELT using the *CombiTable2D* class with Akima splines. The receiver efficiency is calculated based on the annual heat transfer modelling technique discussed in Section 2.3.2. Fluctuations in DNI impact the receiver efficiency and hence receiver output. The receiver output is calculated in the *SodiumReceiver* class, where sodium mass flow rates and enthalpies are calculated and transferred to the heat exchanger mode.

The *HX* class within SolarTherm uses TEMA standards to calculate the dimensions of the heat exchanger to maintain a minimum approach temperature difference of 20°C. The model minimises the amortised cost of the heat exchanger, and the pumping power associated with its operation. The details of the sizing method and equations can be consulted in the study by Guccione [150].

Thermal energy storage (TES) is modelled using dynamic zero-dimensional mass and energy balances. The thermal losses from the tanks are calculated from a constant loss coefficient ($h_{loss,tank} = 0.45 \text{ W/m}^2\text{K}$), the tank wetted area and the ambient temperature. The TES model also assumes an auxiliary heat supply to maintain the temperature of the tanks.

⁵Armando Fontalvo and Salvatore Guccione established the general framework of the system-level model. The author integrated the annual optical and thermal models with the system-level model with the help of Ye Wang. Special thanks are expressed to the team.

For the power block, the transient performance is estimated based on curve-fits to outputs from a normalised off-design sCO₂ power cycle model from Neises and Turchi [152].

Two control components manage the operation of the plant. The receiver control system prescribes the discharge mass flow rate of the cold tank, and also accounts for the fill level of the tank. If the cold tank is empty, the control system will stop the discharge and flag a defocus signal to the field to prevent an increase in the receiver outlet temperature. The power block control system prescribes the mass flow rate for the salt at the power block inlet and aims to achieve constant operation of the power block at the design point output from morning to afternoon unless the elevation angle is less than 15°. However, if the hot tank is empty, the control system will stop the discharge.

Economic calculations are implemented in the system-level model. Levelised Cost of Energy (LCOE) is a commonly-used economic criterion for a CSP plant. The system-level model evaluates the LCOE value based on annual simulation results and cost function evaluations. For certain systems, the cost models will be introduced in Chapters 5 and 7. The LCOE is calculated as:

$$LCOE = \frac{f_{cap}C_{cap} + C_{O\&M}}{E_{ele}} \quad (2.27)$$

where C_{cap} is the capital cost, f_{cap} is the capital recovery factor, $C_{O\&M}$ is the operational and maintenance costs, E_{ele} is the annual electricity output. f_{cap} is calculated from:

$$f_{cap} = \frac{r(1+r)^n}{(1+r)^n - 1} \quad (2.28)$$

where r is the discount rate (4.4%) and n is the lifetime of the plant (30 years).

2.4.2.2 Heliostat field defocusing strategies

The heliostat field needs to be fully or partially defocused at certain circumferences if a CSP plant reaches operational limits. The model in this work incorporates the following operation thresholds to defocus the heliostat field:

- The minimum elevation angle to operate the field is 15° to avoid excessive shading and blocking. Below this limit, energy loss is defined as the elevation defocusing loss ($\dot{Q}_{defoc,ele}$).
- The maximum wind speed to run the heliostat field is 15 m/s. Above this speed, energy loss is defined as the wind defocusing loss ($\dot{Q}_{defoc,wind}$).
- The minimum energy to run the receiver is 25% of the nominal output. Below this power, energy loss is defined as the minimum load defocusing loss ($\dot{Q}_{defoc,min}$).
- The heliostat field is defocused if the receiver exceeds its operational limits. Parts of the heliostat field are defocussed to reduce the irradiance onto the re-

ceiver, keeping the receiver operating under safety constraints, which are commonly related to flux and velocity limits for a sodium receiver. The resulting energy loss is defined as the maximum load defocusing loss ($\dot{Q}_{\text{defoc,max}}$).

- The system model defocuses the heliostat field to meet the maximum capacity of the sodium-salt heat exchanger, which is assumed to equal the receiver's nominal thermal output. The resulted energy loss is defined as the heat exchanger defocusing loss ($\dot{Q}_{\text{defoc,HX}}$).
- The system model defocuses the heliostat field when the storage tank is full. The receiver output is adjusted to be equal to the power block nominal input when storage curtailment occurs. The resulted energy loss is defined as the storage defocusing loss ($\dot{Q}_{\text{defoc,storage}}$).

The *HeliostatsField* class in SolarTherm is improved to consider those operational limits. At each step t , $\dot{Q}_{\text{defoc,wind}}$ and $\dot{Q}_{\text{defoc,ele}}$ are considered before running the optical model. Next, if the heliostat field goes into operation, $\dot{f}_{\text{foc,A}}$ and $\eta_{\text{ope,field}}$ are returned from the interpolation on the OELT, and the maximum receiver input ($\dot{Q}_{\text{rec,inc,max}}$) respecting receiver limits is calculated. Then, if the incident power to the receiver is too low, the heliostat field is shut down. If the receiver output is larger than the maximum capacity of the heat exchanger, the excess thermal power needs to be dumped. The dumped thermal power is calculated as:

$$\dot{Q}_{\text{dump,HX}} = \dot{Q}_{\text{rec,inc}}\eta_{\text{rec}} - \dot{Q}_{\text{HX,max}} \quad (2.29)$$

After dumping the thermal power, the receiver output is equal to $\dot{Q}_{\text{HX,max}}$. Figure 2.11 shows an exemplar illustration of the receiver outputs when heat exchanger defocusing occurs. The excess thermal output is dumped if the output exceeds the maximum capacity of the heat exchanger. Figure 2.11 will be explained to more detail in the specific case studies in Chapter 7.

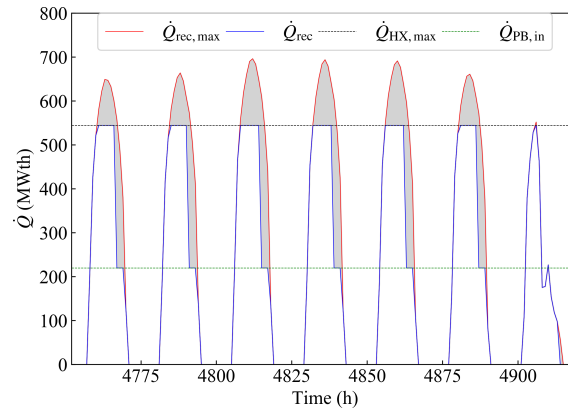


Fig. 2.11: Exemplar illustration of the heat exchanger and storage defocusing strategies. $\dot{Q}_{\text{rec,max}}$ is the maximum receiver output respecting receiver limits.

The dumped energy in Eq. 2.29 is realised by partially defocusing the heliostat

field, and the energy loss due to heliostat defocusing contributes to the heat exchanger defocusing loss ($\dot{Q}_{\text{defoc,HX}}$). To calculate $\dot{Q}_{\text{defoc,HX}}$, the optical efficiency of defocused heliostats needs to be known. However, the calculation of this optical efficiency needs MCRT simulations, which is infeasible in the system-level model. To simplify the calculation, it is assumed that the defocusing heliostats have the same optical efficiency as the entire heliostat field. This leads to:

$$\dot{Q}_{\text{defoc,HX}} = (\dot{Q}_{\text{rec,inc}} - \dot{Q}_{\text{HX,max}}/\eta_{\text{rec}})/\eta_{\text{ope,field}} \quad (2.30)$$

If storage curtailment occurs, the receiver produces a power of $\dot{Q}_{\text{PB,in}}$ to maintain the same charging and discharging rate to the storage tanks, as shown in Figure 2.11. $\dot{Q}_{\text{PB,in}}$ is the nominal input into the power block. The storage defocusing power is calculated from:

$$\dot{Q}_{\text{defoc,storage}} = (\dot{Q}_{\text{rec,inc}} - \dot{Q}_{\text{PB,in}}/\eta_{\text{rec}})/\eta_{\text{ope,field}} \quad (2.31)$$

The receiver output (\dot{Q}_{rec}) can then be obtained after going through the defocusing procedures. The defocusing model established in this section will be tested in Chapters 6 and 7 to demonstrate the effect of the model.

SolarTherm is an open-source project, and most of the code, which includes the base system, is fully accessible and editable on GitHub. The system model applied in this thesis is still being developed by ANU STG and can be found on the GitHub website⁶.

2.5 Conclusion for this chapter

This chapter introduces the methodologies that will be used in following chapters for the design and optimisation of the field and receiver subsystems. Instantaneous modelling methodologies include the optical, heat transfer and thermomechanical models and are the basis for the annual models, which permits quick and reliable modelling of the annual performance. A system-level model is introduced and heliostat field defocusing strategies are integrated into the system-level model. The methodologies introduced in this chapter are used in chapters 3-7 as follows:

- Chapter 3 uses the instantaneous optical and thermal models to simulate the performance of a cavity receiver in both dish and solar systems.
- Chapter 4 develops a heliostat aiming strategy (MDBA) based on the instantaneous models.
- Chapter 5 develops a co-optimisation technique based on the integration of the instantaneous models, annual simulation models and the system-level model.
- Chapters 6 explores the optimal receiver flow options using the MDBA method and annual modelling techniques.

⁶SolarTherm: <https://github.com/SolarTherm>, branch: 'cooptimisation'

- Chapter 7 presents a system-level optimisation based on the developed MDBA and co-optimisation methods.

Performance enhancement of cavity receivers with spillage skirts and secondary reflectors¹

3.1 Introduction

A cavity receiver geometry may represent a better option than an external receiver geometry for high-temperature solar power systems because of reduced thermal losses. However, a limitation is that the small aperture necessary for an efficient (and affordable, practical) cavity receiver may lead to high spillage losses, negating the thermal efficiency gains. As reviewed in Chapter 1, the benefit of adding a spillage skirt and secondary reflectors to cavity receivers has not been systematically examined in literature. The impact of skirts and reflectors on receiver performance will be investigated for both dish and tower power systems in this thesis. In this chapter, MCRT is coupled with heat transfer models to assess the benefit of secondary reflectors and spillage skirts on the performance of cavity receivers. A progressive Monte Carlo evaluation (PMCE) method [142] is used to determine the best geometric designs with the highest receiver-and-interception efficiencies. The spillage skirt and three different types of secondary reflectors, including conical, trumpet and CPC reflectors, are investigated to decrease the energy loss.

The benefit of adding a spillage skirt and secondary reflectors is tested for both dish and tower systems. The concept is first demonstrated in a dish system where the optics of the reflector are regular and simply described. Thus, the analysis mostly relates to performance of the receiver, skirt and secondary reflector themselves, and depends less on assumptions about the concentrator system. Next, the observations using a dish concentrator are tested for a heliostat field. The optical concentrator for a tower system is substantially different from the ideal parabolic dish case, and it is worthwhile investigating if the strategies developed in the context of the dish system can be applied to a tower system.

¹This chapter is based on: S. Wang, C.A. Asselineau, Y. Wang, J. Pye, J. Coventry, Performance enhancement of cavity receivers with spillage skirts and secondary reflectors in concentrated solar dish and tower systems. *Solar Energy*, 2020, 208: 708-727.

3.2 Physical models

In this section, physical models are developed for the cavity receivers, spillage skirts and secondary reflectors.

3.2.1 The cylindrical cavity receiver

The receiver modelled is a cylindrical cavity receiver composed of a helical coil of tubes, as shown in Figure 3.1(a) and (b). For the dish case, the helical coil is a single continuous tube. However, for the larger capacity tower case, the coil comprises a tube bundle of five tubes to keep fluid velocities within acceptable limits. The tube diameter is also higher for the tower case, corresponding to the overall larger dimensions of this case. The tube inlet is at the cavity aperture and the outlet is located at the centre of the circular back plate. The heat transfer fluid (HTF) is chosen as liquid sodium with inlet and outlet temperatures of 520°C and 740°C respectively. Thermal properties of liquid sodium are determined from correlations [154]. The cylindrical radius (R_{cyl}) and height (H_{cyl}) are the two essential geometric parameters in the receiver design. The tubes are made of Haynes 230 alloy. Other key parameters of the receiver are shown in Table 3.1. In this work, coiled loops are approximated with stacked circular toroids. The flux and temperature distributions are non-uniform within the cylindrical receiver. Each coil of tube (or tube bundle of five tubes for the tower case) is assumed to have a constant flux and temperature, based on the average of the non-uniform distribution over that discrete area.

For simplification, the flux and temperature distributions are assumed to be averaged and constant on the surface of a tube (for the dish) or a tube bundle (for the tower).

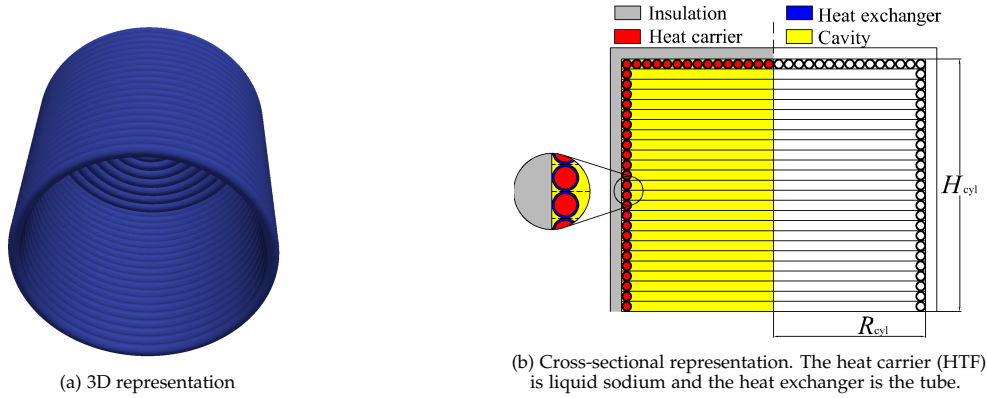


Fig. 3.1: The cylindrical cavity receiver

3.2.2 The spillage skirts

The spillage skirts comprise of coiled tubes (or tube bundles) outside the cavity aperture. Similar to the tubular cavity receiver, spillage skirts are also active ab-

Table 3.1: Parameters for the cylindrical cavity receivers

Parameters	Values	
	Dish	Tower
Inlet temperature (°C)	520	520
Outlet temperature (°C)	740	740
Tube absorptivity	0.9	0.9
Tube thickness (mm)	1.245	1.65
Outer diameter (mm)	17.15	31.75
Tube number per bundle	1	5

sorbers with internal HTF flow. Two kinds of spillage skirts are investigated in this study: a flat spillage skirt and an inclined spillage skirt. The three-dimensional and geometric illustrations of the cavity receivers with skirts are shown in Figure 3.2. Geometry is defined by the skirt length (l_s) and skirt angle (θ_s), as shown in figures 3.2 (b) and (c). θ_s is fixed as 90° for the flat skirt. When a spillage skirt is included, the fluid inlet is the outermost tube (or tube bundle), and the fluid path progresses inwards before transitioning to the bottom of the cylindrical section. Thus, the spillage skirt is the lowest temperature section of the receiver, which is important given that the spillage skirt has a higher view factor to the surroundings compared to the inside of the cavity. For latent systems with constant temperature, such as for receivers designed to work with a Stirling cycle engine, the spillage skirt concept may be less beneficial.

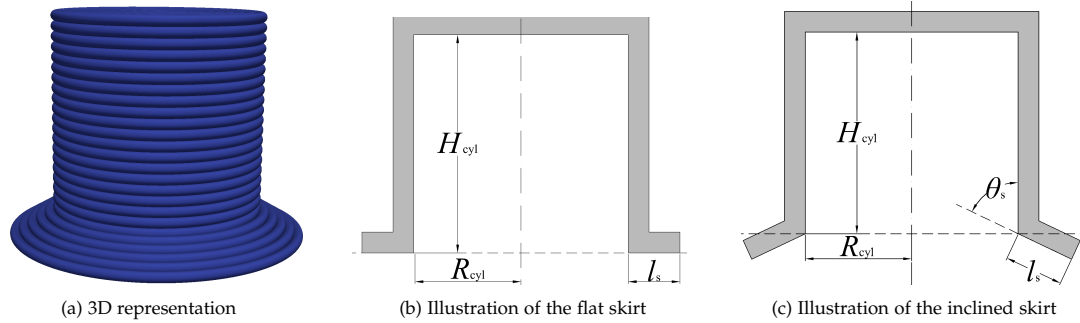


Fig. 3.2: The cavity receiver with spillage skirts

3.2.3 The secondary reflectors

Three typical reflectors (conical, trumpet and CPC) are added to the cavity receiver as second-stage reflectors. The inlet and outlet of the secondary reflectors are defined as the outer and inner apertures, respectively. The reflectivity of the secondary reflectors is set as 0.88 [32]. The mirror slope error is matched to the slope error of the primary concentrator (3 mrad for the dish configuration [155] and 1.45 mrad for the tower configuration [32]). It is noted that no thermal effects are considered in this study for the secondary reflectors, despite the fact that they do absorb some energy (i.e. their temperature is not calculated). Geometries of the conical

reflector are illustrated in Figure 3.3. If a Cartesian coordinate is established with origin on the centre of the inner aperture, the equation of a conical reflector can be expressed as:

$$\begin{cases} z = -(r - R_1) / \tan \theta_c, -H_{\text{out}} \leq z \leq 0 \\ r = \sqrt{x^2 + y^2}, R_1 \leq r \leq R_{\text{out}} \end{cases} \quad (3.1)$$

where R_1 is the radius of the inner aperture and equal to R_{cyl} , θ_c is the reflector angle. The shape of the conical reflector is governed by the outer reflector radius (R_{out}) and the reflector height (H_{out}).

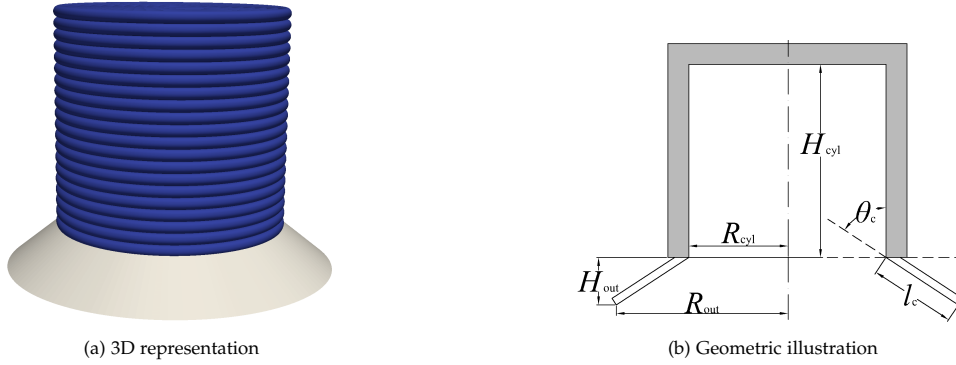


Fig. 3.3: The cavity receiver with a conical reflector

The trumpet reflector is truncated from a hyperboloid surface with two planes according to the minimum and maximum radius, R_1 and R_{out} , respectively. The equation of the trumpet reflector can be expressed with the following equation:

$$\begin{cases} z = -\frac{b}{a} \sqrt{r^2 - a^2} + \frac{b}{a} \sqrt{R_1^2 - a^2} \\ r = \sqrt{x^2 + y^2}, R_1 \leq r \leq R_{\text{out}} \end{cases} \quad (3.2)$$

where a and b are two coefficients from the hyperboloid equation. The trumpet shape is determined by the two hyperboloid coefficients (a , b) and the outer radius (R_{out}). To better illustrate the geometry of the trumpet reflector, the equivalent reflector length (l_t) and reflector angle (θ_t) can be defined by assuming the trumpet reflector is 'flat' as the conical reflector. The definition will be used in a parametric study in Section 3.5.4.2 to compare the trumpet with the conical reflector.

One thing to notice is that the definition of the trumpet in this paper is slightly different from the trumpet definition of O'Gallagher et al. [156]. In O'Gallagher's definition, the trumpet reflector can redirect all radiation originally directed towards the outer aperture into the inner aperture with single or multiple reflections. The equation of O'Gallagher's trumpet is expressed as:

$$z = -\frac{\sqrt{R_{\text{out}}^2 - R_1^2}}{R_1} \sqrt{r^2 - R_1^2}, R_1 \leq r \leq R_{\text{out}} \quad (3.3)$$

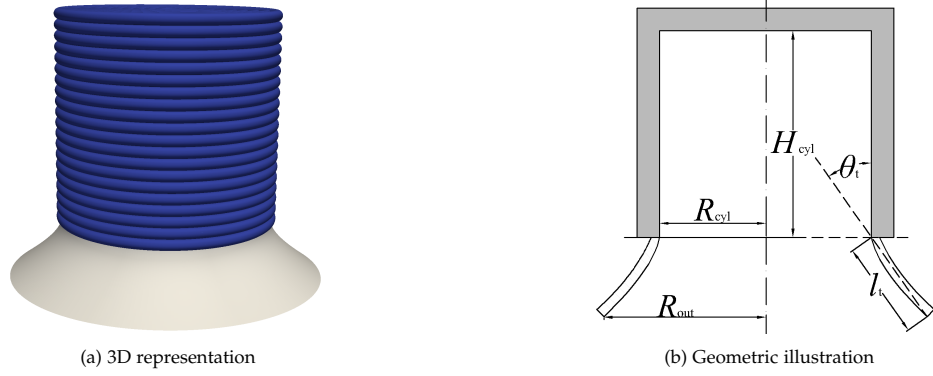


Fig. 3.4: The cavity receiver with a trumpet reflector

Compared with Equation 3.2, it can be seen that O’Gallagher’s trumpet is a special case of the more generic definition with the a and b parameters fixed:

$$\begin{cases} a = R_1 \\ b = \sqrt{R_{\text{out}}^2 - R_1^2} \end{cases} \quad (3.4)$$

More detailed comparison with O’Gallagher’s trumpet will be addressed in Section 3.5.4.2.

The CPC reflector is another commonly-used secondary concentrator. The acceptance angle (θ) is the key geometric parameter of the 3D CPC reflector, and the equation is shown as follows [157]:

$$\begin{cases} ((\sqrt{x^2 + y^2} + R_1) \cos \theta - z \sin \theta)^2 = 4R_1(1 + \sin \theta)(-z \cos \theta - \sqrt{x^2 + y^2} \sin \theta + R_1) \\ h_{\text{CPC}} = R_1(1 + \sin \theta) / \tan \theta, -h_{\text{CPC}} \leq z \leq 0 \end{cases} \quad (3.5)$$

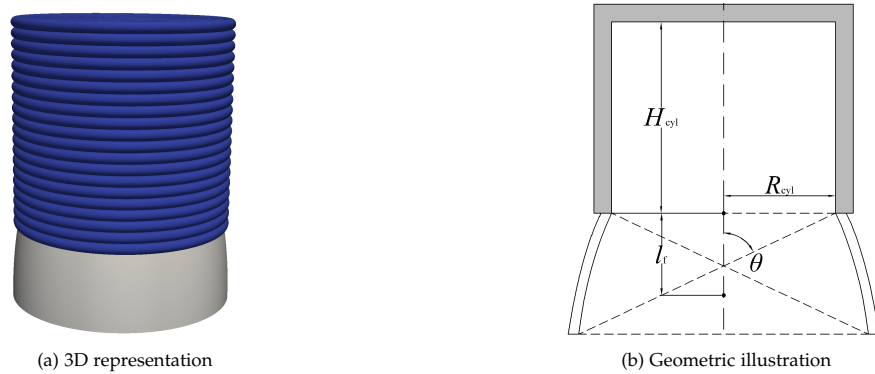


Fig. 3.5: The cavity receiver with a CPC reflector

Similarly, the acceptance angles for conical and trumpet reflectors have been defined in Figures 3.3(b) and 3.4(b).

3.2.4 Combination of spillage skirt and secondary reflectors

Two types of receivers with a combination of a spillage skirt and a secondary reflector are investigated: (1) the flat spillage skirt with the conical reflector and (2) the flat spillage skirt with the trumpet reflector. The equations of reflectors are similar to the prior case with no spillage skirt, except that the inner radius R_1 becomes the sum of the cylinder radius (R_{cyl}) and the skirt length (l_s).

$$R_1 = R_{\text{cyl}} + l_s \quad (3.6)$$

3.3 Modelling methodology

3.3.1 Energy balance

3.3.1.1 Optical processes

The optical process in the dish and tower systems is simulated by ray-tracing codes Tracer [130] and SOLSTICE [131], respectively. In simulating the tower system, the geometries of the cavity receiver, the spillage skirt and secondary reflectors are firstly established in Blender² and exported as Stereo Lithography (stl) files, and then imported into SOLSTICE to do the MCRT calculations. The sunshape is chosen as a pillbox type with angular range of 4.65 mrad.

3.3.1.2 Heat transfer processes

Using absorbed flux data for tube segments calculated from ray-tracing simulations, an energy balance model including heat transfer mechanisms is developed to calculate the surface temperatures of the tubes. To simplify the study, the convective heat transfer coefficient is set to a constant 10 W/m²K, and the ambient temperature is assumed to be 20°C, and atmospheric attenuation is neglected. The constant coefficient is used to calculate the convective loss from the hot surfaces of both the cavity receiver and the spillage skirt. Similar assumptions have been used in previous studies [142]. Inner walls of the cavity receiver are assumed to be grey and diffuse. View factors between tube segments are calculated with the assumption of flat surfaces tangent to the tube. For the case of the receiver with an inclined spillage skirt, view factors cannot be solved analytically and the adaptive view factor calculation algorithm (Asselineau, 2017) based on the MCRT method is used to get results with sufficient accuracy, targeting 1% of the confidence interval widths of all view factors. The heat transfer model is based on the work of Asselineau [142], as introduced in Chapter 2.

²Blender: <https://github.com/blender>.

3.3.1.3 Efficiencies and losses definitions

The energy flow through the concentrators to the receiver is shown in Chapter 2. The spillage loss (\dot{Q}_{spi}) and reflective loss (\dot{Q}_{ref}) are obtained from the optical tools. After obtaining the temperatures of the tubes, the emissive loss (\dot{Q}_{emi}) and the convective loss (\dot{Q}_{conv}) are calculated. The conductive losses through the back of the receiver are neglected. The key performance metric in this study is the receiver-and-interception efficiency ($\eta_{rec,int}$), which is defined as:

$$\eta_{rec,int} = \frac{\dot{Q}_{net}}{\dot{Q}_{con}} = \frac{\dot{Q}_{con} - \dot{Q}_{spi} - \dot{Q}_{ref} - \dot{Q}_{emi} - \dot{Q}_{conv}}{\dot{Q}_{con}} \quad (3.7)$$

where \dot{Q}_{con} and \dot{Q}_{net} are the energy reflected from the concentrator and the net heat gains of the HTE, respectively.

For receivers with secondary reflectors, the definition of the spillage loss is different from the receiver with no reflectors. As shown in Figure 4(b) and (c), after reflection by the primary concentrator, some rays may not enter the outer aperture if they are blocked by the secondary reflector or miss the receiver. These two losses are defined as the secondary blocking loss ($\dot{Q}_{sec,block}$) and the outer spillage loss ($\dot{Q}_{outer,spi}$). After entering the outer aperture, the energy absorbed by the reflector is defined as the secondary absorption loss ($\dot{Q}_{sec,abs}$), while the energy of rays reflected out of the outer aperture is defined as the secondary reflective loss ($\dot{Q}_{sec,ref}$). The sum of the above-defined losses represents the energy that misses the inner aperture and is defined as the inner spillage loss ($\dot{Q}_{inner,spi}$). Two new efficiencies are defined to judge the interception capability (η_{interc}) and the transmission performance (η_{trans}) of the secondary reflectors:

$$\eta_{interc} = \frac{\dot{Q}_{outer}}{\dot{Q}_{con}} = \frac{\dot{Q}_{con} - \dot{Q}_{outer,spi} - \dot{Q}_{sec,block}}{\dot{Q}_{con}} \quad (3.8)$$

$$\eta_{trans} = \frac{\dot{Q}_{inner}}{\dot{Q}_{outer}} = \frac{\dot{Q}_{outer} - \dot{Q}_{sec,ref} - \dot{Q}_{sec,abs}}{\dot{Q}_{outer}} \quad (3.9)$$

where \dot{Q}_{outer} and \dot{Q}_{inner} are the energy incident to the outer and inner apertures, respectively.

3.3.2 Progressive Monte Carlo Evaluation method

The PMCE method is a receiver design method developed by Asselineau [142] to explore optimum geometric configurations of solar receivers. The aim of the PMCE method is to progressively down-select candidates from an initial random population of geometries by discarding under-performing ones. The ‘progressive’ term describes how this screening is done in multiple instances after tracing a bundle of rays, with increasing confidence levels as ray numbers build up. The ‘Monte Carlo evaluation’ means this method can tackle optimisation problems with stochastic approximations of results, so the PMCE method is suitable for the optimisation of solar receivers with

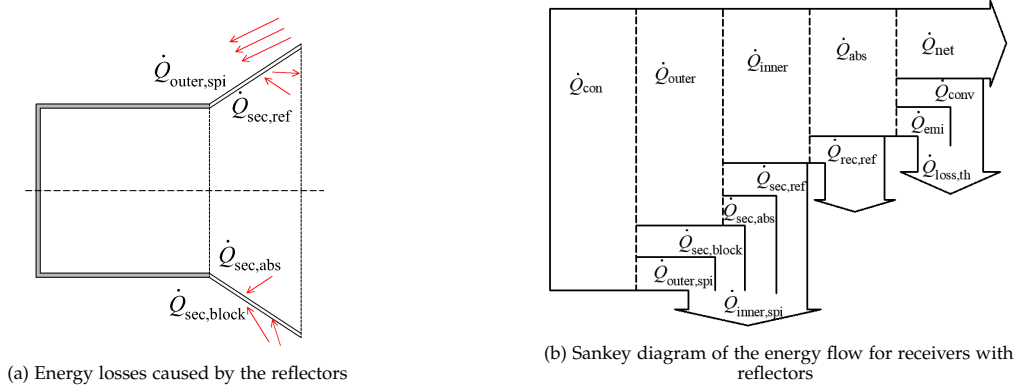


Fig. 3.6: Illustration of the energy flow.

MCRT simulations. A metric M , which is the receiver-and-interception efficiency, is used to assess the performance of each geometry. The values of each parameter are randomly selected within a parameter interval. After each MCRT step (j), the metric values and confidence intervals (CI) can be calculated for each geometry (i) according to the three-sigma rule in the central limit theorem:

$$CI_{j,i} = \frac{3S_{j,i}}{\sqrt{j}\overline{M}_{j,i}} \quad (3.10)$$

where $\overline{M}_{j,i}$ is the weighted average of the metric, and $S_{j,i}$ is the sample standard deviation. If the best-case scenario performance of one candidate is smaller than the worst-case scenario performance of the best-performing candidate, the candidate is discarded, as shown in Equation 3.11. If not, the candidates are retained for the next step of ray-tracing and performance estimation.

$$\overline{M}_{j,i}(1 + CI_{j,i}) \geq \overline{M}_{j,i=\text{best}}(1 - CI_{j,i=\text{best}}) \quad (3.11)$$

The simulation comes to the end once the standard deviations of all candidates meet the requirement of a convergence threshold ($\delta_{\text{thresh}}=0.001$). The candidates still remaining in the active population are regarded as optimum candidates.

It is noted that the selected threshold value of the standard deviation leads to a certain level of the confidence, which is determined by $S_{j,i}$, $\overline{M}_{j,i}$ and j as given in Equation 3.10. The confidence interval increases with more evaluation steps. If it is assumed that the step number is 10, which is generally the case in the subsequent simulations, and that the average efficiency is 0.85, then the precision of the results can be evaluated as approximately 0.001. In other words, for the 3-sigma confidence interval selected, there is a 99.7% probability that the results will be accurate within this precision. Thus, the results are given with three decimal places, or when expressed in percentage terms, with a single decimal place.

3.4 Performance enhancement of cavity receivers in a dish system

This first case study focuses on the case of a parabolic dish where the optics of the reflector are regular, independent of sun angle, and simply described. Thus the observations from the analysis based on a dish system relate almost exclusively to performance of the receiver, skirt and secondary reflector themselves, and depend less on assumptions about the concentrator system, as is the case in the second case study with a heliostat field. However, it is noted that a dish has significantly better ‘optical quality’ (i.e. a closer approximation to a perfect paraboloid) than a heliostat field, so the specific performance values in this case study relate only to dishes.

3.4.1 The SG4 Big Dish

The size and shape of the dish is chosen to match the Solar Generator 4 (SG4) Big Dish at the Australian National University (ANU) [155], which is a parabolic dish concentrator with aperture area of approximately 500 m². The average diameter and focal length are 25.1 m and 13.4 m, respectively. The slope error of the dish concentrator is set as 3 mrad. Other parameters for the physical model of the dish used are summarised in Table 3.2.

Table 3.2: Parameters of the dish model

Parameters	Values
Surface reflectivity	0.9
Average dish diameter (m)	25.1
Focal length (m)	13.4
Rim angle (°)	50.2
Slope error (mrad)	3

3.4.2 Parametric study and optimisation of the cylindrical cavity receiver

For the cylindrical cavity receiver, a parametric study is first conducted to study the effects of cylindrical radius (R_{cyl}) and height (H_{cyl}). Receiver-and-interception efficiencies at different radii and heights are shown in Figure 3.7(a). It can be seen that there are optimum values for the two parameters. For the physical model of the SG4 dish as earlier described by the parameters in Table 3.2, the optimum ranges of radius and height are 0.3-0.4 m and 0.5-0.7 m, respectively. The spillage, reflective, emissive and convective losses at different geometries are shown in Figure 3.7(b) and (c). The spillage loss drops with increasing cylindrical radius. The reflective loss decreases with smaller radius and larger height because less incident radiation is reflected out of the cavity if the receiver shape is narrower and longer. The emissive loss decreases with smaller aperture size. Larger heights also help in reducing emissive power because the high temperature areas are located further away from the cavity aperture. The convective loss decreases with smaller radius and height because of the

reduced surface areas. Due to the combination of all these effects, there are optimum values for both the radius and height.

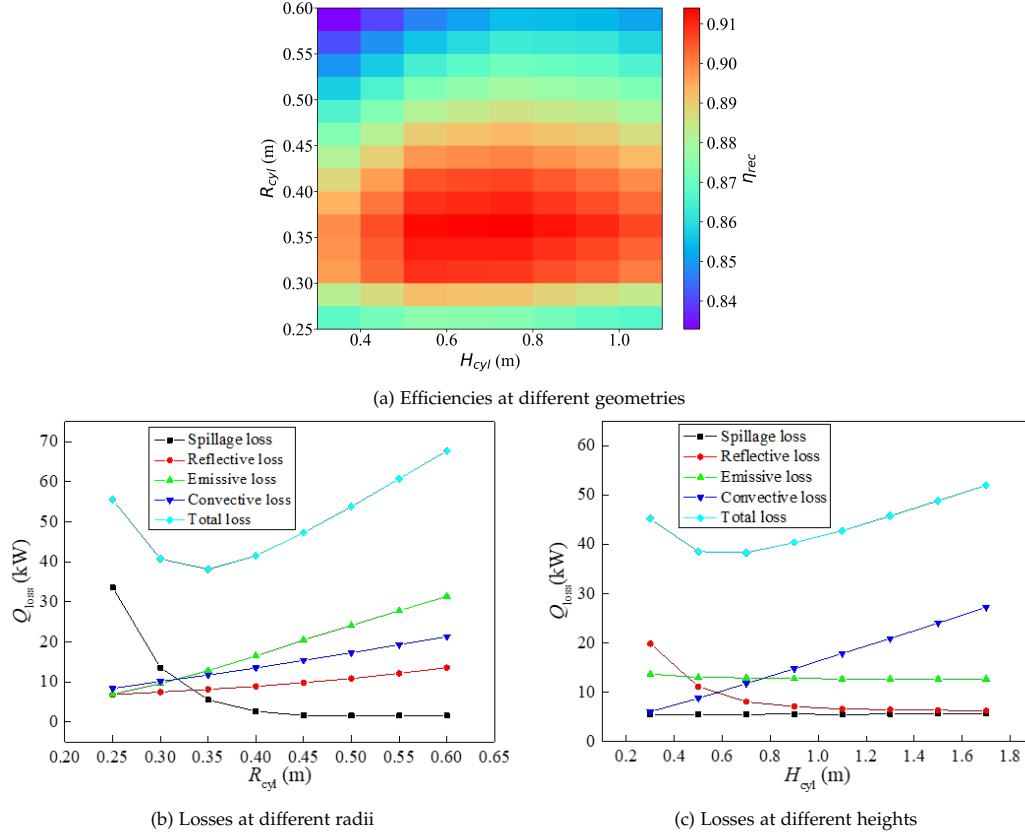


Fig. 3.7: Results of the parametric study for the cylindrical cavity receiver

After this parametric study, the PMCE method is used to obtain the optimum cylindrical radius and height. As shown in Figure 3.8(a) and (b), several candidates are regarded as statistically optimum. Their best-case scenarios efficiency estimates are all better than the worse-case scenario of the best geometry, and their sample standard deviations S are less than the convergence threshold. It is interesting to note that the receiver-and-interception efficiency is significantly less sensitive to changes in height than in radius. The parameters corresponding to the best geometry are shown in Table 3.3 (configuration D1). The best radius and height are 0.334 m and 0.601 m, which match with the optimum range in the above parametric study. Figure 3.9 illustrates the temperature and heat flux distributions of the optimised receiver. In this figure, the cylindrical surface is unfolded and shown as a stretched flat surface. The maximum temperature and flux areas are located on the back cylindrical plate of the cavity receiver.

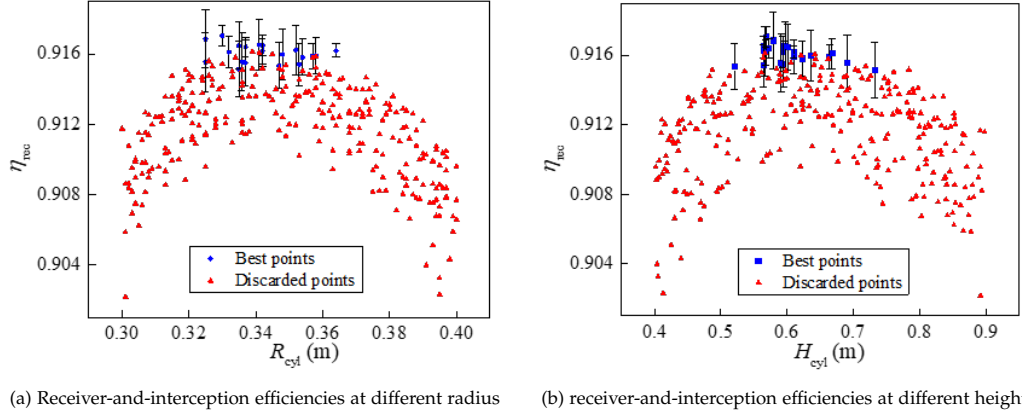


Fig. 3.8: Optimisation results for cylindrical receiver

Table 3.3: Performance of the receivers with and without spillage skirts

Configuration	D1	D2	D3
	Optimised model	With flat skirt	With inclined skirt
R_{cyl} (m)	0.334	0.259	0.272
H_{cyl} (m)	0.601	0.525	0.520
l_s (m)	/	0.125	0.092
θ_s ($^\circ$)	/	/	76.9
\dot{Q}_{spi} (kW)	6.5	2.4	3.8
\dot{Q}_{ref} (kW)	8.9	10.7	10.2
\dot{Q}_{emi} (kW)	11.9	12.9	12.0
\dot{Q}_{conv} (kW)	9.8	8.0	7.9
$\eta_{rec,int}$ (%)	91.6	92.3	92.3

3.4.3 Optimisation of the cylindrical receiver with spillage skirts

In this section, the PMCE method is used to optimise the cylindrical receiver on the dish with inclusion of a spillage skirt. For the flat spillage skirt, the optimised parameters include cylindrical radius, cylindrical height and skirt length. For the inclined skirt, the skirt angle also needs to be included in the optimisation. The optimised results are shown in Table 3.3 (configurations D2 & D3) and Figure 3.10. Compared to the optimum receiver without the skirt, both the cylindrical radius and the height are reduced. The cylindrical radius can be reduced to improve the thermal performance while the spillage skirt captures the radiation that would otherwise spill outside of the aperture, and the spillage loss is reduced because the extent of the spillage skirt is larger than the aperture of the reference cylindrical case. With a smaller cavity aperture, the cylindrical height can then be reduced to reduce the convective loss, offsetting a minor increase in emissive loss because the high temperature areas are closer to the aperture. The addition of the spillage skirts is also able to reduce the receiver irradiated surface area by more than 22% which is expected to translate into receiver manufacturing cost reductions. The disadvantage of the spillage skirts is that the orientation of the skirt surface is such that emissive and

3.4. Performance enhancement of cavity receivers in a dish system

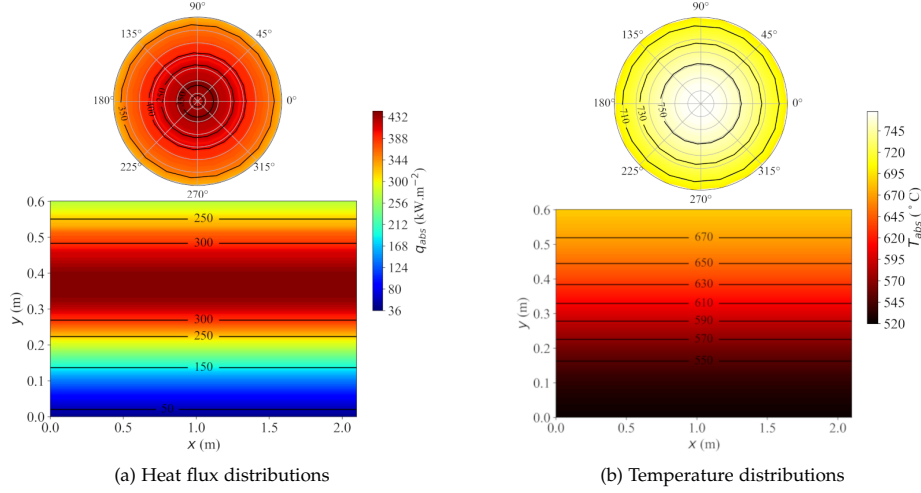


Fig. 3.9: Temperature and heat flux distributions of the optimised cylindrical receiver, shown as a plane “unwrapped” from the cylindrical shape, where x represents the angular range, and y represents the vertical height.

reflective losses may increase locally. However, the reduction of spillage and convective losses overcomes this disadvantage in this configuration. It is notable that for the temperature range studied, the spillage skirt is beneficial, but is significantly smaller than that deployed on the ANU SG4 Big Dish, which was a water-steam receiver with inlet feedwater of only 60 °C [73, 74]. The receiver-and-interception efficiency can be increased by 0.7% with a flat spillage skirt.

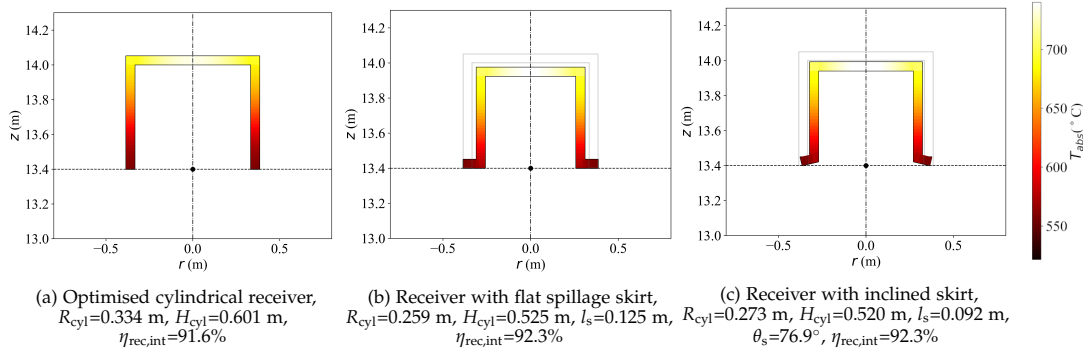


Fig. 3.10: Optimised structures and receiver efficiencies for receivers with and without spillage skirts (Black dots represent the focal points, and the shadows represent the shapes of the optimised cylindrical receiver).

For the receiver with an inclined spillage skirt, the net efficiency gain is similar to the flat case. Figure 3.11 illustrates the receiver-and-interception efficiencies at different skirt angles in the process of the PMCE optimisation. The geometries with higher skirt angles have higher efficiencies than with low skirt angles. The reason is that low skirt angles lead to large blocking effects on the incoming rays. The optimum case D3 achieves a similar performance to case D2, although the trade-offs of the losses are different. In case D3, the outer aperture radius is smaller than in case D2, leading

to higher spillage loss but lower emissive and reflective losses. Overall, the optimum receiver-and-interception efficiencies attained with flat and inclined spillage skirts are equivalent within the 3-sigma confidence interval of the optimisation method.

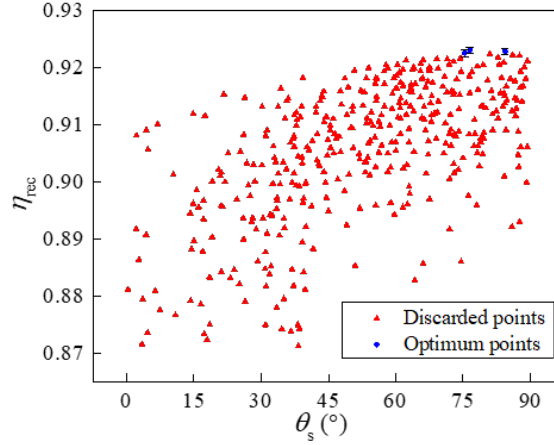


Fig. 3.11: Efficiencies at different skirt angles

3.4.4 Optimisation of a cylindrical receiver with secondary reflectors

The effects of secondary reflectors on solar receiver performance on the dish concentrator are investigated in this section.

First, the conical and trumpet reflectors are added to the cavity receiver and the optimum geometries are obtained with the PMCE method. Optimised results are shown in Table 3.4 (configuration D4-D6) and Figure 3.12. In both cases, the cylindrical radius can be reduced with regards to the receiver with no reflector, leading to lower emissive losses, although the radius reductions are not as high as the receiver with spillage skirts. The convective losses are also reduced due to the decrease of inner receiver surface areas. The reflective losses remain broadly unchanged due to the insignificant change of the aspect ratio while simultaneously decreasing the radius and height. The inner spillage losses are smaller than the bare cylindrical receiver even with smaller inner aperture size, proving that the reflectors work and effectively reflect radiation into the cavity receiver. With conical or trumpet reflectors, the receiver-and-interception efficiencies increase by about 0.6%. It can be seen from the values in Table 3.4 (configuration D4) that the secondary reflective loss dominates in the case of the receiver with the conical reflector, while it remains low for the trumpet reflector (configuration D5). Analysis of this difference shows that the trumpet is more effective at redirecting rays into the cavity in the region near to the aperture, because the reflective surface transitions its shape to be tangential to the inner surfaces of the cavity. This region still has significant incident flux, and although the outer regions of the trumpet are less effective than the conical reflector, the benefits of better performance in the inner, higher flux region slightly outweighs this disadvantage.

3.4. Performance enhancement of cavity receivers in a dish system

Table 3.4: Efficiencies and losses for receivers with reflectors

Case	D1	D4	D5	D6	D7	D8	D9
	Cylinder	Conical	Trumpet	CPC	CPC ($\theta_{\max}=70^\circ$)	CPC ($\alpha = 0$)	CPC (with l_f)
R_{cyl} (m)	0.334	0.320	0.316	0.328	0.327	0.291	0.343
H_{cyl} (m)	0.601	0.590	0.575	0.563	0.490	0.350	0.589
H_{out} (m)	/	0.311	/	/	/	/	/
R_{out} (m)	/	0.750	0.770	/	/	/	/
a	/	/	0.316	/	/	/	/
b	/	/	0.174	/	/	/	/
θ ($^\circ$)	/	/	/	89.2	69.0	52.7	89.0
l_f (m)	/	/	/	/	/	/	0.01
$\dot{Q}_{\text{outer,spi}}$ (kW)	6.5	0.2	0.7	7.0	4.3	1.8	4.8
$\dot{Q}_{\text{sec,block}}$ (kW)	/	1.6	1.9	0.3	0.2	1.5	0.5
$\dot{Q}_{\text{sec,abs}}$ (kW)	/	1.1	2.4	0.1	10.2	0.0	0.1
$\dot{Q}_{\text{sec,ref}}$ (kW)	/	2.7	0.6	0.0	0.2	0.1	0.0
$\dot{Q}_{\text{inner,spi}}$ (kW)	6.5	5.6	5.6	7.4	14.9	3.4	5.4
\dot{Q}_{ref} (kW)	8.9	8.7	8.9	9.3	11.9	14.7	9.3
\dot{Q}_{emi} (kW)	11.9	11.0	10.8	11.6	13.4	12.2	12.5
\dot{Q}_{conv} (kW)	9.8	9.2	8.9	9.1	8.6	6.1	9.9
$\eta_{\text{rec,int}}$ (%)	91.6	92.2	92.2	91.6	88.9	91.8	91.6

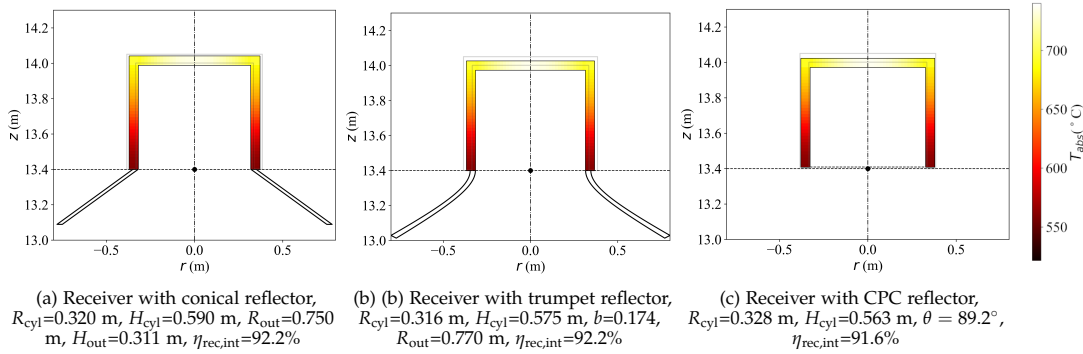


Fig. 3.12: Optimised structures and receiver efficiencies for receivers with secondary reflectors.

Key geometric parameters for the cavity receiver with a CPC reflector include the cylindrical radius, height and the CPC acceptance angle. Theoretically, all rays incoming to the outer aperture with incident angles smaller than the acceptance angle will be reflected into the inner aperture by the CPC reflector [158]. Four different cases are investigated in order to explore the best approach to using a CPC reflector. In the first case, the dish focuses at the centre of the outer aperture to reduce the secondary blocking loss, and the absorptivity of the reflector surface (α) is set to 0.12. As shown in Table 3.4 (configuration D6) and Figure 3.12(c), a very short CPC is chosen as the optimum reflector, which indicates that the optimisation method tends towards removal of the CPC from the cavity receiver. Figure 3.13 illustrates the receiver-and-interception efficiencies at different CPC acceptance angles. All the optimum geometries have high acceptance angles and short reflectors, and the receiver-and-interception efficiency drops quickly with reducing acceptance angle.

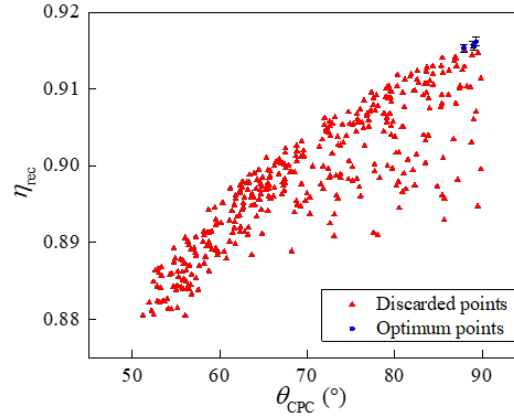


Fig. 3.13: Receiver efficiencies at different CPC acceptance angles.

To explore the reason why the CPC reflector is deemed unfavourable in the optimisation, a constrained case with fixed boundaries for the CPC geometry is studied. An upper boundary for the CPC acceptance angle is set to 70° to ensure the existence of a long enough reflector. Table 3.4 (configuration D7) shows that this approach leads to a receiver-and-interception efficiency of 88.9%, much lower than the receiver without the CPC. The secondary reflective loss is quite low, which proves that the CPC reflector operates as expected, but the secondary absorption loss is much higher than receivers with conical or trumpet reflectors.

To verify whether the high absorption loss is the only drawback of the CPC reflector, an ideal CPC with surface absorptivity of zero is considered. The upper boundary of the CPC acceptance angle is removed in this case. The efficiency of this ideal reflector case is much higher than when realistic reflectivity is assumed, as shown in Table 3.4 (configuration D8); but is still less than receivers with conical or trumpet reflectors. The optimum acceptance angle is 52.7° , which is slightly higher than the rim angle of the concentrator. With such a low acceptance angle, spillage loss is reduced and the concentration ratio increases; however, the reflective and emissive losses are surprisingly high even with a small inner aperture. This is explained in Figure 3.14 where the heat flux distribution on the receiver is analysed. The flux is much higher in regions close to the inner aperture when using a CPC and causes higher emissive and reflective losses. This suggests that using a CPC to minimise the aperture radius may require the internal geometry of the receiver to be modified from a simple cylinder (with diameter the same as the aperture diameter) to a shape that minimises these forms of heat loss, e.g. a cylinder with larger diameter or other more complex shapes [73, 159].

In the fourth case, the location of the dish focus is adjusted along the focal axis between the inner and outer apertures. A new parameter named focus-to-centre distance (l_f) is defined as the distance between the focus and the inner aperture centre. It is expected that with a deeper focus, the secondary absorption loss and receiver reflective loss can be reduced while the secondary blocking loss will increase. Table 3.4 (configuration D9) shows that the optimised acceptance angle is very large, and

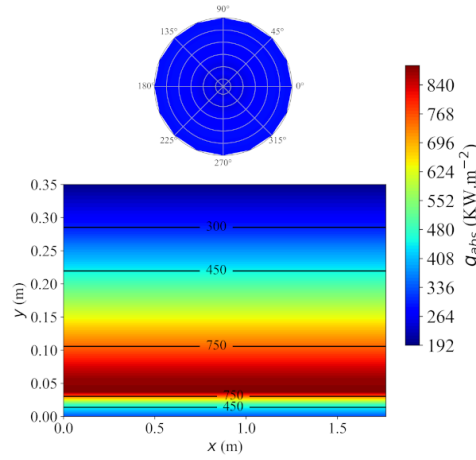


Fig. 3.14: Heat flux distribution of the receiver with CPC surface (configuration D8, $\alpha = 0$)

the optimised focus-to-centre distance is close to zero. Overall, PMCE is attempting to remove the CPC from the system. This indicates that CPC secondary reflectors are not a good option for the parabolic dish/cavity receiver systems, at least for the specific cylindrical receiver and dish configurations considered here and in the temperature range evaluated.

3.4.5 Optimisation of the cylindrical receiver with both spillage skirts and secondary reflectors

The results from the optimisation that includes both spillage skirts and conical or trumpet reflectors, are shown in Table 3.5 (case study 10 and 11) and Figure 3.15. receiver-and-interception efficiencies are similar for both cases and are higher than receivers with the skirt or reflector only. The inner spillage is quite low due to the combined effects of the spillage skirt and reflectors. The emissive loss is lower because of the smaller inner aperture size. The convective loss drops due to the lower surface area of the cavity. Overall, the receiver-and-interception efficiency increases by 1.0% compared to the optimised cylindrical receiver.

3.5 Performance enhancement of a cavity receiver in a tower system

The observations regarding performance of the secondary reflector and skirt in the previous case study using a dish concentrator generally also hold for a heliostat field, as is shown in this section. However, in a tower system, the distances between the concentrator (mirrors) and the receiver depends on the area of the field considered and deviates from the ideal parabolic case which can lead to higher spillage losses than in a dish system. In this work, the heliostat field design is fixed to simplify the analysis of the thermo-optical processes, although it is acknowledged that co-optimisation of both the receiver (including the skirt and secondary reflector) and

Table 3.5: Efficiencies and losses for receivers with skirt and reflectors

Configuration	D1	D10	D11
	Cylinder	Skirt and conical	Skirt and trumpet
R_{cyl} (m)	0.334	0.255	0.262
H_{cyl} (m)	0.601	0.522	0.617
l_s (m)	/	0.102	0.084
H_{out} (m)	/	0.223	0.731
R_{out} (m)	/0.699	/	/
a	/	/	0.346
b	/	/	0.180
$\dot{Q}_{outer,spi}$ (kW)	6.5	0.1	0.7
$\dot{Q}_{sec,block}$ (kW)	/	1.3	1.5
$\dot{Q}_{sec,abs}$ (kW)	/	0.6	1.2
$\dot{Q}_{sec,ref}$ (kW)	/	0.5	0.0
$\dot{Q}_{inner,spi}$ (kW)	2.5	3.1	/
\dot{Q}_{ref} (kW)	8.9	10.7	9.6
\dot{Q}_{emi} (kW)	11.9	11.6	11.1
\dot{Q}_{conv} (kW)	9.8	7.6	8.6
$\eta_{rec,int}$ (%)	91.6	92.6	92.6

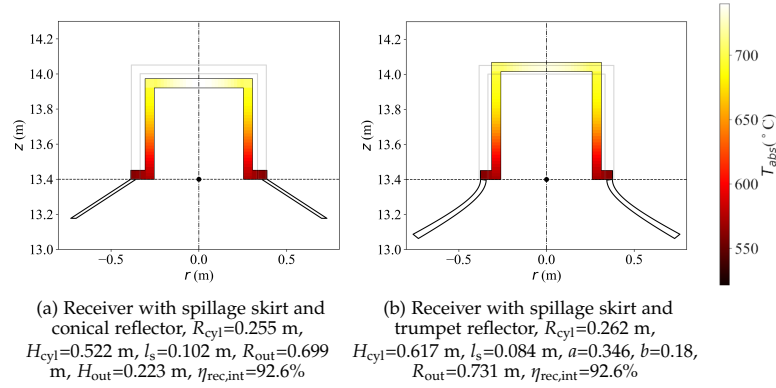


Fig. 3.15: Optimised structures and receiver efficiencies for receivers with skirt and secondary reflectors.

the heliostat field is preferable, and that in later work in this thesis (albeit for an external receiver rather than a cavity receiver) such co-optimisation is carried out.

3.5.1 The PS10 tower field

This case study assumes a fixed reference case heliostat field based on the field of the PS10 solar power tower plant, which was constructed in 2007 near Seville, Spain ($37^{\circ}42'$ N, $5^{\circ}9'$ W). The PS10 field has a north-oriented polar configuration with 624 heliostats. All heliostats are aimed at the centre of the cavity aperture plane to minimise spillage losses. The optical tower height is the vertical distance between the aiming point and the horizontal plane. Other key parameters related to the field model are shown in Table 3.6 [32].

Table 3.6: Parameters of the PS10 tower field

Parameters	Values
Number of heliostats	624
Heliostat width (m)	12.84
Heliostat height (m)	9.45
Mirror reflectivity	0.88
Slope error (mrad)	1.45
Optical tower height (m)	107.7

3.5.2 Analysis and optimisation of the cylindrical cavity receiver for the tower configuration

The optimum geometries for the cylindrical cavity receiver are explored with the PMCE method. Variables include the cylindrical radius, height and the tilt angle of the receiver. The tilt angle (θ_{tilt}) is defined as the angle between the centreline of the receiver and the vertical line ($0^\circ \leq \theta_{\text{tilt}} \leq 90^\circ$), as is shown in Figure 3.16. The results are illustrated in Table 3.7 (configuration T1) and Figure 3.17(a). The optimum radius and height are 5.29 m and 9.68 m, respectively. The aperture size is around 88 m², which is much smaller compared to the PS10 cavity receiver with aperture area of 165 m² [32]. The reason is that an optimised high-temperature receiver has a relatively smaller aperture size to avoid high emissive loss. The optimum tilt angle is 73.1°. Overall, the receiver-and-interception efficiency for the optimised cylindrical geometry is 87.2%.

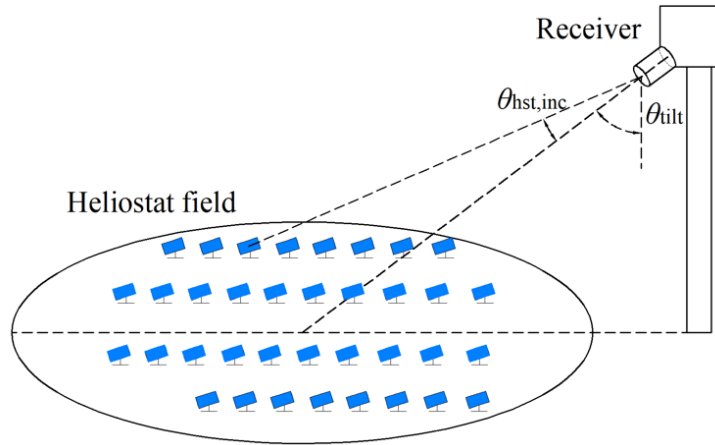


Fig. 3.16: Illustration of the tilt angle

The flux maps on the receiver are shown in Figure 3.18, with high peak fluxes located on the back plate. The influence of the non-axisymmetric field with respect to the viewing (tilt) angle of the receiver can be seen with strong flux peaks on both sides of the cylinder walls. The distributions of the heliostat efficiencies are also given for the design point in Figure 3.19(a). The heliostat efficiency is defined as the power incident to the receiver from each heliostat ($\dot{Q}_{\text{rec,inc},i}$) divided by the energy

Table 3.7: Optimisation results for receivers with the spillage skirts

Configuration	T1	T2	T3
	Cylinder	Flat skirt	Inclined skirt
R_{cyl} (m)	5.29	4.12	4.28
H_{cyl} (m)	9.68	8.09	9.04
l_s (m)	/	1.58	1.58
θ_s (°)	/	/	80.9
θ_{tilt} (°)	73.1	74.4	71.8
\dot{Q}_{spi} (MW)	1.74	1.28	1.11
\dot{Q}_{ref} (MW)	1.29	1.58	1.48
\dot{Q}_{emi} (MW)	2.51	2.66	2.76
\dot{Q}_{conv} (MW)	2.31	1.76	1.98
$\eta_{rec,int}$ (%)	87.2	88.2	88.1

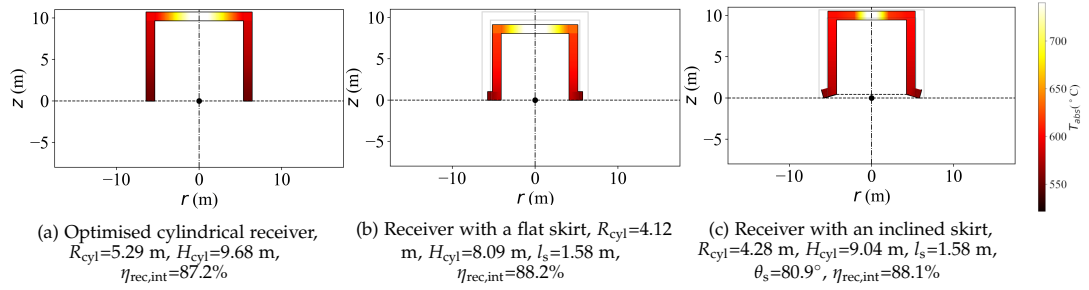


Fig. 3.17: Optimised structures and receiver efficiencies for receivers with and without the skirt.

incident to the same heliostat ($\dot{Q}_{hst,inc,i}$):

$$\eta_{hst,i} = \frac{\dot{Q}_{rec,inc,i}}{\dot{Q}_{hst,inc,i}}, i = 1, 2, \dots, 624 \quad (3.12)$$

The individual heliostat efficiency represents the optical performance of each heliostat. Optical losses include the shading loss, cosine loss, field absorption loss, blocking loss, spillage loss and reflective loss. As shown in Figure 3.19, heliostats closer to the tower have higher efficiency than the more distant ones.

3.5.3 Optimisation for the tower receiver with spillage skirts

The PMCE method is used here for receivers with flat and inclined spillage skirts, with the results in Table 3.7 (configurations T2–T3). Like in the dish study, the cylindrical radius can be reduced with simultaneous reduction of the spillage loss. The cylinder height can also be reduced to decrease the convective loss. Similarly, the emissive and reflective losses are higher than the reference cylindrical case, while the benefits of lower spillage and convective losses compensate for this disadvantage. For the receiver with the inclined spillage skirt, the performance is again close to the flat case. The receiver-and-interception efficiency gains with flat and inclined skirts are approximately 0.9% to 1.0%. The receiver irradiated area reduction is more

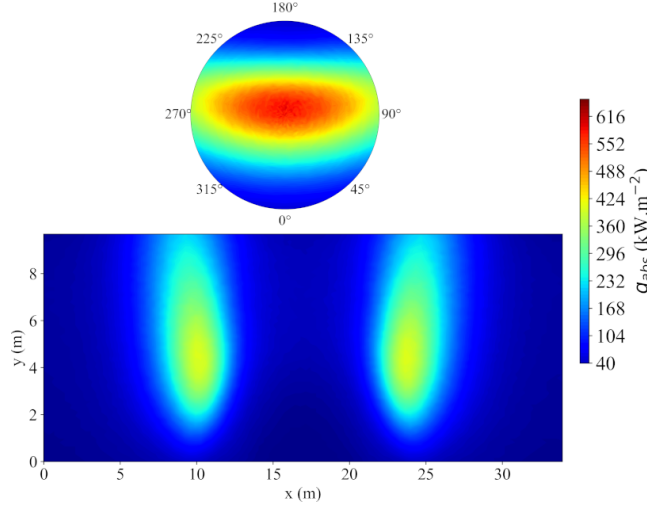


Fig. 3.18: Flux map of the optimised cavity receiver

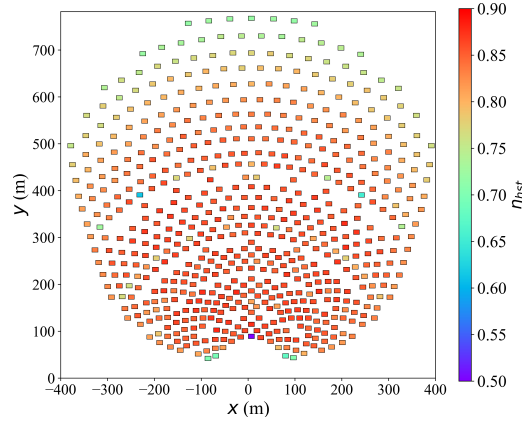


Fig. 3.19: Heliostats' efficiencies for the optimised cavity receiver

than 31%, a significant reduction which would most likely result in beneficial cost reductions.

3.5.4 Optimisation for the tower receiver with secondary reflectors

As the optical interaction between a heliostat field and secondary reflectors on a central receiver system is complex, a parametric study is conducted prior to optimisation to highlight the trends in receiver-and-interception efficiency for different geometries. Subsequently, the PMCE method is used to optimise receivers with secondary reflectors. The parametric studies are all based on the optimised cavity receiver (configuration T1).

3.5.4.1 Parametric study of the tower receiver with a conical reflector

The geometric shape of the conical reflector is controlled by the reflector length and reflector angle. The receiver tilt angle also affects the receiver performance. Figure 3.20 shows the receiver-and-interception efficiencies at different reflector lengths, receiver tilt angle and reflector angle. The influence of the reflector angle on the efficiency depends on the reflector lengths. As the reflector angle decreases (i.e. tends towards the tangent to the receiver side walls), the receivers with longer reflectors see their efficiency drop, while for shorter reflectors, the efficiency first increases and then decreases. Hence an optimal receiver-and-interception efficiency can be obtained with reflector length of $0.5R_{\text{cyl}}$ and an angle of 40° . As shown in Figure 3.20(b), the optimal angle is relatively insensitive to the tilt angle in the range studied. The optimal tilt angle is around 69.1° .

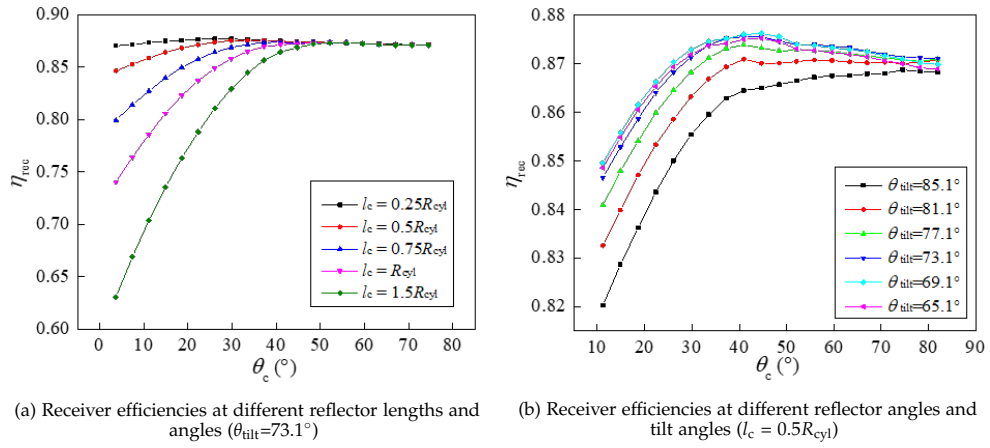


Fig. 3.20: Parametric study for receivers with conical reflectors ($R_{\text{cyl}} = 5.29$ m, $H_{\text{cyl}} = 9.68$ m).

To better understand the effects of the reflector length and angle, the efficiencies of the heliostats are calculated and shown in Figure 3.21 for the optimised cylindrical receiver. In Figure 3.21, the efficiency difference ($\Delta\eta_{\text{hst}}$) points to the difference between the efficiency of individual heliostat in current case and the efficiency of the same heliostat in the reference case as shown in Figure 3.21. An 'acceptance area' is defined as the area where the acceptance cone of the secondary reflector intersects the horizontal plane at the level of the heliostats. In Figure 3.21, the black solid line indicates the boundary of the acceptance area. Radiation coming from heliostats outside of the acceptance area (beyond the black line) will be blocked by the reflector. For heliostats inside the acceptance area but close to the boundary, the reflected radiation may be partly blocked due to the deviation of rays caused by the sunshape and mirror slope error. That is the reason why the black solid lines do not intersect with the field area but the optical efficiencies of some heliostats closer to the boundary are reduced. By comparing Figures 3.21(a)-(c), it can be found that with longer reflectors, the performance of some heliostats at the side areas close to the acceptance area boundary is reduced, explaining why the receiver performance deteriorates. On the other hand, longer reflectors cause an increase in efficiency for heliostats farther from

3.5. Performance enhancement of a cavity receiver in a tower system

the tower as the larger outer aperture reduces spillage loss. Overall, the efficiency gains from farther heliostats does not fully offset the efficiency decrease of the side heliostats, and smaller reflectors are preferred.

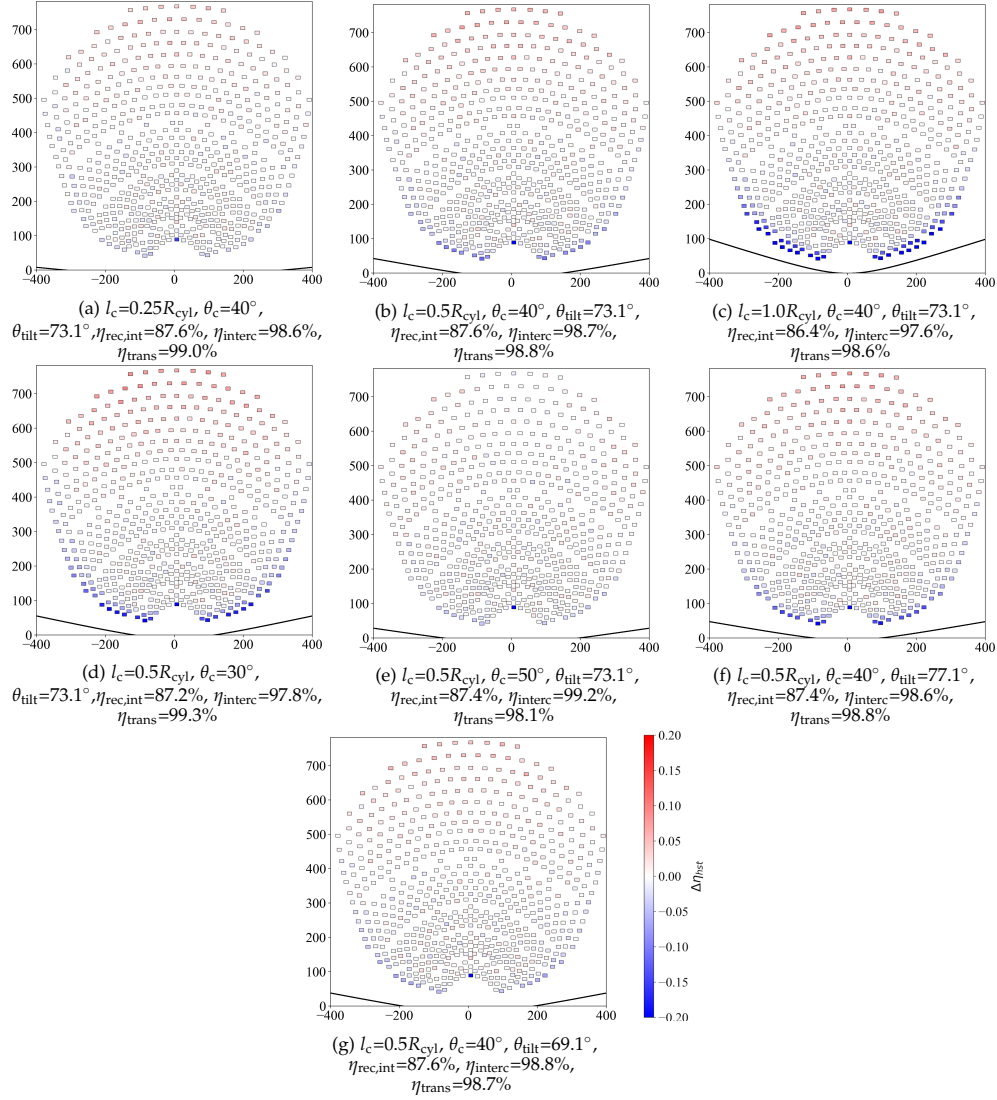


Fig. 3.21: Heliostats' efficiencies at different reflector lengths and angles. The black line marks the boundary of the acceptance area, which is the intersection of the acceptance cone with the heliostat field plane.

Figures 3.21(b), (d) and (e) illustrate the effects of the reflector angle on heliostats' efficiencies. As the reflector angle decreases, the interception efficiency decreases as radiation from side heliostats is blocked. However, the transmission efficiency increases because the reflectors with smaller angles reflect radiation into the cavity receiver more effectively. The performance of the farther heliostats is significantly increased with smaller reflector angles. In total, due to the combined effects of the interception efficiency and the transmission efficiency, an optimum reflector angle is

obtained.

With varying tilt angles, the cavity receiver will ‘face’ different parts of the heliostat field. By comparing Figures 3.21(b), (f) and (g), it can be seen that with a smaller tilt angle, which means the receiver is tilted more downwards, the blocking effects on the side heliostats can be alleviated, while the efficiency gains from farther heliostats gradually disappear. The optimum range for the tilt angle is around 69.1° , which is lower than the optimised cylindrical receiver (73.1°). The reason is that the receiver needs to be tilted more downwards to improve the performances of the side heliostats closer to the tower.

3.5.4.2 Parametric study of the tower receiver with a trumpet reflector

As discussed in Section 3.2.3, for the trumpet reflector, the geometry is controlled by two hyperboloid coefficients (a , b) and the outer reflector radius (R_{out}). The coefficient a determines where the trumpet is truncated from a hyperboloid curve. The maximum value of a equals to R_1 if the trumpet is cut exactly from the middle of the hyperboloid. To better understand the effects of a , a dimensionless parameter a/R_1 is defined and studied. Figure 3.22(a) shows the receiver-and-interception efficiencies at different values of a/R_1 . The receiver efficiency increases with larger a , and the highest receiver-and-interception efficiency is achieved with a equal to R_1 . The shapes of the trumpet reflector with different a are illustrated in Figure 3.22(b). With a/R_1 equal to one, regions of the reflector near to the aperture are more tangential to the inner surface of the cavity, and rays coming from the field can be better reflected into the cavity receiver. This conclusion is consistent with O’Gallagher’s trumpet (see Equation 3.3).

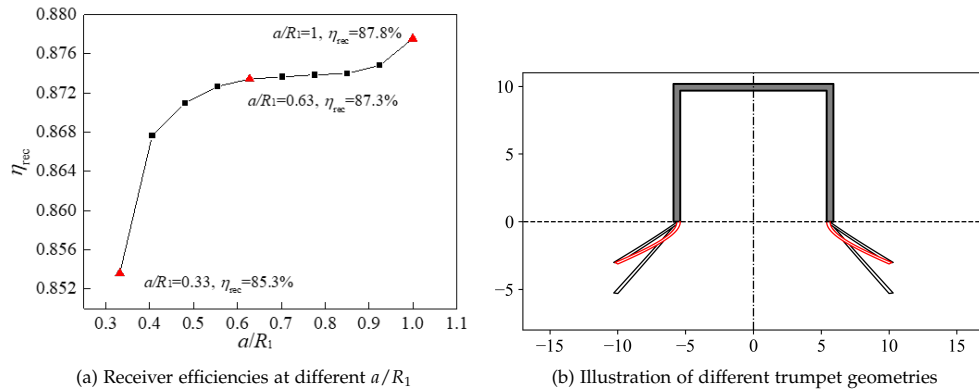


Fig. 3.22: Receiver efficiencies and reflector shapes for the trumpet at different a ($b=2$, $R_{\text{out}}=10$ m).

Next, receiver-and-interception efficiencies are calculated by varying the coefficient b , as shown in Figure 3.23, showing that an optimum value can be found. To better understand the effects of b , two parameters, trumpet reflector length and trumpet reflector angle, are assumed similar to the definition of the conical reflector. The

reflector length and reflector angle can be calculated from:

$$l_t = \sqrt{(R_{\text{out}} - R_1)^2 + b^2/a^2(R_{\text{out}}^2 - R_1^2)} \quad (3.13)$$

$$\tan \theta_t = \frac{R_{\text{out}} - R_1}{b/a \sqrt{R_{\text{out}}^2 - R_1^2}} \quad (3.14)$$

It can be seen from the equations that larger b results in a longer reflector and smaller reflector angle. The trend is identical with the geometries in Figures 3.23(b). In the parametric study of the conical reflector, trade-offs are found to determine the optimum reflector length and angle. Here, due to the similar trade-offs, an optimum value of b exists to achieve the highest receiver-and-interception efficiency.

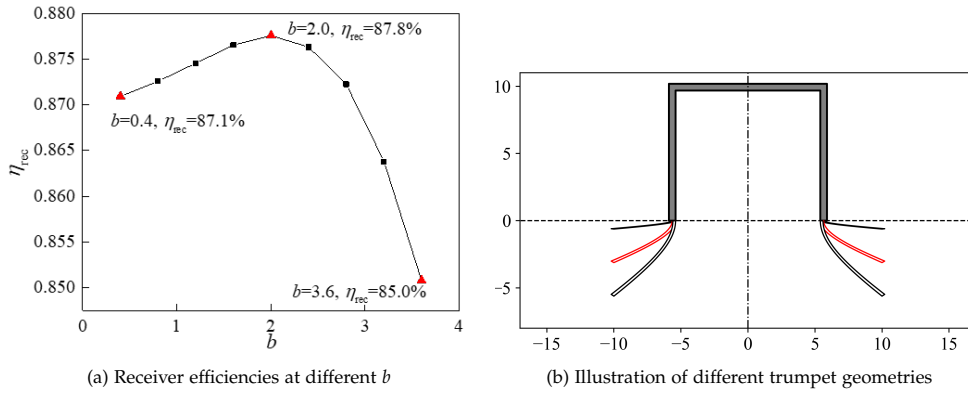


Fig. 3.23: Receiver efficiencies and reflector shapes for the trumpet at different b ($a=5.39$, $R_{\text{out}}=10$ m).

Interestingly, with the value of b in O’Gallagher’s definition, the trumpet reflector is long and has a small reflector angle, as shown in Figure 3.24. The transmission efficiency is very high, proving the good optical performance of O’Gallagher’s trumpet. But the low interception efficiency reduces the overall receiver-and-interception efficiency. The conclusion is that although O’Gallagher’s trumpet has a high optical performance, a more general definition of the trumpet reflector can find a better geometry with a higher receiver-and-interception efficiency.

Figure 3.25(a) shows the receiver-and-interception efficiency at different values of R_{out} . The receiver-and-interception efficiency first increases and then nearly remains unchanged with increasing outer reflector radius. As the outer aperture becomes larger, the interception efficiency increases due to the reduced spillage loss, while the transmission efficiency decreases because of larger secondary reflective and absorption losses, and overall the receiver efficiency slightly increases. However, if the outer radius continues to increase, both the increment of the interception efficiency and decrement of the transmission efficiency drop. This is because the extended part of a long reflector doesn’t receive much flux, thus the impact of further extension on receiver-and-interception efficiency is minor, as shown in Figure 3.25(b).

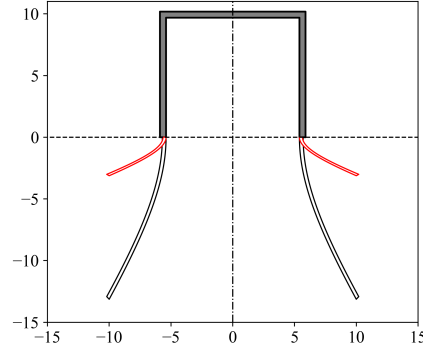


Fig. 3.24: O'Gallagher's trumpet, $b=8.4$, $\eta_{\text{rec}}=58.8\%$, $\eta_{\text{interc}}=67.9\%$, $\eta_{\text{trans}}=99.7\%$

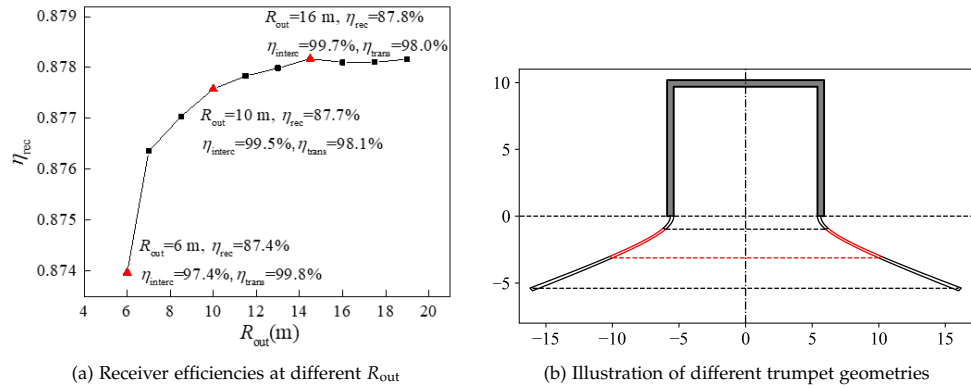


Fig. 3.25: Receiver efficiencies and reflector shapes for the trumpet at different R_{out} ($a=5.39$, $b=2$).

3.5.4.3 Parametric study of the tower receiver with a CPC reflector

For the CPC reflector, the CPC acceptance angle, the receiver tilt angle and the focus-to-centre distance are the three key variables. By default, the focus-to-centre distance is set equal to the CPC length (h_{CPC}) and all heliostats aim at the centre of the outer aperture. As shown in Figure 3.26(a), the receiver-and-interception efficiency directly drops with decreasing the CPC acceptance angle. Figures 3.26(b) shows the reflector shapes at different angles. It can be seen that smaller acceptance angles lead to longer reflectors and larger outer apertures. The heliostats' efficiencies at different CPC acceptance angles are illustrated in Figures 3.27(a)-(d). For a fixed inner aperture dimension, as the CPC acceptance angle decreases, the interception efficiency increases due to the larger outer aperture, so the performance of farther heliostats can be enhanced. However, for the fixed heliostat field used in this case study, sometimes there are heliostats outside the acceptance area which are completely blocked, as can be seen in Figures 3.27(a) and (b). Furthermore, as discussed previously, heliostats inside this area but near the boundary are also impacted, by a gradually decreasing amount as the distance to the boundary increases. The high reflector absorption loss with the long CPC reflector is another cause for decreasing efficiency. In total, the decrease in transmission efficiency overwhelms the increase in interception efficiency, and the receiver-and-interception efficiency drops with re-

duction of the reflector angle.

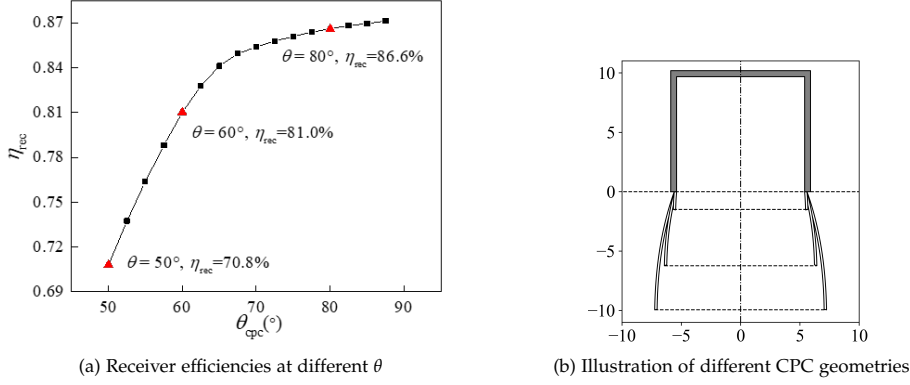


Fig. 3.26: Receiver efficiencies and reflector geometries for the CPC reflectors at different θ .

Tilting the receiver more may be a good option to alleviate the efficiency drops of the side heliostats. However, as shown in Figures 3.27(c), (e) and (f), although the heliostat efficiencies in low efficiency areas are slightly enhanced, the efficiency gains from the distant heliostats gradually disappears. Hence changing tilt angle does not improve the performance of the CPC reflector.

Similar to the parabolic dish case, the aiming point of the field can be adjusted along the axis of the CPC between the inner and outer apertures. The effect of the focus-to-centre distance is shown in Figure 3.27 (c), (g) and (h). Decreasing the focus-to-centre distance, the receiver-and-interception efficiency drops because of the reduction in interception efficiency. The radiation from the side heliostats is absorbed by the back surface of the CPC reflector and is lost as secondary blocking losses. Therefore, the optimum aiming point is at the centre of the outer aperture. But the focus-to-centre distance is still retained as a variable in the following optimisation.

Although CPCs appear to not be beneficial again in this tower configuration, Figure 3.27 highlights that the average field optical efficiency would go up if the assumption of a fixed heliostat field was removed, and poorly performing heliostats from the sides were removed. It is concluded that for a CPC to be effective in a central tower configuration, the CPC and heliostat field need to be co-optimised. This is consistent with the findings of Li et al. [85], who carried out such an optimisation.

3.5.4.4 Optimisation of the tower receivers with secondary reflectors

Having highlighted the fundamental trade-offs between the optical and thermal performance of the tower system configurations with secondary reflectors, the PMCE method is used to find the optimal geometrical configurations. The results are summarised in Table 3.8 and Figure 3.28. The receiver-and-interception efficiency can be enhanced with either the conical or trumpet reflector (configurations T4 & T5), while the CPC reflector cannot achieve an efficiency gain (configuration T6). For receivers with a conical or trumpet reflector, the cylindrical radius is reduced compared to the reference cavity case, while the spillage losses also drop down. This proves the

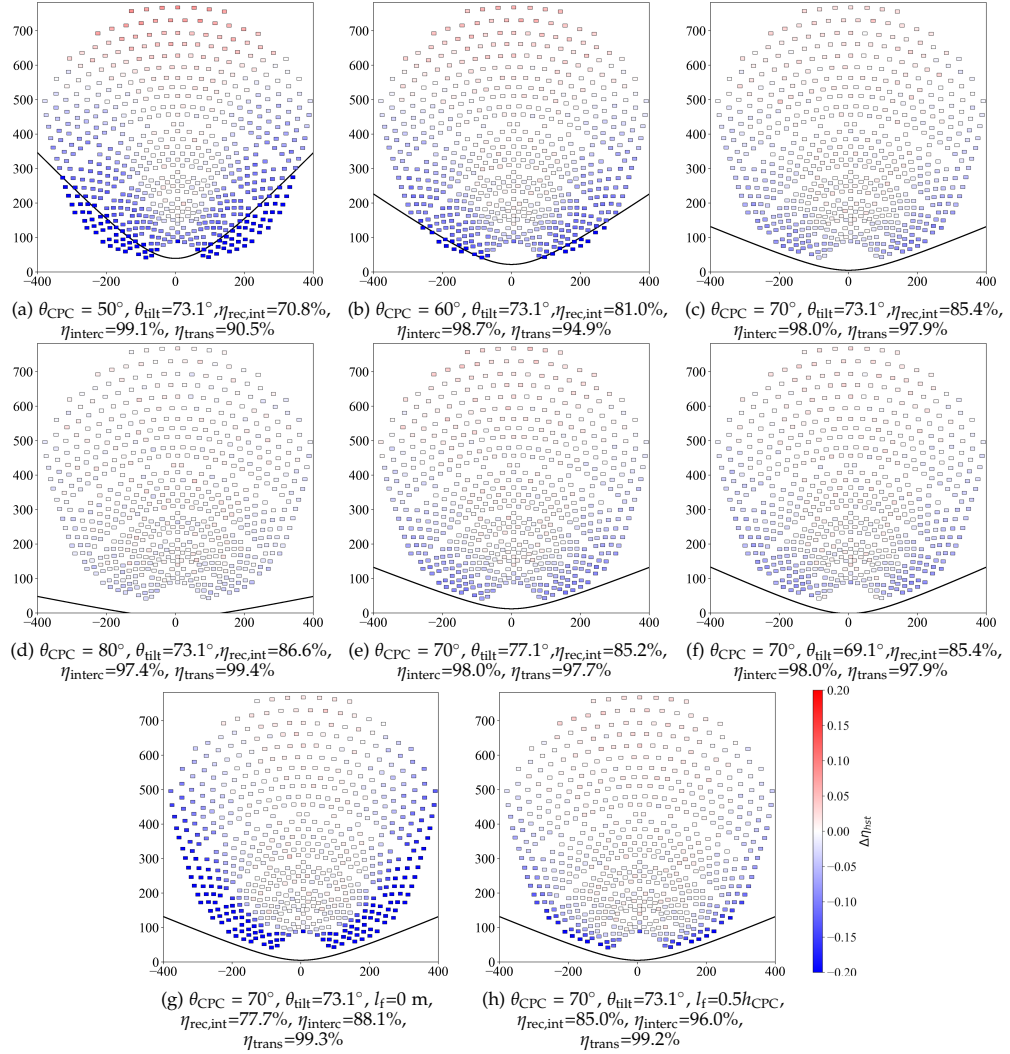


Fig. 3.27: Heliostats' efficiencies at different acceptance angles relevant to the optimised receiver. The black line marks the boundary of the acceptance area, which is the intersection of the acceptance cone with the heliostat field plane.

positive effect of the reflectors reflecting the rays into the inner apertures. The emissive losses drop due to the smaller cavity apertures. The convective losses are lower because of the smaller inner surface areas. In total, the receiver-and-interception efficiencies of receivers with conical and trumpet reflectors can be enhanced by around 0.6% and 0.7%, respectively. Similar to the dish study, a receiver with extremely short CPC is chosen as optimum, and the CPC reflector tends to be removed from the system in the optimisation.

3.5. Performance enhancement of a cavity receiver in a tower system

Table 3.8: Efficiencies and losses for receivers with reflectors

Case	T1 Cylinder	T4 Conical	T5 Trumpet	T6 CPC	T7 Skirt & conical	T8 Skirt & trumpet
R_{cyl} (m)	5.29	5.23	5.23	5.39	4.28	3.97
H_{cyl} (m)	9.68	9.20	9.84	9.20	8.41	7.30
θ_{tilt} ($^\circ$)	73.1	70.7	71.7	72.0	71.7	74.4
l_s (m)					1.42	1.74
l_c (m)	/	1.72	/	/	1.92	/
θ_c ($^\circ$)	/	35.4	/	/	34.8	/
a	/	/	5.23	/	/	5.71
b	/	/	2.27	/	/	2.36
R_{out} (m)	/	/	14.97	/	/	16.97
θ_{CPC} ($^\circ$)	/	/	/	89.1	/	/
l_f (m)	/	/	/	0.06	/	/
\dot{Q}_{spi} (MW)	1.74	1.69	1.55	1.75	1.09	1.04
\dot{Q}_{ref} (MW)	1.29	1.32	1.24	1.35	1.52	1.72
\dot{Q}_{emi} (MW)	2.51	2.38	2.37	2.52	2.65	2.68
\dot{Q}_{conv} (MW)	2.31	2.14	2.26	2.22	1.85	1.61
η_{interc} (%)	/	98.5	99.5	97.1	98.8	99.5
η_{trans} (%)	/	99.0	97.9	99.9	99.4	98.3
$\eta_{rec,int}$ (%)	87.2	87.8	87.9	87.2	88.4	88.5

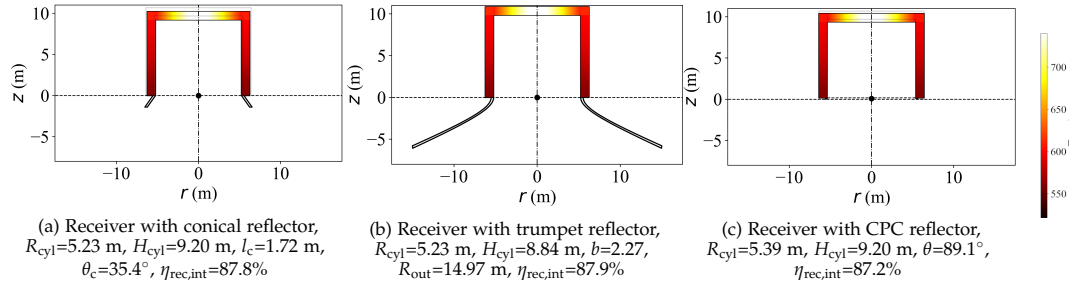


Fig. 3.28: Optimised structures and receiver efficiencies for receivers with secondary reflectors.

3.5.4.5 Optimisation of the tower receiver with both a spillage skirt and secondary reflectors

Receivers with both a flat spillage skirt and a conical or trumpet reflector (configurations T7 & T8) are optimised, with the results illustrated in Table 8 and Figure 27. Similar to the dish case, the cavity radius and the spillage losses are simultaneously reduced due to the combined effects of the spillage skirt and the reflectors. The convective losses are also reduced. The increase of the reflective losses and the emissive losses are mainly caused by the orientation of the skirts. Overall, the receiver-and-interception efficiencies can be enhanced by around 1.2% to 1.3% using a combination of the spillage skirt and conical or trumpet reflectors.

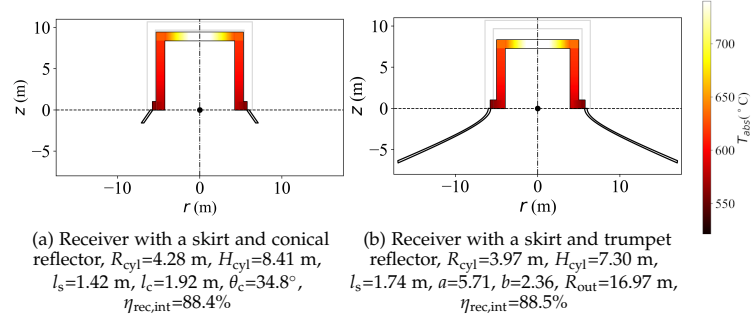


Fig. 3.29: Optimised structures and receiver efficiencies for receivers with spillage skirts and reflectors.

3.6 Conclusion for this chapter

Optimised configurations of spillage skirts and secondary reflectors were developed for representative receiver inlet and outlet temperatures. In both systems, spillage skirts enable a reduction in receiver dimensions while decreasing spillage loss. The conical and trumpet reflectors enable a reduction of aperture size and spillage loss at the same time. CPC reflectors are not favourable for the dish system considered, as secondary absorption losses outweigh the thermal benefits of reducing the receiver aperture. In the tower system considered, the CPC reflector either blocks light from peripheral heliostats or suffers large secondary reflective losses, and co-optimisation of the CPC and field is necessary to demonstrate benefit. The mirror slope error is matched to the slope error of the primary concentrator (3 mrad for the dish configuration [155] and 1.45 mrad for the tower configuration [32]). In a dish system, with a combination of spillage skirt and conical or trumpet reflectors, efficiency enhancement of about 1.0% is achieved, which corresponds to a 12.7% reduction in losses compared to the optimised cylindrical cavity receiver. In a tower system, with the combination of a spillage skirt and conical or trumpet reflectors, the receiver-and-interception efficiencies can be increased by up to 1.3% compared to the cylindrical cavity alone, with reduction in total receiver losses of 10.2% in relative terms. The methods developed in this work could be used for any point-focus CSP system to extract quantitative values regarding the usefulness of adding secondary concentrators and spillage skirts.

As a general conclusion, the spillage skirt appears to be a valuable tool for high-efficiency cavity receiver design: it offers the potential to simultaneously increase the receiver-and-interception efficiency and reduce its cost by reducing the size of the cavity, for a relatively simple geometrical design alteration. Conical and trumpet secondary reflectors, particularly when combined with spillage skirts, offer potential additional benefits provided that the efficiency gains are not counterbalanced by technical challenges or significant increases in cost.

For practical reasons, several simplifying assumptions have been implemented, such as the assumption of uniform flux density on each tube coil or bank, and the assumption of a constant convective heat transfer coefficient or neglecting atmospheric attenuation in the tower case. If the results are to be used for detailed

design purposes, it is suggested that the impact of these simplifying assumptions is further examined. Moreover, this study focuses on a simple cylindrical cavity receiver. Receivers with more tailored geometric configurations (for example, as in [73]), or different flow path structures, would be interesting to investigate in further work. Another assumption in the present work is that the reflectors are cooled; however, thermal management of secondary reflectors represents a significant challenge. A fixed heliostat field layout based on the relatively small PS10 plant is used in this study. A suggestion for further work is to extend the study to commercial-scale heliostat field configurations, and to include co-optimisation of the heliostat field with the receiver and its spillage skirt and secondary reflectors.

MDBA: an accurate and efficient method for aiming heliostats¹

4.1 Introduction

Cavity receivers have the potential to achieve higher thermal efficiency at high temperatures due to the cavity effect. In the investigation on cavity receivers in Chapter 3, it was found that spillage skirts and secondary reflectors could be applied to further increase the efficiency of cavity receivers in a tower system. However, cavity receivers have a limited acceptance angle and are more suitable for polar heliostat fields. As mentioned in Chapter 1, although multiple cavities can potentially alleviate this issue [41, 122], the conventional cylindrical external receiver design has no limitations relating to the field of view and appears more suitable for scaling up to systems with a larger design capacity. The cylindrical external receiver designs, as will be investigated in the following chapters, perform well and achieve an efficiency close to 90% in a commercial-scale tower system. Therefore, this chapter turns the research focus to cylindrical external receiver designs within a surround field.

Solar radiation on receiver tubes results in thermally induced stresses, and flux limits must be respected to avoid shortening receiver lifetime through creep and fatigue damages. The role of a heliostat aiming strategy is to control the radiative flux distribution at the receiver surface to avoid thermally induced damage. As reviewed in Chapter 1, most of the aiming strategies in literature rely on fast convolution-based optical simulations because flux maps of individual heliostats need to be calculated, or quick responses of the aiming strategy are sought-after. Monte Carlo ray-tracing (MCRT) is a more accurate method to simulate heliostat fields compared to convolution-based methods [104], but it is computationally expensive, and new approaches are necessary to reduce the computational requirements in finding optimal aiming parameters. In this chapter, two reference cases are firstly tested: the Image Size Priority (ISP) method, used in SolarPILOT [40]; and the deviation-based aiming (DBA) method, developed by Augsburg [160]. Given the limitations of the

¹This chapter is based on: S. Wang, C.A. Asselineau, W.R. Logie, J. Pye, J. Coventry, MDBA: An accurate and efficient method for aiming heliostats. *Solar Energy*, 2021, 225: 694-707. Sections 4.5.1.4 and 4.5.3 were not included in the paper.

reference methods, this chapter introduces a new parameterisation of heliostat aim-point locations that significantly simplifies the aiming problem. The new aiming model enables efficient use of MCRT to optimise the aiming strategy and, together with receiver thermal and mechanical models, is able to closely match the flux distribution to local values of allowable flux on the receiver. The full field aim-points are also dynamically predicted at different sun positions and direct normal irradiance (DNI). A reference case with a surround field and a cylindrical external receiver compatible with the Gen3 Liquid Pathway project [161, 162] is presented to test the capability of the method developed in this study.

4.2 Models and methodology

4.2.1 The reference system

A system with a surround field and a cylindrical external receiver is chosen as the reference case. Liquid sodium is chosen as the HTF in the receiver and operates between 520°C and 740°C. The reference system is located in Daggett, CA (34.85°N, 116.78°W). The solar multiple (SM) is 2.5, and the receiver nominal output is 543 MWth at design point (equinox solar noon) based on the calculations in equations 2.19-2.21. The oversizing factor (f_{hst}) is 1.0. The DNI at design point is 980 W/m². The receiver is split into 8 flow paths, with two passes per flow path for a total of 16 tube banks (Figure 4.1). The HTF is introduced into the north-facing tube banks and crosses the south-facing banks for the second pass. Detailed information describing the system is found in Table 4.1.

Table 4.1: Parameters for the cylindrical cavity receivers

Parameter	Value	Parameter	Value
Heliostat width (m)	12.2	Receiver diameter (m)	16
Heliostat height (m)	12.2	Outer diameter(mm)	60.3
Mirror reflectivity	0.9	Pipe thickness (mm)	1.2
Slope error (mrad)	1.5	Number of pipe banks	16
Number of heliostats	6764	Number of flow paths	8
Tower height (m)	175	Absorptivity of pipes	0.98
Receiver height (m)	24	Emissivity of pipes	0.91

4.2.2 Methodology

4.2.2.1 Optical model

The optical simulation uses ray-tracing as implemented in the SOLSTICE open-source software [131]. A limb darkened sunshape [163] is used in the optical model. The geometry of the receiver tube bank is established and meshed in the vertical direction into 50 binning sections for each tube bank. The incident flux is assumed to be constant and uniform inside the mesh element of a tube bank. After the optical

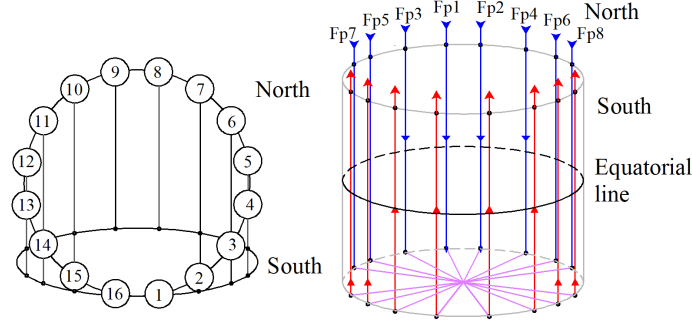


Fig. 4.1: Flow path of the sodium receiver. The receiver is composed of 16 tube banks and 8 flow paths. In each flow path, the HTF is introduced into the top of a north-facing bank, and leaves the receiver at the top of a symmetrically positioned south-facing bank. The equatorial line is located at the vertical centre of the receiver.

simulation, the flux falling onto each mesh element is stored for energy balance simulations. The optical energy losses and the interception efficiency can be obtained from the optical simulation.

4.2.2.2 Heat transfer model

The heat transfer model based on the work by Asselineau [142] is used to calculate the energy balance of the receiver. The convective heat transfer coefficient of the outer wall of the receiver pipes is approximated as a constant $20 \text{ W/m}^2\text{K}$. The ambient temperature is assumed to be 20°C at design point. Illustrative net flux and HTF temperature distributions are shown in Figure 4.2.

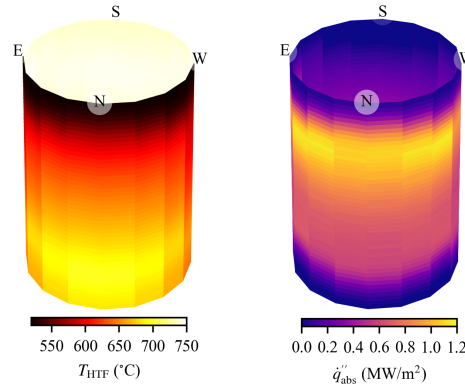


Fig. 4.2: Results of the heat transfer model for case S1

4.2.2.3 Thermo-mechanical stress limits

The combination of high temperature and thermal-induced stress requires the use of creep-resistant nickel-based superalloys. Alloy 740H is chosen as the material for receiver pipes. The flux limits are generated using the method developed by Logie

et al. [143] dependent as functions of HTF temperature and bulk flow velocity, as shown previously in Figure 2.8. The flux limits are applied at each receiver/tube element using 2D linear interpolation. A further safety factor of 0.9 was applied for conservatism.

4.3 Aiming strategy reference cases

As a precursor to the description of the new heliostat aiming strategy described in this chapter, two reference cases are described: the Image Size Priority (ISP) method, used in SolarPILOT [40]; and the deviation-based aiming (DBA) method, developed by Augsburg [160]. The original DBA strategy and the ISP aiming strategy are applied to the reference case in this section.

4.3.1 Image Size Priority method

The ISP method determines heliostat aim position by sequentially placing heliostats on the receiver at points of lowest flux. Flux images of heliostats are obtained from the convolution method. Images with significant distortion or at long distance from the receiver are placed first. After each heliostat placement, a local minimum is identified in the flux distribution and the subsequent heliostat is aimed at that position. The allowable aiming region is defined as a function of the standard deviation of the flux profile from each heliostat. Further details about the ISP method can be found in SolarPILOT software [40].

4.3.2 Deviation-based aiming strategy

The principle of the DBA method is that the aiming points of heliostats gradually deviate from the equatorial line of the receiver (see Figure 4.1). The closer heliostats with a smaller reflected sun image aim to the lower and upper boundaries of the cylindrical receiver, while the farther away heliostats with a larger reflected sun image aim at the centre of the receiver. High spillage loss can be avoided in this way.

A Cartesian coordinate system is established with the origin at the tower base. Positive x and y point to the east and north, respectively. The x and y coordinates of the aiming point of each heliostat is the closest point to the heliostat on the projected cylindrical envelope of the receiver:

$$x_{\text{aim},i} = \frac{x_{\text{hst},i} \times R_{\text{rec}}}{\sqrt{x_{\text{hst},i}^2 + y_{\text{hst},i}^2}} \quad (4.1)$$

$$y_{\text{aim},i} = \frac{y_{\text{hst},i} \times R_{\text{rec}}}{\sqrt{x_{\text{hst},i}^2 + y_{\text{hst},i}^2}} \quad (4.2)$$

All heliostats are sorted in ascending order according to focal length. The z

coordinate of the aiming point for a given heliostat i is determined by:

$$z_{\text{aim},i} = H_{\text{tower}} + M_i E \frac{H_{\text{rec}}}{2} \frac{N_{\text{hst}} - i}{N_{\text{hst}}}, M_i = -1, 1, -1, 1... \quad (4.3)$$

where H_{tower} is the optical tower height and also the z coordinate of the receiver equator, E is the aiming extent, H_{rec} is the receiver height, and N_{hst} is the total heliostat number. M is an index vector consisting alternately of -1 and 1.

The DBA method is a function of a single variable, the aiming extent (E), which determines the vertical extent of the aiming space. Figure 4.3 shows how the aiming extent controls the range of aiming points. By pointing at the upper and lower receiver sections respectively, the flux distribution is vertically symmetric relative to the receiver equatorial line.

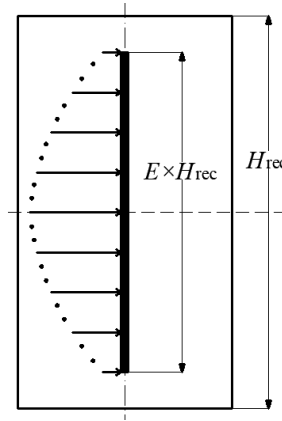


Fig. 4.3: Illustration of the aiming extent (E) in the original DBA method.

4.3.3 Comparison of DBA with ISP

A comparison between the two reference aiming methods is conducted to evaluate the capacity of the original DBA method. The interception efficiency and the receiver peak flux (\dot{q}''_{peak}) are used to compare the DBA and ISP methods, with the results shown in Table 4.2. Equatorial aiming is used in CS-Ø1: all heliostats aim at the receiver equatorial line ($E = 0$). Equatorial aiming generally leads to excessive flux on the receiver, but acts as a reference case for maximum interception efficiency. Cases CS-Ø2 and CS-Ø3 are simulated using the ISP method. The offset from edge is set to 2.2 for CS-Ø2 and 0 for CS-Ø3. In the last four cases (CS-Ø4 to CS-Ø7), DBA is applied with the aiming extent gradually increased from 0.2 to 1.0. Flux maps of the unfolded cylindrical surfaces are shown in Figure 4.4 for selected cases.

As seen from the results in Figure 4.4 and Table 4.2, equatorial aiming results in an extremely high peak flux. The maximum interception efficiency for equatorial aiming ($\eta_{\text{int,equ}}$) is 97.0%. The DBA used in case CS-Ø5 achieves a similar performance to the ISP in case CS-Ø2: both methods reduce the high peak flux by 23%, with the interception efficiency dropping only 0.1% to 0.2% compared to the equatorial

4.3. Aiming strategy reference cases

Table 4.2: Parameters for the cylindrical cavity receivers

Cases	Explanation	\dot{q}''_{peak} (MW/m ²)	η_{int}
CS-Ø1	Equatorial aiming	2.43	97.0%
CS-Ø2	ISP, offset = 2.2	1.47	96.8%
CS-Ø3	ISP, offset = 0	0.62	82.6%
CS-Ø4	DBA, $E = 0.2$	1.87	97.0%
CS-Ø5	DBA, $E = 0.45$	1.44	96.9%
CS-Ø6	DBA, $E = 0.7$	1.15	96.6%
CS-Ø7	DBA, $E = 1.0$	0.86	89.2%

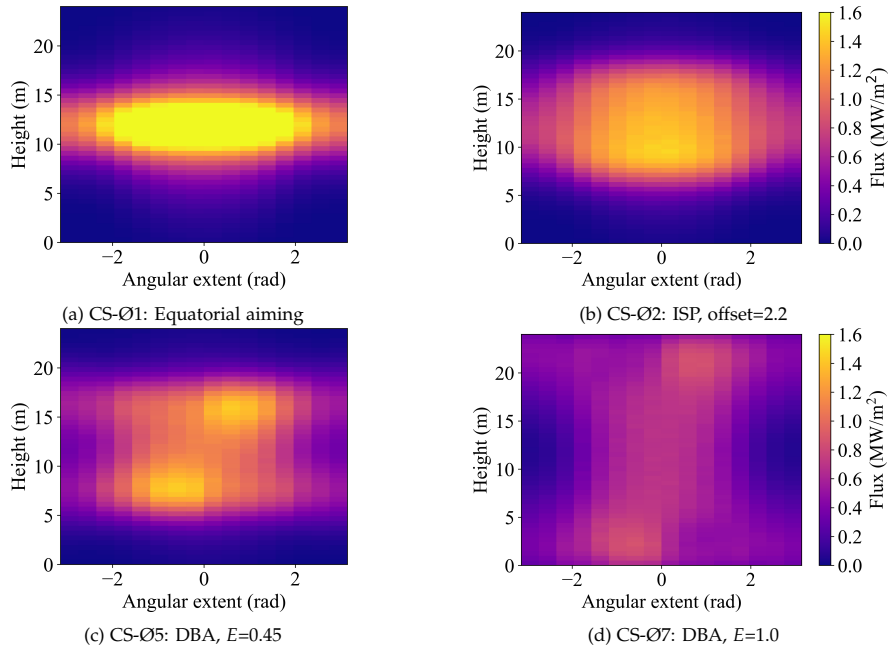


Fig. 4.4: Flux maps of the four reference aiming cases. The cylindrical surface of the receiver is unfolded to show the flux maps. Left to right parts of the map correspond to tube banks 1 to 16.

aiming. Cases CS-Ø4 to CS-Ø7 show that both the peak flux and the interception efficiency drop with increasing aiming extent: the allowable range of aiming points increases with a larger aiming extent (see Figure 4.4(a), (c) and (d)) which leads to more uniform flux profiles but also more spillage. The same effect is observed in ISP method with reducing the offset from edge in cases CS-Ø2 and CS-Ø3.

Although the DBA performs similarly to ISP, two high peak flux regions appear in the flux map, as shown in Figure 4.4(c) and (d). These artefacts were also observed in the original work of Augsburg [160], and are similar to the “shoulders” in other one-parameter aiming strategies as reported by Flesch et al. [90] and Collado and Guallar [89]. The flux distribution is not symmetric in the circumferential direction because the ranking of the heliostats is based solely on their focal distance across the entire field. According to the experience of [98, 100], it is a good idea to divide heliostats into sectors and to aim heliostats within sectors to the corresponding tube banks.

Figure 4.5 compares the net flux transferred to the heat transfer fluid and the flux limit at flow path 2 for cases corresponding to Figure 4.4. As the receiver becomes hotter, the flux limit gradually drop along the flow path. In order to keep the net flux under the limit, a simple choice in DBA method is to increase the aiming extent (E). However, the crossover is not eliminated even with E equal to 1.0 (full height aiming in case CS-Ø7), as shown in Figure 4.5(d), while the interception efficiency drops significantly to 89.2%. In the above cases, the only option to avoid crossovers is to increase the allowable range of aiming points, forming a lower, more uniform flux profile. This may work in some circumstances, but extending the aiming range to the entire receiver results in high spillage losses. An improved approach is to control the shape of the net flux curve and match it to the safe limit curve as closely as possible. The DBA strategy cannot do this because it is a one-parameter method. ISP has the capability to place the net flux curve below the flux limit, but has limited control on the flux distribution. The ISP method is compatible with any optical simulation method but thus far is only implemented in SolarPILOT, where it relies on the speed of convolution-based optics.

4.4 The modified deviation-based aiming (MDBA) method

Given the limitations of the reference methods, the Modified Deviation-Based Aiming (MDBA) method is introduced in this section. A parametric study is conducted to investigate the effects of the variables in the MDBA method.

4.4.1 Description of the method

In the MDBA method, all heliostats are divided into azimuthal sectors corresponding to the receiver tube banks. For the reference case, 16 field sectors are considered, as shown in Figure 4.6. The colour-bar represents the normalised focal length, which is the ratio of focal length of each heliostat to the maximum length in the entire field.

4.4. The modified deviation-based aiming (MDBA) method

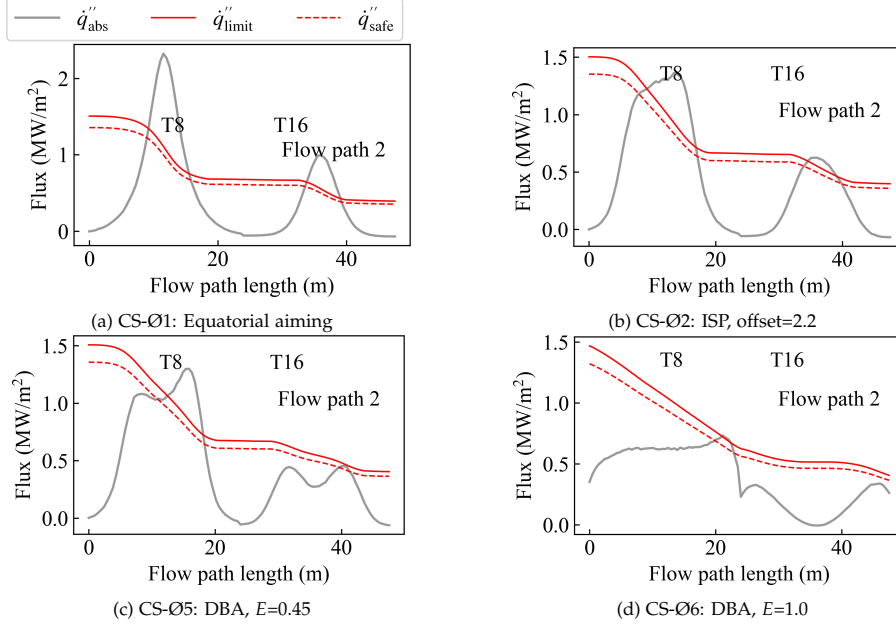


Fig. 4.5: Curves of net flux and flux limit at different cases. The grey solid line represents the net flux along the flow path. The red solid and dashed lines represent the variations of the flux limit and safe limit, respectively.

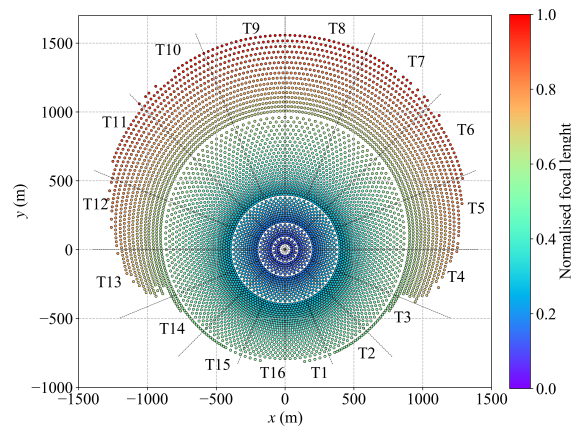


Fig. 4.6: Sectoral division of the heliostat field. The colour-bar represents the normalised focal lengths of each heliostat. The field sectors correspond to the tube banks.

Within each sector j , heliostats are ranked in ascending order according to their focal length. The z coordinate of the aiming point of each heliostat i in sector j , is obtained from the following expression modified from the DBA expression presented in Equation 4.3:

$$z_{\text{aim},i,j} = H_{\text{tower}} + M_{i,j} E_j \frac{H_{\text{rec}}}{2} \left(\frac{f_{\text{max},j} - f_{i,j}}{f_{\text{max},j} - f_{\text{min},j}} \right)^{S_j} \quad (4.4)$$

where E_j is the aiming extent for sector j . $f_{\text{max},j}$ and $f_{\text{min},j}$ are the maximum and minimum focal lengths of all heliostats in sector j . S_j is defined as the shape exponent. M is the index matrix. The determination of the x and y coordinates of the aiming point is the same as the original DBA method.

The index matrix is no longer simply composed of alternate 1 and -1. Instead, the order is determined by an asymmetry factor (A_j) to obtain asymmetric flux distributions about the equatorial line. The definition of the asymmetry factor is the ratio of the heliostats targeting the upper section of the receiver ($N_{\text{hst},\text{up},j}$) to the total number of heliostats ($N_{\text{hst},j}$) within a particular sector j : $A_j = N_{\text{hst},\text{up},j} / N_{\text{hst},j}$. Section 4.4.4 explains in detail how $M_{i,j}$ is obtained from A_j , together with an illustration of the algorithm.

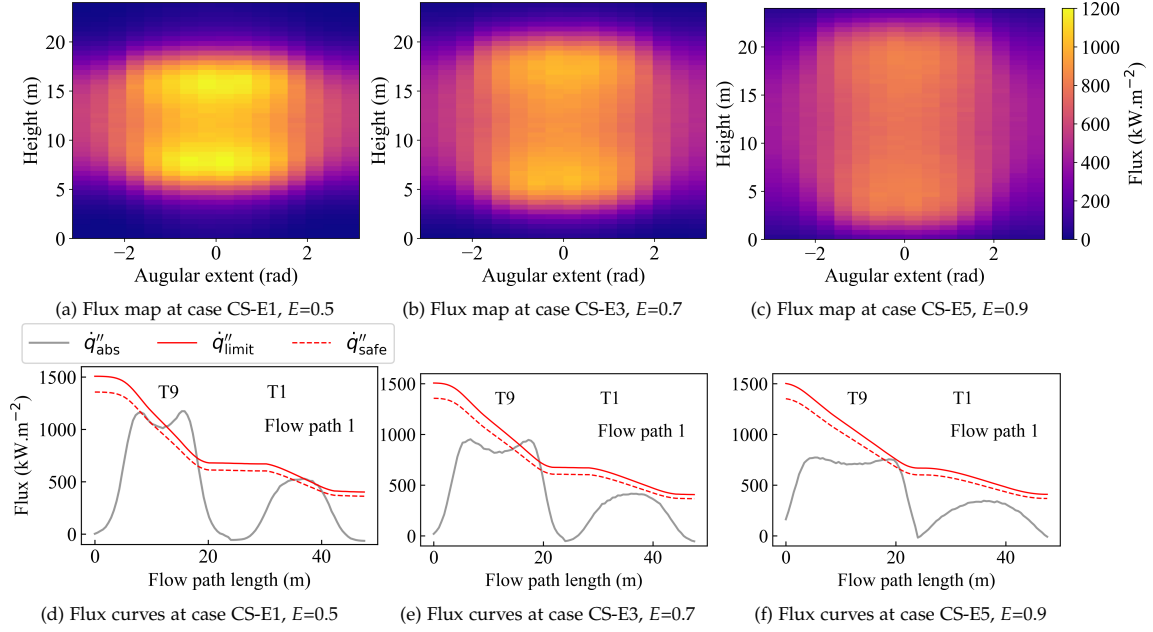
The MDBA method requires three parameters per sector j : the aiming extent E_j , the shape exponent S_j and the asymmetry factor A_j .

4.4.2 Effect of the aiming extent E

In this section, A , E and S are held constant for all sectors. The shape exponent S is assumed to be 1.5, and a symmetrical vertical profile is considered with A equal to 0.5 (symmetrical aiming with respect to the equatorial line). The aiming extent E is gradually increased from 0.5 to 1.0. As shown in Table 4.3, the peak flux and interception efficiency are reduced with increasing aiming extent. Figure 4.7 show the flux maps and flux curves with varying E for selected cases. The aiming range is increased with increasing E , and the flux curve becomes flatter, consistently with the original DBA model introduced in Section 4.3.3.

Table 4.3: Effect of the aiming extent on peak flux and intercept efficiency ($S = 1.5$, $A = 0.5$).

Cases	E	\dot{q}_{peak}'' (MW/m ²)	η_{int}
CS-E1	0.5	1.27	96.9%
CS-E2	0.6	1.14	96.9%
CS-E3	0.7	1.03	96.8%
CS-E4	0.8	0.93	96.5%
CS-E5	0.9	0.84	95.8%
CS-E6	1.0	0.76	94.0%


 Fig. 4.7: Results at different aiming extent E ($S = 1.5$, $A = 0.5$).

4.4.3 Effect of the shape exponent S

To analyse the effect of the shape exponent S , the aiming extent E and the asymmetry factor A for all sectors are set to 0.8 and 0.5, respectively. The shape exponent is varied from 0.5 to 3.0. The results are shown in Table 4.4 and Figure 4.8. With increasing shape exponent, the peak flux firstly decreases and then increases, while the interception efficiency increases. From the flux maps in Figure 4.8(a)-(c), the flux profiles becomes more concentrated towards the equatorial line with increasing S . With a smaller value of S , the flux is split in two components, with peaks located close to the edges of the receiver. As pointed out by Collado and Guallar [89], one-parameter models could lead to two hot spots (“shoulders”) as the irradiation images come closer to the upper and lower edge of the receiver. Common one-parameter aiming models [96, 98] only have one parameter controlling the expanding of aiming points, similar to the effect of the aiming extent. Those one-parameter models fail to control the shape of the flux curve, and this is why two-parameter aiming models were proposed by Collado and Guallar [89] to avoid the flux shoulders. In the MDBA method, the flux “shoulders” gradually disappear with increasing the shape exponent, as shown in figures 4.8(d)-(f) illustrating the flux curves for different shape exponents. S controls the shape of the flux curve and is an important factor to fit the flux curve with the flux limits.

4.4.4 Effect of the asymmetry factor A

The asymmetry factor has the effect of skewing the shape of the flux profile. This is realised by determining the order of +1 and -1 in the index matrix in Equation 4.4.

Table 4.4: Effects of the shape exponent on peak flux and intercept efficiency ($E = 0.8$, $A = 0.5$).

Cases	S	\dot{q}''_{peak} (MW/m ²)	η_{int}
CS-S1	0.5	1.11	93.8%
CS-S2	1.0	0.98	96.1%
CS-S3	1.5	0.93	96.6%
CS-S4	2.0	0.97	96.7%
CS-S5	2.5	1.08	96.8%
CS-S6	3.0	1.18	96.8%

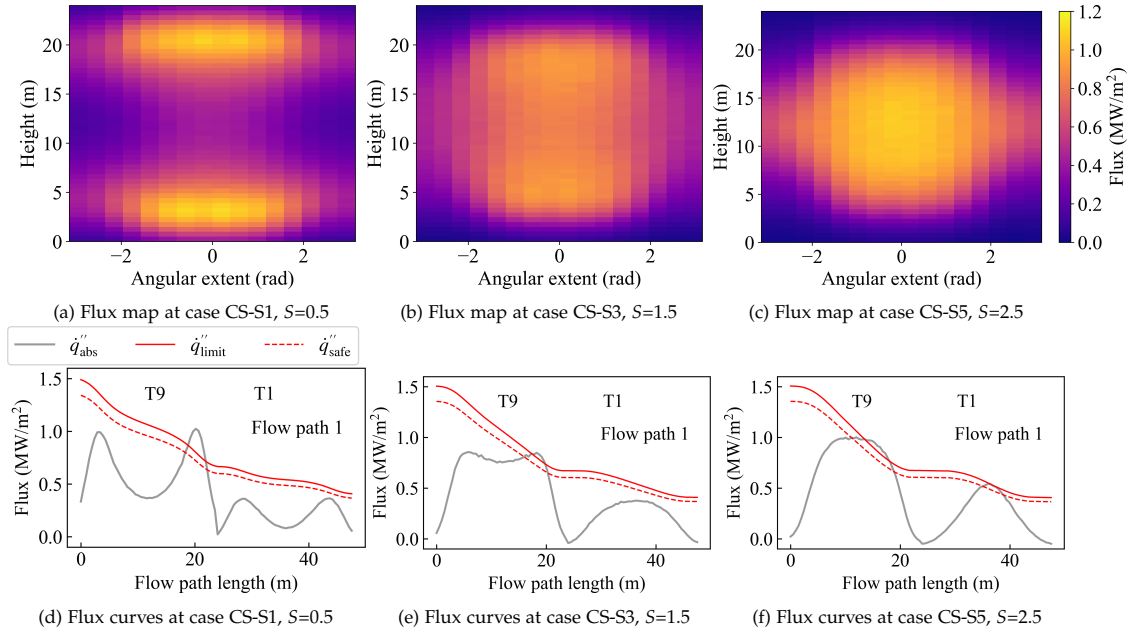


Fig. 4.8: Results at different shape exponents S ($E = 0.8$, $A = 0.5$).

The flowchart shown in Figure 4.9 is used to illustrate how $M_{i,j}$ is obtained from A_j using a simple algorithm that progressively fills the index matrix M with -1 and 1 while ensuring that it stays the closest possible to the target A_j value.

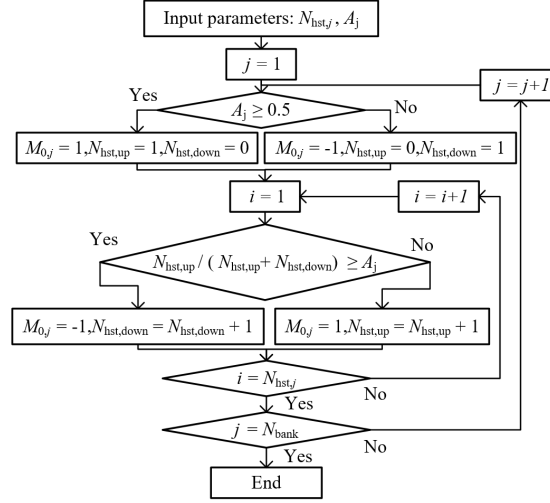


Fig. 4.9: Flowchart for the index matrix algorithm. The algorithm determines the order of +1 and -1 in the index matrix with an input of the asymmetry factor.

Figure 4.10 shows several case studies illustrating how the variation of A can lead to different ordered combinations of -1 and 1 inside M . The number of heliostats is assumed to be 100. It can be seen from Figure 4.10 that if A equal to 1, all heliostats aim at the upper part of the receiver. If A equal to 0.5, half of the heliostats aims at the upper, while the other half aims at the lower section. This leads to a symmetric aiming with flux vertically symmetric across the equatorial line. If A_j equal to 0.7 or 0.3, the aiming points are tilted upwards and downwards, respectively, and an asymmetric flux distribution can be obtained.

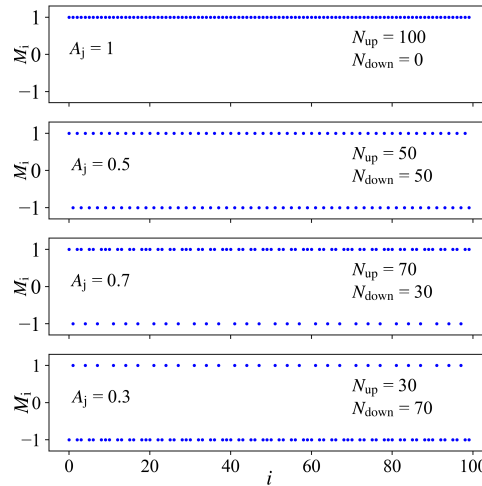


Fig. 4.10: Results of the index matrix at different asymmetry factors.

Two cases for the reference system are tested here to show how the asymmetric flux patterns are beneficial to receiver operations. Aiming extents E and shape exponents S are assumed to be 0.8 and 1.5 for all sectors. In case CS-A1 (Figure 4.11(a)),

the asymmetry factors are set as 0.3 for all south-facing tube banks (T1-T4, T13-T16), and 0.7 for all north-facing tube banks (T5-T12). The opposite setting is applied for case CS-A2 (Figure 4.11(b)). The net flux is controlled below the safe limit for flow path 1 in case CS-A1, but not for case CS-A2, as shown in Figure 4.11(c) and (d). The skewing direction should be dependent on the temperature variation along the bank, which is itself dependent on the HTF flow direction. In the reference system, the HTF is introduced at the top for all north-facing tube banks, so the hotter part is at the bottom of the tube banks. For all south-facing tube banks, the HTF becomes hotter in the upper section of the receiver. The flux limits are always lower at higher temperatures, so more heliostats should always be aimed in the region where cold HTF is introduced to the tube bank. In the reference case, aiming points should be skewed towards the top of the receiver for all north-facing tube banks, and towards the bottom for all south-facing tube banks.

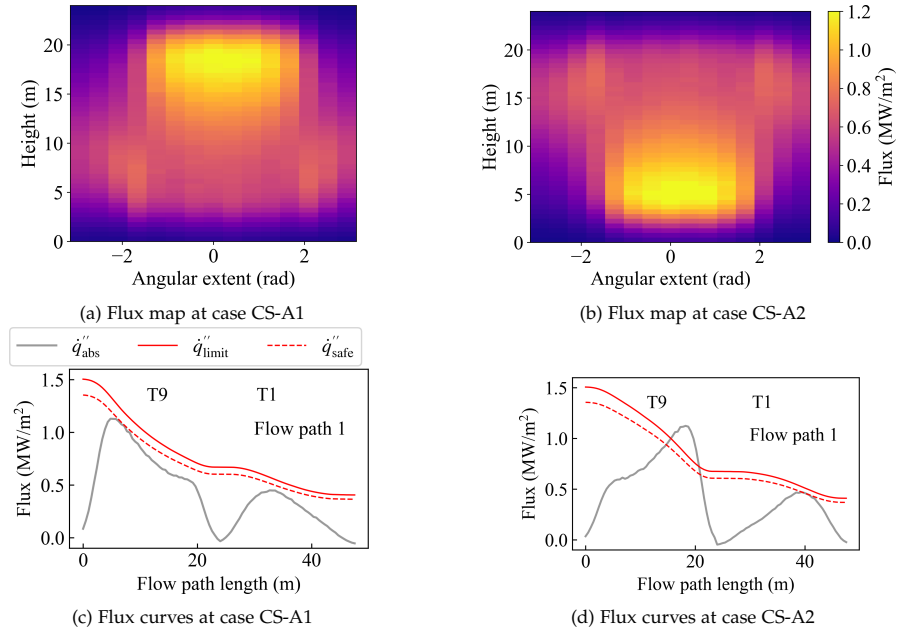


Fig. 4.11: Results with different asymmetry factors A ($E = 0.8$, $S = 1.5$). Case CS-A1: $A = 0.3$ for all south-facing tube banks (T1-T4, T13-T16), $A = 0.7$ for all north-facing tube banks (T5-T12). The opposite setting is applied for the second case.

Figure 4.12 shows the location of all the aiming points for case CS-A1. The colour of the dots corresponds to the focal length of the heliostats as in Figure 4.6. The range of the aiming points is controlled by the aiming extent, which is equal to 0.8. The aiming points are denser in the upper section than the lower section for tube banks T5 to T12, and vice versa for the other eight banks, which is controlled by varying the asymmetry factor.

In summary, the aiming points for heliostats in each sector are determined by three parameters, each with independent functions determining the flux profile. The aiming extent E controls the allowable range of the aiming points. The shape exponent S is used to adjust the shape of the flux profile. By using the asymmetry factor

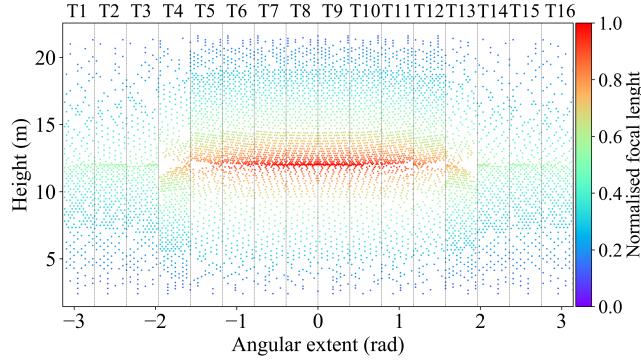


Fig. 4.12: Location of aiming points for case CS-A1. The colour of the dots gives an indication of the heliostat locations with relation to Figure 4.6.

A, the flux distribution can be vertically skewed to adapt to the flux limit curve. For the reference case with 16 field sectors, the aiming points are controlled by 48 parameters in total. The methods used to determine optimal values of all the parameters are introduced in the next section.

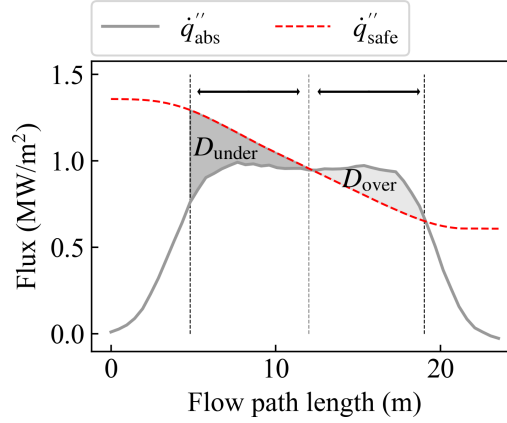
4.5 MDBA parameter determination methods

With given values of aiming parameters, the optical and thermal models are used to calculate the net flux comparing with flux limits. The interception efficiency can also be obtained. In this section, three different methods are explored to generate suitable MDBA parameters by running optical and thermal simulations in iteration: an optimisation-based method, a sequential method and a feedback-based method. The goal is to achieve a high interception efficiency, while guaranteeing a safe flux profile.

4.5.1 Optimisation-based MDBA method

4.5.1.1 Problem formulation

A constrained optimisation approach is adopted for this problem. The objective function is to maximise η_{int} and the constraint condition is that the net flux curve is controlled under the safe limit curve. To mathematically illustrate the constraint condition, the concepts of the safe extent (D_{under}) and the crossover extent (D_{over}) from [99] are adopted. An out-most intersection point is found between the net flux and safe limit curves, and a vertical range is defined between this point and the symmetric point about the middle line of the tube bank. The differences between the net flux and flux limit are computed within that range and integrated to get the values of D_{over} and D_{under} , as shown in Figure 4.13. The constraint is expressed as $D_{\text{over},j} = 0$, where $j = 1, 2, \dots, N_b$. N_b is the number of tube banks.


 Fig. 4.13: Definition of D_{over} and D_{under} .

4.5.1.2 Choice of the optimisation method

The pattern search method, a gradient-free heuristic-based local optimisation method, is used in this study. The DAKOTA [164] implementation of the pattern search method is used. The pattern search method walks through the parameter domain according to a defined stencil of search directions. The optimisation starts from the initial point, then uses a plus and minus offset in each coordinate direction according to an initial step length. The initial step length $L(x)$ for each parameter x is defined as:

$$L(x) = \Delta \times 0.1(x_U - x_L) \quad (4.5)$$

where Δ is the initial delta, x_U and x_L are the upper and lower boundaries for parameter x . The pattern is gradually contracted according to a contraction factor (f_{contra}). Δ is chosen as 3 and f_{contra} is set as 0.75. The optimisation ends once the step length is contracted to 0.1 of the initial step lengths for all variables or a targeted objective function is reached.

4.5.1.3 Results of the optimisation-based method

The optimisation method is used to solve the problem for all variables in a single optimisation computation. The optimisation is expressed as:

$$\begin{aligned} & \text{maximise : } \eta_{\text{int}}(x) \\ & \text{subject to : } \sum_{j=1}^{N_b} D_{\text{over},j}(x) = 0 \\ & x = \{E_0, S_0, A_0, \dots, E_{N_b}, S_{N_b}, A_{N_b}\} \in \mathbb{R}^{3N_b} \end{aligned} \quad (4.6)$$

The optimised parameters are the aiming variables related to all tube banks. The interception efficiency and the crossover extents are updated once parameters are introduced into a new simulation. The problem is a non-linear equality optimisation

problem. The constraint condition is that the sum of the crossover extents (introduced in Section 4.5.1.1) on all tube banks is equal to zero. A conservative initial point is chosen, with all aiming extents equal to 0.9, to guarantee that at least one reliable result can be found in the first iteration. The range of the aiming extents considered is between 0.5 and 1.0. The initial value for the shape exponent is 1.5, with lower and upper boundaries set as 0.5 and 3.0, respectively. For all north-facing tubes, the asymmetry factor varies between 0.5 and 0.75 with initialisation of 0.67, while the factor is adjusted between 0.25 and 0.5 initialising from 0.33 for all south-facing banks.

The results of the optimisation are shown in Table 4.5 (case O1). The optimal interception efficiency is 96.5%, a decrease of 0.5% compared to the equatorial aiming. The flux curves are shown in Figure 4.14. The net flux curve is controlled below the safe limit curve, and the trends of the net flux curves match well with the limit curves.

Table 4.5: Results of the optimisation-based method (case O1). T1-T16 point to tube banks in Figure 4.6.

	T1	T2	T3	T4	T5	T6	T7	T8	T9	T10	T11	T12	T13	T14	T15	T16
<i>E</i>	0.75	0.82	0.81	0.88	0.88	0.70	0.78	0.77	0.82	0.90	0.73	0.90	0.90	0.90	0.74	0.67
<i>S</i>	2.00	1.65	1.55	1.55	1.56	2.00	1.58	2.34	1.58	1.50	1.58	1.64	1.58	1.55	1.62	1.62
<i>A</i>	0.34	0.33	0.33	0.33	0.67	0.68	0.67	0.65	0.67	0.67	0.67	0.67	0.32	0.32	0.33	0.35

The interception efficiency is 96.5%. The number of ray-tracing evaluations (N_{evals}) is 3082.

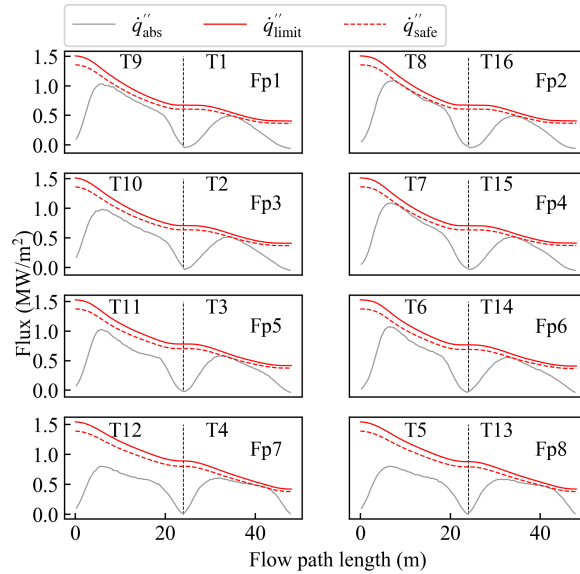


Fig. 4.14: Net flux and flux limit for all flow paths (Case O1).

This single optimisation requires more than 3000 ray-tracing evaluations before convergence. Figure 4.15 shows the gradual convergence of the optimisation with increasing the number of evaluations. The optimisation problem converges if the

step length is contracted to 0.1 of the original step length. This case has a high computational cost requiring 10 CPU hours with 10^7 rays per sun position on a desktop PC with an Intel i7 processor and 16 GB Ram. While feasible, the determination of MDBA parameters using the presented optimisation approaches remains too costly. Therefore, an attempt to divide the optimisation problem into sub-problems is discussed for the acceleration.

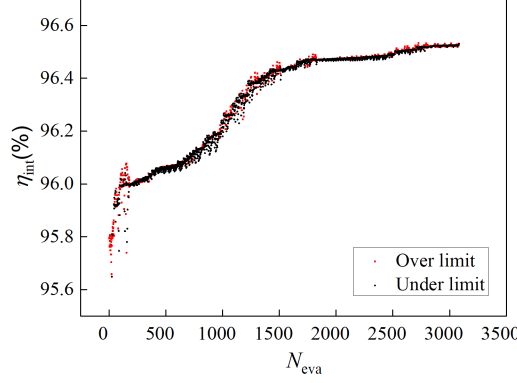


Fig. 4.15: Progress of the optimisation in Case O1. The problem converges when the pattern size is contracted to 0.1 of the original size.

4.5.1.4 Optimisation-based method with division into sub-problems

To accelerate the process, the optimisation problem is divided into sub-problems with fewer optimised variables. The assumptions of initial values, parametric boundaries and the end criterion are kept the same as in case O1. Different division approaches are investigated. In case O2, the optimisation problem is divided into four sub-problems, each considering two symmetric flow paths in the West-East direction. The order of the optimisation is shown in Figure 4.16. The constraint condition is that the sum of crossover extents for the currently-optimised tube banks and the previously-optimised banks is zero. The optimised aiming parameters are progressively introduced into subsequent sub-problems. The optimisation is finished after the last sub-problem converges. For each sub-problem k , the parameter space includes E , S and A from the corresponding tube banks, and the optimisation can be expressed as:

$$\begin{aligned} \text{maximise : } \eta_{\text{int}}(x), \text{ subject to : } & \sum_{j=1}^{4k} D_{\text{over},j}(x) = 0 \\ x = \{E_{4k-3}, S_{4k-3}, A_{4k-3}, \dots, E_{4k}, S_{4k}, A_{4k}\} & \in \mathbb{R}^{12} \\ & \text{for } k \text{ in } \{1, 2, 3, 4\} \end{aligned} \quad (4.7)$$

Case O3 divides the problem into eight sub-problems. Each sub-problem includes six variables and is optimised for one flow path in the sequence of flow path 1, 2, ...,

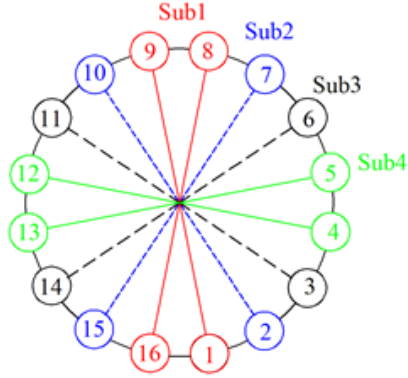


Fig. 4.16: Illustration of the optimisation sub-problems in case O2.

8. Each sub-problem k includes 6 variables, and can be expressed as:

$$\begin{aligned} \text{maximise : } \eta_{\text{int}}(x), \text{ subject to : } \sum_{j=1}^{2k} D_{\text{over},j}(x) &= 0 \\ x = \{E_{2k-1}, S_{2k-1}, A_{2k-1}, E_{2k}, S_{2k}, A_{2k}\} &\in \mathbb{R}^6 \\ \text{for } k \text{ in } \{1, 2, \dots, 8\} \end{aligned} \quad (4.8)$$

In case O4, each sub-problem is implemented for a single tube bank. This means each sub-problem in case O3 is further divided into two sub-problems, each considering for one tube bank. The sub-problems can be expressed as:

$$\begin{aligned} \text{maximise : } \eta_{\text{int}}(x), \text{ subject to : } \sum_{j=1}^k D_{\text{over},j}(x) &= 0 \\ x = \{E_k, S_k, A_k\} &\in \mathbb{R}^3 \\ \text{for } k \text{ in } \{1, 2, \dots, 16\} \end{aligned} \quad (4.9)$$

Results of cases O2 to O4 are shown in Table 4.6 compared to the result in case O1 without division. With division into more sub-problems, the number of evaluations per sub-problem drops quickly because fewer variables are optimised. The total number of evaluations drops, while the optimal interception efficiency is also reduced. This means the division benefits in accelerating the optimisation, at the expense of neglecting part of the interaction between tube banks, which may reduce the achieved interception efficiency.

Even with division, the optimisation-based approaches still remain too costly. This limits the application of the optimisation-based method. For example, if the method is to be used for annual simulation, it would be impractical to run several iterations of such heavy optimisation for different sun positions. Therefore, a new approach is explored in the following section to accelerate the process of determining MDBA parameters.

Table 4.6: Summary of the results for the optimisation-based method. $N_{\text{parameters}}$, $N_{\text{sub-problems}}$ and $N_{\text{evals,sub}}$ represent the number of parameters, number of sub-problems and number of evaluations per sub-problem.

Case	$N_{\text{parameters}}$	$N_{\text{sub-problems}}$	η_{int}	N_{evals}	$N_{\text{evals,sub}}$
O1	48	1	96.5%	3082	3082
O2	12	4	96.4%	1413	353
O3	6	8	96.4%	1184	148
O4	3	16	96.2%	785	49

4.5.2 Sequential determination of MDBA parameters

A three-step sequential method is proposed to address the limitations of the optimisation-based method. The sequential method is an adaptation of the work of Sánchez-González et al. [99] to the MDBA. In their study, preliminary values for the aiming factor were determined in the first step, and a second algorithm was used to select aiming points matching the incident flux with the AFD. A fast but approximate convolution-based optical model was used to determine the aiming points of individual heliostats. Similarly, the parameterisation of the MDBA model is divided into three parts. Preliminary values of the aiming extents are determined in a search algorithm, and the shape exponents and the asymmetry factors are determined in a second fitting algorithm. The third adjustment algorithm aims to fit within the flux limit with further adjustment of the aiming extent and the defocusing procedure if the first two steps fail.

4.5.2.1 Search algorithm

The algorithm roughly fits the flux to the safe limit by gradually adjusting the aiming extent. The algorithm flowchart is illustrated in Figure 4.17. The values of the shape exponents and the asymmetry factors are set constant as the initial values in case O1. The search algorithm starts with $E = 0.5$ for all tube banks. If the acceptance criterion is met for one tube bank, the aiming extent is stored and stays unchanged. If not, 0.05 is added to the aiming extents of the corresponding tube bank and its neighbouring tube banks, and the optical and thermal models are re-run to update the flux limit and compare it to the net flux. The neighbouring tube banks are considered here to take the interaction between adjacent banks into account because the flux typically spills over the side banks. The algorithm ends when values of aiming extent are assigned for all the tube banks.

In the current algorithm, the intersection of the net flux curve and the limit curve is allowed, but an acceptance criterion must be met:

$$\frac{D_{\text{over}}}{D_{\text{under}}} < \frac{1}{m} \quad (4.10)$$

where m is a factor determining the relationship between the safe and crossover extents. In the study of Sánchez-González et al. [99], the acceptance criterion was

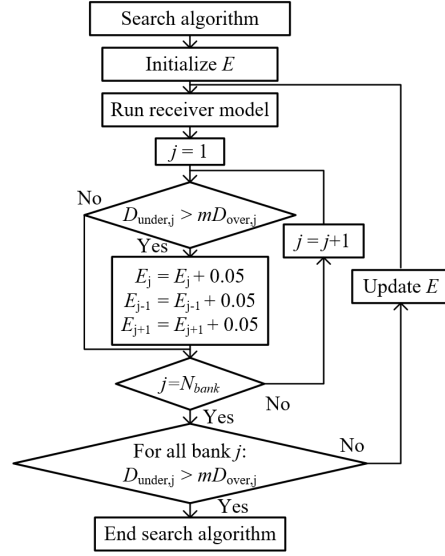


Fig. 4.17: Algorithm flowchart of the search algorithm.

$D_{\text{under}} > D_{\text{under}} (m = 1)$. If m is larger, the crossover extent becomes smaller, and it is easier for the downstream optimisation to converge. The suggested value of m is 5.

Figure 4.18 illustrate results of the search algorithm. The crossover only occurs on T4 and T13. The interception efficiency is 96.6%. The results of the search algorithm are stored and introduced to the following fitting algorithm.

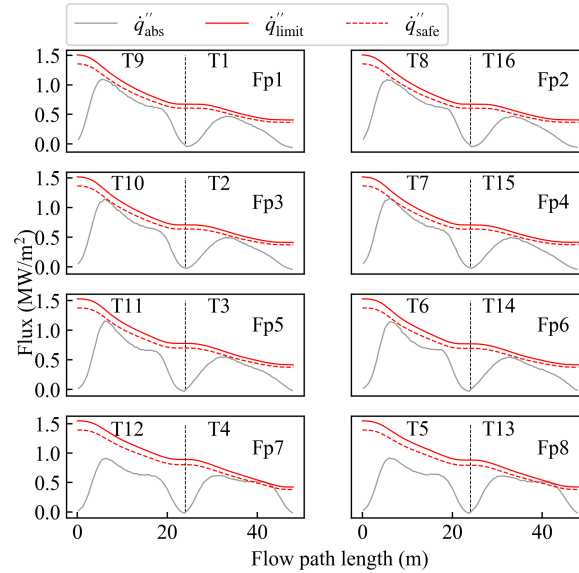


Fig. 4.18: Net flux and flux limit for all flow paths after completion of the search algorithm in the sequential method. The crossover only occurs on tube bank 4 and 13.

4.5.2.2 Fitting algorithm

The fitting algorithm determines the shape exponents and the asymmetry factors able to control the net flux below the safe limit. The results of the aiming extents from the search algorithm are introduced into the current algorithm, and the shape exponent and the asymmetry factor are optimised for the tube banks where flux is exceeded. The flowchart of the fit algorithm is shown in Figure 4.19. Each optimisation sub-problem j is expressed as:

$$\text{minimise : } D_{\text{over},j}(x), \quad x = S_j, A_j \in \mathbb{R}^2 \quad (4.11)$$

The parameter space \mathbb{R}^2 includes S_j and A_j from the corresponding tube bank j . The initialised values and parametric boundaries of the shape exponent and the asymmetry factor are the same as in the optimisation-based method. The optimised variables of previous sub-problems are introduced to the following sub-problems. The end criterion for each optimisation problem is that the crossover is reduced to zero or the step length is contracted to 0.1 of the initialised step length in Equation 4.5.

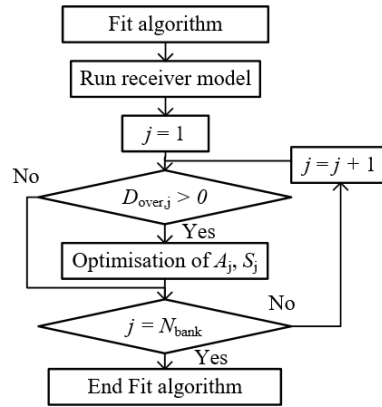


Fig. 4.19: Algorithm flowchart of the fit algorithm.

4.5.2.3 Adjustment algorithm

The adjustment algorithm is used to finalise the aiming strategy if the fitting algorithm fails to eliminate the crossover extents for all tube banks. The flowchart algorithm is shown in Figure 4.20. For the tube banks with excess flux, the aiming extents of the corresponding and neighbouring tube banks are gradually increased until no crossover occurs for the tube bank. If the aiming extent exceeds 1.0, some heliostats aim outside the bounds of the receiver. This has potential to cause excessive heat flux and damage to components outside the receiver and these heliostats are defocused and aimed at a stand-by point.

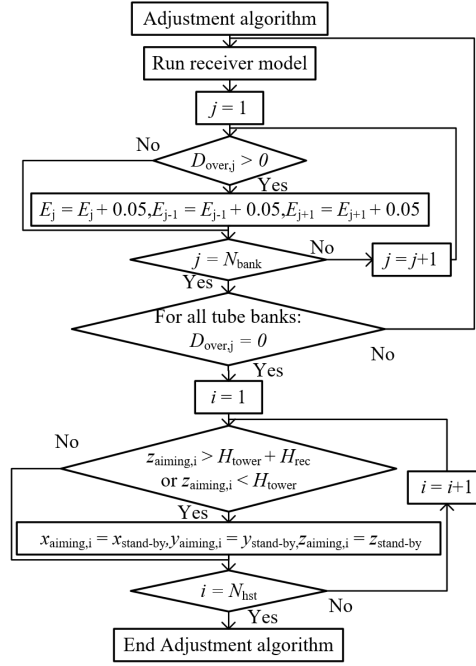


Fig. 4.20: Algorithm flowchart of the adjustment algorithm.

4.5.2.4 Results of the sequential method

The results of the optimal aiming variables and the flux profile (case S1) are shown in Table 4.7 and Figure 4.21. The number of evaluations is greatly reduced (99.4% reduction) compared to the optimisation-based method, while the interception efficiency is equivalent. The high interception efficiency is mainly achieved in the preliminary determination of the aiming extent, which results in a good starting point for the optimisation. The three-steps algorithm also greatly accelerates the parametric determination process. After a simple parametric search of the aiming extent, crossover only occurs at two tube banks, which offer great convenience for the fitting algorithm to reduce the crossover extents through the optimisation. In this case, aiming extents of all tube banks are below one, so the defocusing process is not activated. The simulation in case S1 needs 18 ray-tracing evaluations, which takes about 3 minutes in total with 10^7 rays on a desktop PC with an Intel i7 processor and 16 GB Ram.

Table 4.7: Results of the sequential method (case S1). T1-T16 point to tube banks in Figure 4.6.

	T1	T2	T3	T4	T5	T6	T7	T8	T9	T10	T11	T12	T13	T14	T15	T16
<i>E</i>	0.70	0.80	0.95	0.85	0.75	0.65	0.75	0.80	0.80	0.75	0.65	0.75	0.85	0.95	0.80	0.70
<i>S</i>	1.50	1.50	1.50	0.75	1.50	1.50	1.50	1.50	1.50	1.50	1.50	1.50	0.75	1.50	1.50	1.50
<i>A</i>	0.33	0.33	0.33	0.25	0.67	0.67	0.67	0.65	0.67	0.67	0.67	0.67	0.25	0.33	0.33	0.33

The interception efficiency is 96.5%. The number of ray-tracing evaluations is 18.

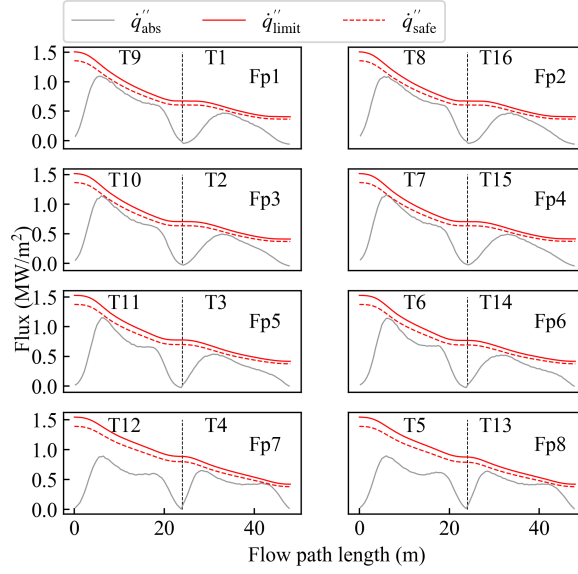


Fig. 4.21: Net flux and flux limit for all flow paths after completion of the sequential method (case S1).

4.5.2.5 Sensitivity analysis of the factor m

The value of the factor m denotes the relationship between D_{over} and D_{under} (see Equation 4.10), and hence affects the result of the search algorithm and the starting point of the fitting algorithm. A suggested value of $m = 5$ is used in case S1. Here a sensitivity analysis is implemented to investigate the effect of m on the results, as shown in Table 4.8. The optimal interception efficiency is reduced with increasing m , while the number of evaluations also drops. In case S2, crossover appears at more tube banks than other cases. This leads to more optimisation sub-problems in the fitting algorithm, and hence the number of evaluations is increased. The interception efficiency is higher than other cases because the aiming extents can remain at low values with larger allowable crossover in the search algorithm. Notably, the interception efficiency in case S2 is even 0.1% higher than in case O1. The reason is that the result in case O1 is likely to be a local optimum. Besides, the interception efficiency and the number of evaluations do not change linearly with increasing m . Cases S1, S3 and S4 lead to the same result because the aiming extent step selected by the search algorithm is identical for all of them. Due to the trade-off between interception efficiency computational speed and method reliability, the suggested value for m is chosen as 5.

In summary of the sequential method, the number of ray-tracing evaluations has been greatly reduced compared to the optimisation-based method, while achieving the same interception efficiency. However, a potential drawback is that an optimisation is still needed in the fit algorithm, which prevents from a further acceleration. To address this factor, and further accelerate the MDBA method, a third variation of the method is proposed where the key variables are determined based upon a feedback method.

Table 4.8: Results of the sensitivity study. $\eta_{\text{int,search}}$ is the efficiency after the search algorithm. The tube bank index points to banks with cross-over after the search algorithm. N_{evals} is the number of evaluations.

Cases	m	$\eta_{\text{int,search}}$	Tube bank index	η_{int}	N_{evals}
S2	1	96.7%	T3,T6,T9-10,T12-13	96.6%	58
S3	3	96.6%	T3,T12	96.5%	18
S1	5	96.6%	T3,T12	96.5%	18
S4	7	96.6%	T3,T12	96.5%	18
S5	9	96.4%	T3,T12	96.4%	14

4.5.3 Feedback-based MDBA method

In the feedback-based method, the values of E , A and S for all tube banks are simultaneously adjusted after each iteration of the ray-tracing simulation. The algorithm flowchart is illustrated in Figure 4.22. The method to adjust E follows the search algorithm in Figure 4.17. The method to adjust A and S is introduced in the following subsections.

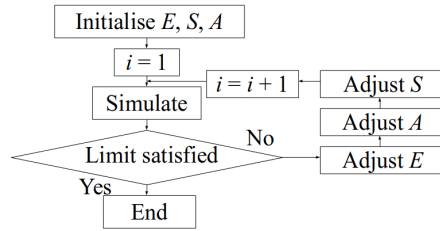


Fig. 4.22: Algorithm flowchart of the feedback-based MDBA method.

4.5.3.1 Determination of the asymmetry factor A

The asymmetry factor is defined as the ratio of heliostats targeting the upper section of the receiver to the total number of heliostats in a given field sector. An appropriate value of A needs to be chosen such that the slope of the net flux curve matches the slope of the safe limit curve. A feedback signal is needed after each simulation iteration to use as a basis for the adjustment of A . The feedback signal chosen is the slope of the net flux curve. The slope of this curve is compared to the slope of the safe limit curve, and the value of A is updated to minimise the difference between the two (i.e. match the slopes of the net flux and the safe limit curves).

The accuracy of the feedback signal is essential in this approach. A linear regression method is implemented to fit both the net flux and safe limit curves. Two examples are shown in Figure 4.23, with A of 0.75 and 0.67, respectively. The part of the flux and limit curves that needs to be fitted is the middle part, where the net flux is high and needs to be matched closely with the safe limit curve. Hence, the boundaries LB_1 and RB_1 are defined as the range of aiming points, which is controlled by

E and symmetric about the equatorial line:

$$\begin{cases} LB_1 = \frac{H_{rec}}{2}(1 - E_j) \\ RB_1 = \frac{H_{rec}}{2}(1 + E_j) \end{cases} \quad (4.12)$$

where E_j is the aiming extent for bank j . The linear regression is performed over this interval LB_1 and RB_1 . The low-flux area at the edge of the receiver is excluded to avoid the less critical low-flux regions influencing the results of the linear regression. The linear regression model is the ‘HuberRegressor’ model implemented in the Python package Sklearn [165]. The slopes of the limit and flux curves are recorded as k_1 and k_2 , respectively.

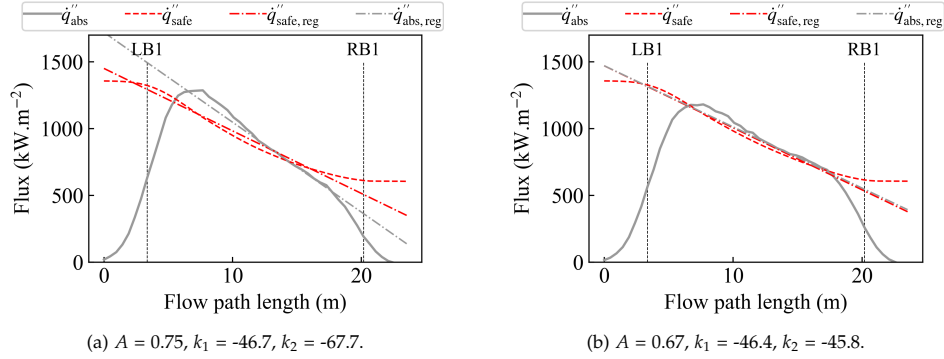


Fig. 4.23: Linear regression of the net flux and safe limit curves with varying asymmetry factor A . The dash-dot lines are the results of the linear regression. LB_1 and RB_1 indicate the boundary of aiming range. k_1 and k_2 are calculated slopes for the safe limit and net flux curves.

For the two cases in Figure 4.23, the dash-dot lines show the results of the linear regression, with the dash-dot red line showing the result for the fit to the dashed red safe limit curve and the dash-dot grey line showing the fit to the net flux. As the plots show, the regression results of both the net flux curve and the safe limit curve match the real plots in both cases. However, the slope of the net flux curve is too steep in Figure 4.23(a) and does not match the slope of the safe limit curve well, as reflected by the big difference between k_1 and k_2 values. In contrast, the slope of the flux curve is fitted better with the slope of the limit curve in Figure 4.23(b), and the difference between k_1 and k_2 is very small. This demonstrates how the comparison between k_1 and k_2 can guide to adjustment of the slope of the two curves.

Therefore, the slope values (k_1 and k_2) are returned after each iterative simulation to adjust A . The algorithm to adjust A is shown in Figure 4.24 and is the process to ‘adjust A ’ shown in the flowchart in Figure 4.22. For each tube bank, the slopes for the two curves are obtained and compared. A tolerance of δ_A is allowed here. When the relative difference between k_1 and k_2 is within the tolerance, A is kept unchanged. δ_A is suggested to be 10% in this study. However, if the relative difference is outside the tolerance and k_1 is larger than k_2 (see Figure 4.23(a)), the flux curve is too steep, so A needs to be reduced when larger than 0.5, and raised when smaller than 0.5. The gap value (Δ_A) to adjust A at each iteration is set to be 0.02 based on the experience

when using the MDBA method. The flux curve is too shallow if k_1 is smaller than k_2 , and adjustments in the opposite direction are made to A as shown in Figure 4.24. The iteration stops when the algorithm loops through all banks.

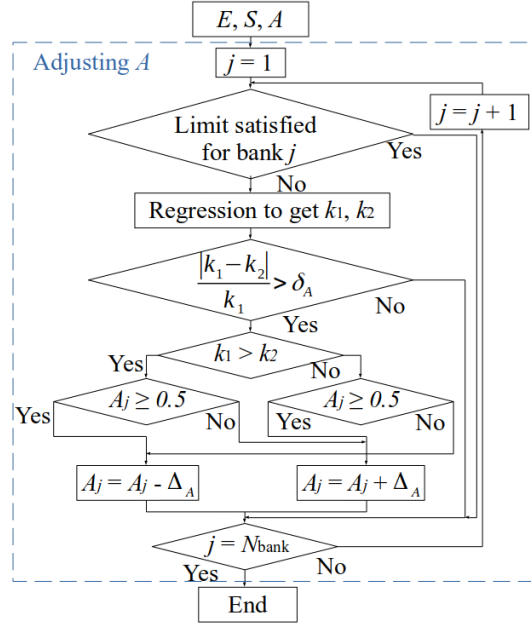


Fig. 4.24: Flowchart to adjust A

4.5.3.2 Determination of the shape exponent S

The shape exponent determines the shape of the flux profile. With a small S , the flux is separated into two high flux zones, one at the top and one at the bottom of the receiver, and the receiver ‘shoulders’ appear. With increasing S , the flux distribution becomes more concentrated towards the receiver’s centre. A suitable S should lead to the net flux curve having a similar shape to the safe limit curve. Figure 4.25 shows examples of three net flux curves with different shape exponents, with S values of 1.0, 3.0 and 1.5. The boundaries LB_1 and RB_1 are defined in the same way as in the method for determining the asymmetry factor A per Section 4.5.3.1. A new interval, bounded by LB_2 and RB_2 , is formed by halving the LB_1 and RB_1 interval and centring it about the equatorial line:

$$\begin{cases} LB_2 = \frac{H_{rec}}{2} \left(1 - \frac{E_j}{2}\right) \\ RB_2 = \frac{H_{rec}}{2} \left(1 + \frac{E_j}{2}\right) \end{cases} \quad (4.13)$$

The shape ratio is defined as the crossover extent (introduced in Section 4.5.1.1) between LB_2 and RB_2 to the total crossover extent:

$$\text{Shape ratio} = D_{\text{over}(LB_2, RB_2)} / D_{\text{over}} \quad (4.14)$$

where $D_{\text{over},(\text{LB}_2, \text{RB}_2)}$ is the crossover extent over the interval LB_2 and RB_2 , and D_{over} is the crossover extent over the entire tube length. The shape ratio is used as the feedback signal to adjust S . An appropriate shape ratio needs to be close to 0.5 without having flux ‘shoulder’ or a concentrated flux peak. For the two cases in Figure 4.25 (a) and (b), the shape ratio is 0 and 0.94, respectively. This means S is too small in Figure 4.25 (a), with crossover located near the edges of the receiver, and S is too large in Figure 4.25 (b), with too highly concentrated flux at the centre. In Figure 4.25 (c), the shape of the net flux curve fits well with the shape of the safe limit curve, as reflected by the shape ratio value close to 0.5.

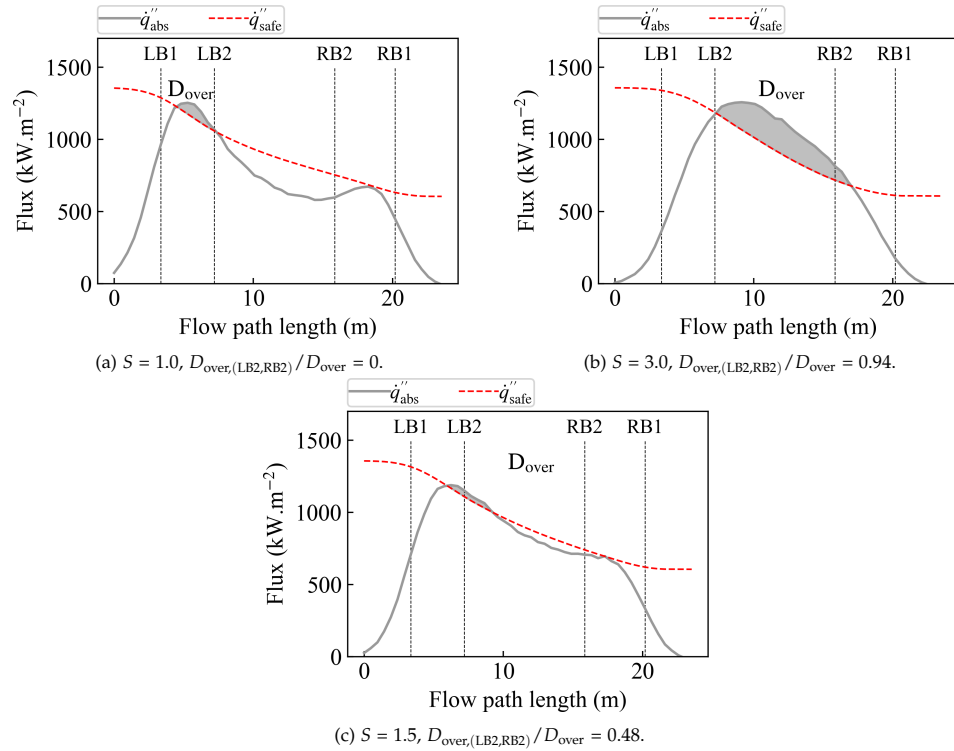
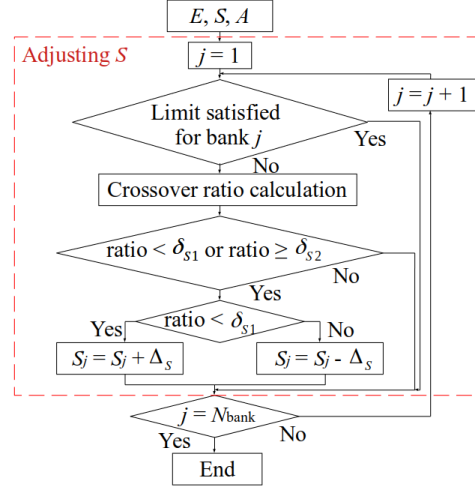


Fig. 4.25: Net flux with varying the shape exponent S . LB_1 and RB_1 are the boundary of aiming range. LB_2 and RB_2 are halved based on the distance from the centre to LB_1 and RB_1 .

Figure 4.26 illustrates the algorithm flowchart to adjust the shape exponent S . A tolerance of δ_S is adopted, and S is kept unchanged if the shape ratio is between δ_{S1} and δ_{S2} :

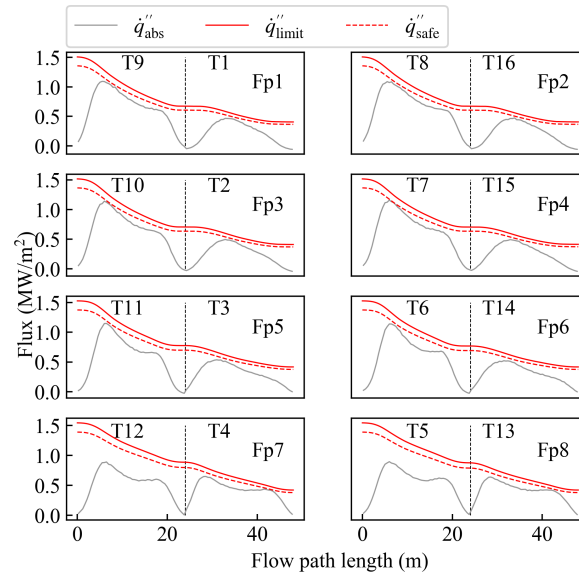
$$\begin{cases} \delta_{S1} = 0.5 - \frac{\delta_S}{2} \\ \delta_{S2} = 0.5 + \frac{\delta_S}{2} \end{cases} \quad (4.15)$$

So δ_{S1} and δ_{S2} are set to be 0.45 and 0.55 when the tolerance δ_S is chosen as 10%. S is increased to concentrate the flux if the shape ratio is too low and vice versa. The gap value (Δ_S) is chosen as 0.2 to adjust S , and works well in practice.


Fig. 4.26: Flowchart to adjust the shape exponent S

4.5.3.3 Results of the feedback-based method

The feedback-based method is used to optimise the aiming strategy for the reference case. The flux curves are shown in Figure 4.27. The net flux can be controlled below the safe limit for all banks. The number of ray-tracing iterations is 8, which is a reduction by more than a half compared to the sequential method. The interception efficiency is 96.5%, which is equal to the sequential method. The reason for the acceleration is that the three aiming parameters are adjusted simultaneously rather than sequentially, and no optimisation algorithm is needed.


Fig. 4.27: The flux profile using the new algorithm. $\eta_{\text{int}}=96.5\%$, $N_{\text{evals}}=8$.

Summarising the above investigations on parameter determination methods, any

one of the three methods can be used to fit the net flux closely to the flux limits, with similar interception efficiency. The feedback-based method is the most computationally efficient approach, obtaining the safe flux map after only 8 evaluations, while the sequential method also converges relatively fast with 16 evaluations.

4.6 Use of the MDBA method in annual simulations

The above sections introduce an instantaneous aiming method to control the flux under limits at design point. Furthermore, the flux limits need to be respected throughout the year, which requires the use of the aiming method in annual simulations. It is noteworthy that the discussion in this section does not attempt to describe a dynamic heliostat control technique, but rather a design method that generalises the MDBA approach so that it is applicable to annual simulation during design studies.

A basic approach to determine heliostat aiming strategy in annual simulations is to perform an optimisation at regular time intervals throughout the year. However, this would mean that simulations would be run at similar sun positions and therefore yield some identical and redundant results. If the time intervals were short, say a minute or even an hour, the large number of computationally costly simulations would not be feasible. Thus, a method based on discretisation of the sun position is applied, given that the optimal aiming variables rely on the solar position. It is noted that each of the three MDBA methods described above can be used for the aiming strategy optimisation at a given sun position. Here the sequential method is used, although the more computationally efficient feedback-based method would be recommended in future work to further increase speed. The sun positions are represented by the declination angle (δ) and the hour angle (ω) [166].

4.6.1 Determination of aiming variables with clear-sky irradiance

To simplify the annual aiming problem, DNI is firstly decoupled, and a clear-sky irradiance model is used where the DNI relies on the zenith angle. The Meinel clear-sky model [147] is applied, which is defined as:

$$I = I_0 \times 0.7^{AM^{0.678}} \quad (4.16)$$

where $I_0 = 1365 \text{ W/m}^2$, $AM = 1/\cos(z)$, z is the zenith angle. A priori optimisation is performed for each discrete node, and the aiming variables at different time points are then obtained from detailed pre-simulated data with an interpolation. Such a simulation scheme results in around a 90-95% reduction in simulation time.

4.6.1.1 Aiming interpolation method

In the interpolation method, the declination and hour angle ranges are discretised with a grid of $N \times M$ to generate a series of (δ_0, ω_0) . The grid size is chosen as 5×25 due to a trade-off between the computational cost and the interpolation

accuracy. Only cases with elevation angle larger than 15° are optimised because the low incident flux below this angle is normally safe for the receiver, and the aiming variables are chosen as initial values for those off-peak hours.

Then, the list of relevant sun-positions (δ_0, ω_0) are introduced into the aiming strategy optimisation algorithm to obtain the optimal aiming variables. For the given grid density of 5×25 , the optimisation is implemented on 47 sun positions after skipping post-sunset and pre-sunrise points. A series of look-up tables (one per variable) are generated to store all the optimal variables. Table 4.10 shows an example of a look-up table for the aiming extent of T4. The aiming extents are larger in the afternoons than in the mornings.

Table 4.9: The look-up table for the aiming extent E at tube bank 4 ($\delta_0 \times \omega_0$, unit: $^\circ$).

	-105	-90	-75	-60	-45	-30	-15	0	15	30	45	60	75	90	105
-23.4	0.50	0.50	0.50	0.50	0.50	0.50	0.55	0.65	0.70	0.65	0.50	0.50	0.50	0.50	0.50
-11.7	0.50	0.50	0.50	0.50	0.50	0.50	0.65	0.70	0.75	0.80	0.70	0.50	0.50	0.50	0.50
0	0.50	0.50	0.50	0.50	0.50	0.55	0.70	0.80	0.85	0.85	0.80	0.70	0.50	0.50	0.50
11.7	0.50	0.50	0.50	0.50	0.50	0.60	0.75	0.85	0.85	0.90	0.85	0.80	0.60	0.50	0.50
23.4	0.50	0.50	0.50	0.50	0.60	0.70	0.80	0.85	0.90	0.90	0.90	0.85	0.70	0.50	0.50

After generating the look-up tables, the value of each aiming variable for any new pair of solar angles (δ, ω) can be calculated using the interpolation method. A 2D linear interpolation method is used. Figure 4.28 illustrates a colormap for the interpolated results for the aiming extent at tube bank 4. The aiming extents are larger in the afternoons than in the mornings.

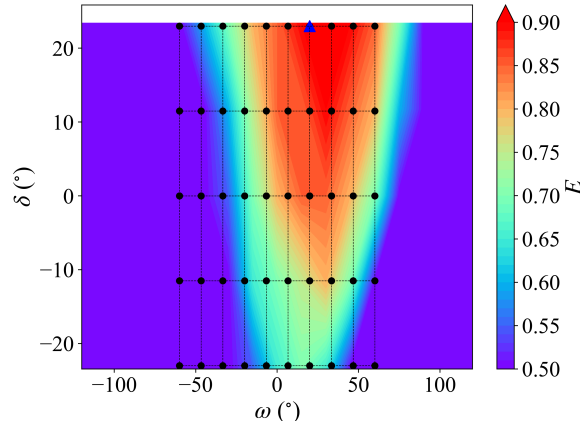


Fig. 4.28: Interpolated results for the aiming extent at tube bank 4. Dots at the black grid represent the points used to validate the interpolated results. The blue solid triangle marks the sun position for case D1.

4.6.1.2 Validation of the interpolation method

A direct way to validate the interpolation method is to check if the net flux can be controlled below the safe limit using the interpolated results. As shown in Figure

4.28, 50 points are selected at positions different to the original calculations in Table 4.10. Calculations confirm that the interpolated results from all 50 points produce a safe flux profile, showing evidence of the capability of the interpolation method as a reliable aiming strategy throughout an annual simulation.

The interpolated results are compared with results obtained from direct optimisation at the same sun positions in Figure 4.29. A typical time point (case D1) is chosen with the declination and hour angles of 23.0° and 20.0° , respectively. The interpolation method is able to obtain aiming variables similar to the optimisation method, and those variables are capable of generating reliable flux profiles, very similar to optimised ones. The R-squared method is applied to quantify this similarity. The optimised and interpolated flux values are marked as f_i and f'_i , respectively, where i represents the mesh element index of the receiver and spans from 1 to N_{ele} (900 in this study). The mean value of the optimised flux is:

$$\bar{f} = \frac{1}{N_{\text{ele}}} \sum_{i=1}^{N_{\text{ele}}} f_i \quad (4.17)$$

The coefficient of determination (R-squared value) is then calculated as:

$$R^2 = 1 - \frac{\sum_{i=1}^{N_{\text{ele}}} (f_i - f'_i)^2}{\sum_{i=1}^{N_{\text{ele}}} (f_i - \bar{f})^2} \quad (4.18)$$

The results show that R^2 is 0.99 for case D1, which proves that the interpolated results match very well with the optimised results.

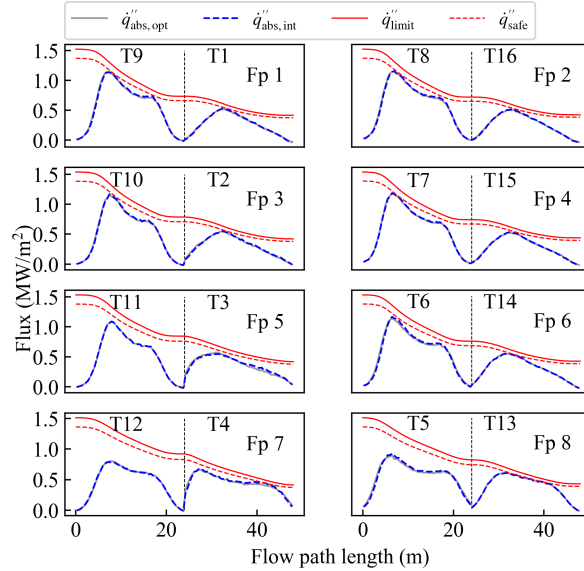


Fig. 4.29: Comparison of the optimised and interpolated results in case D1 ($\delta = 23.0^\circ$, $\omega = 20.0^\circ$, $\text{DNI} = 937.9 \text{ W/m}^2$, $\eta_{\text{int}} = 97.0\%$). Grey solid line and blue dashed line represent the net flux calculated from optimisation and interpolation, respectively.

4.6.2 Use of the MDBA method in annual simulations with varying DNI

In real weather conditions, the DNI may deviate from the clear-sky data. If the real DNI is larger than the data given by the clear-sky model, the adjustment algorithm given in Figure 4.20 is used to spread the flux across the receiver surface. If the real DNI is lower than the clear-sky value, then the aiming extents for all banks are gradually reduced until crossover occurs. This simplified annual strategy is tested in case D1 against the case of fully optimised aiming using the sequential method. The DNI ratio, which is defined as the ratio of real to clear-sky DNI, is varied from 0.8 to 1.2 in the test. The results are shown in Table 4.10, and demonstrate that by adjusting only the aiming extent E (and not S and A), the simplified annual strategy gives a close match to the fully optimised results. In conclusion, the simplified annual method achieves similar performance compared to the sequential method, and is much faster.

Table 4.10: Results with varying the DNI ratio in case D1. $\eta_{\text{int,eq}}$ is 97.6% at this time point.

DNI ratio	Real DNI (W/m ²)	η_{int} (simplified annual)	η_{int} (fully optimised)
0.8	750.3	97.0%	97.4%
0.9	844.1	97.0%	97.2%
1.0	937.9	97.0%	97.0%
1.1	1031.7	96.4%	96.4%
1.2	1125.5	95.4%	95.6%

Figure 4.30 shows the result with DNI ratio of 1.1 in case D1 using the simplified annual method. With such a high incident irradiation, the defocusing process is activated and aiming points of some heliostats are adjusted to the stand-by point.

4.7 Conclusion for this chapter

In this chapter, a ray-tracing based optical simulation is coupled with heat transfer and thermo-mechanical models to accurately simulate the heliostat field and receiver. A new parameterisation method (the MDBA method) is proposed to determine the aiming strategy using three parameters per tube bank. The MDBA method is able to spread the flux over the receiver surface, to control the shape of the flux profile, including vertical asymmetry. Three approaches, the optimisation-based method, the sequential method and the feedback-based method, are investigated to obtain the aiming variables. For a reference heliostat field and receiver system, the optimisation-based method achieves a high interception efficiency of 96.5%, while the number of ray-tracing evaluations is over 3000. The sequential method can achieve an equivalent interception efficiency with only 18 ray-tracing simulations. The feedback-based method can reduce again the number of evaluations to 8. Furthermore, an interpolation and adjustment method is proposed to dynamically predict the aiming variables across different sun positions and DNI levels to enable annual simulations. Safe flux profiles are achieved using the interpolated results.

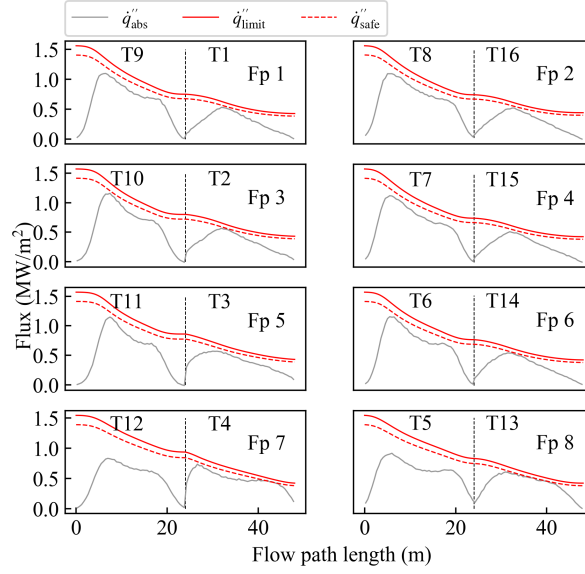


Fig. 4.30: Net flux and flux limit for all flow paths ($\delta = 23.0^\circ$, $\omega = 20.0^\circ$, $\text{DNI} = 1031.7 \text{ W/m}^2$, $\eta_{\text{int}} = 96.4\%$).

An aiming strategy is an essential tool for the design of heliostat fields and receivers. Compared to previous aiming strategy in literature, the MDBA method is able to closely match the net flux with the flux limit. The high accuracy, high performance MDBA method is sped-up sufficiently to be used in annual performance calculations and is fast and simple enough to be incorporated into plant control systems. The methodology is applied here to an external receiver case but could be extended to different receiver geometries including cavity types, an advantage of this ray-tracing based technique compared to alternative convolution methods. The aiming points are adjusted vertically in this chapter. A more advanced aiming strategy with left-right aim points shifting [167] is also suggested as future work. Dynamic control of aiming points under varying DNI is one of the suggested future developments of the MDBA method, so that it can be used as a heliostat control tool in addition to being a design tool.

Co-optimisation of the heliostat field and the receiver

5.1 Introduction

In a concentrated solar power (CSP) tower plant, it is essential to understand the performance of the heliostat field and receiver subsystems. In heliostat field and receiver subsystems, it is necessary to operate the heliostat field with an aiming strategy that guarantees the safety and lifetime of the receiver while maximising performance. As reviewed in Chapter 2, state-of-the-art studies optimise the heliostat field (Section 1.2.1), aiming strategy (Section 1.2.2) and the receiver (Section 1.2.3) independently. However, the field and the receiver are interdependent and co-optimisation of the field-receiver subsystem is necessary to obtain an optimal configuration. In most co-optimisation studies, as reviewed in Section 1.2.4, the fast convolution optics approach is used in optical simulations. Convolution optics are not as accurate as MCRT [104] and can lead to large local flux inaccuracies on the receiver. Such flux inaccuracies can have consequences on the aiming strategy and ultimately affect the system's energy yield. For receivers, correlations or simplified analytical models are always used in annual simulations instead of detailed receiver modelling. No literature study can be found that enables an aiming strategy optimisation within a system design optimisation. In this chapter, MCRT is coupled with a detailed receiver model based on finite differences and an efficient aiming strategy to accurately determine the output of the subsystems while ensuring flux constraints are respected at the receiver. Fast and accurate annual assessments are enabled with a 2D interpolation method for the field. A new loss-breakdown method is proposed to evaluate annual receiver performances. The detailed instantaneous modelling results are integrated into a system-level simulation tool and a genetic algorithm used to enable full co-optimisation for any objective function. The proposed method is used to optimise the reference system composed of a surround field and a liquid sodium-cooled cylindrical external receiver for annual performance and LCOE. A sensitivity study confirms the good behaviour of the method.

5.2 Models and methodology

5.2.1 The reference system

The reference system is located in Daggett, CA and comprises a surround field and a central cylindrical external receiver. The system is kept consistent with the Gen3L system introduced in Chapter 2. The reference heliostat field and receiver subsystems are consistent with Chapter 4 and were developed prior to this work using a manual two-step approach to come up with a good design. The reference subsystem will be used here as a reference to confirm that the optimisation behaves properly. [161, 162].

5.2.2 Instantaneous energy balance methodology

The optical modelling is carried out with MCRT-based SOLSTICE [131]. The sun-shape in the simulation is a Buie sunshape [123] with a circumsolar ratio of 2%. The optical efficiencies and the incident flux at the receiver are obtained from the optical simulation. The heat transfer model from Asselineau [142] is used to simulate the thermal performance of the receiver. The receiver pipe material assumed is Alloy 740H (UNS N7740). The flux limit look-up tables are obtained using the method proposed by Logie et al. [143] considering the thermoelastic stresses. The flux limits at five standard pipe outer diameters (33.40 mm, 42.16 mm, 48.26 mm, 60.33 mm, 73.03 mm [168]) are illustrated in Figure 5.1. At each time step, the maximum allowable flux is calculated for every receiver element using 2D interpolation and compared with the net flux on the tube section to prevent over-flux after running the heat transfer model.

5.3 Annual simulation co-optimisation methodology

The flowchart of the co-optimisation method is illustrated in Figure 5.2. The variables to be optimised include two field expansion parameters, the receiver dimensions and the tower height. The method starts from the field model generating a large field and then trimming the field to reach the nominal output. Next, the receiver flow-path configuration is determined, and the aiming strategy is adjusted accordingly to respect the maximum allowable flux. The performances of the field and receiver at different sun positions are then simulated and compiled into interpolation tables that are imported into a system-level model in Modelica for techno-economic evaluations based on full-year simulations. In this chapter, optimisations are presented and compared for two objective functions: annual solar-to-thermal efficiency and LCOE.

5.3.1 Generation of the field layout

The Campo algorithm [31] is chosen to generate the large field. Campo basically divides the whole field into three zones. Five parameters are essential in the Campo

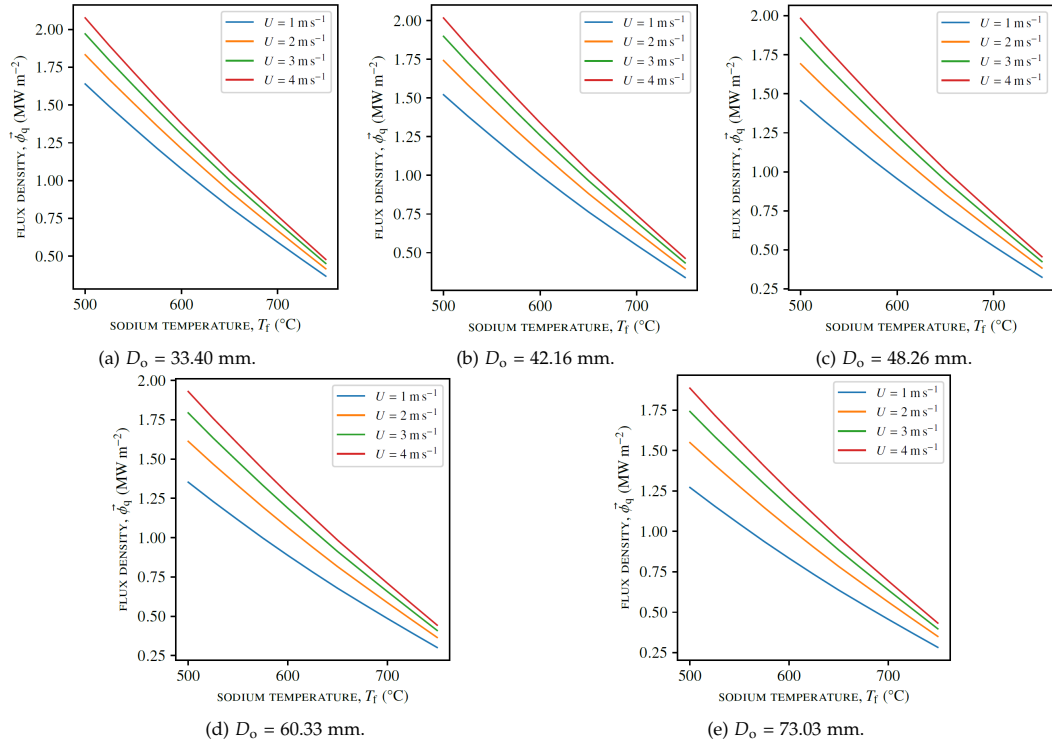


Fig. 5.1: Allowable absorbed flux density at different pipe outer diameter (D_o).

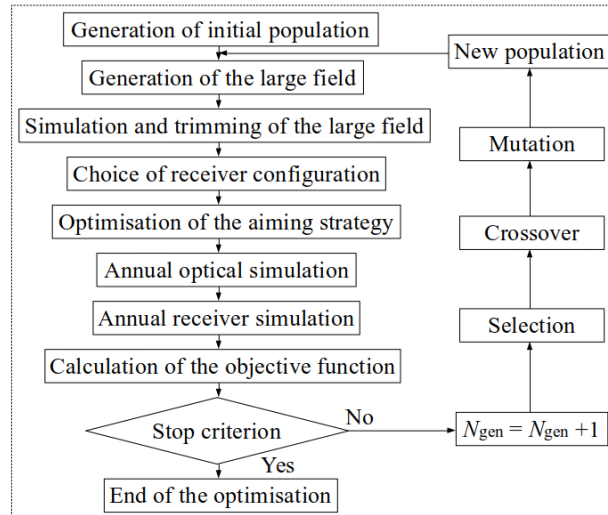


Fig. 5.2: Flowchart of the co-optimisation method. The algorithm returns the annual solar-to-thermal efficiency or the LCOE as the objective function in the genetic algorithm. N_{gen} represents the number of populations.

code [39, 144]: the radius of the first row (R_1), the separation distance between neighbouring heliostats (d_{sep}), and the radial increment for three zones ($\Delta r_1, \Delta r_2$ and Δr_3). R_1 is typically fixed and depends mostly on the size of the plant central island components. d_{sep} is set to 0 and Δr_1 is kept as the minimum value of 0.866. Then, the large heliostat field is generated with two variables: Δr_2 and Δr_3 . The large heliostat field is generated for the trimming process that will be introduced in Section 5.3.3. In the study of Collado and Guallar [39], the authors chose the best 7400 heliostats from a pre-generated field of 10500 heliostats. A ratio of 30% of oversizing, which is similar to the study of Collado and Guallar [39], is used in this chapter.

5.3.2 Annual optical performance

The annual optical simulation method introduced in Section 2.3.1 is applied here. The domain of sun positions is discretised using a two-dimensional grid of N by M points with equidistant steps (see Figure 2.9), where the optical simulations are performed, and results are stored into the optical efficiency look-up table (OELT). Sun position discretisation parameters are set at $N = 10$ and $M = 24$. Notably, only half a day needs to be simulated because east-west symmetry mostly holds for a radial-staggered field layout. Akima splines in the CombiTable2D model are then used to calculate the efficiency for a given pair of solar angles. For the reference system, a comparison of the interpolated and simulated results is shown with the colour map in Figure 5.3. The interpolated results are in good agreement with the simulated results, especially near solar noon. The deviation is larger near sunrise and sunset because the interpolation method does not capture the rapidly decreasing trend of the optical efficiency in these regions as well as in the rest of the sky. However, the field outputs are small at these hours, and the effect on the annual total output is minor [146]. The mean deviation normalised to the nominal input in the afternoon is 0.14%, compared to 0.11% in the morning, which proves that the assumption of the east-west symmetry is accurate.

Furthermore, the annual optical output from this interpolation method is calculated and compared with detailed hourly simulations for the reference system. The results are illustrated in Table 5.1. The results show that the relative difference between the detailed hourly calculation and the 2D interpolation method is 0.2%, while the latter is much faster. The interpolation method requires 32 ray-tracing simulations compared to more than 3000 simulations for the hour-by-hour simulation, leading to a computational gain of 98.9%.

Table 5.1: Verification of the annual optical model. The relative deviation is calculated with results from hour-by-hour simulations as reference.

Case	Annual field output (GWh)	Deviation	Number of simulations
Hour-by-hour simulations	1478.4	\	>3000
New model	1475.9	0.2%	32

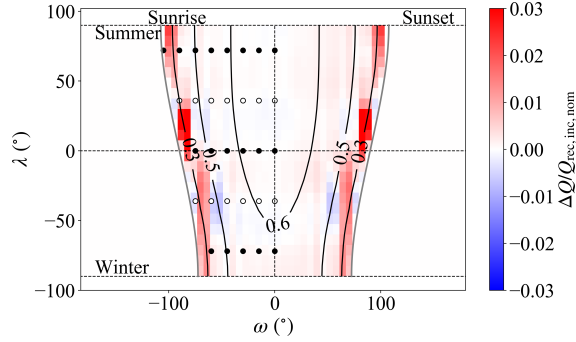


Fig. 5.3: Verification of the annual optical simulation method. $\Delta Q/Q_{\text{rec,inc,nom}}$ is the difference between simulated and interpolated values of the receiver incident power normalised to the nominal incident power (543 MWth). The dots represent sun positions where optical simulations are performed. Receiver thermal simulations are implemented after the optical simulations on the black-dotted sun positions, as introduced in section 5.3.6. The contour lines show the field efficiency and the colour map highlights the difference between the field outputs calculated from the real simulation and the interpolated values. Sunrise and sunset hours are calculated from equations from Duffie et al. [169].

5.3.3 Trimming of the large heliostat field

The large field is trimmed to produce the final field design to deliver a desired input to the receiver. The “annual-ranking”-based method [36] is used here. All heliostats are ranked by their annual optical efficiencies in descending order, and the first N_{hst} of heliostats in the list that provide the required power are selected to form the trimmed heliostat field.

The annual optical efficiency of a heliostat j ($\eta_{\text{a,hst},j}$) is expressed as:

$$\eta_{\text{a,hst},j} = \frac{\sum_{i=1}^{i=365} \int_{\text{sunrise}}^{\text{sunset}} GA(t) \eta_{\text{hst},j}(t) dt}{\sum_{i=1}^{i=365} \int_{\text{sunrise}}^{\text{sunset}} GA(t) dt} \quad (5.1)$$

where $GA(t)$ is the total energy into the heliostat field at time t . $\eta_{\text{hst},j}(t)$ represents the optical efficiency for heliostat j at time t . However, Eq. 5.1 needs a high number of interpolations consuming large amounts of computational resources. A simplification is made by reducing the summation to only the 32 points corresponding to the sun positions shown in Figure 5.3:

$$\eta_{\text{a,hst},j} = \frac{\sum_{i=1}^{i=32} GA(t) \eta_{\text{hst},j}(t)}{\sum_{i=1}^{i=32} GA(t)} \quad (5.2)$$

A verification study shows that the efficiency difference of the trimmed field comparing results using equations 5.2 and 5.1 is less than 0.1%. Hence, the annual optical efficiencies of individual heliostats are calculated using Eq. 5.2.

5.3.4 Determination of the receiver configuration

Cylindrical receivers are composed of identical vertical tube panels. The receiver geometry is mainly determined by a vertical length (H_{rec}), diameter (D_{rec}), tube wall thickness (δ_{th}), tube outer diameter (D_0), tube spacing (δ_s), tube material, number of tube banks (N_b), number of flow-paths (N_{fp}) and the flow-path pattern [47, 170]. Tube wall thickness is fixed to 1.2 mm in this work, the same thickness as the tubes in Solar Two [2]. Tube spacing is fixed as 1.0 mm. A simplified heat transfer model can be used to analyse their effect on receiver performance for other parameters.

The HTF velocity is an essential criterion for designing a tubular receiver. A higher velocity enhances the heat transfer inside the tubes, hence decreasing receiver surface temperature and reducing thermal losses. The thermal stress limit is also lifted with higher velocity, which subsequently benefits the optical performance as the flux on the receiver surfaces can be higher, and the interception efficiency increases. The pumping power increases with increased flow velocity due to pressure drops. However, pressure drops in the receiver tubes are typically low compared to the hydrostatic pressure at the bottom of the tower and are neglected in this simplified design method. Constraints on the upper limit of HTF velocity, caused by erosion and corrosion considerations, have more impact on design.

For a liquid sodium receiver, the HTF velocity should not exceed 2.44 m/s to avoid corrosion according to the "Sodium and Na-K Handbook" [154]. For given receiver height, diameter, tube wall thickness, tube outer diameter and tube spacing, the following simplified heat transfer model evaluates the maximum velocity for a range of the number of banks and flow-path considerations to determine the ones that respect the velocity upper limit threshold. First, the maximum power to the receiver in one flow path is approximated from:

$$\dot{Q}_{\text{net,fp}} = \frac{N_{\text{hst,max}}}{N_{\text{hst,tot}}} \dot{Q}_{\text{net}} \quad (5.3)$$

where $N_{\text{hst,tot}}$ represents the total number of heliostats. The field layout is divided into several field sectors, with heliostats within each field sector aiming to the corresponding tube bank. The number of heliostats is different in different sectors, and $N_{\text{hst,max}}$ points to the flow path with the maximum number of heliostats in corresponding field sectors.

The flow velocity (v_{estim}) is then evaluated as follows:

$$v_{\text{estim}} = \frac{\dot{Q}_{\text{net,fp}}}{(h_{\text{out}} - h_{\text{in}}) N_t \rho_{\text{out}} \pi / 4 (D_0 - 2\delta_{\text{th}})^2} \quad (5.4)$$

where h and ρ are the enthalpy and density of the HTF. The subscript "in" and "out" represent the properties at the inlet and outlet of the flow path. The density at the output is chosen because the temperature of the HTF is the highest, leading to the lowest density, resulting in the highest possible velocity. N_t is the number of tubes

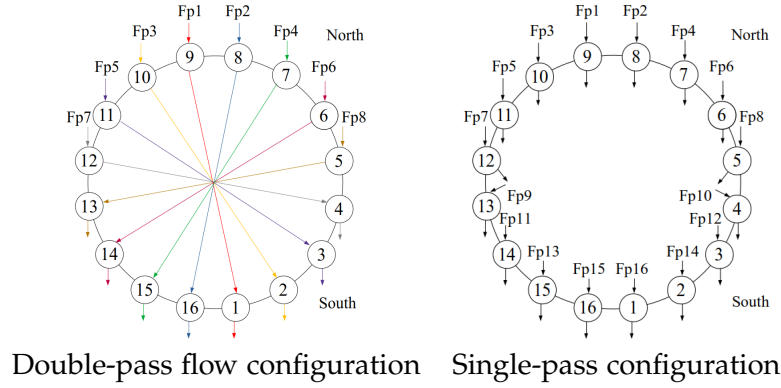


Fig. 5.4: Flow path configuration of the receiver. For the double pass configuration, flow exiting a first tube bank then crosses the cylinder to enter the tube bank diametrically opposite (noting there is no interconnection between pipes at the centre of the cylinder, despite the arrows in this figure crossing each other at that point). Each flow path is plotted with a unique colour in the double-pass configuration to help the illustration.

per tube bank and can be calculated from:

$$N_t = \left\lceil \frac{D_{\text{rec}} \sin(\pi/N_b)}{D_0 + \delta_s} \right\rceil \approx \frac{\pi D_{\text{rec}}/N_b}{D_0 + \delta_s} \quad (5.5)$$

Approximating the width of the receiver banks by assuming a circular base perimeter divided by the number of tube banks, neglecting the influence of the tube thickness and spacing and assuming the field has the same number of heliostats in all directions leads to:

$$v_{\text{estim}} \propto \frac{N_b}{N_{\text{fp}} D_{\text{rec}} D_0} \quad (5.6)$$

Acknowledging the simplifications mentioned above, Eq. 5.6 shows the flow velocity is proportional to the number of passes per flow-path (N_b/N_{fp}) and inversely proportional to the receiver diameter and the pipe diameter.

Equations 5.3 – 5.5 are used to determine values of N_b , N_{fp} and D_0 that lead to v_{estim} remaining below the velocity upper limit. From these candidate configurations, choices can be made based on, for example, least number of banks, flow-paths, tubes, etc., to select a receiver design.

In this study, the application of the flow-path determination method leads to the two options presented in Figure 5.4. Although the double-pass (Figure 5.4 (a)) configuration leads to higher flow-velocity in the pipes, it was recommended during discussions with a receiver manufacturer to reduce the number of flow-path crossings, and thus the single-pass option is preferred here (Figure 5.4 (b)).

With a single-pass flow path, the velocity is mainly determined by the receiver diameter and the pipe diameter. The velocity is firstly calculated using equations 5.3 - 5.5, then the pipe outer diameter is chosen as the one that maximises the velocity and also satisfies the flux limit at a given receiver diameter.

5.3.5 Aiming strategy

The MDBA method is proposed in Chapter 4 for heliostat aiming using three parameters E , A and S . The definition of the aiming parameters can be reviewed in Section 4.4, and Section 4.5.1 introduces methods to determine MDBA parameters. In this study, determining the parameters that control the heliostat aim point strategy is accelerated via two simplifications. Firstly, it was observed that the aiming strategy established with the MDBA parameterisation does not dramatically change from the design point configuration when simulating other conditions. Therefore, the aiming strategy optimised for design point can be applied to other sun positions without a significant difference in efficiency. The second simplification relates to the determination of the design point strategy. Here, the acceleration of the process is obtained by only adjusting the aiming extent E of the MDBA method using the search algorithm while keeping the asymmetry factor A and the shape exponent S unchanged. This typically halves the number of simulations required. Based on our experience using the MDBA method, the suggested value for A is 0.67 for all northern banks and 0.33 for all northern banks. The shape exponent S is set to be 1.5 for all banks.

To illustrate the impact of these simplifications, Table 5.2 presents the results obtained at three sun positions on the reference system: summer solstice solar noon (SS), winter solstice solar noon (WS) and summer solstice solar noon +3h (SS +3h). The solar-to-thermal efficiency (η_{st}) is defined as:

$$\eta_{st} = \eta_{field}\eta_{rec} \quad (5.7)$$

where η_{field} and η_{rec} are the efficiency of the heliostat field and the receiver, respectively. The largest deviation of the solar-to-thermal efficiency using the simplified aiming strategy at design point is less than 0.3% compared to the aiming strategy optimised at the corresponding sun position, which we believe is acceptable. It is noted that the more computationally expensive "optimised" method of determining the heliostat aim points can run to confirm best-case efficiencies.

Table 5.2: Comparison of system efficiencies between an "Optimised" aiming strategy at three design points and a fixed "Design point" aiming strategy that is optimised only for design point (equinox solar noon). "SS", "WS" and "SS +3h" refer to summer solstice solar noon, winter solstice solar noon and summer solstice solar noon +3 hours, respectively. η_{st} is the solar-to-thermal efficiency.

Sun position	Aiming strategy	$\eta_{field}(\%)$	$\eta_{rec}(\%)$	$\eta_{st}(\%)$
SS	Optimised	64.3	88.4	56.8
	Design point	64.4	88.4	56.9
WS	Optimised	59.0	85.1	50.2
	Design point	58.8	85.0	49.9
SS +3h	Optimised	59.4	87.0	51.6
	Design point	59.4	87.0	51.6

5.3.6 Annual receiver performance

The annual receiver efficiency can be obtained by solving the detailed receiver energy balance at each time step, but this requires a high computational load. Acceleration of the receiver annual performance estimation is obtained through the use of the accurate reduced-order model introduced in Section 2.3.2.

A series of carefully selected time points are used to generate a database containing receiver performance information. After obtaining the receiver efficiency look-up table (RELT), the receiver output is estimated using the loss-breakdown or direct regression method (see Section 2.3.2). Table 5.3 shows the correlation coefficients in Eq. 2.15 to 2.18 for both methods. For comparison, a full year simulation is run with the detailed receiver model and both simplified models on the reference system. The results are illustrated in Table 5.4. The relative differences in annual receiver efficiency are 0.4% and 0.1% for the direct regression and loss-breakdown methods, respectively, compared to the full year detailed model results. The direct regression method is less accurate than the ANN model in Schöttl et al. [56], which demonstrates that a simple regression on the receiver output cannot capture the complex behaviour of a receiver. However, the accuracy of the model based on a breakdown of the losses is identical to the work by Schöttl et al. [56] and only requires on the order of 200 simulations. This result suggests that the use of an ANN and the reportedly necessary over 1000 epochs of training and validation could be counter-productive for this task.

Table 5.3: Correlation coefficients in Eq. 2.15 to 2.18 for the reference case.

Coeff	Value	Coeff	Value	Coeff	Value	Coeff	Value
C_0	9.4543e+02	C_4	7.6078e-04	C_9	9.5340e+02	C'_0	-6.2820e+01
C_1	2.8128e-02	C_5	-3.5378e-02	C_{10}	2.2728e-02	C'_1	9.8257e-01
C_2	-1.6475e-03	C_6	5.9290e-01	C_{11}	-1.8794e-03	C'_2	2.5953e-02
C_3	6.7593e-02	C_7	-9.3710e-01	C_{12}	8.0156e-02	C'_3	-2.3848e+00
		C_8	9.2676e+00				

Table 5.4: Verification of the annual receiver models. The relative deviation is calculated with results from hour-by-hour simulations as reference.

Case	Annual receiver output (GWh)	Deviation	Number of simulations
Hour-by-hour simulations	1221.8	\	>3000
Loss-breakdown	1220.3	0.1%	~200
Direct regression	1217.5	0.4%	~200

5.3.7 Integration with system-level simulation

The OELT and RELT are imported into a system-level model to predict the annual energy output, component cost and LCOE of the plant based on full-year simulations. The system-level model was written using the Modelica language and is available as

part of SolarTherm, a computational tool that combines Modelica classes and external Python subroutines to perform a techno-economic evaluation of solar thermal systems [121]. The system-level model is based on the model described by Fontalvo et al. [153] and has been verified based on the SAM software [111], as introduced in Section 2.4.

5.3.8 Techno-economic model

Cost assumptions are essential for techno-economic co-optimisation. The cost models are consistent with the work of Coventry et al. [162] and Fontalvo et al. [153]. The cost functions for the field, receiver and tower are introduced, and the cost for other system components can be referred to in the publications by Coventry et al. [162] and Fontalvo et al. [153] and Github¹.

The cost functions used for the heliostat field (C_{field}) is introduced:

$$C_{\text{field}} = \beta_{\text{field}} A_{\text{field}} \quad (5.8)$$

where β_{field} represents the cost per square meter of the total reflective area of the heliostat field, and A_{field} is the total reflective area of the heliostat field. The receiver cost function follows the method of Kelly et al. [171]:

$$C_{\text{rec}} = C_{\text{rec, fixed}} + C_{\text{rec, size}} \times \frac{D_{\text{rec}}}{D_{\text{rec, ref}}} \times \left(\frac{H_{\text{rec}}}{H_{\text{rec, ref}}} \right)^{0.6} \quad (5.9)$$

where $C_{\text{rec, fixed}}$ is the receiver fixed cost, $C_{\text{rec, size}}$ is the size-dependent cost, $D_{\text{rec, ref}}$ and $H_{\text{rec, ref}}$ are dimensions of the reference receiver. The tower cost function is taken from SAM [111] as follows:

$$C_{\text{tower}} = C_{\text{tower, fixed}} \times \exp(aH_{\text{tower}}) \quad (5.10)$$

where $C_{\text{tower, fixed}}$ is the fixed tower cost and a is the scaling exponent. The values of all coefficients and their reference sources are summarised in Table 5.5. The system-level model is able to return the LCOE value after annual simulation and cost function evaluations.

5.3.9 Optimisation algorithm

Genetic algorithms (GA) have been successfully applied for heliostat field and receiver design [42] and one such algorithm, JEGA [173], is used in this work. The JEGA implementation used is the one found in Dakota [164] by Sandia National Laboratories. The flowchart of the optimisation method is illustrated in Figure 5.2. The population size is fixed as 50 per generation. The crossover rate is 0.8, and the mutation rate is 0.2. The optimisation ends if the number of generations reaches 50, and

¹Solartherm: <https://github.com/SolarTherm>, branch: 'cooptimisation'

Table 5.5: Cost function parameters and references.

Parameters	Units	Values	Reference
β_{field}	(USD/m ²)	75	DoE 2020 SunShot target [172]
$C_{\text{rec, fixed}}$	(USD)	4780420	Abengoa [171]
$C_{\text{rec, size}}$	(USD)	35400613	
$D_{\text{rec, ref}}$	(m)	20	
$H_{\text{rec, ref}}$	(m)	18.4	
$C_{\text{tower, fixed}}$	(USD)	3000000	SAM relationship [111]
a		0.0113	

the configuration with the best ever performance is the optimal one [173]. A sensitivity study in later sections confirms the convergence of the optimisation problem within 50 generations. The main disadvantage of using GAs is the high number of evaluations required, especially when each objective function evaluation takes a long time, which is the case here with the annual performance estimation based on ray-tracing. In the test cases presented in the following section, one objective function evaluation involves 64 ray-tracing simulations, around 200 receiver thermal simulations and one annual simulation. Overall this process takes about 0.5 hours using a desktop PC with an Intel i7 processor and 16 GB Ram. To accelerate the optimisation, the optimisation is executed on Gadi, the supercomputer of the Australian National Computational Infrastructure (NCI) at ANU. Parallel computing of different configurations in each generation leads to large gains in wall time. A typical co-optimisation case takes more than 700 CPU hours on Gadi and is completed within 72 hours of wall time.

5.4 Results and discussion

5.4.1 Design parameter space

The co-optimisation method is used for two objective functions: maximisation of annual solar-to-thermal efficiency and minimisation of LCOE. The efficiency-based optimisation aims to enhance the performance of the field-receiver subsystem, while the LCOE-based optimisation also considers the economic aspect. The optimised parameters include the radial spacings for zone 2 (Δr_2) and zone 3 (Δr_3) of the heliostat field, the receiver height (H_{rec}), the receiver diameter (D_{rec}) and the tower height (H_{tower}). The parametric ranges of these variables are shown in Table 5.6. Notably, the tower height (H_{tower}) is only included as an optimisation parameter in the LCOE-based optimisation. The lower boundary of radial spacings is chosen as the densest possible and equal 0.866. The upper boundary is larger than that in the study of Colorado and Guallar [39] because the tower heights considered in this study are lower. The boundaries of the receiver diameter are chosen to get an interception efficiency between 95% and 99% for the reference case of equatorial aiming. The parametric boundaries of the receiver height are determined based on an aspect ratio of 1.2 as

suggested by Zavoico et al. [174].

Table 5.6: Parameter space of the optimisation. 'LB' and 'RB' represent the lower and upper boundaries. Notably, the tower height (H_{tower}) is only included as an optimisation parameter in the LCOE-based optimisation.

Parameters	Δr_2	Δr_3	$D_{\text{rec}}(\text{m})$	$H_{\text{rec}}(\text{m})$	$H_{\text{tower}}(\text{m})$
LB	0.866	0.866	13	16	150
UB	1.2	2.4	23	28	250

5.4.2 Optimisation for maximum annual solar-to-thermal efficiency using the reference tower height

The optimisation is firstly performed at the reference tower height (175 m) to maximise the annual solar-to-thermal efficiency ($\eta_{\text{a,st}}$). The optimisation leads to an optimal configuration with $\Delta r_2 = 1.05$, $\Delta r_3 = 2.28$, $D_{\text{rec}} = 18.2$ m and $H_{\text{rec}} = 20.1$ m. The progress of the objective function at different generations of the genetic algorithm is shown in Figure 5.5. The average and best values of the objective function grow gradually to the optimal value. The performance of all systems in the final generation is very similar, with less than 0.1% difference between the maximum and average objective functions. The evolution of the values related to four variables in each generation is shown in Figure 5.6. The grey dots represent all values of the corresponding parameters on the generation while the red triangles represent the best values. The optimal values of the variables remain unchanged as the optimisation problem approaches convergence.

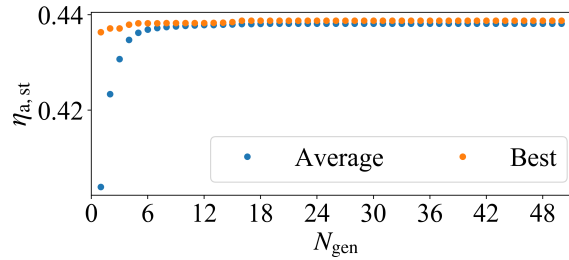


Fig. 5.5: Progression of the optimisation. 'Average' and 'Best' means the average and best values of the objective function within each generation.

A sensitivity study is performed in which each design parameter is varied with a factor of 0.8 to 1.2 from the optimised value to evaluate and confirm the optimisation results. The sensitivity study is performed sequentially for the four parameters, and other parameters are kept as the optimum when one parameter is varied. As seen from Figure 5.7, the annual solar-to-thermal efficiency always drops with deviation from the optimised parameters at last within the local region, which indicates the optimisation correctly identifies optimal values for each parameter. Figure 5.7 is also useful for highlighting the performance trade-offs between different energy loss mechanisms. The field efficiency increases with increased receiver dimensions

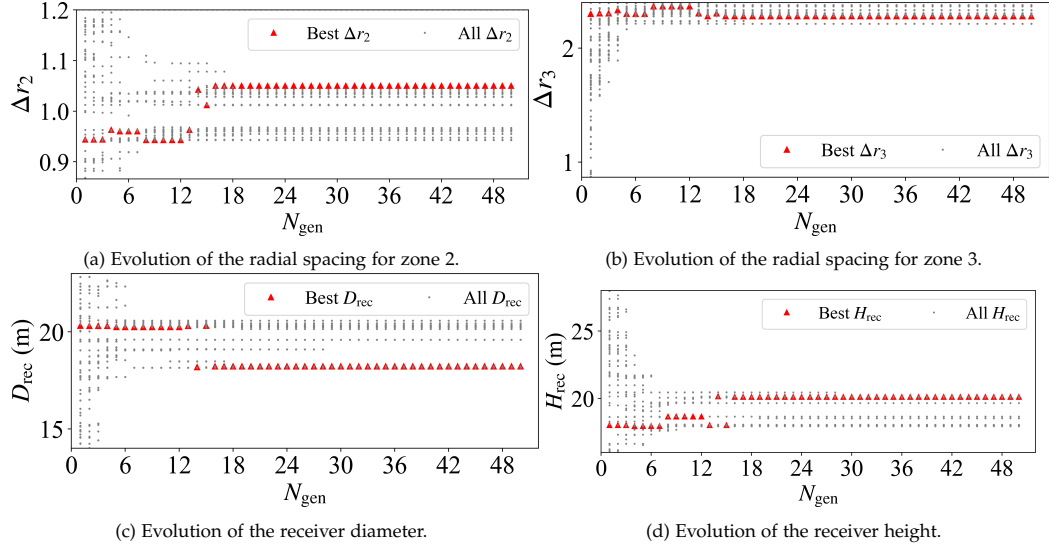


Fig. 5.6: Evolution of the optimised variables. The grey dots represent all values of the corresponding parameters on the generation while the red triangles represent the best values.

due to higher interception efficiency, while the increase of the receiver surface area results in higher thermal losses and lower receiver efficiency. The performance is more sensitive to variation of receiver diameter than height. This is because the aiming strategy is vertically adjusted as the receiver dimension changes, which means that the heliostats can be aimed such that interception efficiency is maintained as receiver height is reduced. The same is not valid for the change of receiver diameter, which directly affects the interception efficiency of far away heliostats that the aiming strategy cannot improve. The receiver efficiency is not sensitive to field expansion, but an optimal field efficiency appears with changing radial spacing because of the well-known trade-off between the various sources of optical losses. The shading and blocking losses are lower with a less dense layout, while the attenuation and spillage losses increase. Overall, the model and optimisation methods behave as expected.

The optimised field layout for the performance-optimal case at the reference tower height is shown in Figure 5.8. The field is composed of 6798 heliostats. The optimised value of Δr_3 is larger than Δr_2 because the farther zone is more widely expanded to alleviate the shading and blocking effects. The annual field efficiency is 51.1%, and the field efficiency at design point is 62.0%.

The flux and temperature distributions of the receiver at design point are shown in Figure 5.9. The flux distribution is non-uniform in both axial and circumferential directions. The flux is higher at the top than the bottom for all tube banks because of the vertically asymmetric distribution of aiming points from the MDBA method. More heliostats are aimed towards the HTF inlet of the bank (the upper part in this case), where the temperature is lower, and the flux limit is higher. The temperature rises more rapidly along the flow path for northern banks due to stronger incident power. The optimal tube outer diameter is 33.40 mm. The annual receiver efficiency is 85.5%, and the receiver efficiency at design point is 88.9%.

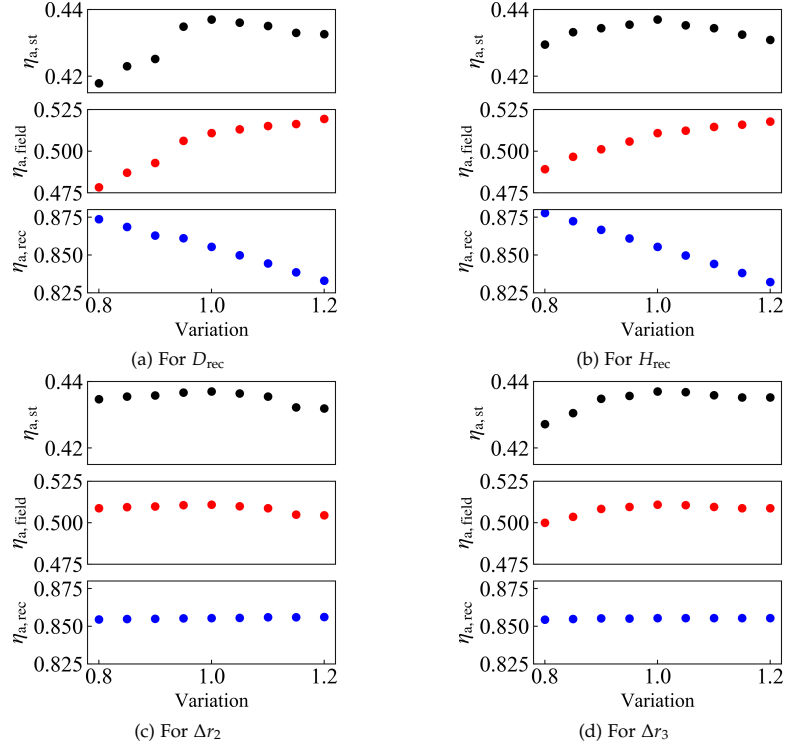


Fig. 5.7: Sensitivity of the system efficiencies to relative variation of optimised variables.

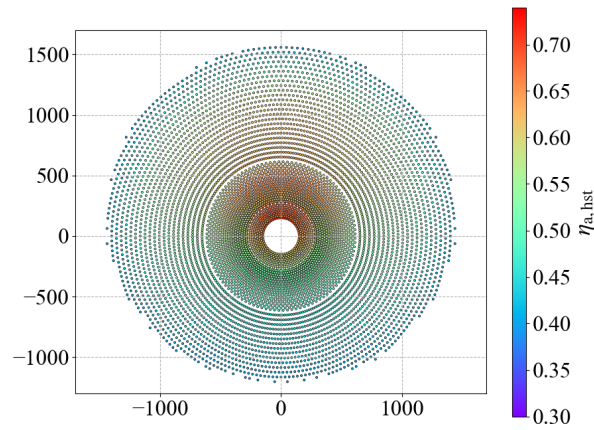


Fig. 5.8: The optimal field layout that achieves the highest annual solar-to-thermal efficiency for a 175m tower height.

The flux profiles for all flow-paths of the efficiency-optimised case are shown in Figure 5.10. After applying the simplified aiming strategy, the net flux is successfully maintained below the safe limit for all tube banks. The excellent match between the flux limit and the net flux trend on all 16 flow paths highlights the adequacy of the simplified aiming strategy if the initialised values for the asymmetric factor and the shape exponent are well-calibrated. The design point interception efficiency is 96.6%, 0.2% lower than for the equatorial aiming limit.

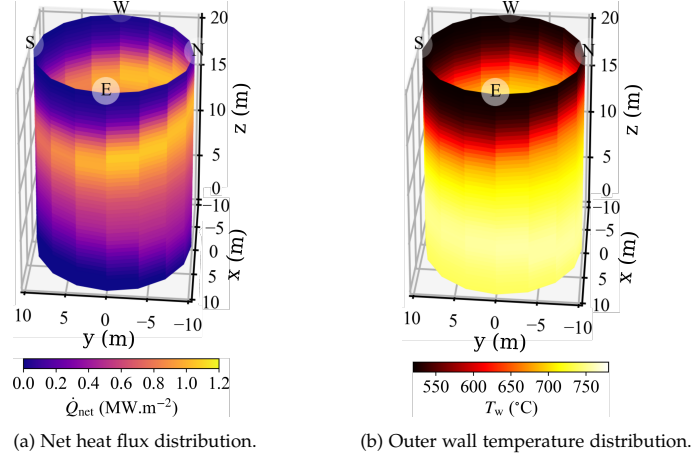


Fig. 5.9: Net heat flux and outer wall temperature profiles at design point of the optimal receiver that achieves the highest annual solar-to-thermal efficiency for a 175 m tower height.

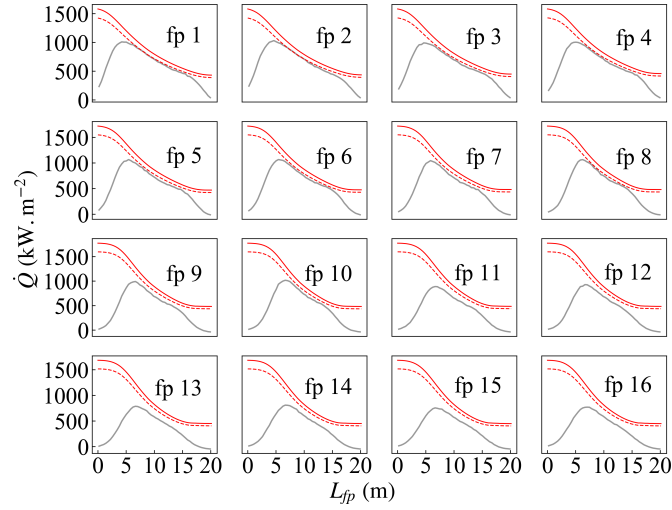


Fig. 5.10: Flux profiles along the flow-paths. Red solid lines represent the flux limit and dashed lines the safe limit. Grey solid line represents the net flux. The safe limit is defined as 0.9 of the flux limit. The index of the flow path corresponds to the single-pass configuration as shown in Figure 5.4.

In summary, an optimal configuration of the sub-system is generated after implementing the co-optimisation method. The field layout, receiver dimension and the aiming strategy are all determined from this single optimisation. The net flux is controlled below the flux limit, guaranteeing the receiver's safety.

5.4.3 Comparison with optimisation at instantaneous condition

The above section applies the annual solar-to-thermal efficiency ($\eta_{a,st}$) as the objective function in the co-optimisation. This section implements field and receiver co-optimisation at design point (equinox solar noon) to investigate the difference of optimised configurations based on instantaneous and annual conditions. The input parameters remain unchanged and are initialised as shown in Table 5.6. In the instantaneous optimisation, a large field is generated and trimmed based on the heliostats' efficiencies at design point. The receiver flow configuration is then determined, and MDBA is performed to determine the receiver output while satisfying receiver flux and velocity limits. The solar-to-thermal efficiency (η_{st}) is returned to the GA for optimisation.

The optimised configuration at design point is illustrated in Table 5.7. The design-point optimisation leads to a larger receiver diameter compared to the annually optimal case. This is explained with the optimised heliostat field, as shown in Figure 5.11. At the design point of equinox solar noon, the field is more polar-like compared to the annually optimal field in Figure 5.8. The reason is that more northern heliostats with high efficiencies are selected at design point. A polar-like field provides higher incident power to northern banks, which results in a larger receiver diameter to satisfy receiver limits. For the performance, the design-point optimal case has a higher annual field efficiency but lower annual receiver efficiency because of the large receiver dimension. The overall effect is that the annual solar-to-thermal efficiency is 0.4% lower than the optimal case based on annual conditions.

Table 5.7: Comparison of the optimal configurations based on design point and annual performances.

Cases	Δr_2	Δr_3	$D_{rec}(m)$	$H_{rec}(m)$	$\eta_{a,field}$	$\eta_{a,rec}$	$\eta_{a,st}$
Design point optimum	0.91	2.25	19.64	20.17	51.3%	84.5%	43.3%
Annual optimum	1.05	2.28	18.20	20.10	51.1%	85.5%	43.7%

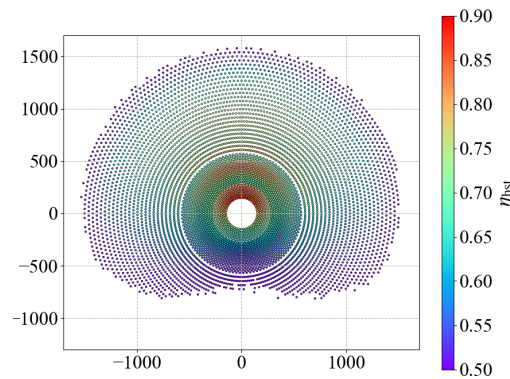


Fig. 5.11: The optimal field layout that achieves the highest design-point solar-to-thermal efficiency for a 175 m tower height. The colour-bar represents the instantaneous optical efficiency of each heliostat.

5.4.4 Optimisation for maximum annual solar-to-thermal efficiency using a range of tower heights

The tower height (H_{tower}) dramatically affects the optical efficiency of the heliostat field. To study its effect, the subsystems are co-optimised for a range of different tower heights: 150 m, 175 m, 200 m, 225 m and 250 m (cases 1-5). The results are shown in Table 5.8, noting that the LCOE results discussed in the following section are also included.

Table 5.8: Co-optimisation results for different cases. Cases 1 to 5 represent performance-based optimised cases with fixed, but increasing tower height. Case 6 is an LCOE-based optimised case, where tower height was a parameter in the optimisation.

Case	Reference case	Case 1	Case 2	Case 3	Case 4	Case 5	Case 6
$H_{\text{tower}} (m)$	175	150	175	200	225	250	173.1
$D_{\text{rec}} (m)$	16.0	18.9	18.2	19.1	20.7	21.5	16.8
$H_{\text{rec}} (m)$	24.0	18.8	20.1	19.8	18.3	19.3	16.6
Δr_2	/	1.00	1.05	1.01	1.00	1.01	1.17
Δr_3	/	2.40	2.28	2.13	2.09	2.07	2.27
N_{hst}	6764	7213	6795	6493	6346	6223	7130
$E_{\text{ele}} (\text{GWh})$	565.6	585.4	582.7	572.2	567.5	559.7	590.5
$C_{\text{field}} (\text{MUSD})$	75.5	80.5	75.9	72.5	70.8	69.5	80.1
$C_{\text{rec}} (\text{MUSD})$	38.0	38.6	38.8	40.1	41.3	43.9	32.8
$C_{\text{tower}} (\text{MUSD})$	21.7	16.3	21.7	28.7	38.1	50.6	20.4
$C_{\text{cap}} (\text{MUSD})$	487.7	491.8	490.8	493.5	501.5	516.2	488.3
$\eta_{\text{a,field}} (\%)$	50.4	48.2	51.1	52.7	53.6	54.6	47.5
$\eta_{\text{a,rec}} (\%)$	84.4	85.9	85.5	85.0	84.9	83.8	88.2
$\eta_{\text{a,st}} (\%)$	42.6	41.4	43.7	44.8	45.6	45.8	41.9
LCOE (USD/MWh)	62.4	60.9	61.0	62.3	63.6	66.0	60.0

As seen in Table 5.8, a higher tower height leads to an improvement in annual field efficiency but a marginal drop in receiver efficiency, leading to an improvement in annual solar-to-thermal efficiency. From the heliostat field perspective, the optimal Δr_2 is insensitive to tower height, while the optimal Δr_3 decreases for a higher tower. To better explain the trade-offs, the breakdown of annual energy losses are shown in Figure 5.12. Even though the field is denser with a higher tower, the shading and blocking losses are still lower. The attenuation loss is also reduced for a higher tower height. The total energy to the heliostat field is reduced with the increase of the tower height, although the energy to the receiver is similar. The reason is that the required heliostat reflective area is reduced with higher field efficiency under higher tower height.

Figure 5.13 shows the optimised field layout for a tower height of 250 m. The field becomes more polar-like for higher towers, as shown in Figure 5.13 with Figure 5.8. This is because the efficiency gain for northern-located heliostats is higher than southern heliostats when the tower height increases, hence more heliostats to the north are selected.

As tower height increases, the optimal receiver diameter increases and decreases.

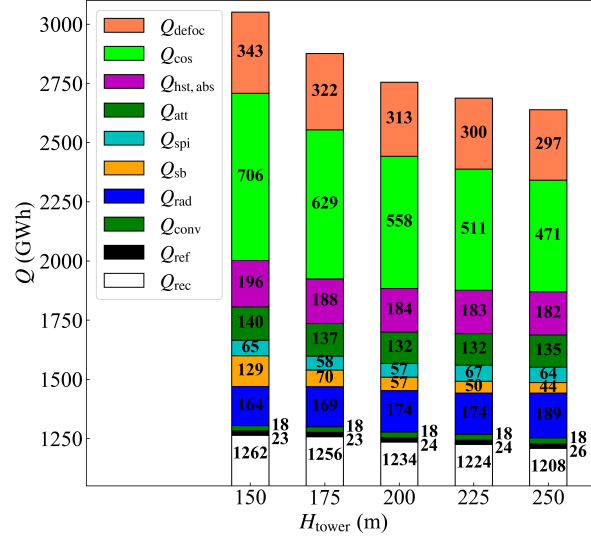


Fig. 5.12: Heliostat field and receiver breakdown of annual energy losses. The definitions of all energy losses can be found in Chapter 2. Q_{defoc} is the total accumulated value of all defocused losses.

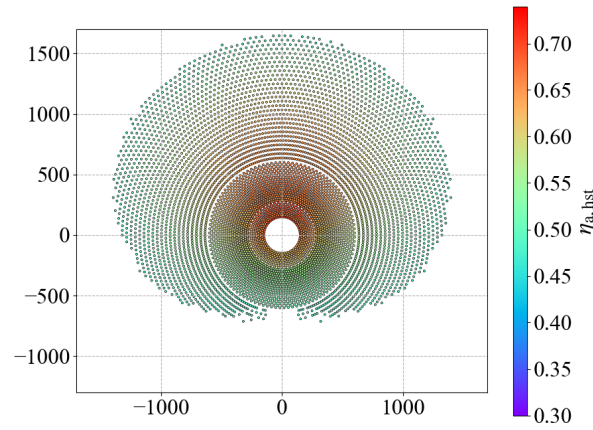


Fig. 5.13: Optimised field layout for a tower height of 250 m.

As the tower height is increased from 150 m to 175 m, the number of heliostats is reduced by 6.1%, and the field is more compact, such that a smaller receiver diameter does not result in excessive spillage loss. However, when the tower height is further increased, the field becomes more polar-based; hence northern banks suffer more from high incident flux which causes HTF velocity to go beyond the maximum design value. In order to keep the velocity under the limit, the receiver diameter is increased (per Eq. 5.6).

Notably, the aspect ratio of the optimal receivers is lower than 1.1, which is different from that of a conventional molten salt receiver. The high-temperature receivers need lower receiver heights to reduce thermal losses. Large diameter is favoured by the optimisation because the spillage losses strongly depend on the diameter.

5.4.5 Optimisation for lowest LCOE

The co-optimisation method is used to minimise the LCOE followed by a sensitivity study on the impact of the cost assumptions. The design variables include Δr_2 , Δr_3 , H_{rec} , D_{rec} and H_{tower} .

The LCOE-based optimal case (case 6) is compared with the reference case and the efficiency-based optimal cases at the reference tower height (case 2), as shown in Table 5.8. The reference case system originally had a tower height of 175 m. As it turns out, the LCOE-optimised case results in a tower height of 173 m, very close to the selected reference case tower height. Therefore, it is possible to discuss three cases with similar tower heights: the reference case, the performance-optimised case at the reference tower height, and the LCOE-optimised case. The field layout for the LCOE-optimised case is shown in Figure 5.14. The higher efficiency configuration (case 2) has a smaller heliostat field with a denser second zone than the LCOE-optimised one, resulting in a significantly higher annual efficiency (3.6%) and 5.2% lower field cost. The receiver in the LCOE-optimised case is significantly smaller, has 2.7% higher efficiency and 15.5% lower cost, at the expense of increased spillage from the field. Overall the solar-to-thermal efficiency of the efficiency-optimised case is 1.8% above the LCOE-optimised one but actually shows a 1% lower capacity factor. The field of the LCOE-optimised case is able to deliver more energy to its receiver than the performance-optimised field does in a range of off-design sun positions, and therefore increases the annual operating hours of the system. The reference system used design-point data to establish the receiver design and unsurprisingly shows a lower capacity factor and higher LCOE than both optimised systems and lower efficiency than the efficiency-optimised configuration.

The result of any techno-economic optimisation is affected by the cost assumptions. A sensitivity study is performed to analyse the effect of cost functions on the optimal configuration. Six new co-optimisation cases are investigated by varying the field, receiver and tower costs to a higher and a lower value by 25%, respectively. A Tornado chart (Figure 5.15) shows the sensitivity analysis results. The change of the field cost has the most impact on the LCOE. The cost assumptions affect the cost trade-offs between different components which determine the optimal configuration.

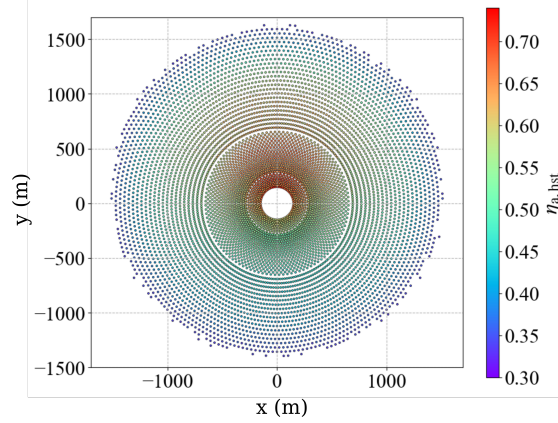


Fig. 5.14: The optimal field layout that achieves the lowest LCOE.

If the co-optimisation method is used in a techno-economic optimisation problem, it is suggested that a cost sensitivity study should also be included.

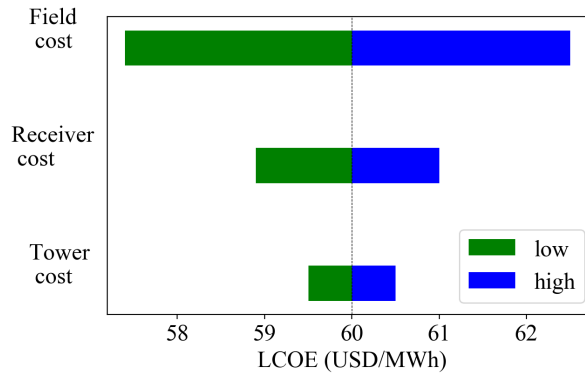


Fig. 5.15: Tornado chart showing sensitivity of LCOE to key components' costs. The optimised LCOE changes with adjusting the cost of each component by $\pm 25\%$.

5.5 Conclusion for this chapter

A co-optimisation method that simultaneously optimises the field, receiver and the aiming strategy based on annual operation conditions is presented. The method includes an integrated optical, thermal and mechanical model to simulate the heliostat field-receiver subsystem accurately while ensuring that the receivers' flux does not exceed allowable limits. A range of modelling and simulation acceleration methods are implemented and verified in order to make the optimisation problem computationally tractable, including:

- An accurate method to interpolate field efficiency results within a regular grid of discrete sun position simulations.

- A fast and accurate reduced-order model of receiver performance (the loss-breakdown method) that outperforms the widely used method of polynomial interpolation of receiver output.
- The implementation of MDBA, a heliostat field aiming method compatible with ray-tracing, along with key simplifications enabling thermo-mechanical flux limits to be considered for any receiver evaluated in the optimisation.

The co-optimisation method integrates a system-level model, which results in annual operations simulation for all evaluated CSP system configurations.

The proposed method is used to co-optimize a reference system with a surround field and a cylindrical external liquid-sodium receiver. The co-optimisation based on annual performance achieves a higher annual solar-to-thermal efficiency than when the co-optimisation is based on design-point performance. A higher tower can improve the solar-to-thermal efficiency but is not preferred by the LCOE-based optimisation due to the higher cost. Comparison of the results of maximum performance and minimum LCOE optimisations with previous work highlights the trade-offs involved in designing optimised CSP tower systems and confirms the good behaviour of the model.

Exploration of optimal receiver flow configurations with an oversized heliostat field

6.1 Introduction

Oversizing a heliostat field relative to the design-point capacity of a receiver has the benefit that consistently high irradiance levels can be maintained even under low DNI conditions, such as in winter or due to haze or light cloud [175]. This can increase the capacity factor and the annual energy yield of a concentrating solar power plant at the design stage. However, oversizing also means that there is a risk of exceeding safe operational limits, mainly concerning the flux, HTF temperature and velocity for tubular receivers. At peak hours, a few heliostats need to be partially defocused to avoid exceeding receiver limits. To mitigate the effects of under-utilisation and to obtain the maximum receiver thermal performance, it is necessary to develop a design and operational strategy whereby the receiver is operated under as high irradiance as possible, but without exceeding these safe operational limits. To do this, new methodologies are needed to quantify the thermal output while respecting the limits carefully. In this study, the MDBA method is further developed with a defocusing capability to determine the receiver output with an oversized field. MDBA is then integrated with a dynamic model in SolarTherm for annual simulations. As reviewed in Section 1.2.2.1, selection of the best flow configuration through tube banks is critical to design optimisation. The flow characteristics mainly include flow path options and pipe geometry. Effects of the receiver flow path pattern and pipe outer diameters are analysed to determine an optimal configuration. Notably, variation of the pipe outer diameters includes five standard values: 33.40 mm, 42.16 mm, 48.26 mm, 60.33 mm and 73.03 mm.

6.2 Physical models

The reference configuration comes from the performance-based optimal case at the reference 175m tower in the co-optimisation study (see Case 2 in Chapter 5.4.2),

but with the addition of an oversized heliostat field. The diameter and height of the receiver are 18.2 m and 20.1 m, respectively. The receiver has a single-pass configuration with outer pipe diameter of 33.40 mm. The system model is identical to the Gen3L system introduced in Chapter 2. SM , f_{HX} , t_{storage} are fixed as 2.5, 1.0 and 12 hours, respectively. The receiver nominal output is 543 MWth at design point. The capacity of the heliostat field is oversized by 20% relative to the performance-based optimal case ($f_{\text{hst}}=1.2$). It is noted that the oversizing factor is fixed as 1.2 in this chapter. The effect of varying f_{hst} will be investigated in Chapter 7.

6.3 Methodology

6.3.1 Generation of an oversized heliostat field

In determining the size of the heliostat field, a large (untrimmed) heliostat field is firstly determined from the radial spacings (Δr_2 , Δr_3) and a given number of heliostats. The number of heliostats for the large field ($N_{\text{hst,large}}$) is estimated as:

$$N_{\text{hst,large}} = \frac{Q_{\text{rec,inc}}}{A_{\text{hst}} \times DNI \times \eta_{\text{hst,estim}}} \times f_{\text{multiplier}} \quad (6.1)$$

where $\dot{Q}_{\text{rec,inc}}$ is the nominal input to the receiver calculated from Eq. 2.24. $\eta_{\text{hst,estim}}$ is an estimated average heliostat optical efficiency to calculate the delivered power at the receiver. With reference to simulated results from prior simulations (e.g. the instantaneous heliostat field efficiency in Table 5.2), $\eta_{\text{hst,estim}}$ is set at 0.6 in this study. As reported by Leonardi et al. [39] and Collado and Guallar [36], a large heliostat field is generated and then trimmed to reach the nominal output. The multiplier $f_{\text{multiplier}}$ is set at 130% to ensure that there are enough performing heliostats to choose from when trimming. The large field can then be generated based on the Campo code [39]. After the trimming process as introduced in Section 5.3.3, the oversized field is obtained, achieving the desired incident power to the receiver ($Q_{\text{rec,inc}}$).

6.3.2 Instantaneous and annual simulation methods

The simulation methods in this chapter are the same as described previously. Thus only the key points are recapped here. The optical simulation is executed in SOLSTICE [131]. The receiver model is from Asselineau [142] and thermal stress limits are evaluated using a model described by Logie et al. [143]. The maximum permitted flow velocity is 2.44 m/s for liquid sodium according to [154]. The system-level simulation is performed using SolarTherm [121] and is based on the model developed by Fontalvo et al. [153].

6.3.3 Improvement of MDBA for defocusing capability

With an oversized heliostat field, the MDBA method introduced in Chapter 4 may fail to find a solution that respects the flux limits by only adjusting the aiming points.

Some heliostats need to be fully defocused when there are too many heliostats. In this chapter, the MDBA method is further improved to quantify the receiver thermal output with an oversized field. Both instantaneous and annual adjustments are discussed in the following sections.

6.3.3.1 Definition of heliostat field defocusing

As introduced in Section 2.2.1, the instantaneous efficiency of a heliostat field is calculated from:

$$\eta_{\text{field}} = f_{\text{foc,A}} \eta_{\text{ope,field}} \quad (6.2)$$

where $f_{\text{foc,A}}$ is the focusing ratio, representing the fraction of the heliostat field area that is in operation. $\eta_{\text{ope,field}}$ is the optical efficiency of the operational part of the field, which includes the cosine, shading & blocking, heliostat absorption, air attenuation and spillage losses. The key modification to the MDBA method for the case of an oversized heliostat field is to determine $f_{\text{foc,A}}$ and $\eta_{\text{ope,field}}$ in order to quantify the receiver thermal output.

6.3.3.2 Instantaneous heliostat field defocusing

The receiver limits arise from factors including the HTF stability limits and thermo-mechanical stress limits in receiver tubes [88]. The limits for the reference sodium receiver in this work include the maximum allowable flux limit and the velocity limit. With an oversized heliostat field, extra power is applied to the receiver. It is possible that even with increasing the aiming extent (E) to 1.0, which means some heliostats aim at the receiver's edge, the limits still cannot be satisfied. A defocusing strategy has to be developed to remove some incident irradiance at the receiver by targeting parts of the heliostat field to a standby point. As mentioned by Schöttl et al. [176], heliostats far away from the receiver should be defocused, as close heliostats offer more flexibility in terms of aiming strategy due to their smaller focal spots.

Figure 6.1 illustrates the algorithm for the MDBA method with a defocusing strategy. The feedback-based method (described in Section 4.5.3) is firstly applied, and the defocusing strategy is activated once the aiming extent (E) reaches one. As previously, the field is divided up into sectors with corresponding tube banks (see Figure 4.6). In the defocusing strategy, the method is to rank heliostats by their focal lengths within each sector and defocus a fraction of furthest-away heliostats if the limits on the corresponding banks are exceeded. The fraction is defined as the defocusing fraction, calculated as the ratio of the number of defocused heliostats to the total number of heliostats in the sector. Heliostats in neighbouring banks are also defocused considering the interaction between sectors.

The defocusing fraction is an essential factor in the defocusing strategy. If the defocusing fraction is too large in one step, the algorithm converges too quickly and may miss the optimal output. Conversely, if the step size is too small, the computational speed is too low. Hence, a sensitivity analysis on the defocusing fraction

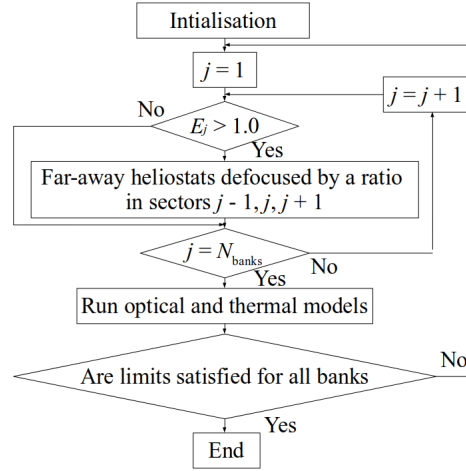


Fig. 6.1: Algorithm flowchart for the MDBA method with a defocusing strategy.

was implemented, and the defocusing fraction is chosen as 0.04 after finding the best trade-off between the achieved thermal output and the computational speed.

The reference case is simulated at design point (equinox solar noon) to test the algorithm in Figure 6.1. The results of the flux profile on each tube bank, the flow velocity and the heliostats' efficiencies are shown in Figure 6.2 and 6.3. Both the flux and velocity limits are satisfied. As shown in Figure 6.3, outer heliostats in several of the northern sectors of the heliostat field are defocused because, at design point, the total irradiance from these sectors results in limits relating to flux and velocity being exceeded. As can be seen by examining Figure 6.2(a), there is space between the net flux and flux limit curves after the defocussing. This is because the flow velocity is the dominant limit for this sun position. The defocusing procedure continued beyond the point where the flux limits were satisfied as the velocity limits were still exceeded. The iteration stops when all constraints are met, and in this case, the velocity requirements for banks 8 and 9 are the limiting case. The field utilisation ($f_{\text{foc,A}}$) is 90.7%, which means 9.3% of all heliostats are defocused. The receiver thermal output is 605 MWth, larger than the nominal output (543 MWth). This demonstrates the potentially higher output brought by the oversized heliostat field.

6.3.3.3 Heliostat field defocusing in annual simulations

The improved MDBA method can be used to calculate $f_{\text{foc,A}}$ and $\eta_{\text{ope,field}}$ at instantaneous conditions. However, it is impractical to do instantaneous simulations over a full-year range. The conventional annual optical simulation method is the 2D interpolation method as introduced in Section 2.3.1, which considers the effect of sun positions (λ, ω) on the optical efficiency. Clear-sky DNI is always applied in 2D interpolation methods. Nevertheless, the MDBA results are greatly affected by the DNI. Higher DNI means more incident power to the receiver, and more heliostats need to be defocused. Using clear-sky DNI may lead to less accurate results.

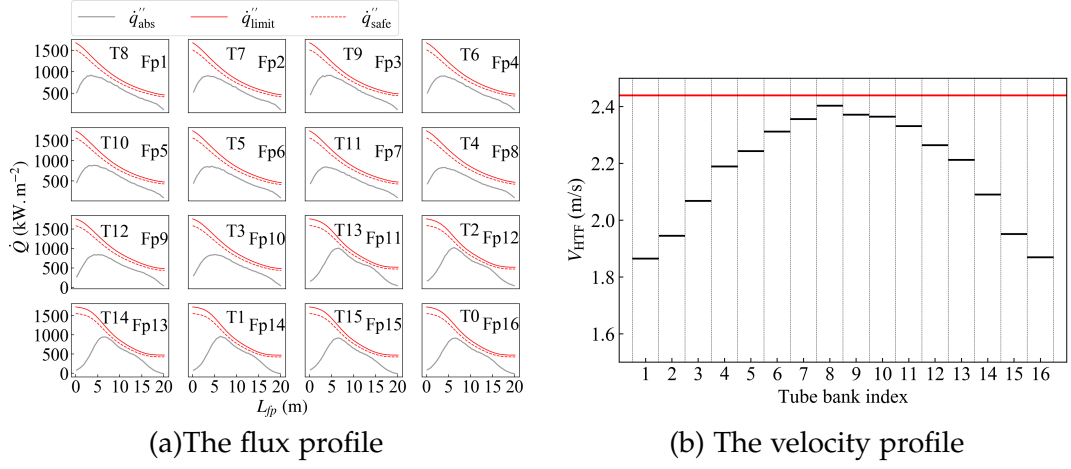


Fig. 6.2: Results after the optimisation for the reference case with a 20% oversized field.

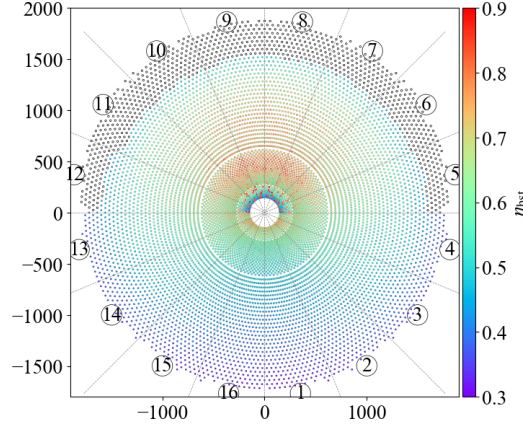


Fig. 6.3: The heliostat field after defocusing for the reference case with a 20% oversized field. Defocused heliostats are represented by grey dots.

A 3D interpolation method is proposed to take into consideration the effect of DNI. An illustration of the method is shown in Figure 6.4. The DNI ratio is defined as the ratio of the real DNI to clear-sky DNI at any given instant. The real DNI is obtained from the Typical Meteorological Year (TMY) file, and the clear-sky DNI is calculated from the Meinel model [147]. The MDBA method is implemented on discrete sun positions and different DNI ratios to generate the OELTs, as shown by the solid dots in Figure 6.4. In the annual simulation with the input of solar angles and the real DNI, the field efficiency is firstly interpolated based on solar angles, and then linear interpolation is used to obtain the results based on the DNI ratio. When evaluating parameters for DNI ratios outside of the simulated values, the interpolated results are constrained to either the upper or lower boundary, as applicable.

Selection of the simulated DNI ratios is essential for accurate interpolation. The cumulative distribution function of the DNI ratio along a year for Daggett is shown in Figure 6.5. The upper and lower boundaries are determined as 1.24 and 0.52,

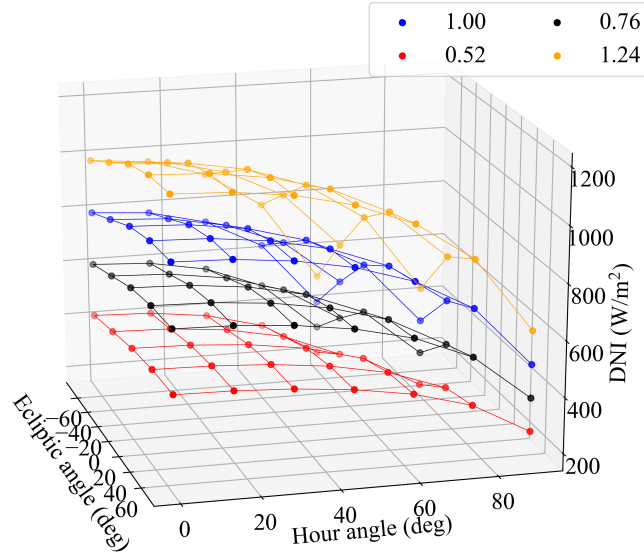


Fig. 6.4: Illustration of the DNI ratio. Optical simulations at different DNI ratios are represented by different colours illustrated in the legend. Defocused heliostats are represented by grey dots.

corresponding to the cumulative probability between 5% and 95%. A total of four OELTs are chosen, which correspond to DNI ratios of 0.52, 0.76, 1.00 and 1.24, as shown in Figure 6.4. The OELT generation starts from the highest DNI ratio. In generating the first OELT, the MDBA algorithm needs to be implemented at all discrete sun positions. For sun positions where the receiver limits are satisfied at the initial value of the aiming extent ($E = 0.5$), the initial aiming is sufficient to satisfy operational conditions with the highest DNI ratio and therefore can be applied to lower DNI conditions.

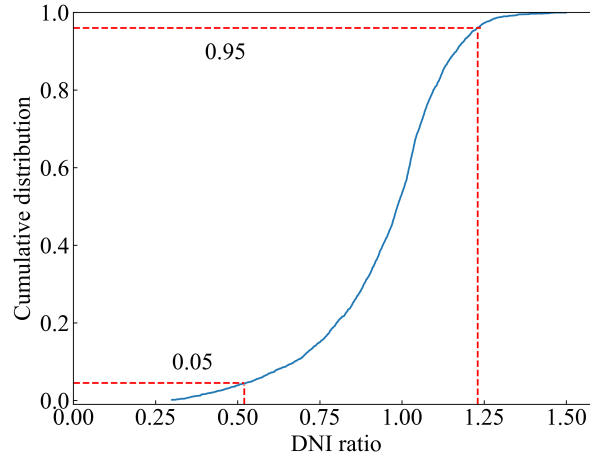


Fig. 6.5: Cumulative distribution of the DNI ratio at Daggett, CA.

To verify the 3D interpolation method, 12 example days, namely the 21st days of each month, are chosen for simulation. At each operational hour, the results obtained from the conventional 2D interpolation method and the 3D interpolation method are

compared with the directly simulated results. The comparison results are shown in Figure 6.6. The match of the simulated results with the 3D interpolated results is much better than the 2D interpolation method, which demonstrates that ignoring the DNI ratio leads to high deviations when examined on an hourly basis. In addition, the total incident power to the receiver over those 12 days is calculated for all three methods. Compared to the simulated results, the relative differences are 0.6% and 1.9% for the 3D interpolation method and the conventional 2D method, respectively, displaying the higher accuracy of the 3D interpolation method again.

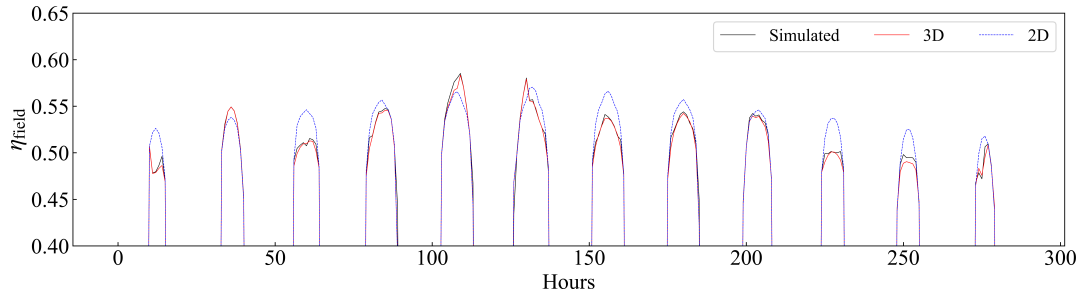


Fig. 6.6: Comparison of the simulated, 2D and 3D interpolated results.

In a summary, the MDBA method is improved for simulating the subsystems including an oversized heliostat field. The improved method can calculate the receiver output respecting operational limits at any given instant and can also be integrated into a 3D interpolation method for annual calculations.

6.4 Results and Discussion

The above instantaneous and annual modelling methods are used to investigate the optimal receiver flow path and pipe outer diameter for the reference system. Several options concerning the flow path are firstly studied, and then the effect of changing the pipe outer diameter is discussed. The goal is to achieve the highest receiver thermal output while respecting the operational limits.

6.4.1 Effect of different flow paths

Based on the discussion in Section 5.3.4, single-pass and double-pass are two possible options for the reference sodium receiver. The flow path pattern may vary in either case, with different connecting options between the tube banks. This study discusses several principles to select the optimal flow path pattern for a sodium receiver: the injection direction, the second-pass option and the east-west crossover option. The double-pass configuration is used to test the principles. The pipe outer diameter is chosen as 60.33 mm.

6.4.1.1 Investigation of the injection direction

Two patterns with different injection directions are discussed, as shown in Figure 6.7 (a) and (b). The HTF is injected from the north in Pattern 1 and from the south in Pattern 2 for all flow paths. Both patterns have the crossover design that requires the flow paths to cross from a panel on one receiver side to a panel diametrically opposite. The improved MDBA method calculates the optical efficiencies and the receiver thermal output for these two patterns at design point. The results (cases 1 and 2) are shown in Table 6.1.

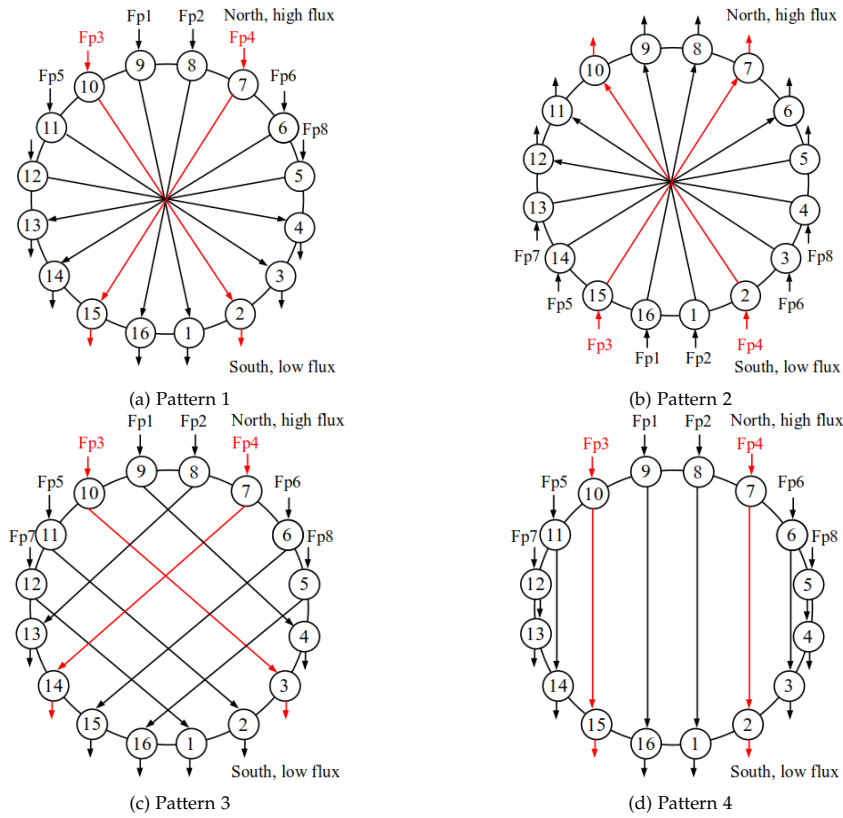


Fig. 6.7: Flow path patterns with double passes.

As shown in Table 6.1, a higher thermal output is achieved for Case 1 (injection from the north) than in Case 2 (injection from the south). Figure 6.8 plots the heliostats' efficiencies and flux limits after meeting receiver limits in both cases. In Case 1, both flux and velocity limits are satisfied without defocusing any heliostats. The achieved thermal output is 653 MWth, which is 20% higher than the nominal value (543 MWth). In Case 2, however, a significant fraction of northern heliostats are defocused. The reason is that in the northern banks, the HTF temperature is relatively high by the second pass and consequently has low flux limits. The overlap of high net flux and low flux limits causes the large fraction of heliostat defocusing in the northern regions. The thermal output is still higher than when the field is not oversized (543 MWth). This explains the benefit of the oversized field even with a

Table 6.1: Performance comparison of different cases of flow path. D_0 is the pipe outer diameter. \dot{Q}_{rec} is the receiver thermal output. Patterns 1 to 4 correspond to different flow path patterns in Figure 6.7. ‘SS +3h’ points to three hours after Summer Solstice (SS) solar noon. Cases 1 and 2 are compared in Section 6.4.1.1. Case 3 is mentioned in Section 6.4.1.2. Cases 4 to 8 are referenced in Section 6.4.1.3.

Case	Pattern	D_0 (mm)	Time	$f_{\text{foc,A}}(\%)$	$\eta_{\text{ope,field}}(\%)$	$\eta_{\text{rec}}(\%)$	$\dot{Q}_{\text{rec}}(\text{MW}_{\text{th}})$
1	1	60.33	Design point	100.0%	55.9%	89.7%	653
2	2			82.8%	57.9%	88.6%	554
3	3			92.2%	57.4%	89.2%	616
4	4			99.8%	55.9%	89.6%	652
5	1	60.33	SS + 3h	96.4%	55.9%	88.8%	564
6	4			95.6%	55.6%	88.7%	556
7	1	48.26	SS + 3h	86.9%	57.0%	88.3%	516
8	4			80.0%	57.3%	87.6%	474

badly-performing flow path direction, although the output is much lower than Case 1.

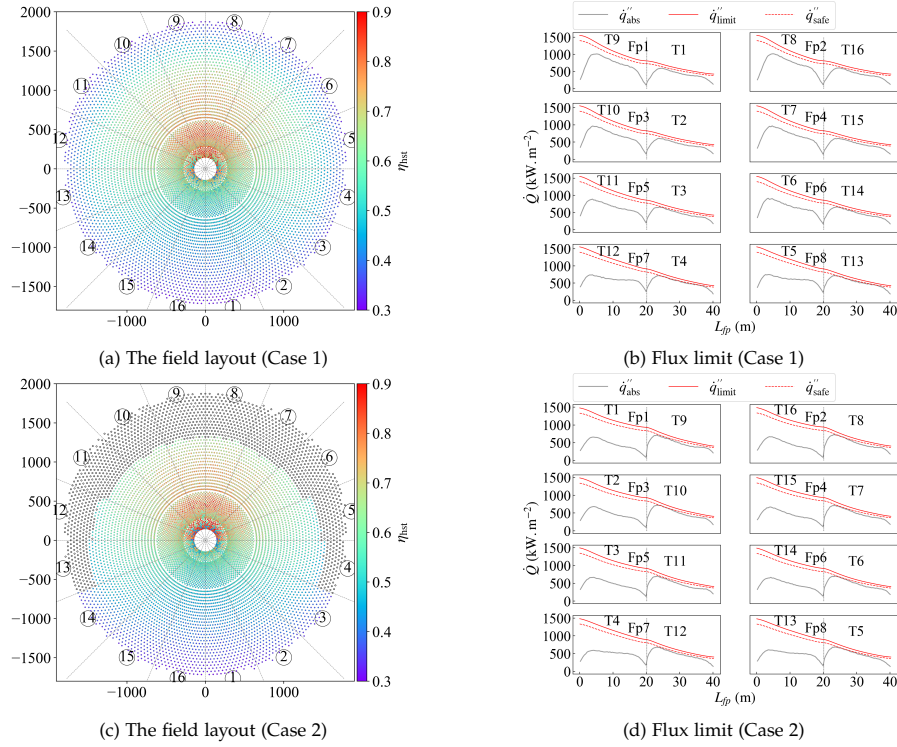


Fig. 6.8: Performance comparison with different injection directions.

This case study quantitatively confirms the conventional wisdom [50, 177] that the flow path should inject from the high-irradiance area and then flow to the lower-irradiance banks of the receiver. This corresponds to north injection for a plant located in the northern hemisphere. Figure 6.9 also shows the temperature profiles for the absorber surface temperature, internal pipe wall temperature and sodium

bulk fluid temperature for cases 1 and 2. It can be seen that temperatures rise more quickly when the HTF is injected from tubes with high irradiance in case 1.

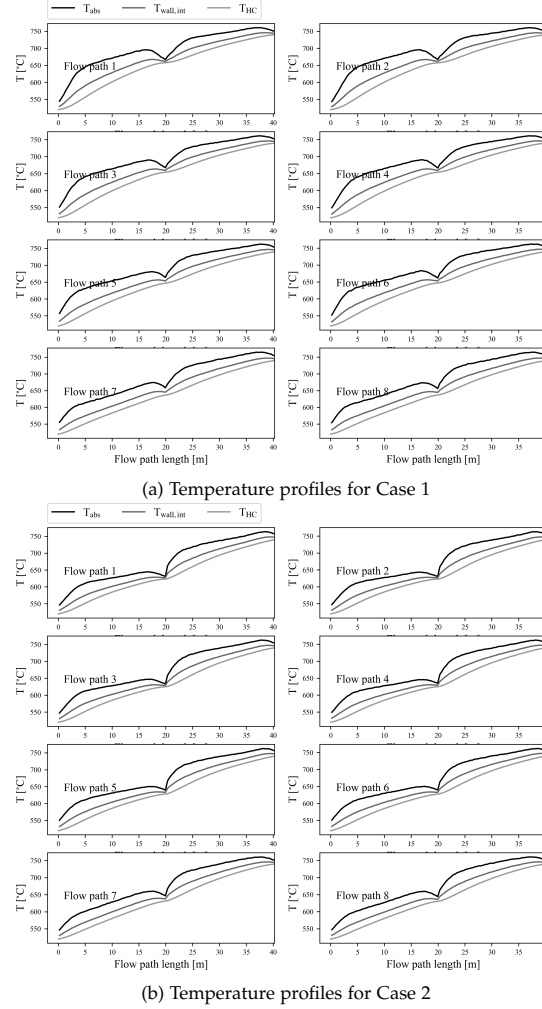


Fig. 6.9: Temperature profiles for the absorber surface temperature, internal pipe wall temperature and sodium bulk fluid temperature.

6.4.1.2 Investigation of the pairing option of tube banks

After determining the injection direction, the next problem is the selection of the pairing of tube banks for the two passes. The decision about the tube bank pairing mainly concerns the power distribution to each flow path. For the reference system operated at design point, the power incident to banks 8 & 9 (i.e. the north-facing banks) is the highest, and the power to southern banks is gradually reduced. Two selected flow paths are investigated, as shown in Figure 6.7 (a) and (c). The difference between the two patterns is that the net irradiance to each flow path is more uniform in Pattern 1 because the north-facing banks with the highest incident irradiance (banks 8 & 9) are connected to south-facing banks with the least irradiance

(banks 1 & 16). In contrast, HTF from banks 8 & 9 flows to banks 4 & 13 in Pattern 3, where the irradiance is also the highest among all south-facing banks. Pattern 3 is simulated in Case 3, and the results are compared with Case 1. As the results in Table 6.1 show, the output in Pattern 3 is lower than Pattern 1. Figure 6.10 shows the heliostats' efficiency, flux and velocity limits in Case 3. The defocusing occurs on sectors 3-5, 7-10 and 12-14, mainly because it is challenging to meet both velocity and flux limits for flow paths 1 & 2, as shown in Figure 6.10(b) and (c). In contrast, both flux and velocity limits are comfortably satisfied for the other flow paths because of the comparatively low incident power.

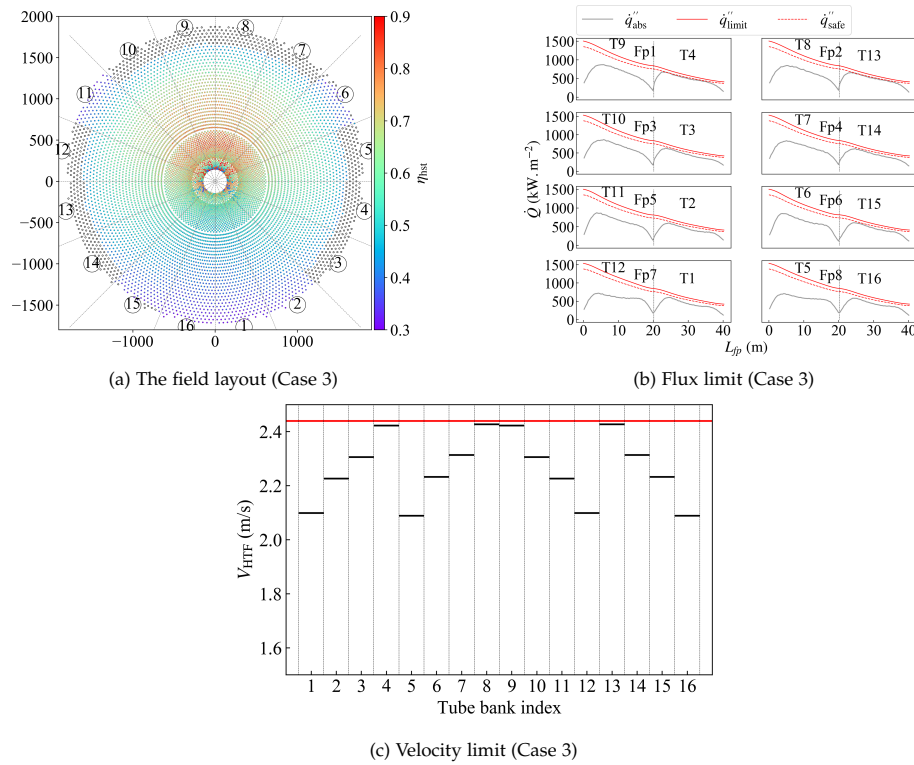


Fig. 6.10: Performance in Case 3 at design point, $D_o=60.33$ mm.

The above case study reflects the importance of selecting appropriate tube bank pairings to balance each flow path's incident power. The performance may be limited by a single flow path that, to ensure flux and velocity limits are met locally, has a disproportionate impact on the defocussing of heliostats and does not allow other tube banks to be effectively used.

6.4.1.3 Investigation of the east-west crossover option

Cases 1-3 all have crossing patterns in the east-west direction. A pattern with a non-crossing flow path is discussed in this section, as shown in Figure 6.7(d). Pattern 4 is simulated at design point, and the results are recorded in Table 6.1 (Case 4). As the results show, the receiver output is similar to Pattern 1. The reason is that the

incident irradiance to the receiver is almost symmetric in the east-west direction at solar noon, so the effect of the crossover option is minor.

However, the benefits of the cross-over pattern are expected in off-design conditions when this symmetry does not apply. A typical off-design time point, three hours after Summer Solstice solar noon, is chosen to compare between flow patterns 1 & 4. The results are recorded in cases 5 & 6. In the afternoon, the irradiance from eastern heliostats is higher because of the weaker astigmatic effect, so the most challenging parts are the eastern banks. As the results in Table 6.1 show, the non-crossing pattern achieves a lower thermal output than the crossing pattern, although the difference is less than 2%. Figure 6.11 shows both cases' field efficiency and receiver limits. Both patterns have a fraction of the heliostat field that is defocused on the eastern side. The flux limit is the dominant limit for cases 5 & 6, and the flow velocity is safe, as seen from figures 6.11(c), (d), (e) and (f).

The following case studies discuss two velocity-dominated cases with reduced pipe diameter. As the pipe diameter decreases, the inside tube flow is accelerated, which risks in exceeding the velocity limit. The pipe outer diameter is reduced to a smaller nominal value of 48.26 mm for patterns 1 and 4. The results are shown in Table 6.1 (cases 7 and 8) and Figure 6.12. The non-crossing pattern has an 8.8% lower thermal output than the crossing pattern. The defocusing characteristics are quite different between the two cases. In Case 7, defocusing heliostats are uniformly distributed around the whole field, as the flow velocities approach the limits for all banks (see Figure 6.12(c)). However, a large fraction of the eastern heliostats is defocused in Case 8. Reiterating the principal discussed in Section 6.4.1.2, the incident irradiance to all flow paths needs to be balanced so that the performance is not limited by a single flow path with a disproportionately high share of incident power. In Case 8, flow paths 2, 4, 6 and 8 receive more irradiance than the corresponding four western paths, and the performance is mainly limited by the high-velocity flow in flow path 8. Hence, the achieved thermal output is lower than in Case 7.

In a conclusion, the non-crossing pattern achieves similar performance to the crossing pattern at design point, but the performance is worse at off-design times. For the reference case, the crossing pattern shows a 2% performance benefit over the non-crossing pattern when D_o is 60.33 mm, and the performance gain is raised to be 8.8% if D_o is reduced to be 48.26 mm. The performance gain of the crossing pattern still seems to be marginal but may get accumulated in the annual simulation. Therefore, both the crossing and non-crossing patterns will be tested in annual simulations with more off-design simulations in Section 6.4.3.

6.4.2 Effect of different pipe outer diameters

The effect of the pipe outer diameter is discussed for both single-pass and double-pass configurations. Pattern 1 is chosen for the double-pass configuration in this design-point analysis. The simulations are implemented for the reference system. The results are illustrated in Table 6.2. With increasing pipe diameter, the thermal output firstly increases and then decreases. An optimal pipe outer diameter exists for

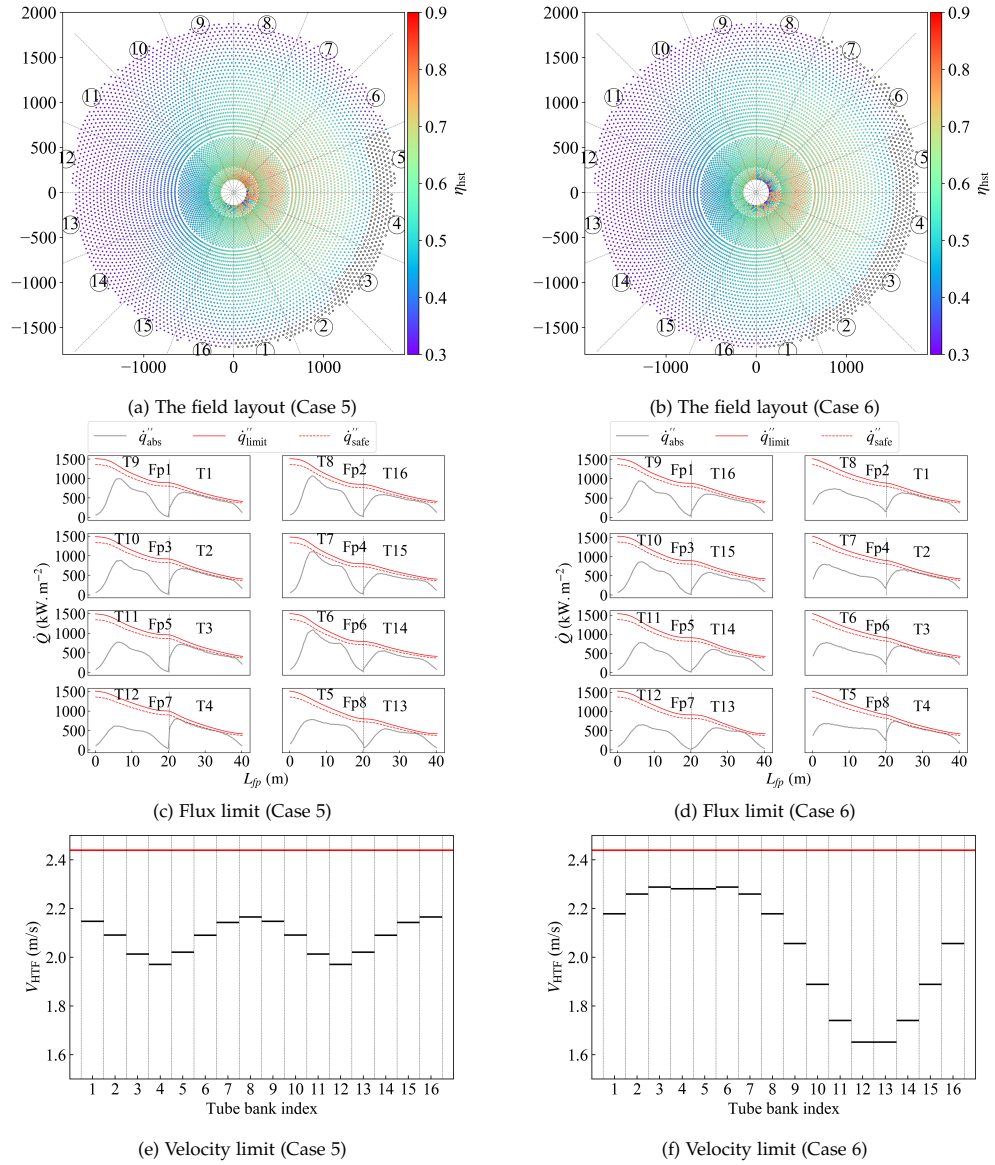


Fig. 6.11: Performance comparison with different crossing flow path strategies in the afternoon, $D_o=60.33$ mm. Cases 5 and 6 correspond to patterns 1 and 4, respectively.

6.4. Results and Discussion

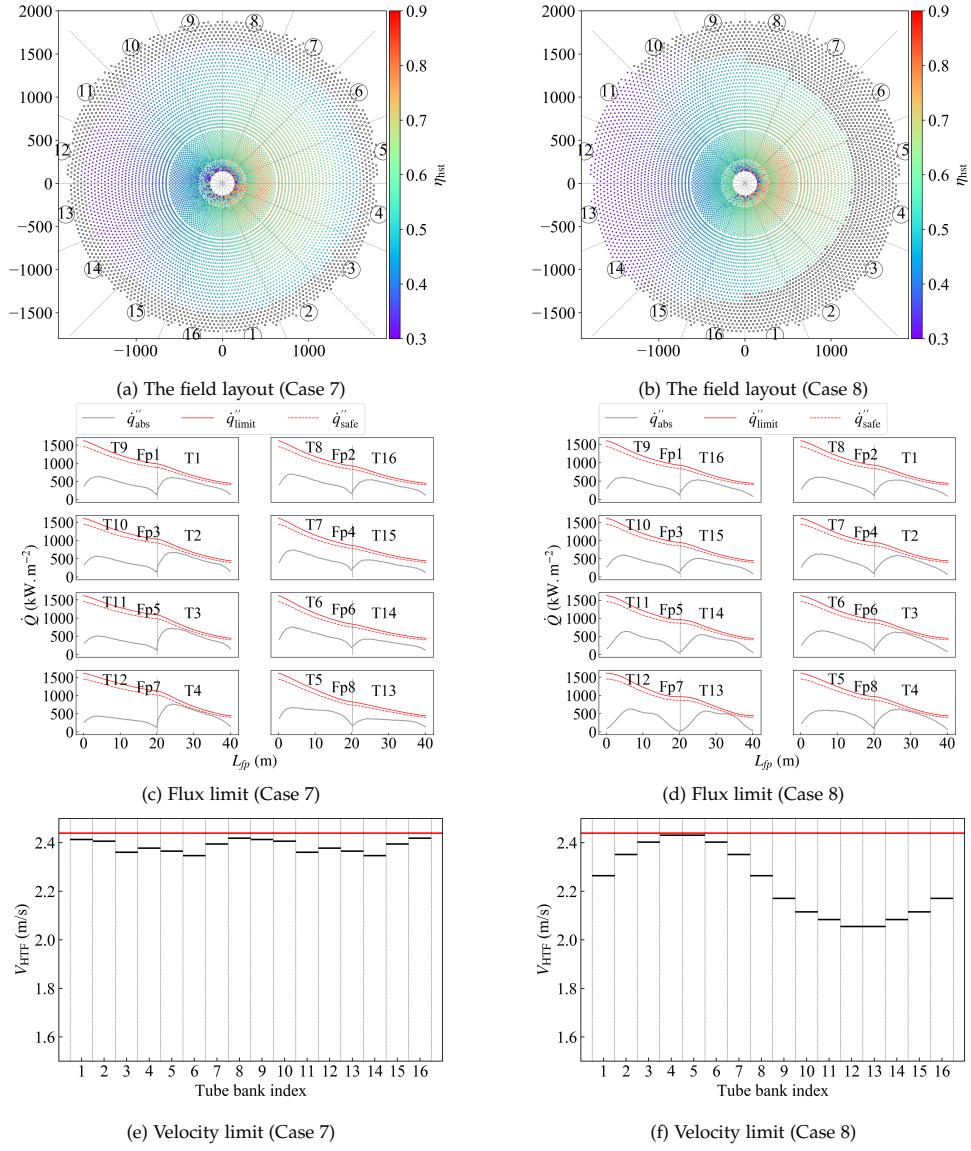


Fig. 6.12: Performance comparison with different crossing flow path strategies in the afternoon, $D_o=48.26$ mm. Cases 5 and 6 correspond to patterns 1 and 4, respectively.

both the single and double pass options. With a small pipe diameter, the performance is limited by the high flow velocity, while the flux limit is the dominant limitation with large pipe diameter. The best pipe diameters for single-pass and double-pass options are 60.33 mm and 42.16 mm, respectively. The best pipe diameter is larger for double-pass flow because the overall hydraulic cross-section of the receiver is half compared to the single-pass configuration. Both cases have no heliostat defocusing with $f_{\text{foc,A}}$ of 100%.

Table 6.2: Results with variation of pipe outer diameter (D_o).

Configuration	D_o (mm)	$f_{\text{foc,A}}(\%)$	$\eta_{\text{ope,field}}(\%)$	$\eta_{\text{rec}}(\%)$	$\dot{Q}_{\text{rec}}(\text{MW}_{\text{th}})$
Single-pass	33.40	90.6%	57.3%	89.5%	605
	42.16	100.0%	55.7%	89.8%	651
	48.26	97.2%	55.8%	89.4%	631
	60.33	87.1%	56.8%	88.2%	568
	73.03	82.4%	56.9%	87.2%	533
Double-pass	33.40	46.9%	64.9%	84.1%	334
	42.16	61.2%	63.0%	86.7%	436
	48.26	73.3%	61.0%	88.0%	512
	60.33	100.0%	55.9%	89.7%	653
	73.03	92.2%	57.7%	88.8%	615

The next step is to test the annual performance of the receiver with different flow configurations. The optimal and near-optimal cases for both single-pass and double-pass configurations are selected for annual simulations. For double-pass flow, selected cases include receivers with pipe diameters of 48.26 mm, 60.33 mm and 73.03 mm and both crossing and non-crossing patterns. For single-pass flow, receivers with pipe diameter of 42.16 mm, 48.26 mm and 60.33 mm are selected. Nine cases in total are put into annual simulations.

6.4.3 Annual performance with different flow configurations

The results of annual simulations for selected cases are shown in Figure 6.13. The focus is on the maximum load defocusing energy ($\dot{Q}_{\text{defoc,max}}$), which represents the energy loss caused by receiver over-velocity and over-flux. By comparing Pattern 1 and Pattern 4 in Figure 6.13, and observing the yellow $\dot{Q}_{\text{defoc,max}}$ results, it can be seen that the crossing pattern has a lower maximum load defocusing loss than the non-crossing pattern for each of the three different pipe diameters. This result is consistent with the instantaneous analysis in Section 6.4.1.3, and demonstrates that the crossing pattern is a better choice than the non-crossing one. It is noted that other types of losses counteract the benefit of the crossing pattern at the reference heat exchanger and storage capacities. For example, although $\dot{Q}_{\text{defoc,max}}$ for 60.33 mm diameter is nearly half for the crossing pattern, this is offset by $\dot{Q}_{\text{defoc,HX}}$ and in the end, the results of \dot{Q}_{rec} are nearly the same. This proves that the field-receiver model strongly interacts with the heat exchanger and storage systems. Maximising the receiver output should be done simultaneously considering the design capacity

of other system components.

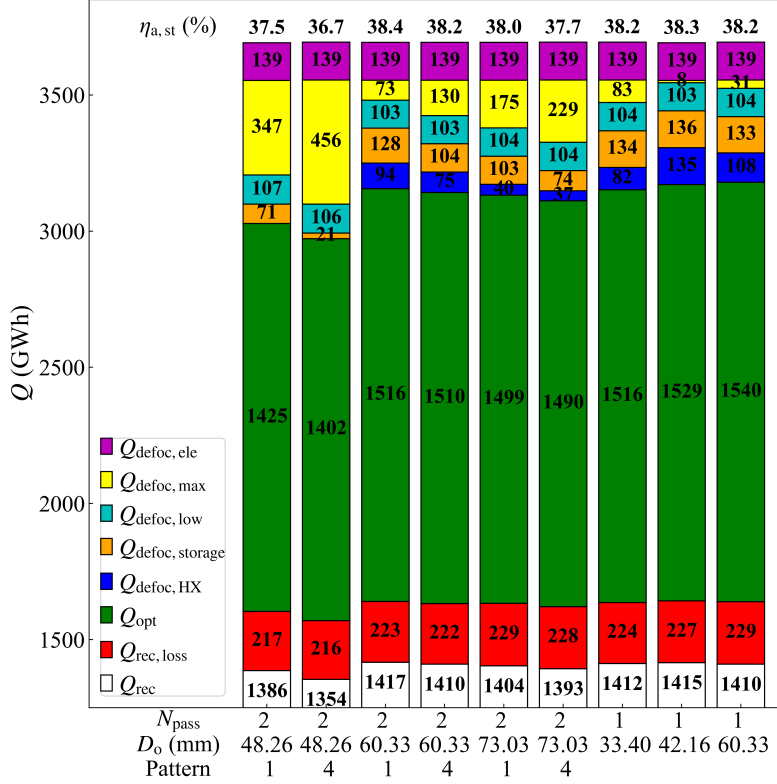


Fig. 6.13: Results of the annual simulations. The annual solar-to-thermal efficiency is illustrated at the top of the bar-chart. It is noted that this is a stacked bar chart and only loss mechanisms are highlighted. The receiver output (shown in white) is truncated at the bottom of the figure, but the values are indicated. Units are GWh. N_{pass} is the number of passes, D_o is the pipe outer diameter, and flow path patterns correspond to the patterns in Figure 6.7.

At different pipe diameters, the maximum load defocusing is the lowest when D_o is equal to 60.33 mm and 42.16 mm for double-pass and single-pass configurations, which is the same finding as from the simulation results at design point. Therefore, it appears reasonable to choose the best pipe diameter based on a design point simulation without the need to run more computationally expensive annual simulations.

If the best case with a double-pass is compared to the best case with a single-pass, the single-pass case has very low receiver defocusing losses. However, heat exchanger and storage defocusing losses are high, and the overall annual efficiency between the two cases is similar again. This study offers a performance comparison between different number of passes; however, the cost impacts of single vs multi-pass need to be discussed to determine the best configuration. Multi-pass requires more crossover pipework, which has cost and imposes drainage challenges. Single-pass probably requires more control valves, which could be super-expensive. These are not performance-related trade-offs but might be just as important.

6.4.4 Selection procedure

A procedure can be developed to choose the best receiver flow configuration from the above discussion. A flowchart is shown in Figure 6.14 for better explanation. Firstly, several principles are used to choose the flow path pattern for a given number of passes. The flow paths should all inject into panels in a high-irradiance area. The next passes are chosen to make net irradiance to each flow path balanced. Crossing patterns are preferred to achieve balanced power at off-design hours. Next, the optimal pipe outer diameter is obtained by parametric studies at the design point for a given number of passes. Annual simulations are performed for selected cases to obtain the best number of passes, pipe diameter and flow path pattern.

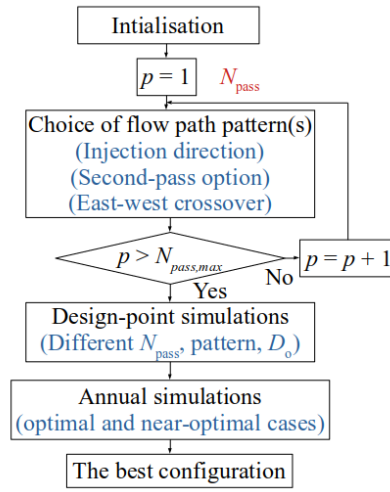


Fig. 6.14: Flowchart of the selection procedure to choose the best receiver flow configuration.

6.4.5 Application on a triple-pass receiver

The above procedure is applied to choose the best flow configuration for a receiver designed in the Gen3 Liquid Pathway project [151]. The diameter and height of the receiver are 14 m and 14.5 m, respectively. The number of banks is 12, and the flow path is triple-pass. The flow path pattern is illustrated in Figure 6.15. It is noted that the original flow path of the Gen3L receiver was determined independently and will be tested in this work. This receiver is called the ‘Gen3L’ receiver in the following study.

Following the selection procedure, the considered number of passes is one, two and three. Pattern 1 in Figure 6.7 is used for the double-pass cases. It is noted that the number of banks is 16 for single-pass and double-pass cases, and it is 12 for the triple-pass configuration. The number of banks is not the dominant parameter affecting the flow characteristics, as reflected in Eq. 5.6. A low value of 12 is chosen to avoid overcomplicating the interconnections between banks, identical to the Gen3L receiver.

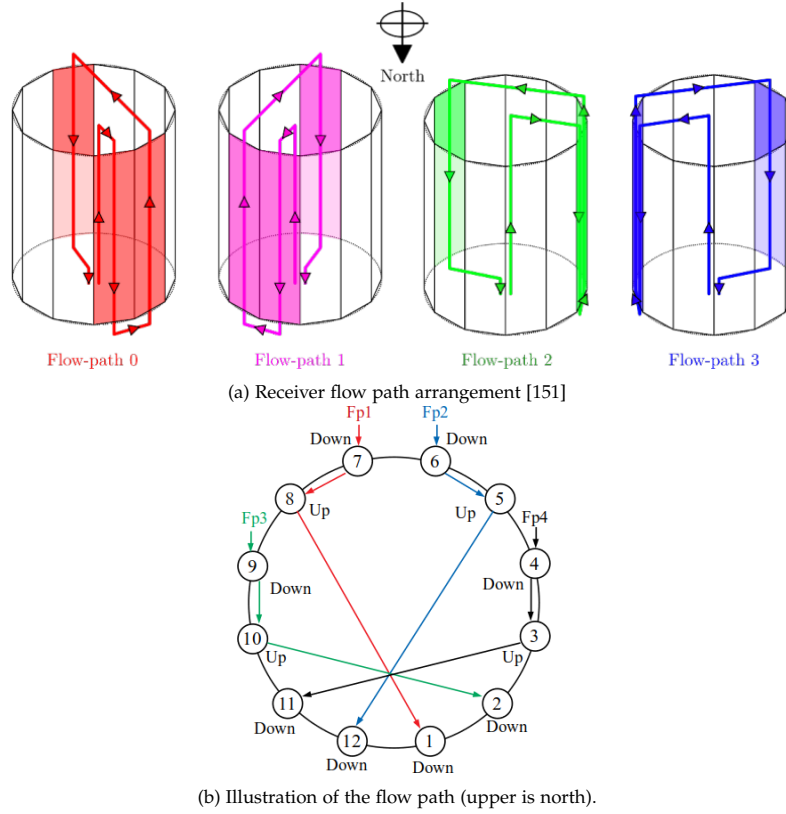


Fig. 6.15: Illustrations of the flow path pattern for the Gen3L receiver.

The principles outlined above are used to select the best pattern for the triple-pass configuration. Firstly, the HTF is injected into the two banks located at the north (banks 7 & 6) in flow paths 1 & 2. Next, HTF is injected into banks 9 & 4 in flow paths 3 & 4. The second and third passes in flow paths 1 & 2 are determined as banks 5 & 8 and 1 & 12. Pattern 3-1 in Figure 6.16 is obtained as possible optimal patterns. Similarly, if flow paths 3 & 4 start from banks 5 & 8, patterns 3-2, 3-3, 3-4 and 3-5 are all possible patterns satisfying the selection criterion, as shown in Figure 6.16. The flow directions on all banks are marked in Figure 6.16. For a vertically asymmetric aiming strategy (i.e. MDBA), it is better to avoid opposite flow directions on neighbouring banks because of the interaction between banks [178]. Therefore, patterns 3-1 and 3-5 are ruled out because of the high number of opposite flows. Patterns 3-2, 3-3 and 3-4 are put into the simulation to test their performance.

The next step is to simulate the optimal pattern(s) at different pipe diameters. The results are shown in Table 6.3. The results indicate a particular pipe diameter that gives a higher receiver output for each number of passes. For single-pass flow, the better pipe diameter is the smaller one because the flow velocity is lower in this configuration and smaller pipes help keep velocity at a level that maintains heat transfer and efficiency. For double-pass flow, the best performance is achieved with D_o equal to 48.26 mm. The velocity is either too high or too low if the pipe diameter is of the other nominal sizes. For triple-pass flow, the HTF velocity is too high,

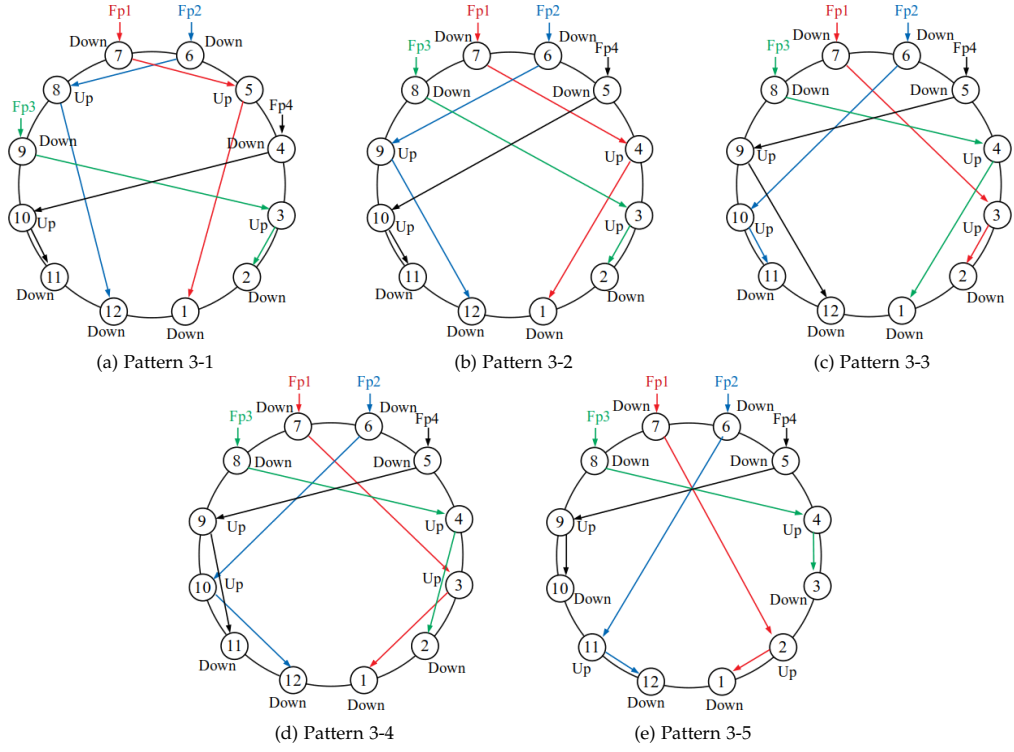


Fig. 6.16: Different flow path patterns.

and better performance is achieved with the larger pipe diameter. Among the three optimal patterns, Pattern 3-4 has the highest thermal output. Figure 6.17 shows the performances with Pattern 3-4. Both flux and velocity limits can be satisfied with partial defocusing of the heliostat field.

Table 6.3: Results at different pipe diameters for the Gen3L receiver

Configuration	D_0 (mm)	$f_{\text{defoc,max}}(\%)$	$\eta_{\text{ope,field}}(\%)$	$\eta_{\text{rec}}(\%)$	$Q_{\text{rec}}(\text{MWth})$
Single-pass	33.40	89.6%	62.2%	89.6%	354
	42.16	83.9%	62.4%	88.8%	329
Double-pass	42.16	83.3%	64.3%	89.2%	339
	48.26	97.3%	62.4%	89.9%	387
	60.33	88.8%	63.5%	88.9%	355
Pattern 3-2	60.33	79.3%	64.9%	88.4%	322
	73.03	92.8%	63.0%	89.0%	369
Pattern 3-3	73.03	93.9%	63.0%	89.1%	374
Pattern 3-4	73.03	94.8%	62.9%	89.2%	376

In designing the Gen3L receiver, the flow velocity limit was lifted from 2.44 m/s to 3.0 m/s. This revision was made after discussion with the materials compatibility research team in ASTRI, and with Nooter/Eriksen, based on experience with testing sodium receivers at Sandia in the early 1980s [151]. The receiver with Pattern 3-4 is

6.4. Results and Discussion

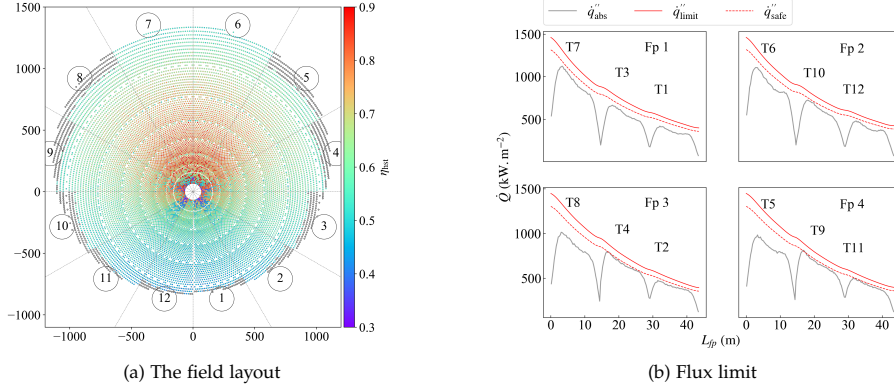


Fig. 6.17: Performances of the Gen3L receiver with Pattern 3-4.

re-simulated with the released velocity limit for a fair comparison with the original Gen3L receiver. The pipe outer diameter is 60.33 mm. The results are shown in Table 6.4. The receiver with Pattern 3-4 has nearly no field defocusing. The heliostats' efficiency and the flux curves are plotted in Figure 6.18 for the receiver with the Gen3L pattern in Figure 6.15. A large fraction of northern heliostats is defocused. The reason is that neighbouring banks facing north all have opposite flow directions and suffer from the interaction between banks. Although the performance of Pattern 3-4 is better, there are multiple crossing connections between banks, which makes the practical manufacture difficult and may increase the manufacturing price of the receiver. A more detailed receiver cost model is needed to obtain the best pattern for practical application in future research.

Table 6.4: Results for the Gen3L receiver with Pattern 3-4 and the original pattern

D_0 (mm)	$f_{\text{defoc,max}}(\%)$	$\eta_{\text{ope,field}}(\%)$	$\eta_{\text{rec}}(\%)$	$Q_{\text{rec}}(\text{MWth})$	Notes
73.03	99.3%	62.4%	89.9%	395	Pattern 3-4
73.03	87.6%	63.7%	89.2%	352	Gen3L [151]

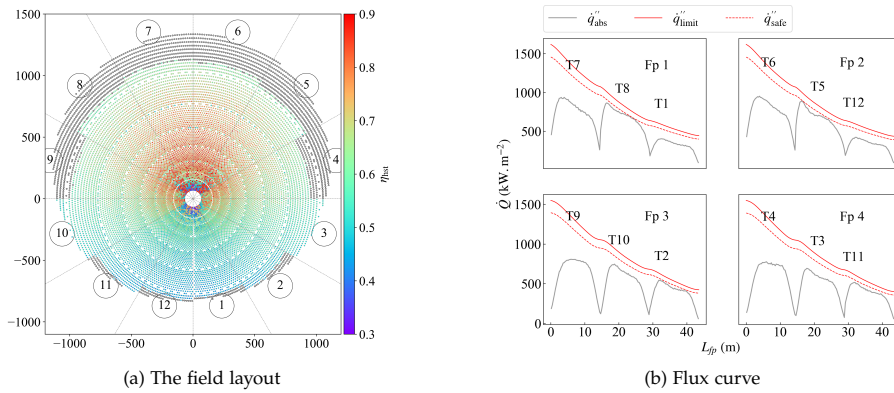


Fig. 6.18: Performances of the Gen3L receiver with the original pattern in Figure 6.15(b).

Interestingly, it is discovered that the receiver output is enhanced by 5.6% with the velocity limit released from 2.44 m/s to 3.0 m/s when the first example in Table 6.4 is compared to the last case in Table 6.3. This suggests that a less constrained velocity can be used to increase the heat output and receiver efficiency. The outcomes of receiver designs are influenced by the precise velocity limit for a steady flow of liquid sodium inside tubes, which is currently an open scientific subject.

Next, optimal and near-optimal cases in Table 6.3 are put into annual simulations. The flow velocity limit is 2.44 m/s. The results are illustrated in Figure 6.19. The general conclusions are identical to the reference case. The configuration with the best design-point output achieves the lowest maximum load defocusing losses. Pattern 3-4 is the best flow pattern amongst the triple-pass cases, which is also identical to the design-point analysis.

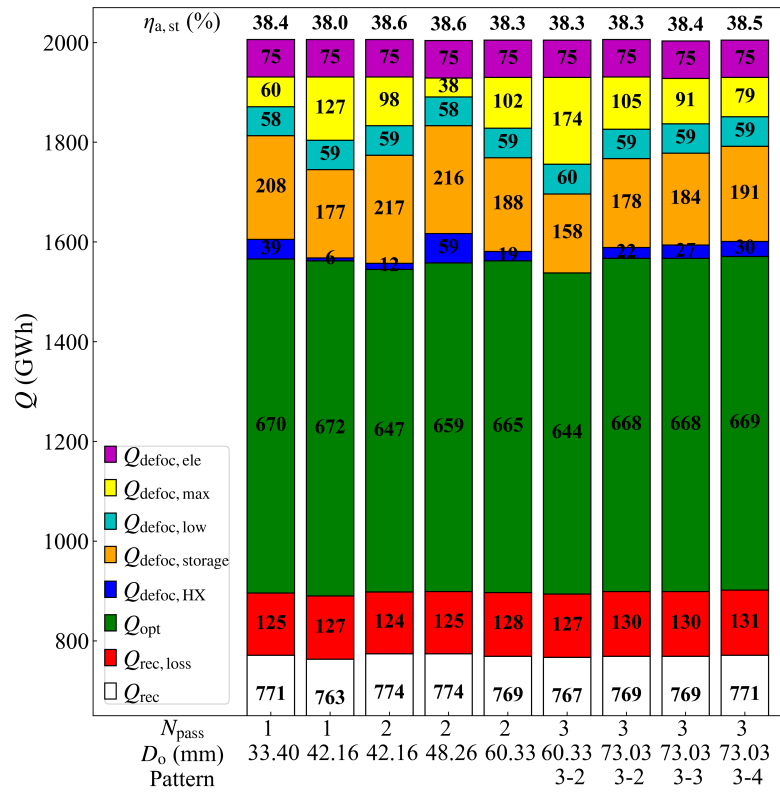


Fig. 6.19: Results of the annual simulation for the Gen3L receiver. Similar to Figure 6.13, this figure is a stacked bar chart and only loss mechanisms are highlighted. The receiver output (shown in white) is truncated at the bottom of the figure, but the values are indicated. Units are GWh. N_{pass} is the number of passes, D_o is the pipe outer diameter, and flow patterns correspond to the patterns in Figure 6.7.

6.5 Conclusion for this chapter

In this chapter, the MDBA method is improved with a defocusing capacity to calculate the receiver output with an oversized field. The improved MDBA calculation is further integrated with the system-level model for annual simulations. Different receiver flow path options and pipe outer diameters are investigated. The best flow path for double-pass flow is found for the reference receiver, and an optimal pipe diameter exists for both single-pass and double-pass options. The annual simulations result in identical optimal flow configurations as for the design-point simulations, although the benefits achieved from the optimal receiver flow configuration are weakened by defocusing from the heat exchanger and the storage. A selection procedure is summarised to determine the optimal receiver flow configuration and is successfully adapted to the Gen3L receiver with its triple-pass option.

The methodology proposed in this chapter is used to increase the performance of the receiver. However, the effect on receiver cost is not considered. The optimal receiver configuration may suffer from having a too high manufacturing cost. A detailed receiver cost model is needed if a techno-economical optimisation is implemented in the future. Besides, the oversizing factor, heat exchanger capacity factor, storage hours and the solar multiple are all fixed in this study, and the trade-off between all defocusing losses is not the best. The next chapter will discuss a system-level optimisation changing the relative sizing of system components.

In this chapter, the heliostat field defocusing is investigated in the context of hourly averaged DNI in annual simulations. More accurate reflection of the dynamic changes in the tube wall temperature of the receiver can be obtained if the receiver is simulated at smaller time intervals. Investigation on the effect of the dynamic change in DNI is suggested future work.

Surrogate-based optimisation with varying relative sizing of system components

7.1 Introduction

In Chapter 6, it was shown that system components other than the receiver at times become critical with respect to reaching their maximum capacity, and therefore cause the heliostat field to be partially defocused, mitigating the benefits of optimising flow path in the receiver. This motivates the work presented in this chapter, where the capacity of system components is optimised to increase system output and reduce the LCOE. A parametric study is firstly presented to investigate the effect of changing the capacity of the heliostat field, the heat exchanger and the TES. This is followed by a system-level optimisation with varying relative sizing of system components. The optimisation goal is to achieve the lowest LCOE. An iterative surrogate-based optimisation (SBO) method is proposed to accelerate the process. It is noted that the power block capacity is fixed in this chapter.

7.2 Models and methodology

The reference field and receiver subsystems come from the performance-based optimal case at the reference 175m tower with a 20% oversized heliostat field and are identical to Chapter 6. The reference values for the solar multiple (SM), the oversizing factor (f_{hst}), the heat exchanger capacity ratio (f_{HX}) and the storage hours ($t_{storage}$) are 2.5, 1.2, 1.0 and 12, respectively. The definitions of f_{hst} , f_{HX} , $t_{storage}$ and SM were introduced in Section 2.4.

The modelling methodology mainly concerns the system-level model, which can be used to calculate the annual electricity yield, system components' costs, and the LCOE. The system-level model is identical to that in Chapter 6, where the 3D interpolation method is applied with four OELTs, as introduced in Section 6.3.3.3. The cost model is updated to be consistent with the final report in the Gen3 Liquid Pathway

Project [151] and differs from the model introduced in Section 5.3.8. The new cost model has updates to the cost function for several system components including the tower, riser and downcomer, sodium loop, and salt piping and valves. Detailed cost functions are not introduced because they are not the original work of this thesis. The cost functions can be found in the project report [151] or the SolarTherm script in GitHub¹. Using the new costs, the LCOE for the performance-based optimal case (without an oversized heliostat field) and the reference case (with a 20% oversized heliostat field) are 63.9 USD/MWh and 59.6 USD/MWh, respectively.

7.3 Parametric study on relative sizing of system components

Ahead of the system-level optimisation, parametric studies are performed in which the capacities of the heliostat field, the heat exchanger and the TES subsystems are varied.

7.3.1 Effect of varying the oversizing factor f_{hst}

The heat exchanger capacity ratio and the storage hours are fixed as the reference values in this section. The oversizing factor (f_{hst}) is increased from 1.0 to 1.3 with an increment of 0.05. Annual simulations are performed at different values of f_{hst} . Figure 7.1 illustrates the simulation results. As the results show, the number of heliostats increases with the increase of the oversizing factor, so the total irradiance to the field increases. This increases the annual electricity output, while the annual solar-to-thermal efficiency drops because more low-efficiency heliostats are included. The capacity factor also increases with the rise of the oversizing factor. To further illustrate the results, Figure 7.2 shows the receiver net power across a year with f_{hst} of 1.0 and 1.2, respectively. It can be observed that the annual receiver outputs are greatly enhanced with an oversized field.

Although the annual outputs are enhanced with a larger field, the capital cost becomes higher because of the higher field cost. An optimal LCOE appears when f_{hst} is equal to 1.20. The lowest LCOE is 59.6 USD/MWh, compared to 63.9 USD/MWh without oversizing the heliostat field, which demonstrates the significant effect of heliostat field oversizing.

However, as shown in Figure 7.2(b), the receiver outputs exceed the maximum heat exchanger capacity at some operating hours, especially during summer hours with high DNI. This causes heat exchanger defocusing losses, and storage defocusing happens when the storage tanks are full. The trend of defocusing losses changing with f_{hst} is shown in Figure 7.3. Definitions of the defocusing losses can be referred to Section 2.4.2.2. With the increase in the oversizing factor, the heliostat field capacity becomes larger, so the overall solar irradiance to the heliostat field increases. This increases the energy which is counted into elevation defocusing losses when elevation defocusing occurs near sunrise and sunset. The minimum load defocusing

¹Solartherm: <https://github.com/SolarTherm>, branch: 'cooptimisation'

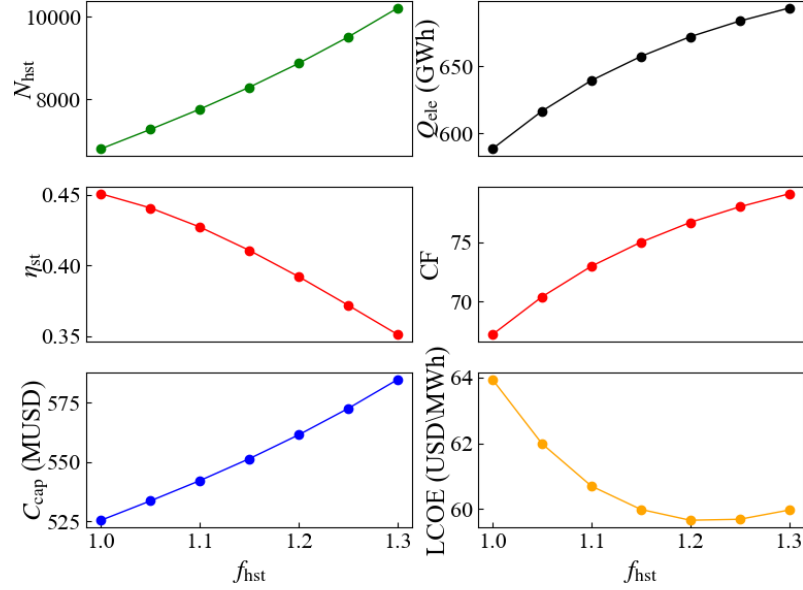


Fig. 7.1: Effect of the oversizing factor on the number of heliostats (N_{hst}), the annual electricity output (Q_{ele}), the annual solar-to-thermal efficiency ($\eta_{a,st}$), the capacity factor (CF), the capital cost (C_{cap}) and the LCOE.

loss decreases because the receiver goes into operational mode more frequently. The maximum load defocusing loss, heat exchanger defocusing loss and the storage defocusing loss all increase. The increase of those defocusing losses weakens the benefits of the oversized field. One way to mitigate this weakening effect is to change the capacity of the heat exchanger and the storage subsystems, which will be discussed in the next section.

7.3.2 Effect of varying the heat exchanger capacity ratio f_{HX}

The design capacity of the heat exchanger is controlled by the heat exchanger capacity ratio (f_{HX}). With changing f_{HX} in this section, f_{hst} is fixed as 1.20 and $t_{storage}$ is kept as 12 hours. Figure 7.4 shows the results when increasing f_{HX} from 0.9 to 1.2 with an increment of 0.05. The heat exchanger defocusing loss decreases to approach zero when f_{HX} is equal to 1.2. However, the storage defocusing loss increases. Figure 7.5 shows the variation of different power terms at seven consecutive summer days with f_{HX} equal to 1.0 and 1.2, respectively. The solid blue lines represent the real receiver thermal output (\dot{Q}_{rec}), while $\dot{Q}_{rec,max}$ is the maximum output of the receiver respecting receiver operational limits without considering the defocusing of the heat exchanger and the storage tanks. Following the defocusing strategy in Section 2.4.2.2, \dot{Q}_{rec} cannot exceed the heat exchanger maximum capacity and energy exceeding this capacity led to heat exchanger defocusing loss. \dot{Q}_{rec} drops to equal $\dot{Q}_{PB,in}$ when the storage tanks are full. Figure 7.5(a) shows that the storage tanks are already full on the first of the seven selected days for the case where $f_{HX} = 1.0$. Increase of the heat exchanger capacity ($f_{HX} = 1.2$) does allow more output from the receiver to the heat

7.3. Parametric study on relative sizing of system components

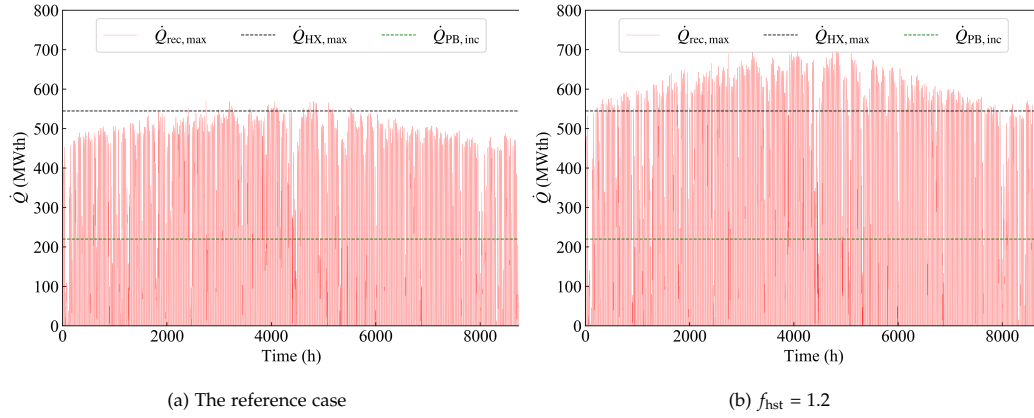


Fig. 7.2: Plot of the power over a year. $\dot{Q}_{rec,max}$ is the maximum receiver output respecting receiver limits. $\dot{Q}_{HX,max}$ is the maximum heat exchanger capacity. $\dot{Q}_{PB,in}$ is the power block nominal input.

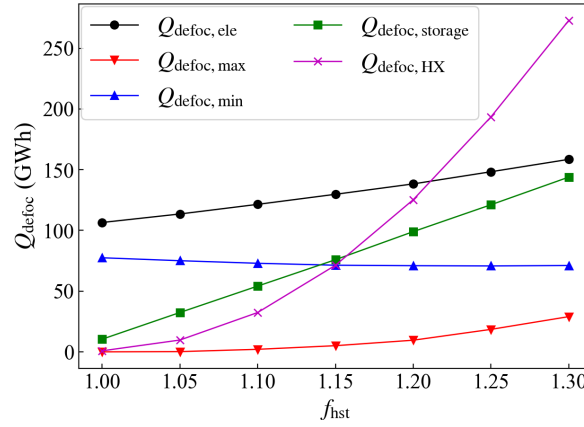


Fig. 7.3: Defocusing losses at different oversizing factors.

exchanger, but this extra thermal output does not result in more energy collection overall, as storage capacity limitations now cause defocusing losses.

The capital cost increases with a larger heat exchanger, and an optimal LCOE is achieved when the heat exchanger capacity ratio is 1.1 due to the trade-off between the higher annual electricity yield and the higher cost.

7.3.3 Effect of varying the storage hours $t_{storage}$

The results of the parametric study are shown in Figure 7.6. While varying the storage capacity, the oversizing factor and the heat exchanger capacity ratio are fixed as 1.2 and 1.0, respectively. The storage hours are changed from 9 to 15 hours with an increment of 1 hour. The storage defocusing loss is reduced with the increase of storage hours; therefore, the electricity output is enhanced. However, the capital cost is increased because of the more expensive storage tanks. The combined effect is that the optimal LCOE is achieved with 11 hours of storage capacity.

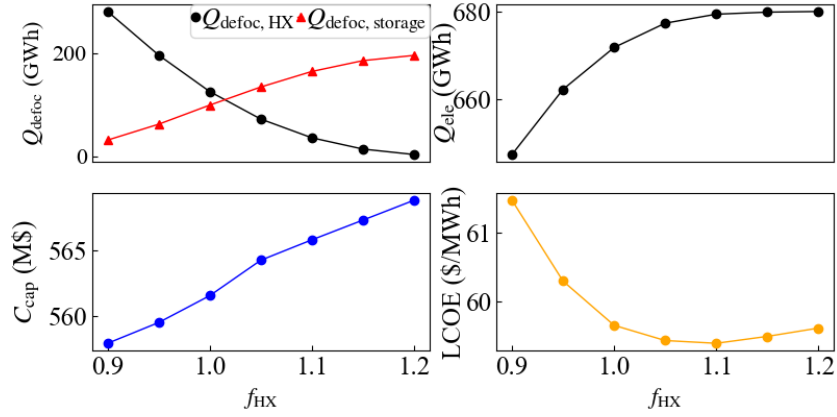


Fig. 7.4: Effect of the heat exchanger capacity ratio. Both the heat exchanger and storage defocusing losses are plotted in (a).

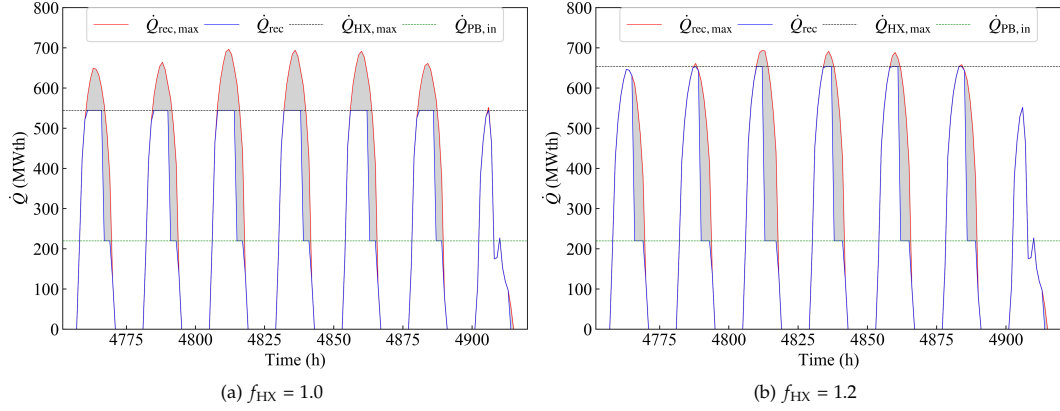


Fig. 7.5: Plot of the power at a selected week in summer. Shaded area is attributed to defocusing losses.

7.3.4 Parametric study varying both the heat exchanger capacity ratio and the storage hours

From the above analysis, it is found that the system components interact with each other. Hence, a parametric study is implemented varying both f_{HX} and $t_{storage}$. The oversizing factor is fixed as 1.2. The results are shown in Figure 7.7. The impact on LCOE is strong with increase f_{HX} from 0.9 to 1.0, but becomes weak after. The optimal storage hours are close to 12 with different f_{HX} . The lowest LCOE is achieved with f_{HX} and $t_{storage}$ equal to 1.1 and 12 hours, respectively.

The parametric study is re-implemented with different heliostat field oversizing factors, and the results are illustrated in Figure 7.8. The optimal f_{HX} is 1.0 when the storage hours are 9, and then the optimal f_{HX} gradually increases to 1.1 with the increase of the storage hours. The results demonstrate that a large heat exchanger prefers a large storage system. The optimal heat exchanger and storage capacities increase with a larger heliostat field. The best LCOE is achieved with a 25% oversized heliostat field, 10% oversized heat exchanger and 12 storage hours. The optimal LCOE is 59.2 USD/MWh.

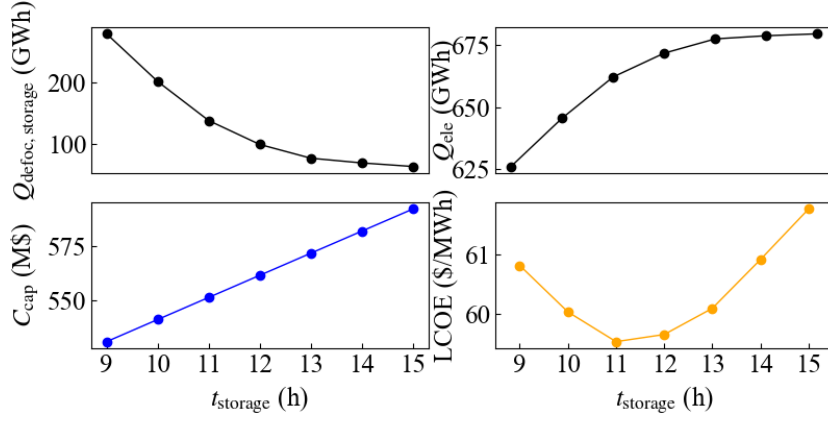


Fig. 7.6: Effect of the storage hours.

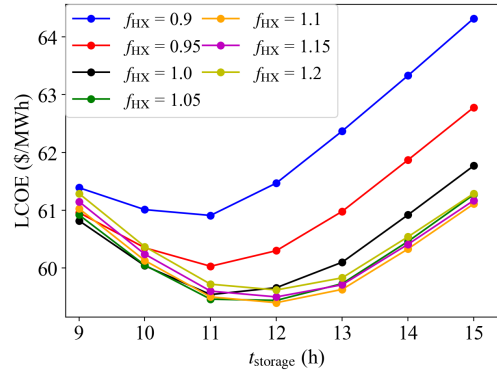


Fig. 7.7: Results of the parametric study varying both the heat exchanger and storage capacities.

In summary, the LCOE is reduced from 63.9 USD/MWh to 59.6 USD/MWh by using the oversized heliostat field, and is reduced again to 59.2 USD/MWh by varying the capacity of the heliostat field, the heat exchanger and the TES, based on the results of the parametric studies. However, this is not an optimised design. In the next section, a system-level optimisation will be applied to optimise the relative sizing of system components.

7.4 Optimisation of the system

7.4.1 Optimisation problem

Given the interactions between system components, a system-level optimisation is implemented to find the best relative sizing to achieve the lowest LCOE. The process of objective function evaluation generally follows the structure of the co-optimisation study in Chapter 5, with the main steps illustrated in Figure 7.9. The input parameters include two heliostat field layout factors ($\Delta r_2, \Delta r_3$), receiver dimension ($D_{\text{rec}}, H_{\text{rec}}$), tower height (H_{tower}), oversizing factor (f_{hst}) and the solar multiple (SM). The oversized heliostat field is firstly generated using the approach discussed in Section 6.3.1.

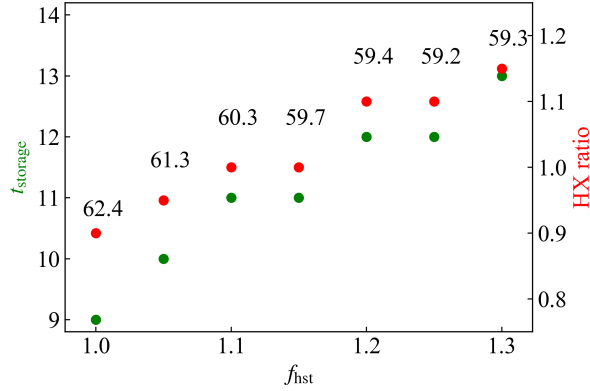


Fig. 7.8: Results of the optimal heat exchanger and storage capacities at different heliostat field oversizing factors. The LCOE values are indicated with units of USD/MWh.

The receiver flow path configuration is determined from a simplified method introduced in the following section. Then, OELTs and RELT are generated using the 3D interpolation method and the loss-breakdown regression method. The look-up tables are imported into SolarTherm for the annual simulation and cost evaluations. The simulation's most time-consuming part is the ray-tracing, whereas running a system-level model for fixed heliostat field and receiver design is comparatively very fast. As a consequence it is more efficient to determine f_{HX} and $t_{storage}$ inside the optimisation loop, and the method to do this will be introduced later. The parametric range of all parameters is illustrated in Table 7.1.

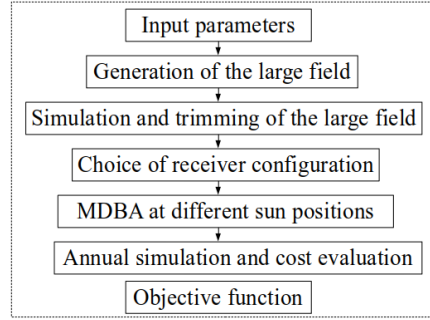


Fig. 7.9: Algorithm flowchart for the objective function evaluation.

Table 7.1: Setup of the optimisation.

Variable	Δr_2	Δr_3	D_{rec} (m)	H_{rec} (m)	H_{tower} (m)	f_{hst}	SM
Lower	0.866	0.866	14.0	14.0	150.0	1.0	1.5
Upper	1.4	2.8	22.0	22.0	250.0	1.4	3.5

7.4.2 Choice of the receiver configuration

The study of receiver flow configuration in Chapter 6 draws several conclusions. Firstly, the optimal flow path pattern for each number of passes ($N_{\text{pass}} \leq 3$) is obtained. An optimal pipe diameter exists for each number of passes, and the performance at design point can be used for pipe diameter selection. Based on these conclusions, a simplified heat transfer calculation and some design-point simulations are used to choose the best receiver flow configuration.

Firstly, a simplified heat transfer calculation is used to discard pipe diameter candidates that are far away from the optimum. The HTF velocity inside pipes is estimated using the method introduced in Section 5.3.4 as:

$$v_{\text{estim}} = \frac{f_{\text{hst}} \dot{Q}_{\text{rec}} N_{\text{hst,max}}}{N_{\text{hst,tot}} (h_{\text{out}} - h_{\text{in}}) N_t \rho_{\text{out}} \pi / 4 (D_0 - 2\delta_{\text{th}})^2} \quad (7.1)$$

where $f_{\text{hst}} \dot{Q}_{\text{rec}}$ considers the heliostat field oversizing effect on the nominal receiver output. For each number of passes, the velocity is estimated using different nominal pipe diameters (33.40 mm, 42.16 mm, 48.26 mm, 60.33 mm and 73.03 mm). Next, Figure 7.10 shows an illustration of the selection process. Cases with velocity higher than $f_{\text{hst}} V_{\text{lim}}$ are discarded because, even with all the oversizing heliostats defocused, velocity still exceeds the limit. This means the receiver output will be lower than the nominal output for these cases. Next, for all cases with a velocity lower than V_{lim} , only the smallest pipe diameter is kept. This is because none of these cases suffers from the over-velocity issue, and the case with the smallest pipe diameter has the best thermo-mechanical performance (see Figure 5.1). Cases with velocity between V_{limit} and $f_{\text{hst}} V_{\text{limit}}$ are all selected.

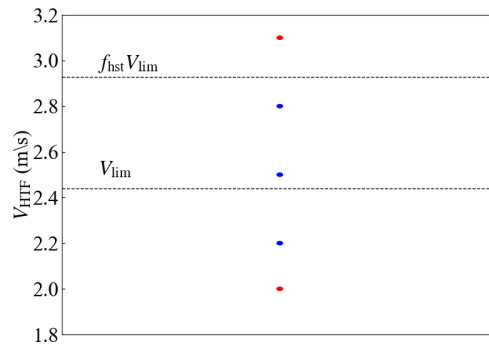


Fig. 7.10: Illustration of the algorithm to select pipe outer diameters. Blue dots are the selected cases, while red dots are discarded.

Next, selected cases are put into MDBA simulations at design point, and the flow configuration with the highest output is selected as the optimum and is imported into later annual simulations.

7.4.3 Determination of the heat exchanger capacity ratio and the storage hours

The heat exchanger capacity ratio and the storage hours are determined by running the system-level model iteratively. f_{HX} is varied between 1.0 and 1.2 with a gap of 0.05, and at each given f_{HX} , the optimal storage hours are obtained by using a line-search optimisation with fixed step size (1 hour). The starting point for $t_{storage}$ is 12 hours. Figure 7.11 shows an illustration of the bi-directional search. At the starting point, the algorithm chooses to go along the direction where the objective function drops. Along this direction, the optimum is located where the objective function increases. The method quickly converges for the problem with a single optimum, which is the case in this study (see the parametric study in Figure 7.7). The bi-directional search is repeated at different values of f_{HX} until the lowest LCOE is achieved. This lowest LCOE is returned as the objective function illustrated in Figure 7.9.

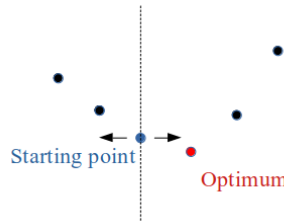


Fig. 7.11: Illustration of the bi-directional search to find the optimal storage hours at a given heat exchanger capacity ratio.

7.4.4 The iterative surrogate-based optimisation (SBO) method

The process illustrated in Figure 7.9 is computationally expensive because of the heavy ray-tracing simulations generating four OELTs, which makes conventional optimisation algorithms (i.e. a genetic algorithm) nearly intractable. The surrogate-based optimisation (SBO) method uses surrogate modelling techniques to quickly find optimal results, with a novel optimisation framework in which conventional optimisation algorithms are used for inner loop optimisation. The SBO method can be used to improve significantly the optimisation speed when computationally expensive analysis codes are used [179], which is the case in this study.

A typical flowchart of a surrogate-based optimisation is shown in Figure 7.12. The process of the SBO method includes:

- Design of experiment: After specifying the design space, the design of experiment is applied to find the simulated samples. A sampling plan with a uniform but not the regular spread of points across the design space makes intuitive sense to explore unknown landscapes. Hence, the Latin Hypercube sampling (LHS) method is used to generate design points with the size of $N_{samples}$.

- True model simulation: The true response quantities are evaluated at these design points using the simulation tools illustrated in Figure 7.9.
- Surrogate establishment: The surrogate model is built using the response data. The polynomial quadratic model in DAKOTA [164] is used to build the surrogate.
- GA optimisation: The genetic algorithm optimises the surrogate model to find the optimum, which is defined as the inner optimisation. The genetic algorithm is one of the most commonly used algorithm for the inner optimisation[179].

After the process, the objective is returned from the surrogate model in the genetic optimisation instead of the computationally heavy true simulation. Therefore, the number of true simulations can be reduced compared to using conventional optimisation algorithms directly.

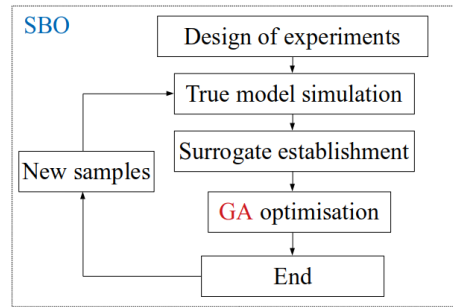


Fig. 7.12: Flowchart of a surrogate-based optimisation

A highly accurate surrogate model would require many expensive simulations of the true model. However, the SBO method aims not to make a global approximation of the true model, but to find an optimal candidate. A lot of simulation time is wasted to match with the trend in regions away from the optimal parametric space. Therefore, an alternative method is used to iterate on the SBO process based on an infill criterion. The infill criterion is that new points are added to the sample set and reconstruct the surrogate, and the sub-optimisation is performed on the new surrogate. The surrogate is expected to become more accurate in the optimal area as the iteration goes on, so the new sampling points need to be established near the optimum. The addition of new simulation results can help refine the surrogate model.

Inspired by the pattern search optimisation method [180], an iterative SBO algorithm with multiple infills is proposed. At each iteration, an optimal point is obtained after the surrogate model is optimised by GA optimisation. The parametric space for the subsequent iterations gets gradually contracted following several rules. Figure 7.13 shows an example to help illustrate this iterative process.

- Firstly, the parametric space gets contracted if the optimum is located inside the parametric range in the previous step. For instance, the space gets con-

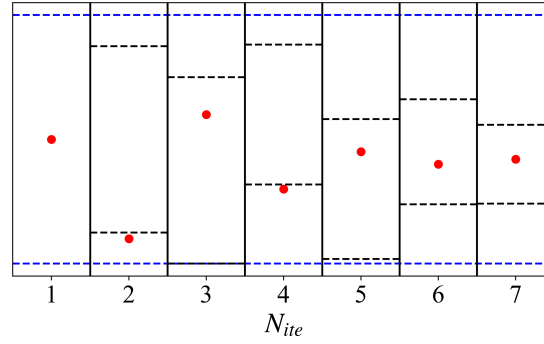


Fig. 7.13: Illustration of the process in the iterative SBO method. The inner loop in Figure 7.12 is repeated at each iteration with sampling - true simulation - surrogate building - GA optimisation. Blue dashed lines are the original boundaries. The red dots present the optimal solution at the current iteration. The black dashed lines are the parametric space for the current iteration.

tracted in step 2 compared to the initialised space in Figure 7.13. Otherwise, the parametric range remains unchanged, as shown in steps 3 and 5.

- Next, the parametric boundaries are not allowed to exceed the original boundaries. This principle is true given that a conservative initial parametric range is defined in Table 7.1.
- The parametric boundary in the next iteration is established with the optimum as the centre point, except where the new boundary exceeds the original space. For example, the centre of the boundary in iteration 2 is the optimum in iteration 1. Because in iteration 2 the optimal solution is found below the parametric range, from iteration 2 to 3, the new boundary is fitted to the lower part of the original boundary, without any change in the range.
- The iteration stops if the parametric space is small compared to the original range. The contraction factor and the ratio of the converged parametric range are chosen as 0.75 and 0.33, respectively. The sample size for each iteration is chosen as 50 in this study.

The proposed iterative SBO method is tested in the following system-level optimisation. The key feature of the method that is examined is whether the parametric space converges to the optimum, and if so how quickly this convergence happens.

7.4.5 Results of the optimisation

The system-level optimisation is implemented for the optimisation problem described in Section 7.4.1 using the iterative SBO method. The iterative SBO results are illustrated in Figure 7.14 showing the parametric boundaries and optimal points for all variables. The optimisation ends after ten iterations after the parametric space is contracted to be less than 0.33 of the original range. Figure 7.15 shows the variation of the objective function values along with the optimisation. The grey dots represent the true model evaluations at all sampling points. The LCOE value tends to

go down as the optimisation progresses, which means true model is implemented closer to the optimal parametric space. The optimum is evaluated by both the surrogate and true models at each iteration. As Figure 7.15 shows, the difference between the LCOE values calculated by the surrogate and true models becomes smaller. This demonstrates that the surrogate model is getting more accurate as the optimisation progresses, which results in better estimation of the LCOE in the region close to the optimum. The optimisation problem ends once the parametric space gets contracted to less than 0.33 of the original range. The number of true model evaluations is 500 in total, with 50 per iteration, and is reduced by 80% compared to the co-optimisation study in Chapter 5 using the genetic algorithm.

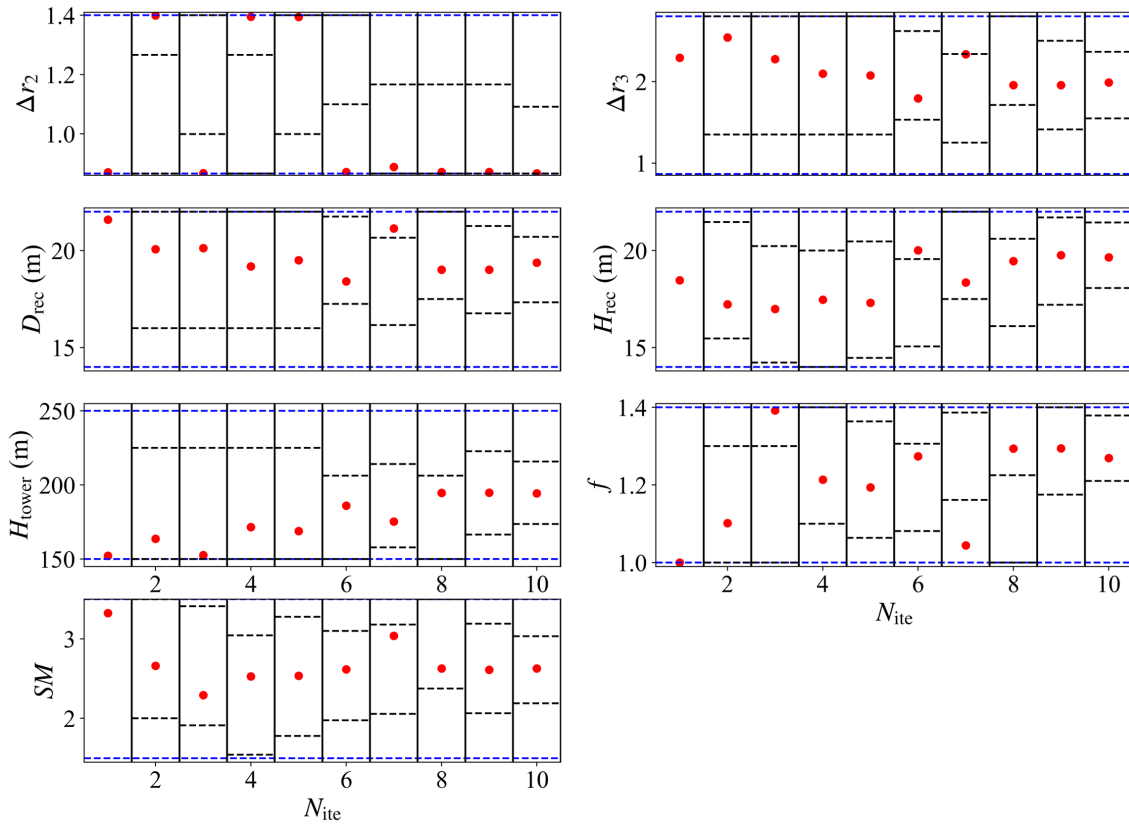


Fig. 7.14: Process of the optimisation. Red dots represent the optimal value at each iteration. The number of simulations is 500, 20% of the GA method.

The results of the optimal design are illustrated in Table 7.2 and compared to the reference system. The optimal value of Δr_2 is 0.87, which is just above the lower parametric boundary of 0.866. This suggests that heliostats in Zone 2 of the field favour smaller spacing between each other. This is because these heliostats do not experience significant shading and blocking losses, while the attenuation and spillage losses are increased due to the denser field. The optimal solar multiple is 2.72, compared to 2.5 in the reference case. For the heliostat field, in the optimal design the oversizing is 25%, compared to 20% in the reference case. The heat exchanger is oversized by 10%,

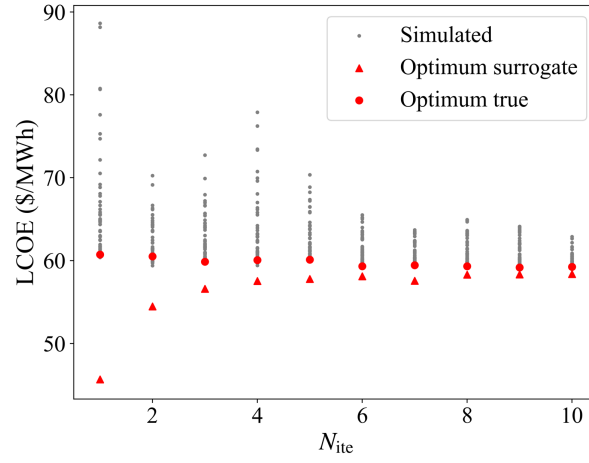


Fig. 7.15: Variation of the objective function. Grey dots represent the sampling results evaluated by the true model. Red triangles and dots represent the optimal point evaluated by the surrogate and true models, respectively.

and the storage has a higher capacity with 13 hours of storage. The optimal design leads to 8.5% more annual electricity output than the reference case and an increase of the capacity factor from 76.7% to 83.2%. The capital cost is higher in the optimal design because of the higher heliostat field, heat exchanger and storage costs. The LCOE is reduced by 0.6 USD/MWh compared to the reference case.

Table 7.2: Comparison of the reference and optimal designs.

		Reference system	Optimal design
Design parameter	Δr_2	1.05	0.87
	Δr_3	1.99	2.28
	N_{hst}	8868	10064
	D_{rec} (m)	18.20	19.0
	H_{rec} (m)	20.10	19.8
	D_o (mm)	33.40	42.16
	H_{tower} (m)	175	188.6
	f_{hst}	1.2	1.25
	t_{storage} (h)	12	13
	f_{HX}	1.0	1.1
	SM	2.5	2.72
Reference data	Q_{ele} (GWh)	671.9	728.8
	C_{cap} (MUSD)	561.5	606.6
	CF (%)	76.7	83.2
	LCOE (USD/MWh)	59.6	59.0

The energy breakdown of the heliostat field and receiver subsystems is illustrated in Figure 7.16 for the optimal case. The optical loss is the largest proportion of all energy terms, even higher than the receiver thermal output. This is because of the high number of heliostats in a single-tower system. Figure 7.17 shows the annual

optical efficiency of all heliostats. The optical efficiency of many far-away heliostats is lower than 30%, which leads to high energy loss.

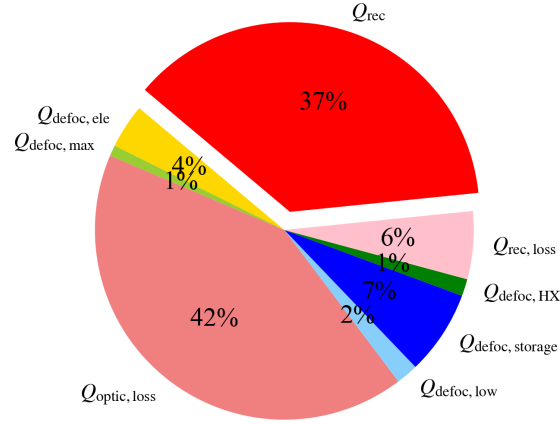


Fig. 7.16: Energy breakdown of the field and the receiver subsystem.

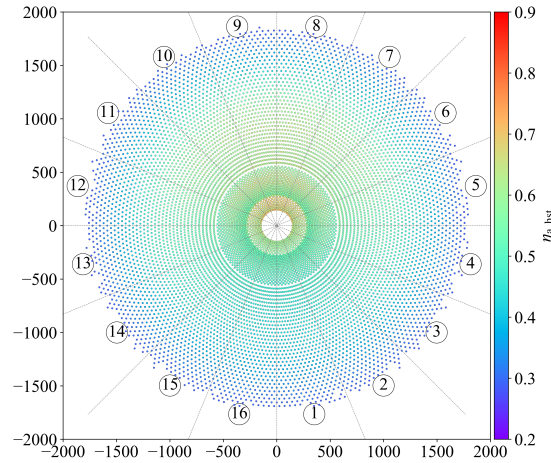


Fig. 7.17: Annual optical efficiency of heliostats for the optimal design. The optical efficiencies are evaluate using the method presented in Section 5.3.2

7.5 Conclusion for this chapter

In this chapter, a parametric study firstly shows the benefits of changing the capacity of the heliostat field, the heat exchanger and the storage system with a fixed power block capacity. A system-level optimisation is then applied to reduce the LCOE by varying the relative sizing of system components. An iterative SBO method is proposed for acceleration of the optimisation. The results show that the number of true model evaluations is reduced by 80% using the iterative SBO method compared to the conventional GA optimisation. The LCOE drops to 59.0 USD/MWh for the optimal design, compared to 59.6 USD/MWh for the reference case. A high capacity factor of 83.2% is achieved in the optimal design.

The optical loss makes up a high proportion of energy losses. New configurations, such as multi-tower [181], modular [182] or multi-cavity [183] may be better options with higher optical efficiency. The design of these more advanced systems can also be done with the optimisation structure discussed in this thesis. The effects of varying receiver/ power block operational temperatures or the power block capacity can also be investigated in a future work.

Conclusions and future work

8.1 Summary of the contributions

This thesis presents original methods for the design of the field-receiver subsystem of next-generation CSP plants and applies them to a series of design cases. Firstly, modelling technologies are introduced, including the instantaneous optical, thermal and mechanical models, annual models and system-level models. These methodologies are the basis of the modelling work concerning the heliostat field and the receiver subsystems in the following sections of this thesis. The specific contributions to the field are highlighted in the following subsections.

8.1.1 Contribution to the topic of cavity receiver performance enhancement

The instantaneous optical and receiver models are evaluated in a performance enhancement study for a cavity receiver. Trade-offs between spillage, reflective, radiative and convective losses determine the best receiver aperture size and the geometry of spillage skirts and secondary reflectors. Absolute efficiency gains of 1 to 1.3 %, equivalent to energy loss reduction of 10.2 to 12.7 % are reported. As a general conclusion, the spillage skirt appears to be a valuable tool for high-efficiency cavity receiver design. Conical and trumpet secondary reflectors, particularly when combined with spillage skirts, offer potential additional benefits provided that the efficiency gains are not counterbalanced by technical challenges or significant cost increases.

8.1.2 Contribution to the topic of heliostat field aiming strategy

A new heliostat aiming strategy (MDBA) is proposed for a cylindrical external receiver with a surround field to closely match net flux with flux limits. A ray-tracing based optical simulation is coupled with heat transfer and thermo-mechanical models. Different optimisation techniques are explored. For a reference heliostat field and receiver system, the feedback-based method can achieve an interception efficiency within 0.5% of equatorial aiming with only 8 ray-tracing simulations. Furthermore, an interpolation and adjustment method is proposed to dynamically predict

the aiming variables across different sun positions and DNI levels to enable annual simulations. Safe flux profiles are achieved using the interpolated results. Compared to previous aiming strategies in literature, the MDBA method is able to more closely match the net flux with the flux limit. The MDBA method is accurate because it is based on ray-tracing and is sufficiently fast, with the optimisation completed within few iterations.

8.1.3 Contribution to the optimisation of the design of central receiver systems

The high accuracy, high-performance MDBA method is sped-up sufficiently to be used in annual performance calculations and is therefore coupled to a co-optimisation method. The co-optimisation method is proposed to simultaneously optimise the field, receiver and the aiming strategy based on annual operation conditions. The method includes an integrated optical, thermal and mechanical model, a system-level model and an optimisation method. Rapid assessments of optical and thermal performances are achieved compared to hour-by-hour simulations. The proposed method is used to co-optimize a system with a surround field and a cylindrical external liquid-sodium receiver. The field layout, the receiver dimensions and the aiming strategy are simultaneously determined to find the optimal design. This is the first time a system optimisation based on an accurate optical model (MCRT) and detailed aiming strategy has been reported in the literature, to the authors' knowledge.

The MDBA method is improved to include a defocusing capacity such that the receiver output can be determined with an oversized heliostat field. An oversized heliostat field enhances the receiver output, especially at low-DNI conditions, and can reduce the LCOE. The improved MDBA calculation is further integrated with the system-level model for annual simulations. Different receiver flow path options and pipe outer diameters are investigated, and a selection procedure is summarised to determine the optimal receiver flow configuration. The proposed method is applied to both a reference receiver with single-pass and double-pass options, and to the Gen3L receiver with a triple-pass option.

Lastly, a system-level study is implemented to achieve the lowest LCOE. Parametric studies show LCOE can be reduced by varying the capacity of the heliostat field, heat exchanger and storage subsystem. A system-level optimisation is applied and accelerated using an iterative surrogate-based optimisation (SBO) method. The results show that the number of true model evaluations is reduced by 80% using the iterative SBO method. The LCOE drops to 59.0 USD/MWh in the optimal design, compared to 59.6 USD/MWh in the reference case. The optimal design with 25% oversizing of the field, 10% oversizing of the heat exchanger, 13 storage hours achieves a high capacity factor of 83.2%.

8.2 Future work

The MDBA method is able to determine the heliostat aiming strategy and defocusing at instantaneous conditions, but cannot yet capture the effect of cloud disturbances. A dynamic aiming strategy is needed for real CSP plant operation. A more advanced aiming strategy with left-right aim points shifting is also suggested as a future study.

The co-optimisation method can be used to explore other types of CSP systems, such as multi-tower, multi-module or multi-cavity systems. Separating a large plant into multiple subsystems can increase the optical efficiency of each subsystem, but may lead to high capital cost. A co-optimisation method could help to find optimised designs by solving the trade-off between output and cost. Similarly, the method developed could be applied to systems with other types of HTFs, such as high-temperature molten salt, and to systems with other temperature ranges.

The developed methodologies can be applied to the design of solar receivers with novel concepts. For example, the pipe diameter and material can be varied between different tube panels, and larger pipe diameter and cheaper materials may be better options for southern banks to reduce the receiver cost. The receiver with novel design ideas can be optimised using the performance and reliability models developed in this work. Similar design and optimisation methodologies can also be applied to heat exchangers and storage tanks designs.

This thesis uses the MCRT technique as the optical tool due to its high accuracy. Convolution methods are widely applied in literature for large ensembles of heliostats on planar or cylindrical surfaces and are faster than MCRT. Future work suggests applying convolution methods to the aiming strategy, receiver design and system-level optimisation for a comparison with those achieved using MCRT.

Bibliography

1. M Hoeven. Solar thermal electricity–technology roadmap. Technical report, International Energy Agency, 2014. (cited on pages xix and 1)
2. James E Pacheco, Robert W Bradshaw, Daniel B Dawson, Wilfredo De la Rosa, Rockwell Gilbert, and Steven H Goods. Final test and evaluation results from the Solar Two project. Technical report, Sandia National Laboratories Albuquerque, NM, 2002. (cited on pages 1 and 106)
3. Juan Ignacio Burgaleta, Santiago Arias, and Diego Ramirez. Gemasolar, the first tower thermosolar commercial plant with molten salt storage. *SolarPACES, Granada, Spain*, pages 20–23, 2011. (cited on pages xix, 1, and 2)
4. Thomas W Overton. Crescent Dunes solar energy project, Tonopah, Nevada. *Power*, 160(12):26–26, 2016. (cited on page 1)
5. Jun Wang, Song Yang, Chuan Jiang, Yaoming Zhang, and Peter D Lund. Status and future strategies for concentrating solar power in China. *Energy Science & Engineering*, 5(2):100–109, 2017. (cited on page 2)
6. Craig S Turchi, Zhiwen Ma, and John Dyreby. Supercritical carbon dioxide power cycle configurations for use in concentrating solar power systems. In *Turbo Expo: Power for Land, Sea, and Air*, volume 44717, pages 967–973. American Society of Mechanical Engineers, 2012. (cited on page 2)
7. Ty Neises and Craig S Turchi. A comparison of supercritical carbon dioxide power cycle configurations with an emphasis on CSP applications. *Energy Procedia*, 49:1187–1196, 2014. (cited on page 2)
8. RW Bradshaw and RW Carling. A review of the chemical and physical properties of molten alkali nitrate salts and their effect on materials used for solar central receivers. *ECS Proceedings Volumes*, 1987(1):959, 1987. (cited on page 2)
9. Eli S Freeman. The kinetics of the thermal decomposition of potassium nitrate and of the reaction between potassium nitrite and oxygen. *Journal of the American Chemical Society*, 79(4):838–842, 1957. (cited on page 2)
10. Clifford Ho. A review of high-temperature particle receivers for concentrating solar power. *Applied Thermal Engineering*, 109:958–969, 2016. (cited on page 2)
11. Antonio L Avila-Marin. Volumetric receivers in solar thermal power plants with central receiver system technology: a review. *Solar Energy*, 85(5):891–910, 2011. (cited on page 2)

12. Jean-Francois P. Pitot de la Beaujardiere and Hanno C.R. Reuter. A review of performance modelling studies associated with open volumetric receiver CSP plant technology. *Renewable and Sustainable Energy Reviews*, 82:3848–3862, 2018. (cited on page 2)
13. Janna Martinek, Sameer Jape, and Craig S Turchi. Evaluation of external tubular configurations for a high-temperature chloride molten salt solar receiver operating above 700°C. *Solar Energy*, 222:115–128, 2021. (cited on page 2)
14. Nicholas Boerema, Graham Morrison, Robert Taylor, and Gary Rosengarten. Liquid sodium versus Hitec as a heat transfer fluid in solar thermal central receiver systems. *Solar Energy*, 86(9):2293–2305, 2012. (cited on pages 2, 3, and 7)
15. M Romero and J González-Aguilar. Next generation of liquid metal and other high-performance receiver designs for concentrating solar thermal (CST) central tower systems. In *Advances in Concentrating Solar Thermal Research and Technology*, pages 129–154. Elsevier, 2017. (cited on page 2)
16. Joe Coventry, Charles Andraka, John Pye, Manuel Blanco, and James Fisher. A review of sodium receiver technologies for central receiver solar power plants. *Solar Energy*, 122:749–762, 2015. (cited on page 3)
17. Craig Wood and Kurt Drewes. Vast solar: Improving performance and reducing cost and risk using high temperature modular arrays and sodium heat transfer fluid. In *Proceedings of the SolarPaces Conference*, 2019. (cited on page 3)
18. Simone Polimeni, Marco Binotti, Luca Moretti, and Giampaolo Manzolini. Comparison of sodium and KCl-MgCl₂ as heat transfer fluids in CSP solar tower with sCO₂ power cycles. *Solar Energy*, 162:510–524, 2018. (cited on page 3)
19. Mattia Cagnoli, Alberto De La Calle, John Pye, Laura Savoldi, and Roberto Zanino. A CFD-supported dynamic system-level model of a sodium-cooled billboard-type receiver for central tower CSP applications. *Solar Energy*, 177: 576–594, 2019. (cited on page 3)
20. Alberto de la Calle, Alicia Bayon, and John Pye. Techno-economic assessment of a high-efficiency, low-cost solar-thermal power system with sodium receiver, phase-change material storage, and supercritical CO₂ recompression Brayton cycle. *Solar Energy*, 199:885–900, 2020. (cited on pages 3 and 13)
21. Andreas Fritsch, Cathy Frantz, and Ralf Uhlig. Techno-economic analysis of solar thermal power plants using liquid sodium as heat transfer fluid. *Solar Energy*, 177:155–162, 2019. (cited on page 4)
22. Tim Conroy, Maurice N Collins, James Fisher, and Ronan Grimes. Thermo-hydraulic analysis of single phase heat transfer fluids in CSP solar receivers. *Renewable Energy*, 129:150–167, 2018. (cited on pages 4 and 24)

23. Tim Conroy, Maurice N Collins, and Ronan Grimes. Integrated optical-thermal-mechanical model for investigations into high temperature sodium receiver operation. *Solar Energy*, 194:751–765, 2019. (cited on pages 4, 6, and 11)
24. Tim Conroy, Maurice N Collins, and Ronan Grimes. Sodium receiver designs for integration with high temperature power cycles. *Energy*, 187:115994, 2019. (cited on pages 4 and 11)
25. Gregory J Kolb. An evaluation of possible next-generation high-temperature molten-salt power towers. Technical report, Sandia National Laboratories Albuquerque, NM, 2011. (cited on page 4)
26. Emilio José Carrizosa Priego, Carmen Ana Domínguez Bravo, Enrique Fernández Cara, and Manuel Quero García. A heuristic method for simultaneous tower and pattern-free field optimization on solar power systems. *Computers & Operations Research*, 57, 109-122., 2015. (cited on pages 4 and 12)
27. Marcelino Sánchez and Manuel Romero. Methodology for generation of heliostat field layout in central receiver systems based on yearly normalized energy surfaces. *Solar Energy*, 80(7):861–874, 2006. (cited on pages 4 and 5)
28. FW Lipps and Lorin L Vant-Hull. A cellwise method for the optimization of large central receiver systems. *Solar Energy*, 20(6):505–516, 1978. (cited on page 4)
29. FW Lipps and Lorin L Vant-Hull. Programmer’s manual for the University of Houston computer code RCELL: cellwise optimization for the solar central receiver project. Technical report, Houston Univ., TX (USA). Energy Lab., 1980. (cited on page 4)
30. A Monreal, M Burisch, M Sanchez, D Pérez, C Villasante, E Olabarrieta, D Olasolo, and A Olarra. EASY: An innovative design for cost effective heliostats/solar fields. *Energy Procedia*, 49:174–183, 2014. (cited on page 4)
31. Francisco J Collado and Jesús Guallar. Campo: Generation of regular heliostat fields. *Renewable Energy*, 46:49–59, 2012. (cited on pages 5 and 102)
32. Corey J Noone, Manuel Torrilhon, and Alexander Mitsos. Heliostat field optimization: A new computationally efficient model and biomimetic layout. *Solar Energy*, 86(2):792–803, 2012. (cited on pages 5, 39, 53, 54, and 65)
33. Maolong Zhang, Lijun Yang, Chao Xu, and Xiaoze Du. An efficient code to optimize the heliostat field and comparisons between the biomimetic spiral and staggered layout. *Renewable Energy*, 87:720–730, 2016. (cited on page 5)
34. Mohamed Gadalla and Mohammad Saghafifar. Thermo-economic and comparative analyses of two recently proposed optimization approaches for circular heliostat fields: Campo radial-staggered and biomimetic spiral. *Solar Energy*, 136:197–209, 2016. (cited on pages xix and 5)

35. Iñigo Les, Amaia Mutuberria, Peter Schöttl, Peter Nitz, Erminia Leonardi, and Lorenzo Pisani. Optical performance comparison between heliostat field generation algorithms. In *AIP Conference Proceedings*, volume 2033, page 040020. AIP Publishing LLC, 2018. (cited on page 5)
36. Erminia Leonardi, Lorenzo Pisani, Iñigo Les, Amaia Mutuberria Larrayoz, Shahab Rohani, and Peter Schöttl. Techno-economic heliostat field optimization: Comparative analysis of different layouts. *Solar Energy*, 180:601–607, 2019. (cited on pages 5, 105, and 124)
37. E Carrizosa, C Domínguez-Bravo, E Fernández-Cara, and M Quero. Boiler and Pressure Vessel Code. Technical report, Institute of Mathematics of University of Seville (IMUS), 2014. (cited on page 5)
38. JG Barberena, A Mutuberria Larrayoz, Marcelino Sánchez, and Ana Bernardos. State-of-the-art of heliostat field layout algorithms and their comparison. *Energy Procedia*, 93:31–38, 2016. (cited on page 5)
39. Francisco J Collado and Jesus Guallar. Quick design of regular heliostat fields for commercial solar tower power plants. *Energy*, 178:115–125, 2019. (cited on pages 5, 104, 111, and 124)
40. Michael J Wagner and Tim Wendelin. SolarPILOT: A power tower solar field layout and characterization tool. *Solar Energy*, 171:185–196, 2018. (cited on pages 5, 7, 11, 12, 20, 67, and 70)
41. Mark Schmitz, Peter Schwarzbözl, Reiner Buck, and Robert Pitz-Paal. Assessment of the potential improvement due to multiple apertures in central receiver systems with secondary concentrators. *Solar Energy*, 80(1):111–120, 2006. (cited on pages 5, 12, 13, and 67)
42. Saeb M Besarati and D Yogi Goswami. A computationally efficient method for the design of the heliostat field for solar power tower plant. *Renewable Energy*, 69:226–232, 2014. (cited on pages 5 and 110)
43. Clotilde Corsi, Manuel Blanco, Jin-Soo Kim, and John Pye. Point-focus multi-receiver fresnel loop—exploring ways to increase the optical efficiency of solar tower systems. In *AIP Conference Proceedings*, volume 2033, page 170001. AIP Publishing LLC, 2018. (cited on page 6)
44. Pasha Piroozmand and Mehrdad Boroushaki. A computational method for optimal design of the multi-tower heliostat field considering heliostats interactions. *Energy*, 106:240–252, 2016. (cited on page 6)
45. Chao Li, Rongrong Zhai, Hongtao Liu, Yongping Yang, and Hao Wu. Optimization of a heliostat field layout using hybrid PSO-GA algorithm. *Applied Thermal Engineering*, 128:33–41, 2018. (cited on page 6)

46. C-J Winter, Rudolf L Sizmann, and Lorin L Vant-Hull. *Solar power plants: fundamentals, technology, systems, economics*. Springer Science & Business Media, 2012. (cited on pages 6, 7, 10, and 26)
47. María Reyes Rodríguez-Sánchez, Antonio Soria-Verdugo, José Antonio Almendros-Ibáñez, Antonio Acosta-Iborra, and Domingo Santana. Thermal design guidelines of solar power towers. *Applied Thermal Engineering*, 63(1): 428–438, 2014. (cited on pages 6 and 106)
48. DC Smith. Design and optimization of tube-type receiver panels for molten salt application. *Solar Engineering*, 2, 1992. (cited on pages 6 and 10)
49. Nicholas Boerema, Graham Morrison, Robert Taylor, and Gary Rosengarten. High temperature solar thermal central-receiver billboard design. *Solar Energy*, 97:356–368, 2013. (cited on page 7)
50. María de los Reyes Rodriguez-Sanchez, Alberto Sanchez-Gonzalez, Carolina Marugan-Cruz, and D Santana. Flow patterns of external solar receivers. *Solar Energy*, 122:940–953, 2015. (cited on pages 7 and 131)
51. Germain Augsburg, Apurba K Das, Erik Boschek, and Michael M Clark. Thermo-mechanical and optical optimization of the molten salt receiver for a given heliostat field. In *AIP Conference Proceedings*, volume 1734, page 030005. AIP Publishing LLC, 2016. (cited on page 7)
52. Charles-Alexis Asselineau, Jose Zapata, and John Pye. Geometrical shape optimization of a cavity receiver using coupled radiative and hydrodynamic modeling. *Energy Procedia*, 69:279–288, 2015. (cited on page 7)
53. Chongzhe Zou, Yanping Zhang, Quentin Falcoz, Pierre Neveu, Cheng Zhang, Weicheng Shu, and Shuhong Huang. Design and optimization of a high-temperature cavity receiver for a solar energy cascade utilization system. *Renewable Energy*, 103:478–489, 2017. (cited on page 7)
54. María de los Reyes Rodríguez-Sánchez, Alberto Sánchez-González, and D Santana. Feasibility study of a new concept of solar external receiver: Variable velocity receiver. *Applied Thermal Engineering*, 128:335–344, 2018. (cited on page 7)
55. Wen-Qi Wang, Yu Qiu, Ming-Jia Li, Feng Cao, and Zhan-Bin Liu. Optical efficiency improvement of solar power tower by employing and optimizing novel fin-like receivers. *Energy Conversion and Management*, 184:219–234, 2019. (cited on page 7)
56. Peter Schöttl, Gregor Bern, José Antonio Fernández Pretel, Thomas Fluri, Peter Nitz, et al. Optimization of solar tower molten salt cavity receivers for maximum yield based on annual performance assessment. *Solar Energy*, 199:278–294, 2020. (cited on pages 7, 11, 28, and 109)

57. Tim Conroy, Maurice N Collins, and Ronan Grimes. A review of steady-state thermal and mechanical modelling on tubular solar receivers. *Renewable and Sustainable Energy Reviews*, 119:109591, 2020. (cited on page 7)
58. María Reyes Rodríguez-Sánchez, Carolina Marugan-Cruz, Antonio Acosta-Iborra, and Domingo Santana. Comparison of simplified heat transfer models and CFD simulations for molten salt external receiver. *Applied thermal engineering*, 73(1):993–1005, 2014. (cited on pages xix, 8, and 24)
59. Ka Lok Lee, Mehdi Jafarian, Farzin Ghanadi, Maziar Arjomandi, and Graham J Nathan. An investigation into the effect of aspect ratio on the heat loss from a solar cavity receiver. *Solar Energy*, 149:20–31, 2017. (cited on page 7)
60. KS Reddy and N Sendhil Kumar. Convection and surface radiation heat losses from modified cavity receiver of solar parabolic dish collector with two-stage concentration. *Heat and Mass Transfer*, 45(3):363–373, 2009. (cited on pages 7 and 9)
61. KS Reddy, T Srihari Vikram, and G Veershetty. Combined heat loss analysis of solar parabolic dish–modified cavity receiver for superheated steam generation. *Solar Energy*, 121:78–93, 2015. (cited on page 7)
62. LC Ngo, Tunde Bello-Ochende, and Josua P Meyer. Numerical modelling and optimisation of natural convection heat loss suppression in a solar cavity receiver with plate fins. *Renewable Energy*, 74:95–105, 2015. (cited on page 7)
63. Fuqing Cui, Yaling He, Zedong Cheng, and Yinshi Li. Study on combined heat loss of a dish receiver with quartz glass cover. *Applied Energy*, 112:690–696, 2013. (cited on page 7)
64. Yu Qiu, Ya-Ling He, Ming Wu, and Zhang-Jing Zheng. A comprehensive model for optical and thermal characterization of a linear Fresnel solar reflector with a trapezoidal cavity receiver. *Renewable Energy*, 97:129–144, 2016. (cited on page 7)
65. Shuai Yong, Wang Fu-Qiang, Xia Xin-Lin, Tan He-Ping, and Liang Ying-Chun. Radiative properties of a solar cavity receiver/reactor with quartz window. *International Journal of Hydrogen Energy*, 36(19):12148–12158, 2011. (cited on page 7)
66. Jiabin Fang, Nan Tu, Juan F Torres, Jinjia Wei, and John Pye. Numerical investigation of the natural convective heat loss of a solar central cavity receiver with air curtain. *Applied Thermal Engineering*, 152:147–159, 2019. (cited on page 7)
67. Song Yang, Jun Wang, Peter D Lund, Siyu Wang, and Chuan Jiang. Reducing convective heat losses in solar dish cavity receivers through a modified air-curtain system. *Solar Energy*, 166:50–58, 2018. (cited on page 7)

68. J Jack Zhang, John Pye, and Graham Hughes. Active air flow control to reduce cavity receiver heat loss. In *Energy Sustainability*, volume 56840. American Society of Mechanical Engineers, 2015. (cited on page 7)
69. Aldo Steinfeld and Markus Schubnell. Optimum aperture size and operating temperature of a solar cavity-receiver. *Solar Energy*, 50(1):19–25, 1993. (cited on page 8)
70. Andreas Luzzi, Keith Lovegrove, Ermanno Filippi, Hans Fricker, Manfred Schmitz-Goeb, Mathew Chandapillai, and Stephen Kaneff. Techno-economic analysis of a 10 MWe solar thermal power plant using ammonia-based thermochemical energy storage. *Solar Energy*, 66(2):91–101, 1999. (cited on page 8)
71. M Prakash, SB Kedare, and JK Nayak. Investigations on heat losses from a solar cavity receiver. *Solar Energy*, 83(2):157–170, 2009. (cited on page 8)
72. Sawat Paitoonsurikarn, Keith Lovegrove, Graham Hughes, and John Pye. Numerical investigation of natural convection loss from cavity receivers in solar dish applications. *Journal of Solar Energy Engineering*, 133(2), 2011. (cited on page 8)
73. John Pye, Graham Hughes, Ehsan Abbasi, Charles-Alexis Asselineau, Greg Burgess, Joe Coventry, William Logie, Felix Venn, and José Zapata. Development of a higher-efficiency tubular cavity receiver for direct steam generation on a dish concentrator. In *AIP conference proceedings*, volume 1734, page 030029. AIP Publishing LLC, 2016. (cited on pages xix, 8, 9, 48, 51, and 66)
74. John Pye, Joe Coventry, Felix Venn, José Zapata, Ehsan Abbasi, Charles-Alexis Asselineau, Greg Burgess, Graham Hughes, and William Logie. Experimental testing of a high-flux cavity receiver. In *AIP Conference Proceedings*, volume 1850, page 110011. AIP Publishing LLC, 2017. (cited on pages 8, 21, and 48)
75. Mark Mehos, Craig Turchi, Judith Vidal, Michael Wagner, Zhiwen Ma, Clifford Ho, William Kolb, Charles Andraka, and Alan Kruienza. Concentrating solar power Gen3 demonstration roadmap. Technical report, National Renewable Energy Lab.(NREL), Golden, CO (United States), 2017. (cited on page 8)
76. T Hahm, H Schmidt-Traub, and B Leßmann. A cone concentrator for high-temperature solar cavity-receivers. *Solar Energy*, 65(1):33–41, 1999. (cited on page 9)
77. R Winston and WT Welford. Design of nonimaging concentrators as second stages in tandem with image-forming first-stage concentrators. *Applied Optics*, 19(3):347–351, 1980. (cited on page 9)
78. R Winston, J O’Gallagher, and U Ortabasi. Point focus dishes with relaxed optical tolerances utilizing nonimaging secondary concentrators. In *Proc. Annual Meeting of the American Solar Energy Socie*, page 191, 1984. (cited on page 9)

79. D Suresh, J O’Gallagher, and R Winston. A heat transfer analysis for passively cooled “trumpet” secondary concentrators. 1987. (cited on page 9)
80. John R Bean and Richard B Diver. Technical status of the dish/stirling joint venture program. Technical report, Sandia National Laboratories, 1995. (cited on page 9)
81. Huawei Chang, Chen Duan, Ke Wen, Yuting Liu, Can Xiang, Zhongmin Wan, Sinian He, Changwei Jing, and Shuiming Shu. Modeling study on the thermal performance of a modified cavity receiver with glass window and secondary reflector. *Energy Conversion and Management*, 106:1362–1369, 2015. (cited on page 9)
82. H Hinterberger and R Winston. Efficient light coupler for threshold Čerenkov counters. *Review of Scientific Instruments*, 37(8):1094–1095, 1966. (cited on page 9)
83. Meng Tian, Yuehong Su, Hongfei Zheng, Gang Pei, Guiqiang Li, and Saffa Rif-fat. A review on the recent research progress in the compound parabolic concentrator (CPC) for solar energy applications. *Renewable and Sustainable Energy Reviews*, 82:1272–1296, 2018. (cited on page 9)
84. Srikanth Madala and Robert F Boehm. A review of nonimaging solar concentrators for stationary and passive tracking applications. *Renewable and Sustainable Energy Reviews*, 71:309–322, 2017. (cited on page 9)
85. Lifeng Li, Bo Wang, John Pye, and Wojciech Lipiński. Temperature-based optical design, optimization and economics of solar polar-field central receiver systems with an optional compound parabolic concentrator. *Solar Energy*, 206:1018–1032, 2020. (cited on pages 9, 12, and 62)
86. Lorin L Vant-Hull. Central tower concentrating solar power (CSP) systems. In *Concentrating solar power technology*, pages 240–283. Elsevier, 2012. (cited on page 10)
87. Shuang Wang, Charles-Alexis Asselineau, Ye Wang, John Pye, and Joe Coventry. Performance enhancement of cavity receivers with spillage skirts and secondary reflectors in concentrated solar dish and tower systems. *Solar Energy*, 208:708–727, 2020. (cited on pages 10 and 12)
88. William Logie, John Pye, and Joe Coventry. Thermoelastic stress in concentrating solar receiver tubes: A retrospect on stress analysis methodology, and comparison of salt and sodium. *Solar Energy*, 160:368–379, 2018. (cited on pages xix, 10, 25, 26, and 125)
89. Francisco J Collado and Jesus Guallar. A two-parameter aiming strategy to reduce and flatten the flux map in solar power tower plants. *Solar Energy*, 188: 185–189, 2019. (cited on pages 10, 73, and 76)

90. Robert Flesch, Cathy Frantz, Daniel Maldonado Quinto, and Peter Schwarzbözl. Towards an optimal aiming for molten salt power towers. *Solar Energy*, 155: 1273–1281, 2017. (cited on pages 10, 11, and 73)
91. Adrien Salomé, Fabien Chhel, Gilles Flamant, Alain Ferrière, and Frederik Thiery. Control of the flux distribution on a solar tower receiver using an optimized aiming point strategy: Application to themis solar tower. *Solar Energy*, 94:352–366, 2013. (cited on page 10)
92. Saeb M Besarati, D Yogi Goswami, and Elias K Stefanakos. Optimal heliostat aiming strategy for uniform distribution of heat flux on the receiver of a solar power tower plant. *Energy Conversion and Management*, 84:234–243, 2014. (cited on page 10)
93. Boris Belhomme, Robert Pitz-Paal, and Peter Schwarzbözl. Optimization of heliostat aim point selection for central receiver systems based on the ant colony optimization metaheuristic. *Journal of Solar Energy Engineering*, 136(1), 2014. (cited on page 10)
94. Thomas Ashley, Emilio Carrizosa, and Enrique Fernández-Cara. Optimisation of aiming strategies in solar power tower plants. *Energy*, 137:285–291, 2017. (cited on page 10)
95. Nicolas C Cruz, Juana López Redondo, José Domingo Álvarez, Manuel Berenguel, and Pilar Martínez Ortigosa. A parallel teaching–learning-based optimization procedure for automatic heliostat aiming. *The Journal of Supercomputing*, 73(1):591–606, 2017. (cited on page 10)
96. Lorin L Vant-Hull. The role of “allowable flux density” in the design and operation of molten-salt solar central receivers. *Journal of Solar Energy Engineering*, 124(2):165–169, 2002. (cited on pages 10 and 76)
97. Alberto Sánchez-González and Domingo Santana. Solar flux distribution on central receivers: A projection method from analytic function. *Renewable Energy*, 74:576–587, 2015. (cited on page 10)
98. Alberto Sánchez-González, María Reyes Rodríguez-Sánchez, and Domingo Santana. Aiming factor to flatten the flux distribution on cylindrical receivers. *Energy*, 153:113–125, 2018. (cited on pages 10, 73, and 76)
99. Alberto Sánchez-González, María Reyes Rodríguez-Sánchez, and Domingo Santana. Aiming strategy model based on allowable flux densities for molten salt central receivers. *Solar Energy*, 157:1130–1144, 2017. (cited on pages xix, 10, 11, 25, 80, and 85)
100. Marco Astolfi, Marco Binotti, Simone Mazzola, Luca Zanellato, and Giampaolo Manzolini. Heliostat aiming point optimization for external tower receiver. *Solar Energy*, 157:1114–1129, 2017. (cited on pages 10 and 73)

101. Jesús García, Yen Chean Soo Too, Ricardo Vasquez Padilla, Andrew Beath, Jin-Soo Kim, and Marco E Sanjuan. Dynamic performance of an aiming control methodology for solar central receivers due to cloud disturbances. *Renewable Energy*, 121:355–367, 2018. (cited on pages 10 and 11)
102. Jesús García, Rodrigo Barraza, Yen Chean Soo Too, Ricardo Vásquez Padilla, David Acosta, Danilo Estay, and Patricio Valdivia. Aiming clusters of heliostats over solar receivers for distributing heat flux using one variable per group. *Renewable Energy*, 160:584–596, 2020. (cited on page 11)
103. David Roberto Acosta Villamil, Jesus Garcia, Marco Sanjuan, Laurin Oberkirsch, and Peter Schwarzbözl. Flux-feedback as a fast alternative to control groups of aiming points in molten salt power towers. *Solar Energy*, 2021. (cited on page 11)
104. Ye Wang, Daniel Potter, Charles-Alexis Asselineau, Clotilde Corsi, Michael Wagner, Cyril Caliot, Benjamin Piaud, Manuel Blanco, Jin-Soo Kim, and John Pye. Verification of optical modelling of sunshape and surface slope error for concentrating solar power systems. *Solar Energy*, 195:461–474, 2020. (cited on pages xix, 11, 20, 21, 22, 67, and 101)
105. Kun Wang, Ya-Ling He, Xiao-Dai Xue, and Bao-Cun Du. Multi-objective optimization of the aiming strategy for the solar power tower with a cavity receiver by using the non-dominated sorting genetic algorithm. *Applied Energy*, 205:399–416, 2017. (cited on page 11)
106. Qiang Yu, Zhifeng Wang, and Ershu Xu. Analysis and improvement of solar flux distribution inside a cavity receiver based on multi-focal points of heliostat field. *Applied Energy*, 136:417–430, 2014. (cited on page 11)
107. Benjamin Grange and Gilles Flamant. Aiming strategy on a prototype-scale solar receiver: Coupling of Tabu search, ray-tracing and thermal models. *Sustainability*, 13(7):3920, 2021. (cited on page 11)
108. Wen-Qi Wang, Ming-Jia Li, Ze-Dong Cheng, Dong Li, and Zhan-Bin Liu. Coupled optical-thermal-stress characteristics of a multi-tube external molten salt receiver for the next generation concentrating solar power. *Energy*, page 121110, 2021. (cited on page 11)
109. A Ramos and F Ramos. Strategies in tower solar power plant optimization. *Solar Energy*, 86(9):2536–2548, 2012. (cited on page 12)
110. Francisco J Collado and Jesus Guallar. Two-stages optimised design of the collector field of solar power tower plants. *Solar Energy*, 135:884–896, 2016. (cited on page 12)
111. Nate Blair, Aron P Dobos, Janine Freeman, Ty Neises, Michael Wagner, Tom Ferguson, Paul Gilman, and Steven Janzou. System advisor model, SAM 2014.1. 14:

- General description. Technical report, National Renewable Energy Lab.(NREL), Golden, CO (United States), 2014. (cited on pages 12, 28, 110, and 111)
112. Mehdi Aghaei Meybodi and Andrew C Beath. Impact of cost uncertainties and solar data variations on the economics of central receiver solar power plants: An Australian case study. *Renewable Energy*, 93:510–524, 2016. (cited on page 12)
113. Clifford Ho, Mark Mehos, Craig Turchi, and Michael Wagner. Probabilistic analysis of power tower systems to achieve sunshot goals. *Energy Procedia*, 49: 1410–1419, 2014. (cited on page 12)
114. Emiliano Casati, Francesco Casella, and Piero Colonna. Design of CSP plants with optimally operated thermal storage. *Solar Energy*, 116:371–387, 2015. (cited on pages 12 and 13)
115. Ahmed Aly, Ana Bernardos, Carlos M Fernandez-Peruchena, Steen Solvang Jensen, and Anders Branth Pedersen. Is concentrated solar power (CSP) a feasible option for Sub-Saharan Africa: Investigating the techno-economic feasibility of CSP in Tanzania. *Renewable Energy*, 135:1224–1240, 2019. (cited on page 12)
116. Lidia Martín and Mariano Martín. Optimal year-round operation of a concentrated solar energy plant in the south of Europe. *Applied Thermal Engineering*, 59 (1-2):627–633, 2013. (cited on page 12)
117. Zhao Zhu, Da Zhang, Peggy Mischke, and Xiliang Zhang. Electricity generation costs of concentrated solar power technologies in China based on operational plants. *Energy*, 89:65–74, 2015. (cited on page 13)
118. Thomas Schinko and Nadejda Komendantova. De-risking investment into concentrated solar power in north africa: Impacts on the costs of electricity generation. *Renewable Energy*, 92:262–272, 2016. (cited on page 13)
119. Edouard González-Roubaud, David Pérez-Osorio, and Cristina Prieto. Review of commercial thermal energy storage in concentrated solar power plants: Steam vs. molten salts. *Renewable and Sustainable Energy Reviews*, 80:133–148, 2017. (cited on page 13)
120. Ren Ling-zhi, Yu Xin-xuan, Zhang Yu-zhuo, et al. Cost-benefit evolution for concentrated solar power in China. *Journal of Cleaner Production*, 190:471–482, 2018. (cited on page 13)
121. Paul Scott, Alberto de la Calle Alonso, James T Hinkley, and John Pye. Solartherm: A flexible Modelica-based simulator for CSP systems. In *AIP Conference Proceedings*, volume 1850, page 160026. AIP Publishing LLC, 2017. (cited on pages 13, 30, 110, and 124)

122. Austin Fleming, Charles Folsom, Heng Ban, and Zhiwen Ma. A general method to analyze the thermal performance of multi-cavity concentrating solar power receivers. *Solar Energy*, 150:608–618, 2017. (cited on pages 13 and 67)
123. Daniel Buie, AG Monger, and CJ Dey. Sunshape distributions for terrestrial solar simulations. *Solar Energy*, 74(2):113–122, 2003. (cited on pages 17 and 102)
124. Lifeng Li, John Pye, and Wojciech Lipiński. Review of optical studies on central tower concentrators. In *Optics for Solar Energy*, pages RTu3C–3. Optical Society of America, 2015. (cited on pages xix and 19)
125. Francisco J Collado, A Gómez, and JA Turégano. An analytic function for the flux density due to sunlight reflected from a heliostat. *Solar Energy*, 37(3):215–234, 1986. (cited on page 20)
126. Theodore A Dellin and Miriam J Fish. User’s manual for DELSOL: a computer code for calculating the optical performance, field layout, and optimal system design for solar central receiver plants. Technical report, Sandia National Laboratories, Livermore, CA, 1979. (cited on page 20)
127. Peter Schwarzbözl, Robert Pitz-Paal, and Mark Schmitz. Visual HFLCAL-a software tool for layout and optimisation of heliostat fields. In *Proceedings*, 2009. (cited on page 20)
128. Manuel J Blanco, Amaia Mutuberria, Pierre Garcia, Raquel Gastesi, and Victor Martin. Preliminary validation of Tonatiuh. In *SolarPACES 2009 International Conference, At Berlin (Germany)*, volume 1, page 2009, 2009. (cited on page 20)
129. Tim Wendelin. SolTRACE: a new optical modeling tool for concentrating solar optics. In *International Solar Energy Conference*, volume 36762, pages 253–260, 2003. (cited on page 20)
130. Y. Meller. Tracer package: an open source, object oriented, ray-tracing library in python language. 2013. (cited on pages 20 and 42)
131. Cyril Caliot, Hadrien Benoit, Emmanuel Guillot, Jean-Louis Sans, Alain Ferriere, Gilles Flamant, Christophe Coustet, and Benjamin Piaud. Validation of a monte carlo integral formulation applied to solar facility simulations and use of sensitivities. *Journal of Solar Energy Engineering*, 137(2), 2015. (cited on pages 20, 21, 42, 68, 102, and 124)
132. Daniel F Potter, Jin-Soo Kim, Alex Khassapov, Ric Pascual, Lachlan Hetherton, and Zikai Zhang. Heliosim: An integrated model for the optimisation and simulation of central receiver CSP facilities. In *AIP Conference Proceedings*, volume 2033, page 210011. AIP Publishing LLC, 2018. (cited on page 20)

133. Charles N Vittitoe and Frank Biggs. User's guide to HELIOS: a computer program for modeling the optical behavior of reflecting solar concentrators. Technical report, Sandia National Laboratories, Albuquerque, NM, 1981. (cited on page 21)
134. Charles-Alexis Asselineau, Jose Zapata, and John Pye. Integration of Monte-Carlo ray tracing with a stochastic optimisation method: application to the design of solar receiver geometry. *Optics Express*, 23(11):A437–A443, 2015. (cited on page 21)
135. James Ahrens, Berk Geveci, and Charles Law. Paraview: An end-user tool for large data visualization. *The Visualization Handbook*, 717(8), 2005. (cited on page 22)
136. Benjamin Grange, Antoine Perez, William Baltus, Alex Le Gal, and Gilles Flamant. Comparison of simulated and measured flux distributions at the aperture of the next-CSP solar receiver. *SolarPACES*, 2020. (cited on page 22)
137. Michael F Modest and Sandip Mazumder. *Radiative heat transfer*. Academic Press, 2021. (cited on page 23)
138. Dennis L Siebers and John S Kraabel. Estimating convective energy losses from solar central receivers. Technical report, Sandia National Labs., Livermore, CA (USA), 1984. (cited on page 23)
139. AM Clausing. An analysis of convective losses from cavity solar central receivers. *Solar Energy*, 27(4):295–300, 1981. (cited on page 23)
140. Richard N Lyon. Liquid metal heat transfer coefficients. *Chem. Eng. Prog.*, 47: 75–79, 1951. (cited on page 23)
141. Peter Schöttl, Gregor Bern, De Wet van Rooyen, Anna Heimsath, Thomas Fluri, and Peter Nitz. Solar tower cavity receiver aperture optimization based on transient optical and thermo-hydraulic modeling. In *AIP Conference Proceedings*, volume 1850, page 030046. AIP Publishing LLC, 2017. (cited on page 24)
142. Charles-Alexis Asselineau. *Geometrical optimisation of receivers for concentrating solar thermal systems*. PhD thesis, The Australian National University, 2018. (cited on pages 24, 25, 37, 42, 43, 69, 102, and 124)
143. William Logie, Sameer Jape, Janna Martinek, John Pye, and Joe Coventry. Structural integrity of chloride salt and sodium cooled advanced solar central alloy 740H receiver tubes. *SolarPACES*, 2020. (cited on pages xix, 25, 26, 70, 102, and 124)
144. Francisco J Collado and Jesús Guallar. A review of optimized design layouts for solar power tower plants with campo code. *Renewable and Sustainable Energy Reviews*, 20:142–154, 2013. (cited on pages 26 and 104)

145. Peter Schöttl, Karolina Ordóñez Moreno, Gregor Bern, Peter Nitz, et al. Novel sky discretization method for optical annual assessment of solar tower plants. *Solar Energy*, 138:36–46, 2016. (cited on page 27)
146. Victor Grigoriev, Clotilde Corsi, and Manuel Blanco. Fourier sampling of sun path for applications in solar energy. In *AIP Conference Proceedings*, volume 1734, page 020008. AIP Publishing LLC, 2016. (cited on pages xix, 27, and 104)
147. Meinel A B and Meinel M P. Applied solar energy, 1976. (cited on pages 27, 95, and 127)
148. Peter Fritzson, Peter Aronsson, Adrian Pop, Hakan Lundvall, Kaj Nystrom, Levon Saldamli, David Broman, and Anders Sandholm. OpenModelica-a free open-source environment for system modeling, simulation, and teaching. In *2006 IEEE International Symposium on Intelligent Control*, pages 1588–1595. IEEE, 2006. (cited on page 27)
149. Wolfgang Schiel, M Geyer, and RC Contreras. The IEA/SSPS high flux experiment. 1987. (cited on page 29)
150. Salvatore Guccione. Design and optimization of a sodium-molten salt heat exchanger for concentrating solar power applications, 2020. (cited on pages 30 and 32)
151. Craig Turchi, Samuel Gage, Janna Martinek, Sameer Jape, Ken Armijo, Joe Coventry, John Pye, Charles-Alexis Asselineau, Felix Venn, William Logie, et al. CSP Gen3: Liquid-phase pathway to sunshot. Technical report, National Renewable Energy Lab.(NREL), Golden, CO (United States), 2021. (cited on pages 30, 139, 140, 141, 142, and 146)
152. Ty Neises and Craig Turchi. Supercritical carbon dioxide power cycle design and configuration optimization to minimize levelized cost of energy of molten salt power towers operating at 650°C. *Solar Energy*, 181:27–36, 2019. (cited on pages 30, 31, and 33)
153. Armando Fontalvo, Salvatore Guccione, Ye Wang, Shuang Wang, Zebedee Kee, Charles-Alexis Asselilneau, Daniel Potter, Felix Venn, Janna Martinek, Craig Turchi, Joe Coventry, and John Pye. System-level comparison of sodium and salt systems in support of the Gen3 liquids pathway. SolarPACES, 2020. (cited on pages 32, 110, and 124)
154. J. K. Fink and L. Leibowitz. Thermodynamic and transport properties of sodium liquid and vapor. *Office of Scientific Technical Information Technical Reports*, 1995. (cited on pages 38, 106, and 124)
155. Keith Lovegrove, Gregory Burgess, and John Pye. A new 500 m² paraboloidal dish solar concentrator. *Solar Energy*, 85(4):620–626, 2011. (cited on pages 39, 45, and 65)

156. J. O’Gallagher and R. Winston. Test of a "trumpet" secondary concentrator with a paraboloidal dish primary. *Solar Energy*, 36(1):37–44, 1986. (cited on page 40)
157. G. L. Dai, X. L. Xia, C. Sun, and H. C. Zhang. Numerical investigation of the solar concentrating characteristics of 3D CPC and CPC-DC. *Solar Energy*, 85(11): 2833–2842, 2011. (cited on page 41)
158. Roland Winston, Juan C Miñano, Pablo G Benitez, et al. *Nonimaging optics*. Elsevier, 2005. (cited on page 50)
159. Fuqiang Wang, Riyi Lin, Bin Liu, Heping Tan, and Yong Shuai. Optical efficiency analysis of cylindrical cavity receiver with bottom surface convex. *Solar Energy*, 90:195–204, 2013. (cited on page 51)
160. Germain Augsburger. *Thermo-economic optimisation of large solar tower power plants*. PhD thesis, EPFL, 2013. (cited on pages 67, 70, and 73)
161. Charles-Alexis Asselineau, William Logie, John Pye, Felix Venn, Shuang Wang, and Joe Coventry. Design of a heliostat field and liquid sodium cylindrical receiver for the Gen3 liquids pathway. SolarPACES, 2020. (cited on pages 68 and 102)
162. Joe Coventry, Charles-Alexis Asselineau, Armando Fontalvo, Salvatore Guc-cione, Jin-Soo Kim, William Logie, Daniel Potter, John Pye, Wes Stein, Felix Venn, and Shuang Wang. Development of an integrated sodium-salt CSP plant for Gen3. SolarPACES, 2020. (cited on pages 68, 102, and 110)
163. David Charbonneau, Timothy M Brown, David W Latham, and Michel Mayor. Detection of planetary transits across a sun-like star. *The Astrophysical Journal Letters*, 529(1):L45, 1999. (cited on page 68)
164. Michael S Eldred, Anthony A Giunta, Bart G van Bloemen Waanders, Steven F Wojtkiewicz, William E Hart, and Mario P Alleva. DAKOTA, a multilevel parallel object-oriented framework for design optimization, parameter estimation, uncertainty quantification, and sensitivity analysis. Technical report, 2006. (cited on pages 81, 110, and 154)
165. Fabian Pedregosa, Gaël Varoquaux, Alexandre Gramfort, Vincent Michel, Bertrand Thirion, Olivier Grisel, Mathieu Blondel, Peter Prettenhofer, Ron Weiss, Vincent Dubourg, et al. Scikit-learn: Machine learning in python. *Journal of Machine Learning Research*, 12:2825–2830, 2011. (cited on page 91)
166. John A Duffie, William A Beckman, and Nathan Blair. *Solar engineering of thermal processes, photovoltaics and wind*. John Wiley & Sons, 2020. (cited on page 95)
167. Fabian Gross, Willem A Landman, Markus Balz, and Dengke Sun. Robust aim point strategy for dynamic solar tower plant operation. In *AIP Conference Proceedings*, volume 2303, page 030018. AIP Publishing LLC, 2020. (cited on page 99)

168. ISO 6708 1995. Pipework components—definition and selection of DN (nominal size). Standard, 1995. (cited on page 102)
169. John A Duffie and William A Beckman. *Solar engineering of thermal processes*. John Wiley & Sons, 2013. (cited on pages xxii and 105)
170. Meige Zheng, José Zapata, Charles-Alexis Asselineau, Joe Coventry, and John Pye. Analysis of tubular receivers for concentrating solar tower systems with a range of working fluids, in exergy-optimised flow-path configurations. *Solar Energy*, 211:999–1016, 2020. (cited on page 106)
171. Bruce D Kelly. Advanced thermal storage for central receivers with supercritical coolants. Technical report, Abengoa Solar Inc., 2010. (cited on pages 110 and 111)
172. Caitlin Murphy, Yinong Sun, Wesley J Cole, Galen J Maclaurin, Mark S Mehos, and Craig S Turchi. The potential role of concentrating solar power within the context of DOE’s 2030 solar cost targets. Technical report, National Renewable Energy Lab.(NREL), Golden, CO (United States), 2019. (cited on page 111)
173. John Eddy and Kemper Lewis. Effective generation of pareto sets using genetic programming. In *Proceedings of ASME design engineering technical conference*, volume 132, 2001. (cited on pages 110 and 111)
174. Alexis B Zavoico. Solar power tower design basis document. Technical report, Sandia National Laboratories Albuquerque, NM, 2001. (cited on page 112)
175. Alexander H Slocum, Daniel S Codd, Jacopo Buongiorno, Charles Forsberg, Thomas McKrell, Jean-Christophe Nave, Costas N Papanicolas, Amin Ghouseity, Corey J Noone, Stefano Passerini, et al. Concentrated solar power on demand. *Solar Energy*, 85(7):1519–1529, 2011. (cited on page 123)
176. Peter Schöttl, Gregor Bern, Jonathan Flesch, Thomas Fluri, Peter Nitz, et al. Efficient modeling of variable solar flux distribution on solar tower receivers by interpolation of few discrete representations. *Solar Energy*, 160:43–55, 2018. (cited on page 125)
177. Michael J Wagner. Simulation and predictive performance modeling of utility-scale central receiver system power plants. 2008. (cited on page 131)
178. Shuang Wang, Charles-Alexis Asselineau, William R Logie, John Pye, and Joe Coventry. Mdba: An accurate and efficient method for aiming heliostats. *Solar Energy*, 225:694–707, 2021. (cited on page 140)
179. Alexander IJ Forrester and Andy J Keane. Recent advances in surrogate-based optimization. *Progress in Aerospace Sciences*, 45(1-3):50–79, 2009. (cited on pages 153 and 154)

180. Virginia Torczon. On the convergence of pattern search algorithms. *SIAM Journal on Optimization*, 7(1):1–25, 1997. (cited on page 154)
181. Florian Arbes, Willem Landman, Gerhard Weinrebe, Markus Wöhrbach, Daniel Gebreiter, José M Estebaranz, Daniel Pereira, and Alfonso Jurado. Multi tower systems and simulation tools. In *AIP Conference Proceedings*, volume 2126, page 030004. AIP Publishing LLC, 2019. (cited on page 159)
182. C Tyner and D Wasyluk. eSolar’s modular, scalable molten salt power tower reference plant design. *Energy Procedia*, 49:1563–1572, 2014. (cited on page 159)
183. E Carrizosa, C Domínguez-Bravo, Enrique Fernández-Cara, and M Quero. Optimization of multiple receivers solar power tower systems. *Energy*, 90:2085–2093, 2015. (cited on page 159)